Vassilis Theofilis
Julio Soria   *Editors*

Instability and Control of Massively Separated Flows

Proceedings of the International Conference on Instability and Control of Massively Separated Flows, held in Prato, Italy, from 4–6 September 2013

Fluid Mechanics and Its Applications

Volume 107

Aims and Scope of the Series

The purpose of this series is to focus on subjects in which fluid mechanics plays a fundamental role.

As well as the more traditional applications of aeronautics, hydraulics, heat and mass transfer etc., books will be published dealing with topics which are currently in a state of rapid development, such as turbulence, suspensions and multiphase fluids, super and hypersonic flows and numerical modeling techniques.

It is a widely held view that it is the interdisciplinary subjects that will receive intense scientific attention, bringing them to the forefront of technological advancement. Fluids have the ability to transport matter and its properties as well as to transmit force, therefore fluid mechanics is a subject that is particularly open to cross fertilization with other sciences and disciplines of engineering. The subject of fluid mechanics will be highly relevant in domains such as chemical, metallurgical, biological and ecological engineering. This series is particularly open to such new multidisciplinary domains.

The median level of presentation is the first year graduate student. Some texts are monographs defining the current state of a field; others are accessible to final year undergraduates; but essentially the emphasis is on readability and clarity.

Vassilis Theofilis · Julio Soria
Editors

Instability and Control of Massively Separated Flows

Proceedings of the International Conference on Instability and Control of Massively Separated Flows, held in Prato, Italy, from 4–6 September 2013

Springer

Editors
Vassilis Theofilis
School of Aerospace Engineering
Technical University of Madrid
Madrid
Spain

Julio Soria
Department of Mechanical
   and Aerospace Engineering
Monash University
Melbourne, VIC
Australia

and

Department of Aeronautical Engineering
King Abdulaziz University
Jeddah
United Kingdom of Saudi Arabia

Preface

Instabilities and Boundary Value Problems

M Gaster
(Michael.Gaster.1@city.ac.uk)

Prato Italy September 2013

CITY UNIVERSITY
LONDON

In 1954 I started my research on separation bubbles.

A sharp nosed aerofoil has a steep adverse pressure gradient aft of the nose that causes the boundary layer to separate. At high Reynolds numbers the separated shear layer will become turbulent and reattach forming a 'short bubble'.

At lower Reynolds numbers the flow may fail to reattach, or it may form a 'long bubble'.

This so-called bursting of the bubble causes a drastic loss of lift and is called a leading edge stall.

Inviscid flow

High Reynolds number

Low Reynolds number
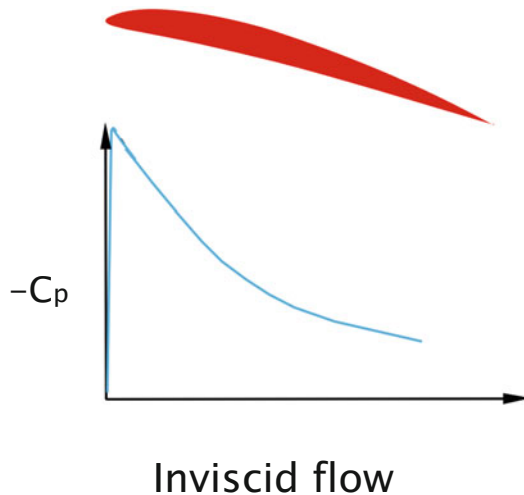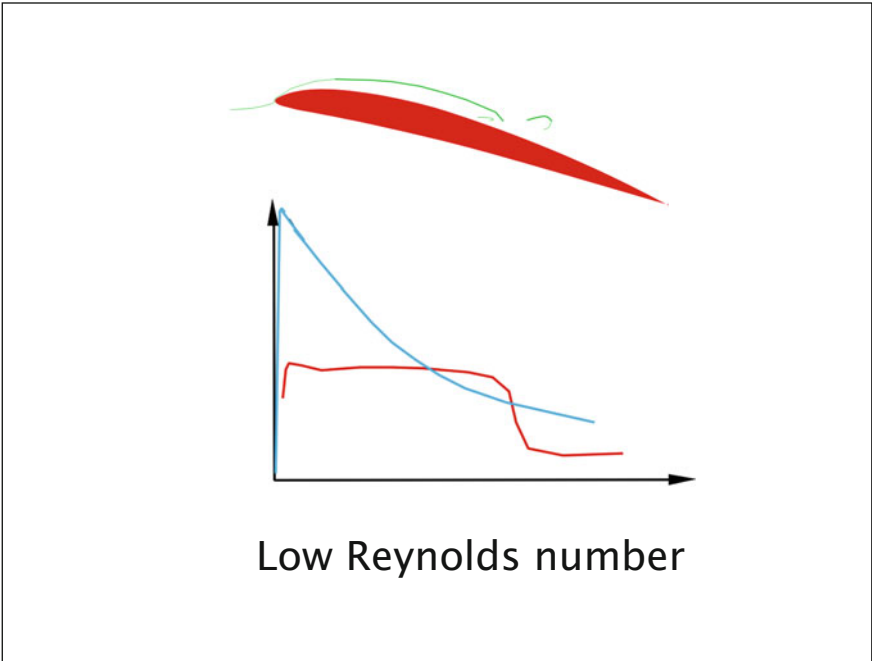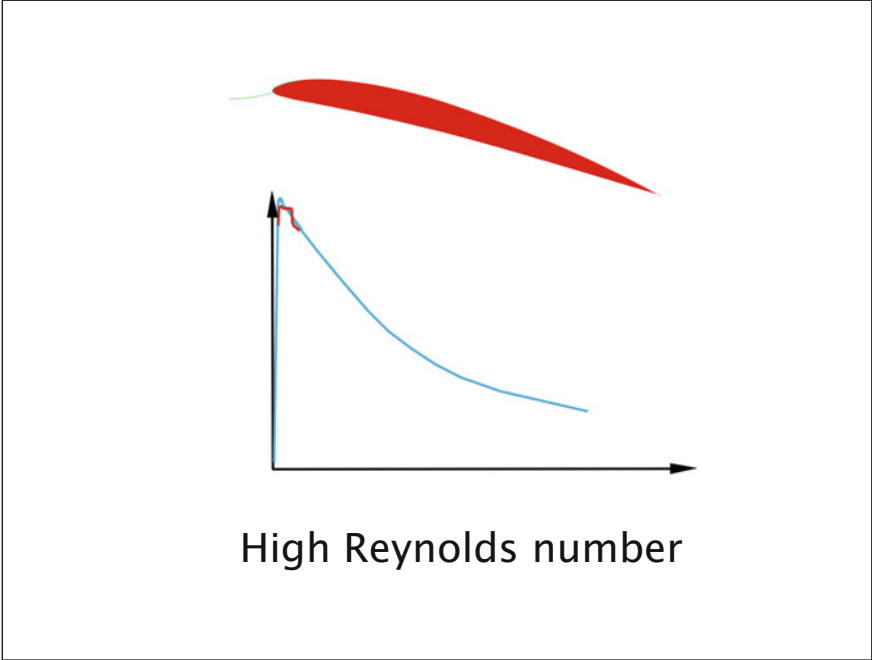
I was asked to find the cause of this devastating form of stall on swept wings. I considered the problem of zero sweep.

The next slide shows contours of the velocities measured with a hot-wire anemometer through a short bubble. The hot-wire signals clearly indicated roughly periodic oscillations in the shear layer. These oscillations increased in amplitude as the wire was moved downstream and eventually the signals became chaotic in the turbulent zone near reattachment.

Was the growth of perturbations the key to the problem?

Velocity contours through the bubble

Velocity profiles
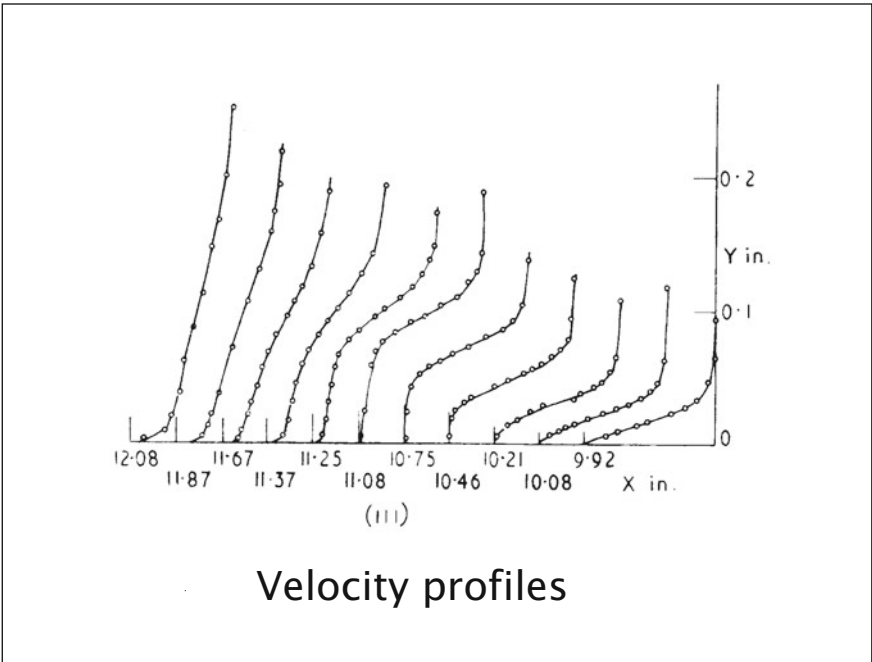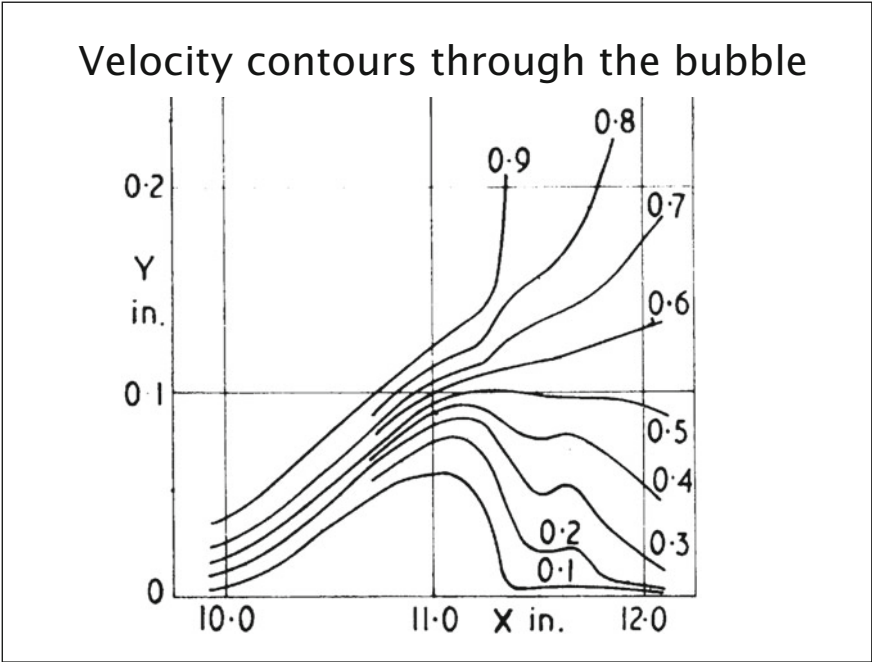
The simplest theoretical approach assumed a base flow that was parallel. This flow seems far from parallel until one looks at the contour plot scaled correctly.

The local profile shapes were approximated by three straight lines. The inviscid dispersion could then be obtained.

$$(\phi'' - \alpha^2\phi)(U - c) - U''\phi = 0$$

$$\phi \sim e^{-\alpha y}$$
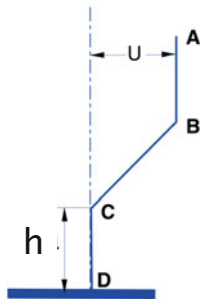
$$\phi \sim e^{-\alpha y}, e^{\alpha y}$$

$$\phi \sim e^{-\alpha y}, e^{\alpha y}$$

At B ϕ is continuous, but ϕ' has a jump.
$$\phi'(B^-) = \phi'(B^+) + \phi(B)/(U - c)$$

Straight line velocity profile

If we neglect any viscous effects and critical layer curvature we reduce the characteristic function to :-

$$(\omega - \tfrac{1}{2})(\alpha - \omega - \tfrac{1}{2}) = \tfrac{1}{4}e^{-2\alpha h}$$

The solution is dominated by the first term

$$\omega = \tfrac{1}{2}$$

Travelling waves could be excited by sound and a controlled sound was introduced to create regular waves suitable for measurement.

The wavenumbers and frequencies were roughly given by the simple model treated as a 'locally parallel' flow.

Growth rates and wavenumbers were deduced from the perturbations outside the boundary layer where the solution was simply -

$$e^{-\alpha y}$$

where the wavenumber is complex.
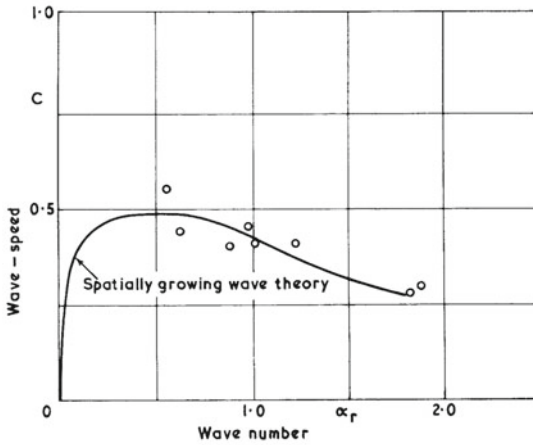
Measured and theoretical dispersion
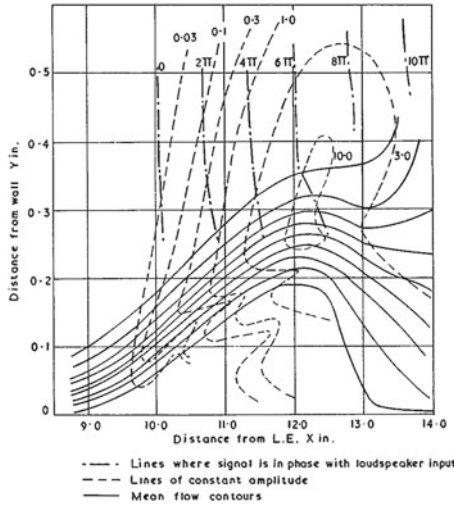
Phase and amplitude of excited waves

I discussed this work with Dr Stuart and his colleagues at the NPL in (1957).

We didn't speak the same language.

They spent quite a long time with me and tried to be helpful, but could not accept the idea of looking at slices of a developing flow and they certainly didn't like a complex wavenumber.

They even questioned using such an approach on Blasius flow as had been done by Schlichting etc. Their focus was on 'Closed' systems in classic geometries.

I argued that the Schubauer's experiment could be modelled by boundary conditions chosen to represent a ribbon.

So I tackled that problem, but could not evaluate the integrals involved.

The solution arose in two parts: -

The near-field portion, that decayed and the Eigen-solution - the downstream T-S wave - *when the group velocity was positive.*

Even then I recall that Dr Stuart said that this solution had nothing to do with the flow Stability!

Of course he was correct, but I believe that the sort of situation that arises in 'open systems', like boundary layers, involve forced excitations.

At Cambridge around 1990 I realised that one could readily evaluate the integrals numerically in a boundary value problem.

I tackled a number of problems with some very able MPhil students.

The simplest case was that posed by a two-dimensional suction slit in a Blasius boundary layer.

Computational zone
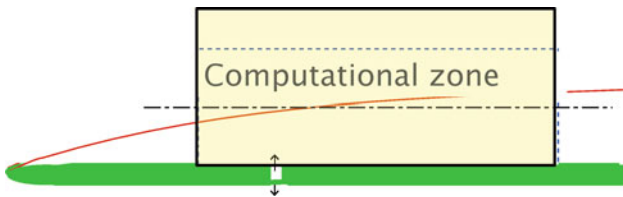
A suction slit may be represented by

$$u(0, x) = 0$$
$$v(0, x) = Q\delta(0),$$

Providing the transform -

$$\hat{v}(0, \alpha) = Q$$

Model of a suction slit

1) Linearize the perturbation.

2) Treat the base flow as parallel, $U(y)$ only.

The governing equation for the transform of the stream function reduces to:-

$$(\phi'' - \alpha^2\phi)U - \phi U'' = \frac{i}{\alpha R}(\phi'''' - 2\alpha^2\phi'' + \alpha^4\phi)$$

a reduced form of the *Orr-Sommerfeld* equation.

There are no eigen solutions so the perturbation consists solely of the near field.

$$u(y,x) = \frac{1}{2\pi}\int \frac{\hat{u}(y,\alpha)}{\hat{v}(0,\alpha)} e^{i\alpha x} d\alpha$$

Integrated over alpha along the real axis from minus alphamax to plus alphamax, where alphamax is chosen to provide solutions at the required physical spacing.

Contours of velocity perturbation over on an X~Y plane

Velocity perturbations induced by suction
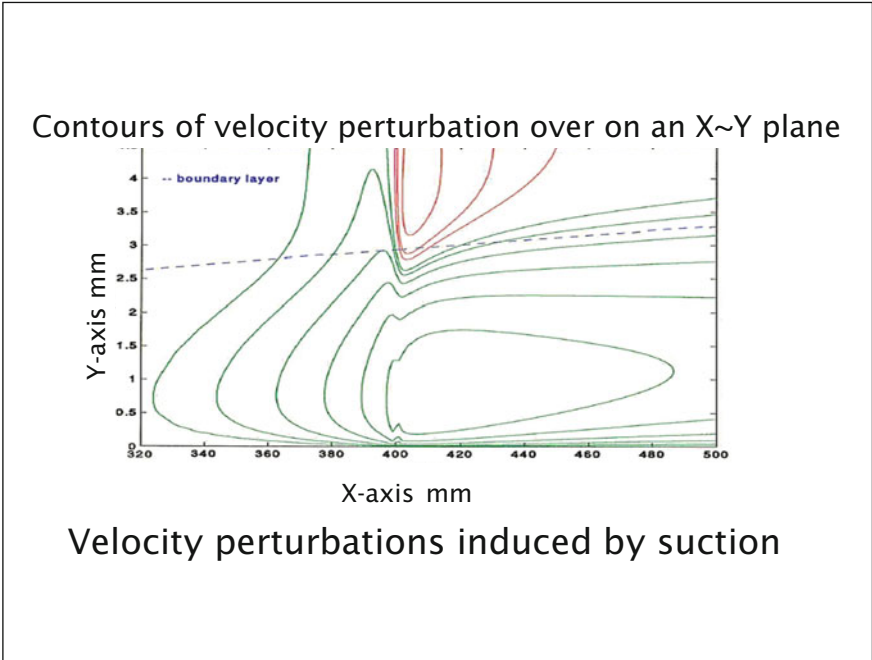
When I discussed this work in Cambridge I was told that these approximations were invalid.

Firstly, it was inconsistent to treat the local Reynolds numbers as finite, while at the same time as infinite so as to form a parallel flow.

Secondly, I could not use a spatial Fourier representation involving small wavenumbers because the boundary layer scale would change significantly over a wavelength. The Fourier inversion was therefore invalid.

There was a Third one as well??

Modelling and experiment by Mark Linnick

MPhil Cambridge

Contour levels decrease in powers of 2
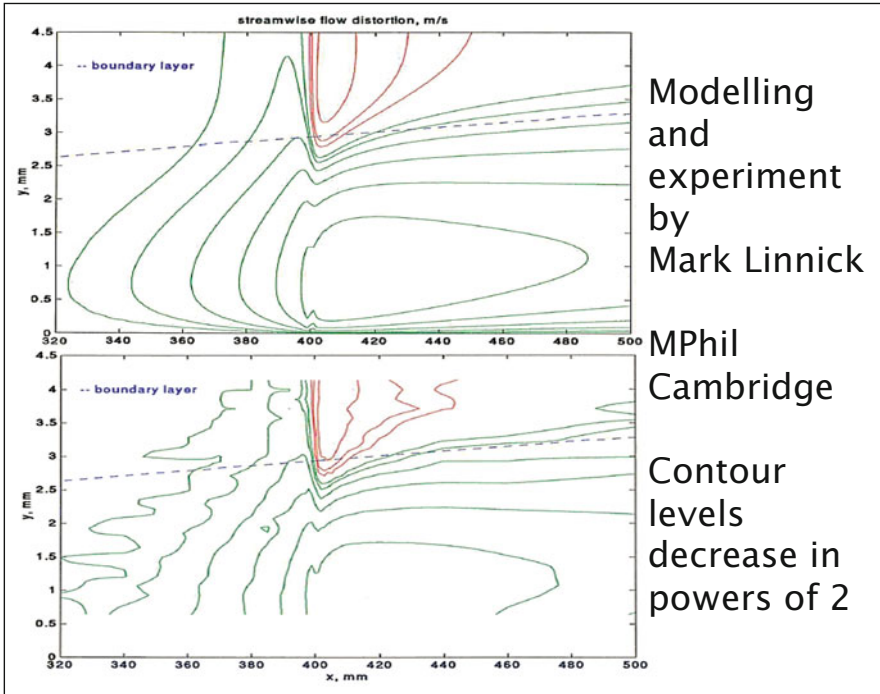
It turned out that the experiment validated the model very well indeed. Why were the doubters so wrong?

We can tackle the slow mean flow variation by either an iterative scheme using the P.D.E. or by modelling the base flow as a series of parallel segments coupled together.

The major element in T-S waves arises through stream wise coupling at different stations or by a transmission factor across discontinuities. The errors are small.

At Queen Mary we went on look at periodically excited jets.

Experimental setup for a periodic jet

Boundary conditions on the surface of the plate

$$u(x,0,z,t) = Sin(\theta)Q\delta(0,0)e^{i\omega t}$$

$$v(x,0,z,t) = Cos(\theta)Q\delta(0,0)e^{i\omega t}$$
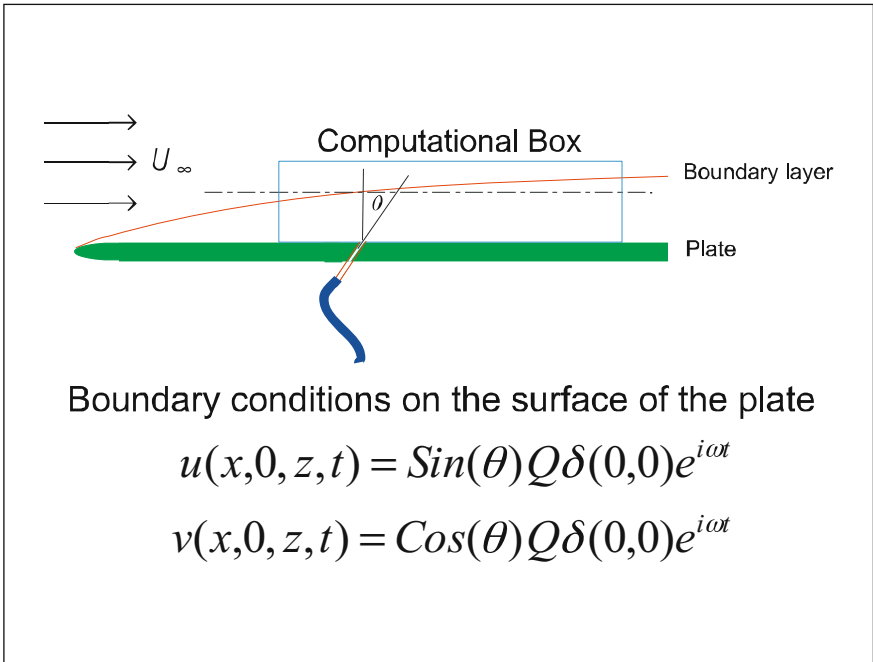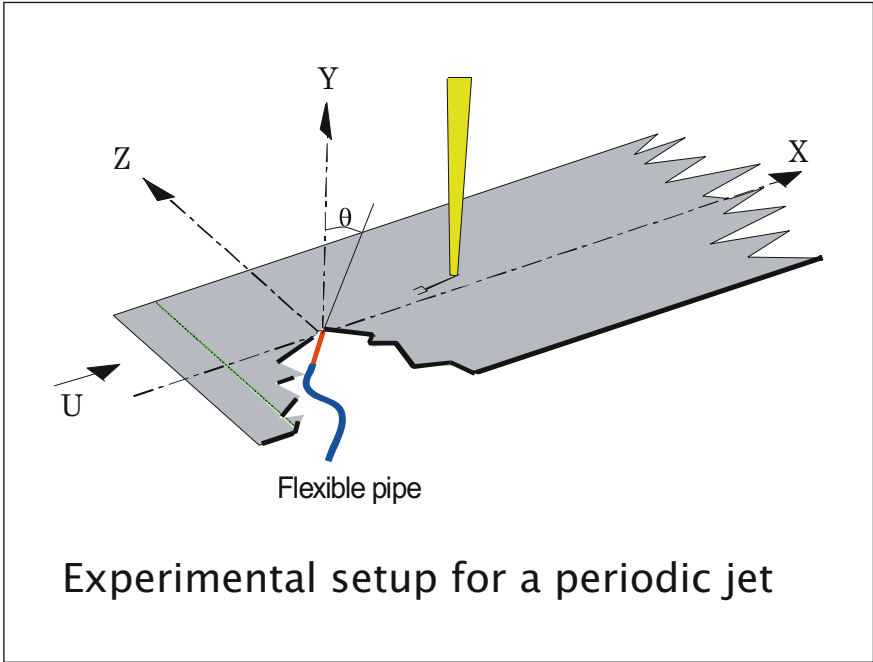
The experiments on periodic jets were carried
out by an MSc student, Emmanuel Caloupis,
with the support of EOARD in co-operation with
Hermann Fasel at the University of Arizona.

Mike G did the calculations.

Again a hot-wire was traversed across the
boundary layer and ensemble averaged plots of
the wavy motion obtained. The next slide
shows an x~y slice of the flow field taken
through the source.

Then z~y cuts through the wedge shape zone
are plotted.
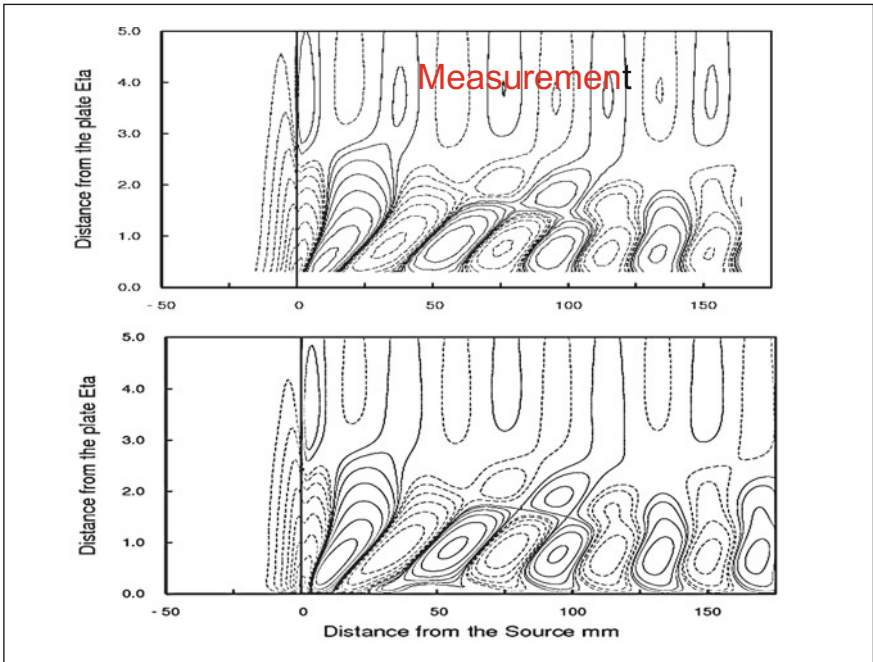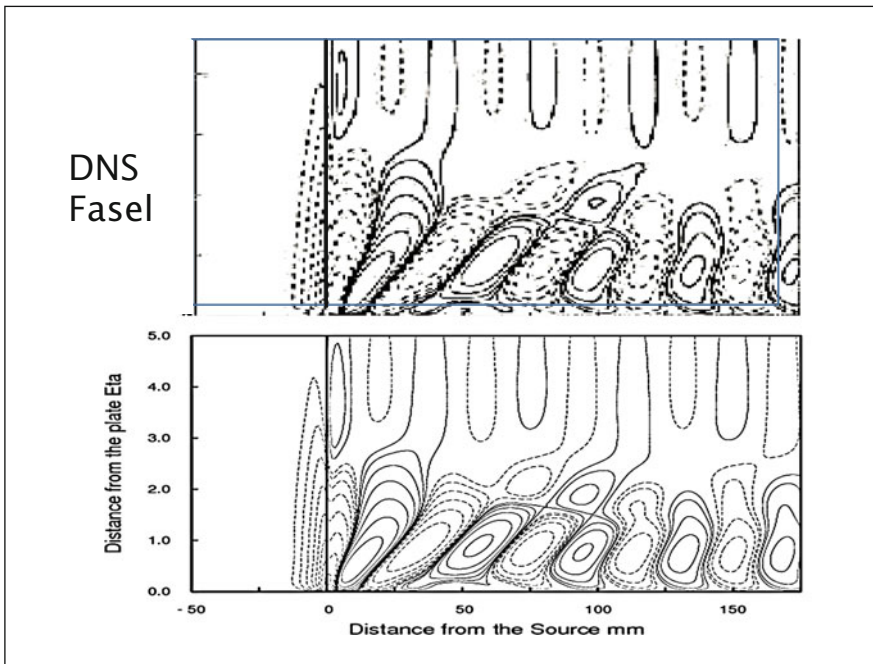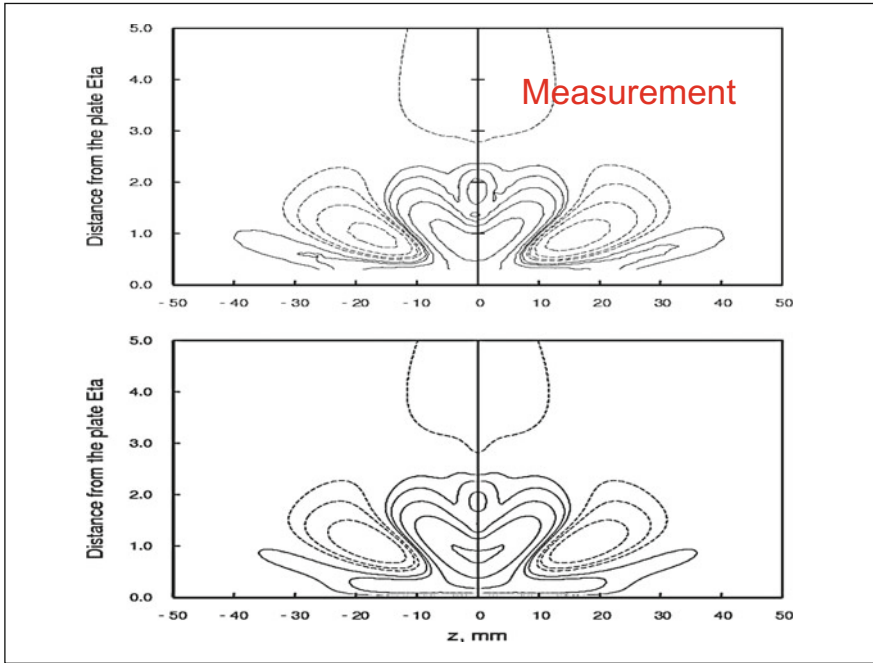
The flow was also evaluated using a DNS code by
A PhD student working with Hermann Fassel at
the University of Arizona in Tucson.

The agreement with our calculations and
experiment must surely give support to the
validity of the simple model.

Further work was done by myself over much
longer fetches. When plotted using non-
dimensional measures of the distance from the
wall some compensation for flow divergence is
approximately catered for and we get good
correlation over long distances.

Distance from the plate Eta

Distance from the Source mm

Measurement

Velocity
fluctuations
at a height of
eta =1.0

Distance across the span

Distance downstream from the leading edge
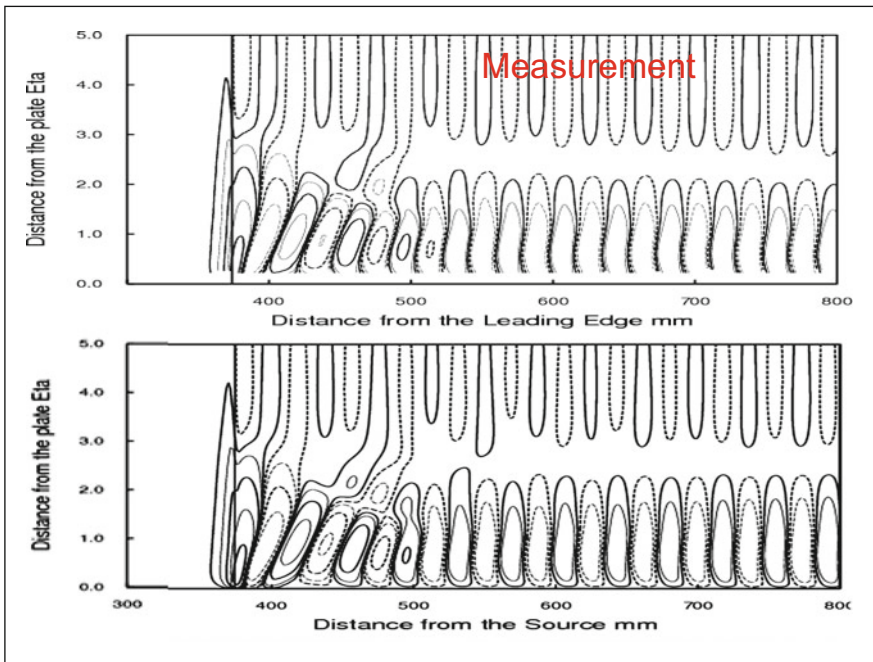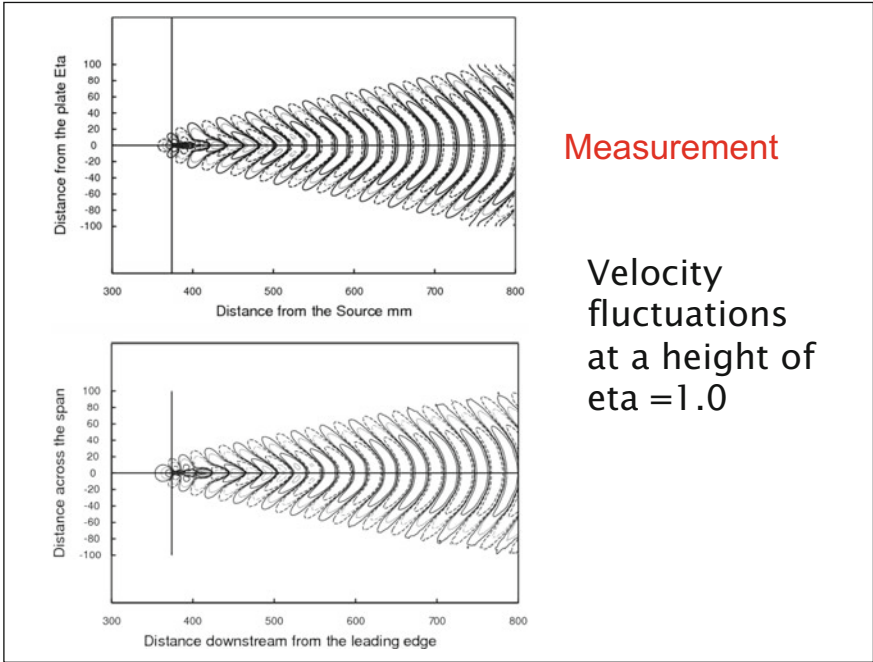
Similar modelling methods have now been
applied to wall ripples to represent roughness.

h

h
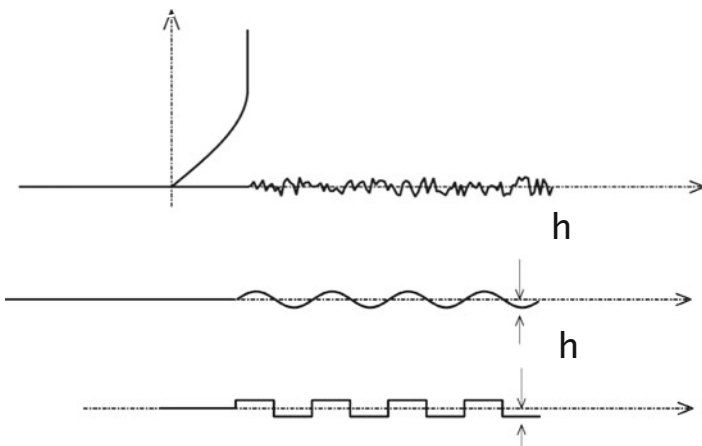
Similar treatment has now been applied to wall ripples to model surface roughness.

The overall mean flow is modelled by:-

Base boundary layer plus a summation of solutions of the governing equations for *u* & *v*.

The weights are chosen so that *u* & *v* are zero on the boundary.

A *best fit* solution at a large number of collocations points is found by SVD.

Two fundamental solutions, A & B, for the transform of velocities components are:-

$$_A\hat{u}_k(y), \ _A\hat{v}_k(y)$$

and $$_B\hat{u}_k(y), \ _B\hat{v}_k(y)$$

With boundary conditions:-

$$_A\hat{u}_k(0) = 1.0, \quad _A\hat{v}_k(0) = 0$$

and $$_B\hat{u}_k(0) = 0, \quad _B\hat{v}_k(0) = 1.0$$

The form of solution is then -

$$u(x, y) = U(y) + \sum_k A_k e^{ikx} \,_A\hat{u}_k(y)$$
$$+ \sum_k B_k e^{ikx} \,_B\hat{u}_k(y)$$

Similarly for the normal velocity component
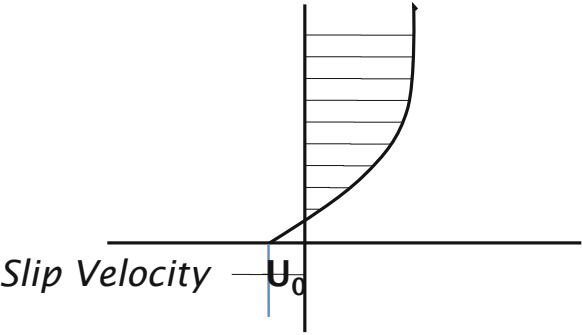
The coefficients are found by SVD so that the proper hydrodynamics boundary conditions apply.

6 mm wavelength ripples of 300 microns

Slip Velocity = -0.0671

6 mm wavelength ripples of 500 microns

Streamfunction   Streamwise Velocity

Distance from the Surface mm

X-Axis mm

Slip Velocity = -0.121

6 mm wavelength ripples of 750 microns

Streamfunction   Streamwise Velocity

Distance from the Surface mm

X-Axis mm

Slip Velocity = -0.187

6 mm wavelength spikes of 500 microns

Streamfunction   Streamwise Velocity

Distance from the Surface mm

X-Axis mm

Slip Velocity = -0.108

The best fit is obtained with a slip flow boundary condition for the boundary layer.

Slip Velocity U_0

The behaviour is similar to that seen by a moving observer.

The behaviour of excited two-dimensional periodic travelling waves can be tackled in a similar way using the new boundary layer with the negative slip velocity. Again the perturbations velocities are made zero on the boundary.

The final two frames show the solutions obtained.

The model is being extended to cater for oblique waves so that the experiments from a point source can be properly compared with the theory.

The method will then be capable of treating fully three-dimensional roughness.

Streamwise Velocity Perturbations

Blasius Flow

Boundary Layer over Sinusoidal Ripples 500 microns
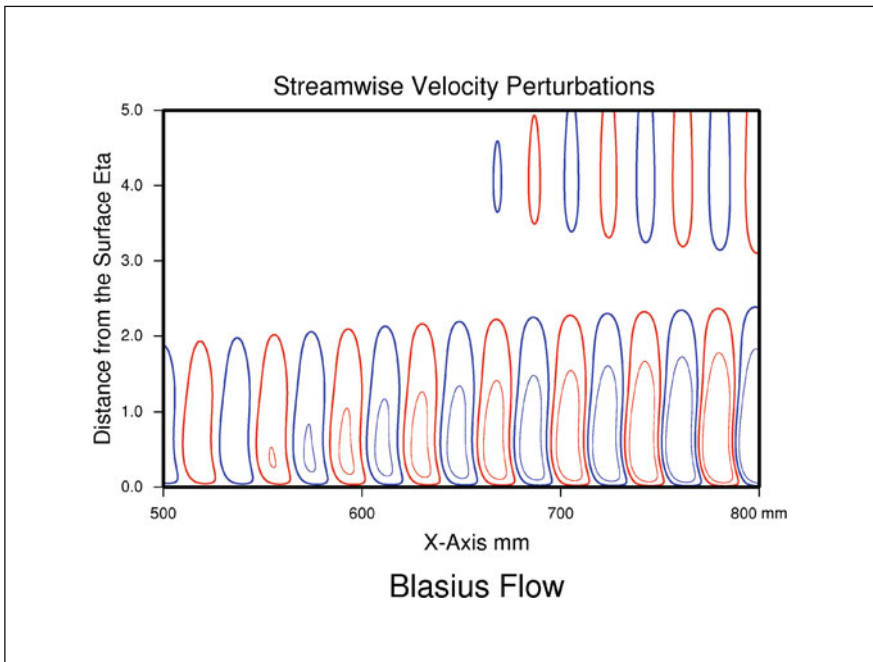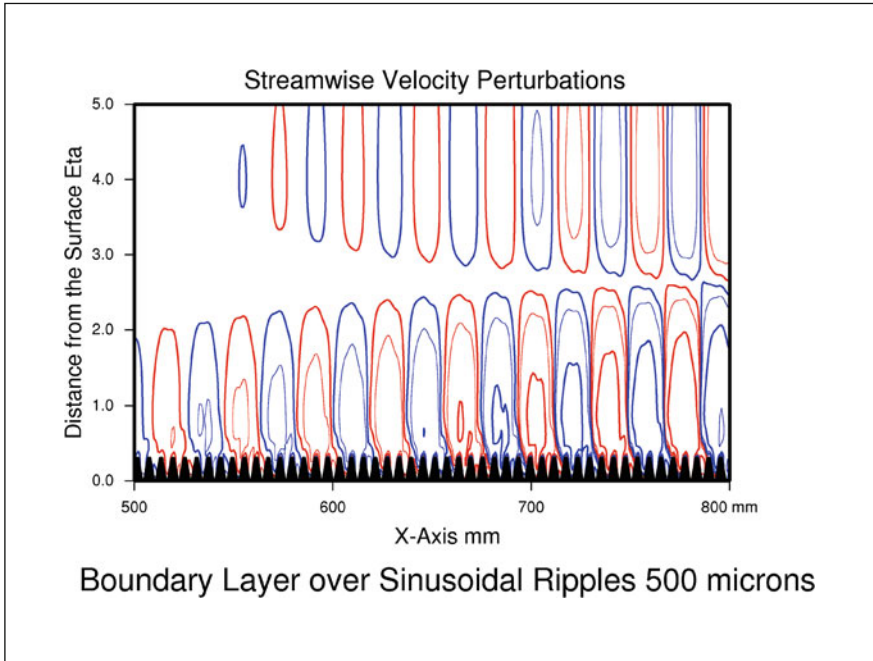
Conclusions

The linearized locally parallel flow model provides an excellent representation of the perturbations when the flow is slowly developing..

For even quite large flow non-uniformity we get the correct physical picture and often adequate quantitative values. We are of course looking at 'Open systems' that require some form of excitation, like turbulence or noise.

But now people are going full circle and again considering stability using global models that seem appropriate for 'closed systems'.

Contents

Contributors

F. Alizard DynFluid Laboratory, CNAM, Paris, France

I. M. AlQadi King Abdulaziz University, Jeddah, Saudi Arabia

Leonardo S. de B. Alves Departmento de Engenharia Mecânica, Universidade Federal Fluminense, Niterói, RJ, Brazil

S. Alzahrani King Abdulaziz University, Jeddah, Saudi Arabia

Michael Amitay James L. Decker Endowed Professor of Aerospace Engineering, RPI, Troy, NY, USA

Gustavo R. S. Assi Fluid Dynamics Research Group (NDF), Escola Politécnica, University of São Paulo (EPUSP), São Paulo, Brazil

C. Atkinson Laboratory of Turbulence Research in Aerospace and Combustion, Monash University, Melbourne, VIC, Australia

Jérémy Basley Laboratoire d'Informatique pour la Mécanique et les Sciences de l'Ingénieur (LIMSI/CNRS), Orsay, Cedex, France; Université Paris-Sud, Orsay, Cedex, France

N. Benard Futuroscope, Poitiers, France

A. S. Bonatto Embraer, Sao Jose dos Campos-SP, Brazil

J. P. Bonnet Futuroscope, Poitiers, France

Christian Breitsamter Lehrstuhl für Aerodynamik und Strömungsmechanik, Technische Universität München, Garching bei München, Germany

N. A. Buchmann Laboratory of Turbulence Research in Aerospace and Combustion, Monash University, Melbourne, VIC, Australia; Institut für Strömungsmechanik und Aerodynamik LRT-7, Fakultät für Luft-und Raumfahrttechnik, Universität der Bundeswehr, Munich, Germany

B. S. Carmo Department of Mechanical Engineering NDF-POLI, University of Sao Paulo, São Paulo, Brazil

S. Cherubini Laboratoire DynFluid, Arts et Métiers ParisTech, Paris, France

P. Cobo Centro de Acústica Aplicada y Evaluación No Destructiva (CAEND), CSIC, Madrid, Spain

N. De Tullio Department of Mathematics, Imperial College London, London, UK

J. de Vicente School of Aerospace Engineering, Universidad Politécnica de Madrid, Madrid, Spain

Edward Paisley DeMauro Mechanical, Aerospace, Nuclear Engineering, RPI, Troy, NY, USA

Yosef El Sayed Mohamed Institut für Strömunsmechanik, Technische Universität Braunschweig, Braunschweig, Germany

E. Erdem Aero-Physics Laboratory, School of Engineering, University of Glasgow, Scotland, UK

G. S. Franco Department of Naval Architecture and Ocean Engineering, University of São Paulo, São Paulo, Brazil

J. S. Frederiksen Centre for Australian Weather and Climate Research, CSIRO Marine and Atmospheric Research, Aspendale, VIC, Australia

Cesar M. Freire Fluid Dynamics Research Group (NDF), Escola Politécnica, University of São Paulo (EPUSP), São Paulo, Brazil

Rafael S. Gioria Fluid Dynamics Research Group (NDF), Escola Politécnica, University of São Paulo (EPUSP), São Paulo, Brazil

Francisco Gómez Department of Mechanical and Aerospace Engineering, Monash University, Melbourne, VIC, Australia

R. Gómez National Institute of Aerospace Technology INTA, Madrid, Spain

L. M. González School of Aerospace Engineering, Universidad Politécnica de Madrid, Madrid, Spain

Rama Govindarajan Tata Institute of Fundamental Research, Centre for Interdisciplinary Sciences, Hyderabad, India

F. Guiho DynFluid Laboratory, Arts et Métiers ParisTech, Paris, France

S. Hafez King Abdulaziz University, Jeddah, Saudi Arabia

Wei He School of Aeronautics, Universidad Politécnica de Madrid, Madrid, Spain

D. S. Henningson Linné FLOW Centre and Swedish e-Science Research Centre (SeRC), KTH Mechanics, Royal Institute of Technology, Stockholm, Sweden

J. Hermida National Institute of Aerospace Technology INTA, Madrid, Spain

Mamta Jotkar Tata Institute of Fundamental Research, Centre for Interdisciplinary Sciences, Hyderabad, India

K. A. Juhany King Abdulaziz University, Jeddah, Saudi Arabia

Kentaro Kato Lehrstuhl für Aerodynamik und Strömungsmechanik, Technische Universität München, Garching bei München, Germany

Asimina Kazakidi Institute of Computer Science Foundation for Research and Technology—Hellas (FORTH), Heraklion, Greece

F. Kerhervé Laboratoire de Mécanique de Lille, UMR CNRS 8107, Lille, France

V. Kitsios Laboratory for Turbulence Research in Aerospace and Combustion, Department of Mechanical and Aerospace Engineering, Monash University, Melbourne, Clayton, VIC, Australia

K. Kontis Aero-Physics Laboratory, School of Engineering, University of Glasgow, Scotland, UK

Chia Min Leong Mechanical, Aerospace, Nuclear Engineering, RPI, Troy, NY, USA

E. Leriche Laboratoire de Mécanique de Lille, Université Lille-1, Villeneuve d'Ascq, France

Qiong Liu School of Aeronautics, Universidad Politècnica de Madrid, Madrid, Spain

J.-Ch. Loiseau Laboratoire DynFluid, Arts et Métiers ParisTech, Paris, France

G. Lubinsky School of Mechanical Engineering, Faculty of Engineering, Tel Aviv University, Tel Aviv, Israel

François Lusseyran Laboratoire d'Informatique pour la Mécanique et les Sciences de l'Ingénieur (LIMSI/CNRS), Orsay, Cedex, France

Juan A. Martín ETSI Aeronáuticos, Universidad Politécnica de Madrid, Madrid, Spain

Marcello A. F. Medeiros University of São Paulo, Escola de Engenharia de São Carlos EESC, São Carlos-SP, Brazil; Universidade de São Paulo, São Carlos, Brazil

Julio R. Meneghini Fluid Dynamics Research Group (NDF), Escola Politécnica, University of São Paulo (EPUSP), São Paulo, Brazil

F. Meseguer-Garrido School of Aerospace Engineering, Universidad Politécnica de Madrid, Madrid, Spain

Abhijit Mitra Indian Institute of Science, Bangalore, India

E. Moreau Futuroscope, Poitiers, France

Aimee S. Morgans Department of Aeronautics, Imperial College London, London, UK

Jonathan F. Morrison Department of Aeronautics, Imperial College London, London, UK

Andrew Ooi Department of Mechanical Engineering, University of Melbourne, Parkville, VIC, Australia

R. M. Orselli Fluid and Dynamics Research Group, Department of Mechanical Engineering, Escola Politecnica, University of São Paulo, São Paulo, Brazil

S. Ortiz Centro de Acústica Aplicada y Evaluación No Destructiva (CAEND), CSIC, Madrid, Spain

Anthony R. Oxlade Department of Aeronautics, Imperial College London, London, UK

P. Paredes School of Aeronautics, Universidad Politécnica de Madrid, Madrid, Spain

Luc R. Pastur Laboratoire d'Informatique pour la Mécanique et les Sciences de l'Ingénieur (LIMSI/CNRS), Orsay, Cedex, France; Université Paris-Sud, Orsay, Cedex, France

A. Peplinski Linné FLOW Centre and Swedish e-Science Research Centre (SeRC), KTH Mechanics, Royal Institute of Technology, Stockholm, Sweden

José Miguel Pérez School of Aeronautics, Universidad Politécnica de Madrid, Madrid, Spain

R. L. Queiroz Embraer, Sao Jose dos Campos-SP, Brazil

C. Raibaudo Laboratoire de Mécanique de Lille, UMR CNRS 8107, Lille, France

O. N. Ramesh Indian Institute of Science, Bangalore, India

Georgios Rigas Department of Aeronautics, Imperial College London, London, UK

J.-Ch. Robinet DynFluid Laboratory, Arts et Métiers ParisTech, Paris, France

G. Rocco Department of Aeronautics, Imperial College London, London, UK

Daniel Rodríguez School of Aeronautics, Universidad Politécnica de Madrid, Madrid, Spain

Miquel Roura Gamesa Innovation and Technology S.L., Madrid, Spain

N. D. Sandham Aeronautics and Astronautics, Faculty of Engineering and the Environment, University of Southampton, Southampton, UK

P. Schlatter Linné FLOW Centre and Swedish e-Science Research Centre (SeRC), KTH Mechanics, Royal Institute of Technology, Stockholm, Sweden

Avraham ("Avi") Seifert Meadow Aerodynamics Laboratory, School of Mechanical Engineering, Faculty of Engineering, Tel Aviv University, Tel Aviv, Israel

Richard Semaan Institut für Strömunsmechanik, Technische Universität Braunschweig, Braunschweig, Germany

D. Serson NDF, Department of Mechanical Engineering, POLI, University of São Paulo, São Paulo, Brazil

S. J. Sherwin Department of Aeronautics, Imperial College London, London, UK

J. Soria Laboratory for Turbulence Research in Aerospace and Combustion, Department of Mechanical and Aerospace Engineering, Monash University, Melbourne, VIC, Australia; Department of Aeronautical Engineering, King Abdulaziz University, Jeddah, United Kindom of Saudi Arabia

Daniel S. Souza Universidade de São Paulo, São Carlos, Brazil

M. Stanislas Laboratoire de Mécanique de Lille, UMR CNRS 8107, Lille, France

Paul Stegeman Laboratory for Turbulence Research in Aerospace and Combustion, Department of Mechanical and Aerospace Engineering, Monash University, Melbourne, VIC, Australia

P. Sujar-Garrido Futuroscope, Poitiers, France

Renan de S. Teixeira Pós-Graduação em Engenharia de Defesa, Instituto Militar de Engenharia, Rio de Janeiro, RJ, Brazil

Juan Ángel Tendero School of Aeronautics, Universidad Politécnica de Madrid, Madrid, Spain

V. Theofilis School of Aerospace Engineering, Universidad Politécnica de Madrid, Madrid, Spain

Victor Troshin Meadow Aerodynamics Laboratory, School of Mechanical Engineering, Faculty of Engineering, Tel Aviv University, Tel Aviv, Israel

E. Valero School of Aerospace Engineering, Universidad Politécnica de Madrid, Madrid, Spain

M. S. Vestri Department of Naval Architecture and Ocean Engineering, University of São Paulo, São Paulo, Brazil

E. V. Volpe NDF, Department of Mechanical Engineering, POLI, University of São Paulo, São Paulo, Brazil

H. Zare-Behtash Aero-Physics Laboratory, School of Engineering, University of Glasgow, Scotland, UK

Prologue to the International Conference on Massively Separated Flows and Their Control

Vassilis Theofilis and Julio Soria

An international meeting on *Massively Separated Flows*, focusing on instability and control of and noise generated by flow separation from the incompressible to the hypersonic regime was organized at the Monash Center in Prato, Italy, Sept. 4–6, 2013. This focused workshop brought together 50 leading specialists in the subject matter of the conference from the USA, UK, Israel, Spain, Germany, Sweden, France, Brazil, Australia, India, Japan, and Saudi Arabia, in order to assess the state-of-the-art of theory, experimentation and computation of massively separated flows in aeronautics and related fields.

The inaugural lecture was offered by Prof. Mike Gaster, whose first seminal papers on separation characterization were published in the 50s of the last century.

V. Theofilis (✉)
School of Aerospace Engineering, Universidad Politécnica de Madrid, Plaza Cardenal Cisneros 3, 28040 Madrid, Spain
e-mail: vassilios.theofilis@upm.es

J. Soria
Laboratory for Turbulence Research in Aerospace and Combustion, Department of Mechanical and Aerospace Engineering, Monash University, Melbourne, VIC 3800, Australia
e-mail: julio.soria@monash.edu

Prof. Gaster presented an authoritative view of progress made since the early days and introduced a theoretical model for the prediction of separated flow instabilities in a boundary layer which compares favorably with direct numerical simulation predictions, the latter performed independently by Prof. Hermann Fasel. He also discussed key open issues which hamper control of separated flow instabilities and limit performance of flying devices.

Four invited speakers introduced the main themes of the meeting. Prof. Louis Cattafesta presented synthetic-jet-based control of turbulent separated flows mainly from an experimental point of view, while discussion of the same theme was completed from a computational point of view by Prof. Rajat Mittal. Both speakers reviewed success stories of flows around airfoils at typical subsonic cruising speeds. Prof. Kostas Kontis discussed from an entirely experimental point of view separated flow instabilities in supersonic flow over axisymmetric configurations, and highlighted the strong need for new efforts to be undertaken in order to cover the knowledge gap in this flow regime. Prof. Dan Henningson introduced modern theoretical and computational tools for the prediction and control of separated flow instabilities, using the jet-in-crossflow configuration as a demonstrator; he also pointed out the initial value problem approach to transition prediction in separated flows over complex geometries as a most promising avenue for future theoretical research.

Sessions were held on the topics of separated flow over airfoils, bluff bodies and their wakes, separation behind a roughness element in incompressible, supersonic and hypersonic flow, as well as separation generated by a supersonic jet impinging on a flat surface or on a laminar boundary layer. Aeroacoustic themes presented at the meeting and related to flow separation included noise generation, prediction and control in a slat-cove configuration as well as in open two-dimensional and closed three-dimensional cavities. Beyond exclusively aeronautics-related applications, a number of presentations were motivated by separation related to naval engineering and included control of wake separation by means of splitter plates, staked-cylinders and free-to-rotate plates. Theoretical techniques for flow separation discussed during the meeting included proper orthogonal and dynamic mode decomposition, while experimental techniques demonstrated included synthetic jets and plasma actuations. In the emerging field of prediction of separated flow (global) instabilities in flows

with three inhomogeneous spatial directions optimal perturbations in an impinging jet-in-crossflow and the generated wave packet were discussed, theoretical prediction of three-dimensional eigenmodes of spanwise-varying-diameter cylinder wake flow were obtained for the first time, while theoretical prediction of the leading three-dimensional eigenmode of flow in the wake of a 3D staked-cylinder was presented at the meeting. Numerical methods were presented aiming at accurate prediction of base separated flows, while efforts to assess the applicability of meshless methods to separated flow predictions were also discussed.

Editors of the 6 major journals in aeronautics, fluid mechanics and computational physics attended the conference. Support was provided by the European Office of Aerospace Research and Development, while the meeting also served as the final review of the EU-FP7-IRSES *ICOMASEF—Instability and Control of Massively Separated Flows* travel grant. Large representations of all *ICOMASEF* partners, from Imperial College London, Monash University (Melbourne), the University of São Paulo, the Indian Institute of Science and Jawaharlal Nehru Center for Advanced Scientific Research (Bangalore) attended the meeting. These proceedings contain both the invited and the contributed papers, all of which were subjected to a rigorous independent peer-review process before they were accepted for publication into the present volume.

Part I
Invited Lectures (with Contributed Publication)

Investigations of Stability and Transition of a Jet in Crossflow Using DNS

A. Peplinski, P. Schlatter and D. S. Henningson

Abstract We study the stability of a jet in crossflow at low values of the jet-to-crossflow velocity ratio R focusing on direct numerical simulations (DNS) and the global linear stability analysis adopting a time-stepper method. For the simplified setup neglecting a meshed pipe in the simulations, we compare results of the fully-spectral code SIMSON with the spectral-element code Nek5000. We find the calculated critical value R for the first bifurcation to be dependent on the numerical method used. This result is related to a large sensitivity of the eigenvalues and to the large spatial growth of the corresponding eigenmodes, making the use of periodic domains, even with the fringe method, difficult. However, we observe a similar sensitivity to reflection from the outflow boundary in the inflow/outflow configuration as well. We apply in our studies both modal and non-modal analyses investigating transient effects and their asymptotic fate, and we find transient wavepacket that develop almost identically in the stable and unstable cases. Finally, we compare these results with the simulation including the pipe in the computational domain finding the latter one to be much more unstable.

1 Introduction

The jet in crossflow (JCF) refers to fluid that exits a nozzle and interacts with the boundary layer flowing across the nozzle. This case has been extensively studied both experimentally and theoretically over the past decades due to its high practical relevance. Smoke and pollutant plumes, fuel injection and mixing or film cooling are

A. Peplinski (✉) · P. Schlatter · D. S. Henningson
Linné FLOW Centre and Swedish e-Science Research Centre (SeRC),
KTH Mechanics, Royal Institute of Technology,
100 44 Stockholm, Sweden
e-mail: adam@mech.kth.se

D. S. Henningson
e-mail: henning@mech.kth.se

just a few applications. It is considered a canonical flow problem with complex, fully three-dimensional dynamics, making it a perfect tool for testing simulation methods. Recent reviews on this flow configuration are given in Refs. [7, 8].

The JCF can be characterised by three independent non-dimensional parameters: free-stream and jet Reynolds numbers ($Re_{\delta_0^\star}$, Re_{jet}) and jet to free-stream velocity ratio R, which is the key parameter in this work. The major flow features are (see e.g. Fig. 1 in Ref. [7]): the counter-rotating vortex pair (CVP) in the far field, the horseshoe vortex developing upstream of the jet orifice, and vortices shed from the shear layers that result from the interaction of the jet with the cross-flow both upstream and downstream of the jet trajectory. Some other features, such as wake vortices or upright vortices, are visible at higher values of the cross velocity ratio R only. As the ratio R increases, the flow evolves from a stable (and thus steady) configuration consisting of (steady) CVPs and horseshoe vortices, through simple periodic vortex shedding (a limit cycle) to more complicated quasi-periodic behaviour, before finally becoming turbulent. In Refs. [2, 6, 13] the stability of the JCF was studied by means of modal analysis. The first linear global stability analysis of this flow at $R = 3$ was presented by Bagheri et al. [2, 13]. For this jet to free-stream velocity ratio, the JCF was found to be dominated by an interplay of three common instability mechanisms: a Kelvin–Helmholtz shear layer instability, a possible elliptic instability of the CVPs, and a near-wall vortex shedding mechanism similar to a von Kármán vortex street. It was also shown that the flow acts as an oscillator, with high-frequency unstable global eigenmodes associated with shear-layer instabilities on the CVP and low-frequency modes resulting in vortex shedding in the jet wake. This work was later extended to the wider range of $R \in (0.55, 2.75)$ [6], focusing on transition from steady to unsteady flow as R is increased. The first bifurcation (appearance of the first unstable eigenmode) was found to occur at $R \approx 0.675$, when shedding of hairpin vortices characteristic of a shear layer instability was observed, and the source of this instability (*wavemaker*) was located in the shear layer just downstream of the orifice. Results of linear stability analysis were consistent with nonlinear direct numerical simulations (DNS) at the critical value of R predicting well the frequency and initial growth rate of the disturbance. It was also concluded that, based on linear analysis, good qualitative predictions about the flow dynamics can be made even for higher R, where multiple unstable eigenmodes are present. The authors pointed out, however, that the critical R cannot be determined exactly due to sensitivity of the results to changes in the domain length as well as to the presence of the fringe region enforcing periodic boundary condition (BC).

In the current study, we follow Ilak et al. [6], focusing on the transition from steady to unsteady flow and, using linear global stability analysis, searching for the value of R at which the first bifurcation occurs. The scope of this work is to test the numerical methods and techniques, and to identify the major difficulties related to linear stability of this type of complex flows. As purely modal analysis is known to fail in predicting the practical critical Reynolds number for transition to turbulence in a number of systems, we apply in our studies both modal and non-modal analyses. A classical example of such a flow is the convectively unstable flat-plate boundary layer [4], which behaves as broadband amplifier of incoming disturbances and is globally

stable according to linear global analysis. However, a global stability analysis based on the asymptotic behaviour of single eigenmodes of the system does not capture relevant dynamics, and transition to turbulence at lower Re occurs due to transient effects. Following Ref. [14] we investigate the linear growth of perturbations in the JCF for a limited time, before the exponential modal behaviour is most dominant, and determine an *optimal initial condition* (initial condition yielding largest possible growth in energy) adopting a time-stepper method.

The previous stability results for this flow [2, 6, 13] were obtained for simplified setups, in which the inflow jet was represented by a Dirichlet BC due to the limitations of the applied pseudo-spectral simulation method. We avoid this limitation using the more flexible spectral-element method (SEM), which provides spectral accuracy while allowing for complex geometries. However, to be able to compare our results with the previous ones we adopt in most of the simulations simplified setup of Ref. [6]. In addition we perform a few simulations with the more realistic one with the pipe included in the computational domain.

This work is an extension to our previous work [11], where preliminary results were presented.

2 Numerical Setup

In this work we perform simulations of JCF for two numerical setups: the simplified (S1, with Dirichlet BC) and the more realistic (S2, with pipe section) one. We adopt the simplified S1 setup similar to Ref. [6], modelling the interaction of a (laminar) boundary layer with a perpendicular (laminar) jet exiting a circular pipe with diameter $D = 3 * \delta_0^\star$, where $\delta_0^\star$ is the displacement thickness at the inflow placed $9.375 * \delta_0^\star$ upstream the centre of the pipe orifice; $\delta_o^\star$ is adopted as length unit. Following Ref. [6] we use both laminar cross-flow and jet inflow profile and, as the jet pipe is absent in the simulations, an inhomogeneous (Dirichlet) BC prescribing the inflow jet profile. This is an important limitation of the problem, modifying the flow pattern at the pipe orifice and affecting its stability properties (see Fig. 4). In addition, the jet profile is modified by a Gaussian function (Eq. 2.1 in [6]) to keep the velocity field smooth in the whole domain. The mass flux of the modified profile is 20.6 % lower compared to the parabolic one. The consequence of this setup is that a direct connection to the physical problem is not possible, and our synthetic setup serves as a well-defined test problem for the numerical tools. We will list here only the key parameter of the setup referring the reader to [2, 6] for more details. The flow is fully described by the pipe diameter D, cross-flow Reynolds number $Re_{\delta_0^\star} = U_\infty \delta_0^\star / \nu$ and jet to cross-flow velocity ratio $R = V/U_\infty$, where U_∞, V and ν are free-stream velocity, *peak* jet velocity and the kinematic viscosity, respectively. As before [6], we set $Re_{\delta_0^\star} = 165$, and choose R as 1.0, 1.4, 1.5 and 1.6.

The more realistic S2 setup is similar to S1, however the pipe of length $20\delta_o^\star$ is included in computational domain. In this case there is no need for smoothing of the jet profile by a Gaussian function and we use a parabolic profile as pipe inflow.

Because of that the results of S1 and S2 setups cannot be compared directly. Sample results of simulations with S2 setup are described in Sect. 4.2.

The simulations are performed with two different massively parallel DNS solvers for the incompressible Navier–Stokes equations: SIMSON [3] and Nek5000 [5]. SIMSON was used in Refs. [2, 6, 13] and is a fully-spectral code suitable for stability computations. However, a major constraint is the requirement for periodic BC in streamwise direction necessitating a fringe region (Chap. 4.2.2 in Ref. [3] and references therein) for damping disturbances. We use SIMSON to investigate the influence of the fringe length L_F on the stability results from nonlinear DNS in S1 setup. Fringe parameters are adopted from Ilak et al. [6] with varying L_F set to 15 (as in [6]), 45 and 75 units. Since the fringe region reduces the useful part of the computational domain, we doubled the length of the box as compared to Ref. [6], setting its size to $L_x = 150$, $L_y = 20$, $L_z = 30$, with the resolution of $512 \times 201 \times 144$ modes in the streamwise (x), wall-normal (y), and spanwise (z) directions, respectively.

Nek5000 is a spectral-element code providing spectral accuracy while allowing for complex geometries. In this method the governing equations are cast into weak form and discretised in space by the Galerkin approximation, following the $P_N - P_{N-2}$ approach with the velocity space spanned by Nth-order Lagrange polynomial interpolants. In our studies we use Nek5000 to investigate the influence of resolution ($N = 6$, 9 and 12), box length ($L_x = 150$ and 250) and grid structure. Domain decomposition into hexahedral elements is used to reduce resolution where it is not needed. We keep uniform resolution in the pipe vicinity within 5 unit distance from the orifice, and reduce it at larger distance by smooth element stretching (mesh M1). In mesh M2 we double the vertical resolution next to the wall. There are no periodic BC in streamwise direction, however, we found our results to be dependent on the outflow BC unless we set a sponge layer at the outflow as well as making the computational domain longer to reduce reflections from the boundary. The forcing function for the sponge was adopted from the fringe in SIMSON, and the sponge length was set to 25 and 35 units for $L_x = 150$ and 250, respectively. Nek5000 is also used as time-stepper for solving the linearised Navier–Stokes equations in modal and non-modal linear stability analyses in setups S1 and S2. In the case of modal linear stability analysis and $L_x = 250$ we increase the height of the computational domain $L_y = 30$ to ensure CVPs fit within the box. Detailed descriptions of the implementation of Nek5000 can be found in Ref. [5].

3 Direct Numerical Simulations

We performed a number of nonlinear DNS to investigate the dependence of the critical inflow ratio R value on the various simulation parameters.

The studies results pertaining to the damping sensitivity in the fringe for $R = 1$ were performed with SIMSON and are presented in Fig. 1. The left plot shows the time-dependent amplitude of a single Fourier component in the signal of the streamwise velocity component of a probe located 15 units downstream of the pipe centre for $L_F = 15$, 45 and 75 (curves 1, 2 and 3). The chosen Fourier component
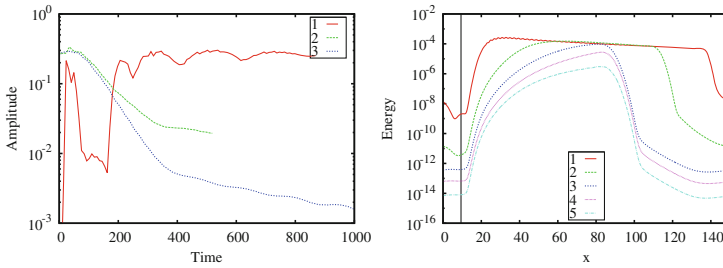
Fig. 1 Temporal evolution of disturbance amplitude (*left*) and energy as function of streamwise position (*right*) of the single most unstable Fourier component for $R = 1$ and different fringe lengths L_F (1, 2, 3) and simulation time (4, 5). Simulation results of `SIMSON`

is the most dominant one in the flow, and its amplitude at time t is calculated by projection of the signal on sine and cosine functions within the window $(t - T_p/2, t + T_p/2)$ (T_p being the component period) and finally smoothed by Bézier curves. The right plot presents the energy of the same Fourier component of the streamwise velocity component integrated over $y - z$ plane and plotted as a function of streamwise position x. Curves 1 and 2 correspond to $L_F = 15, t = 800$ and $L_F = 45, t = 500$ respectively, and curves 3, 4 and 5 give the time evolution of energy distribution for $L_F = 75$ and t equal 500, 1000 and 1500 (time is counted from the beginning of simulation). The pipe centre is marked by the vertical line, and the size of the fringe layer is clearly visible. The first simulation was performed with $L_F = 15$ and Blasius boundary layer as initial condition, and run up to $t = 880$, when the probe signal saturated. This state provided the initial conditions for the two other runs. Note that the final velocity field of the first run consists of more than one frequency component, and curve 1 in Fig. 1 gives only an estimate of observed oscillations.

According to Ilak et al. [6] the JCF for $R = 1$ appears globally unstable, however, closer examination of Fig. 1 shows this flow to be convectively unstable, and the misinterpretation of the instability mechanism to stem from insufficient damping in the fringe. The temporal amplitude evolution of the simulation with the shortest fringe features a short phase of approximately exponential decay (after initial transient phase) ending at $t \approx 160$, when the signal from the fringe reaches the pipe after re-entering the domain and triggers instability. It occurs because the damping in the fringe (of the order of 10^5) is too weak compared to the growth rate in the domain leading to nonlinear saturation of the signal. Similar conclusions can be drawn from the second run ($L_F = 45$), where the nonlinear saturation on the energy plot is still visible. To achieve sufficient damping, the fringe with at least $L_F = 75$ (50 % of the domain) is required. Then, the signal amplitude decays exponentially and the saturation is no longer visible after 500 time units. However, even in this case, the decay rate after $t = 400$ is relatively low leaving considerable energy in the strongest Fourier mode after $t = 1500$. This proves that methods relying on periodic domains to be unsuited for flow cases with considerable spatial growth rates. To employ those methods one has to ensure the damping within the fringe
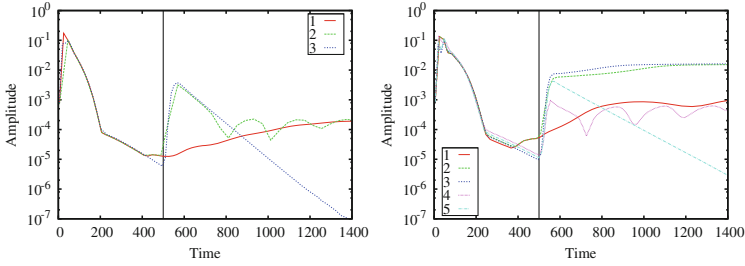
Fig. 2 Time dependent amplitude evolution of the single Fourier component of the velocity probe for $R = 1.4$ (*left*) and 1.5 (*right*) for different domain length and grid resolution. See text for description. Runs with `Nek5000`

region is larger than the expected (physical) spatial growth in the domain to make perturbations re-entering the domain not relevant for the flow dynamics (see as well Ref. [12]).

All subsequent runs are performed with `Nek5000`, which does not require periodicity in streamwise direction. Nevertheless, even in this case a correct treatment of outflow BC was found to be crucial. The time-dependent amplitudes of a single Fourier component in the signal of the streamwise velocity component of a probe located 15 units downstream of the pipe for $R = 1.4$ and 1.5 are shown in Fig. 2. Curves 1–3 correspond to lower resolution runs with $N = 6$, and curves 4 and 5 show results with higher order $N = 9$ for $R = 1.5$. Two different domain lengths are studied: $L_x = 150$ (curves 1, 2 and 4) and 250 (curves 3 and 5). All DNS start with undisturbed Blasius initial condition, and in runs 2, 3, 4 and 5 the instability is triggered by adding non-symmetric noise of amplitude 10^{-4} to the velocity field at $t = 500$ (marked by vertical line). All presented simulations were performed on the M1 mesh. For all cases, an initial transient phase (ending around $t = 220$) is followed by short phase of nearly exponential decay. Depending on the domain size and whether noise was added or not, this phase ends with a rapid amplitude increase followed by exponential decay/saturation, or with the slow growth of low amplitude oscillations. Strong dependency on grid resolution is clearly visible, as the $R = 1.5$ run is globally unstable for $N = 6$ and stable for $N = 9$. On the other hand, small amplitude ($10^{-4} - 10^{-3}$) oscillations visible at the end of all runs with shorter domain (independently whether noise was added or not) are manifestation of interaction between pipe vicinity and outflow BC. In the lower resolution simulations those oscillations are excited during the phase of exponential decay (at $t \approx 400$ and 370 for $R = 1.4$ and 1.5) and reach a final amplitude of $10^{-4} - 10^{-3}$. In the unstable case $R = 1.5$ (curve 1 in right plot) they are later overtaken by growing unstable modes with similar frequency. Such oscillations are not visible in the simulations with longer domain, where all the disturbances are damped exponentially. Increased resolution allows excitation of those waves (no longer visible in the first decay phase) to be delayed, but it does not reduce significantly the final amplitude. Note that for the low resolution runs at $R = 1.5$ the final saturation is reached faster in the longer domain, and the maximum amplitude reached after the noise is added

for $N = 9$ is higher in the longer domain as well. This illustrates the need for proper non-reflective BC.

4 Modal Analysis

Modal stability analysis is the classical method of hydrodynamics stability, where the critical value of a given parameter, for which a single exponentially growing disturbance exists, is computed. In the linear theory for global analysis, those disturbances, the so-called linear global modes, are associated with eigenmodes of the linearised Navier–Stokes operator. Their identification requires finding the base flow U_b, i.e. stationary solution to the nonlinear Navier–Stokes equations, and next solving an eigenvalue problem of the linearised operator. As the considered flow configuration is usually unstable, one option is to calculate U_b adopting an additional stabilisation mechanism to eliminate time dependency in a time-stepper. In our calculations selective frequency damping (SFD) [1] was used. To calculate the eigenvalues, the dimension of the state space of the eigenvalue problem $\dim(U) \sim 10^7$ makes explicit construction of the matrix impossible and requires projection on a low dimension subspace. To achieve this we adopt the Arnoldi algorithm using special matrix-free methods based on time-steppers. Detailed description of the problem with governing equations, implementation in Nek5000, validation and application to JCF can be found in Peplinski et al. [10]. An example of the base flow and spectra (growth rate ω_i vs frequency ω_r) is shown in Figs. 1 and 5 in Ref. [10].

4.1 Setup Without Pipe

Here we present results of the DNS with S1 setup performed on meshes M1 and M2 with domain length $L_x = 150$ for two polynomial orders $N = 6$ and 9, and two velocity ratios $R = 1.5$ and 1.6. To confirm numerical convergence of our results with respect to box length and polynomial order, we performed additional simulations with $L_x = 250$, $L_y = 30$ and resolutions $N = 9$ and 12 for $R = 1.6$. However, since those high resolution runs are computationally very expensive, we calculated only the single strongest mode and we do not present the whole spectra in this case.As the spectra are symmetric with respect to $\omega_r = 0$ we utilise the negative and positive ω_r parts to compare different cases, and we plot only those parts of the spectra matching both direct and adjoint operators (compare positive ω_r part of the left plot in Fig. 5 in Ref. [10]).

Selected results are presented in Fig. 3. In all studied cases increasing resolution decreases the growth rates of all the modes except the ones with zero frequency. The upper left plot presents spectra for $R = 1.5$ and two meshes M1 and M2 (negative versus positive ω_r part of spectra) for two resolutions $N = 6$ (symbols 1 and 3) and 9 (symbols 2 and 4). The importance of high resolution close to the wall is clearly shown, as the low resolution run on mesh M1 is globally unstable, and the run on mesh M2 is stable. On the other hand, most of the converged modes in the spectra of
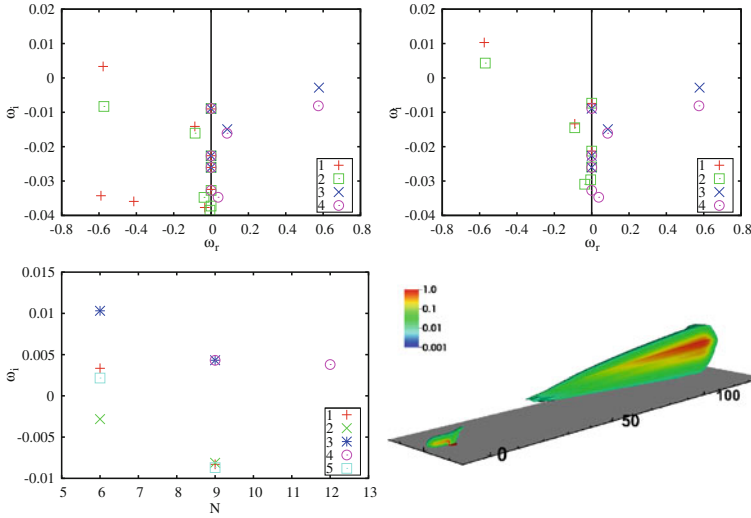
Fig. 3 *Upper row* sensitivity of the spectra to the mesh structure and resolution for different velocity ratios. *Left* spectra for $R = 1.5$ run on M1 (negative ω_r) and M2 (positive ω_r) meshes. *Right* spectra for $R = 1.6$ (negative ω_r) and $R = 1.5$ (positive ω_r) run on M2 mesh. *Lower left* growth rate of the strongest mode as the function of polynomial order N for the modal analysis and nonlinear DNS. *Lower right* Modulus of the direct (far field) and adjoint (pipe orifice) strongest eigenmode

higher resolution runs match each other for both meshes suggesting the resolution necessary for numerical convergence was reached. Simulations with $R = 1.6$ and 1.5 performed on mesh M2 are presented in the upper right plot (negative versus positive ω_r). As before, symbols 1,3, and 4, 5 correspond to $N = 6$ and 9, respectively. The shift of ω_i is larger for higher ω_r, and it seems to be independent of the value of R. The $R = 1.6$ case remains unstable even with the highest resolution and $L_x = 250$. All results are summarised in the lower left plot presenting the growth rate of the strongest mode as a function of N for both linear modal analysis and nonlinear DNS. Symbols 1, 2, 3, and 4 correspond to simulations at $R = 1.5$, mesh M1; $R = 1.5$, mesh M2; $R = 1.6$, mesh M2; $R = 1.6$, mesh M1 with $L_x = 250$, respectively, while symbol 5 gives the growth rate of the strongest Fourier component in DNS for $R = 1.5$ (mesh M1). Higher resolution runs of the linear analysis and nonlinear DNS are consistent with each other in all cases.

The lower right plot in Fig. 3 shows the modulus of the strongest eigenmodes of the direct (far field) and adjoint (pipe vicinity) operators for $R = 1.5$ and $N = 9$. The pipe, marked by a red circle, is located at $x = 0$ and the modes maxima are normalised to unity. The colour scale is logarithmic and the surface of the plotted region corresponds to 1 % of the maximum value illustrating fast decay of the eigenmodes. The total growth of the direct mode (ratio of the maximum to the value at the pipe orifice) is of order 10^9. The visible strong streamwise separation of the direct and adjoint global modes is induced by the base-flow advection and is a signature of non-normality of the linearised operator. This is important since such a high degree
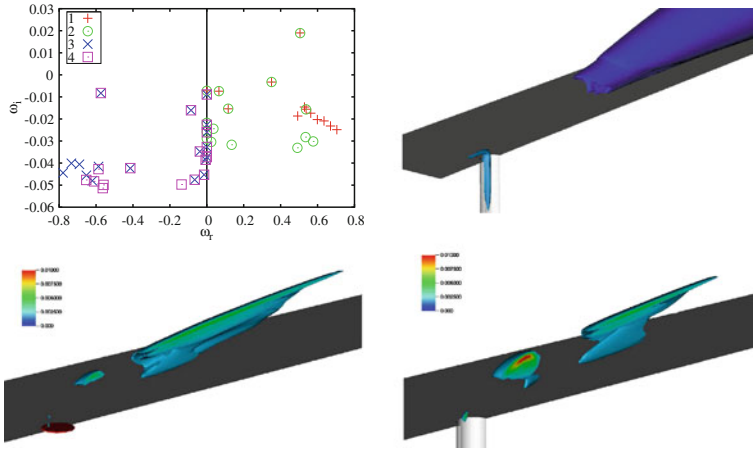
Fig. 4 *Upper left* comparison of the spectra for $R = 1.5$ for setup S1 (negative ω_r) and S2 (positive ω_r). Both direct (symbols 1 and 3) and adjoint (symbols 2 and 4) spectra are plotted. *Upper right* Modulus of the direct (far field) and adjoint (pipe orifice) strongest eigenmode for setup S2. The isosurface corresponds to 20 % of the maximum value. *Lower row* wavemaker for setup S1 (*left plot*) and S2 (*right plot*). The overlap of direct and adjoint modes is re-normalised and the colour scale on both plots is the same. The isosurface corresponds to 20 % of the maximum value

of operator non-normality leads to great sensitivity of the corresponding eigenvalues. It is also well-known that, as a result of non-normality, the perturbation energy may experience strong transient growth even though the flow is globally stable.

4.2 Setup Including Pipe

Simulations with setup S2 were performed for $R = 1.5$ on mesh M1 with $L_x = 150$ and $N = 9$, which are minimal values for box length and polynomial order securing convergence. Results of this run together with comparison to the corresponding S1 simulation are presented in Fig. 4. In the more realistic setup, the $R = 1.5$ case is unstable with relatively large growth rate $\omega_i = 0.019$ suggesting considerable reduction of critical R. It is related to the modified shape of the adjoint eigenmode extending down into the inlet pipe and is clearly visible in the wavemaker plot, as the overlap of direct and adjoint modes next to the pipe orifice and in the shear layer is considerably stronger for setup S2. However, the difference in mass flux can also affect stability, and more studies are necessary to confirm its influence.

5 Non-Modal Analysis

In this section we discuss results of linear optimal disturbances, which is a well established technique to identify the initial condition leading to the largest growth of the disturbance at finite time. We look for the perturbation $\mathbf{u}(t = 0)$ which leads to

maximum energy $\langle \mathbf{u}(T), \mathbf{u}(T) \rangle$ at time T. This problem is equivalent to solving the eigenvalue problem $\lambda \mathbf{u}(0) = \exp(\mathbf{A}^\dagger T) \exp(\mathbf{A} T) \mathbf{u}(0)$, where $\exp(\mathbf{A}^\dagger T) \exp(\mathbf{A} T)$ is the forward and adjoint composite propagator, and $\mathbf{A}$ is a linearised Navier–Stokes operator. The largest eigenvalue can be found iteratively by (matrix-free) power iterations, where the state is first marched forward in time with the standard numerical solver (direct propagator) and then backward with the corresponding adjoint solver (adjoint propagator). The initial condition is white noise and the procedure is repeated until the assumed convergence criterion for $|\mathbf{u}_n(0) - \mathbf{u}_{n-1}(0)|$ is reached, where n is the iteration number. For a more detailed discussion and description of implementation in Nek5000 see Ref. [9].

Our simulations were performed for setup S1 on the fine mesh M2 with domain length $L_x = 150$ and optimisation time $T = 77$ for $R = 1.5$ and 1.6. The initial state $\mathbf{u}(0)$ for each of step (direct and adjoint) was normalised $\langle \mathbf{u}(0), \mathbf{u}(0) \rangle = 1$, and the assumed convergence criterion was 5×10^{-5}, reached after 36 iterations. Note that the backward time marching in our simulations does not mean negative time steps, so the energy increases in both direct and adjoint stepper phases. To keep direct and adjoint problems consistent we apply sponge layers together with homogeneous Dirichlet BC both at the inflow and outflow in the flow. The results are presented in Figs. 5 and 6.

The left plot in Fig. 5 presents the energy growth with time for direct (curves 1, 3) and adjoint (curves 2, 4) phases for stable ($R = 1.5$; curves 1, 2) and unstable ($R = 1.6$; curves 3, 4) cases. The energy evolution is similar in both cases and its final value differs only by factor of 2 ($E = 8 \times 10^{11}$ and 1.6×10^{12} for $R = 1.5$ and 1.6 respectively) showing the transient growth to be only weakly dependent on R. Similar conclusions can be drawn from the nonlinear DNS, in which the optimal disturbance superposed on a steady base flow is used as initial condition. The evolution of time-dependent amplitude of a single Fourier component in the signal of the velocity probe (located 15 units downstream from the pipe) is presented in the right plot in Fig. 5 (curves 1 and 2 correspond to $R = 1.5$ and 1.6, respectively). The initial amplitude development is identical both for stable and unstable cases, however, the final (asymptotic) fate is consistent with modal analysis. The amplitude saturation at 10^{-4} for the stable case $R = 1.5$ (curve 1) is caused by interaction with outflow BC discussed in Sect. 3 above.

Figure 6 presents a comparison of the optimal initial conditions for the streamwise velocity component $u_x(0)$ (upper row) and corresponding final wave packet $u_x(T)$ (lower row) for stable $R = 1.5$ and unstable $R = 1.6$ cases. Angled and top view are shown. As the optimal conditions and wave packets are symmetric with respect to the grid symmetry plane ($y = 0$) we plot results of both simulations on a single frame placing the stable case in the front/lower part of the plot. The maximum value of all the functions are normalised to unity, and the plotted isosurface corresponds to 0.2. Both the optimal disturbances and wave packets for stable and unstable cases are almost identical, however they are slightly shifted with respect to each other due to different shape of the base flow. The wave packets differ also by the wavelength, which is minimally shorter for the stable case.
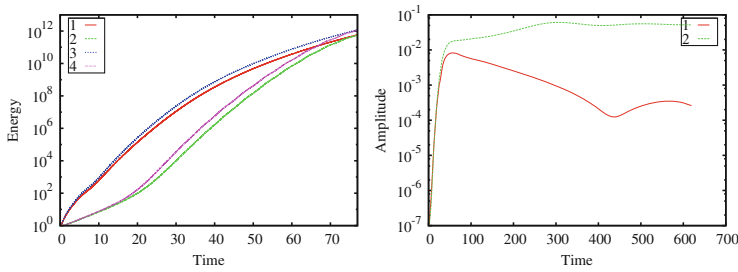
Fig. 5 Energy (*left*) and time-dependent amplitude (*right*) evolution for the transient growth of the optimal disturbance. See text for description
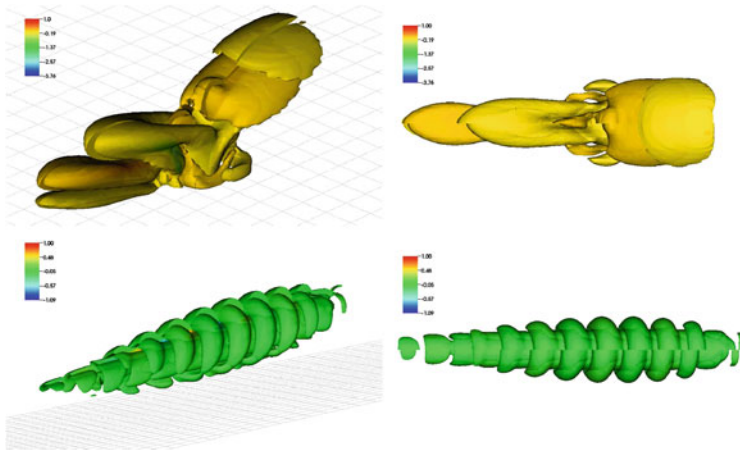
Fig. 6 Comparison of the optimal disturbance (*upper row*) and the resulting wave packet (*lower row*) for the stable (*front*, $R = 1.5$) and unstable (*back*, $R = 1.6$) case

An important advantage of the non-modal analysis is its insensitivity to the outflow BC, as the travelling wave packet never reaches the outflow. However, in our simulations we could see the influence of the inflow (with respect to the direct operator) BC on the adjoint stepper phase manifesting itself by small oscillations of the energy curve at the end of integration period (barely visible in Fig. 5).

6 Conclusions

In the current work, we performed a stability analysis of the jet in crossflow (JCF) testing the numerical methods and stability techniques. We focus on the calculation of the critical velocity ratio R at which first bifurcation (transition from the steady to unsteady flow) occurs. We performed a number of simulations using different numerical methods and codes, including fully spectral (Fourier-Chebyshev) and spectral element discretisation. We find the JCF to be so sensitive to the simulation

parameters and setup that the critical velocity ratio can be found for a particular numerical setup only. In particular we found that methods based on streamwise Fourier decomposition to be not well suited for the present cases with considerable disturbance growth due to the periodic BC in streamwise direction, as insufficient damping in the fringe region can significantly change the flow dynamics. Even for codes with inflow/outflow BC, we demonstrate the need for proper non-reflective BC, and the sensitivity of the modal stability analysis to the grid resolution. This great sensitivity of the eigenvalue at the bifurcation point indicates that it may not be a particularly interesting quantity to consider, as the flow itself is very sensitive to external disturbances and that transient effects are more relevant than the asymptotic growth rate associated with a particular global mode. We calculated the optimal disturbance finding its growth and shape robust and almost independent on R.

References

1. Åkervik E, Brandt L, Henningson DS, Hœpffner J, Marxen O, Schlatter P (2006) Steady solutions of the Navier-Stokes equations by selective frequency damping. Phys. Fluids 18:1–4
2. Bagheri S, Schlatter P, Schmid PJ, Henningson DS (2009) Global stability of a jet in crossflow. J. Fluid Mech. 624:33–43
3. Chevalier, M., Schlatter, P., Lundbladh, A., Henningson, D.S.: SIMSON: a pseudo-spectral solver for incompressible boundary layer flows. Tech. Rep. 2007:07, KTH Mechanics (2007).
4. Ehrenstein U, Gallaire F (2005) On two-dimensional temporal modes in spatially evolving open flows: the flat-plate boundary layer. J. Fluid Mech. 536:209–218
5. Fischer, P., Lottes, J., Kerkemeier, S.: nek5000 Web page http://nek5000.mcs.anl.gov (2008)
6. Ilak M, Schlatter P, Bagheri S, Henningson DS (2012) Bifurcation and stability analysis of a jet in cross-flow: onset of global instability at a low velocity ratio. J. Fluid Mech. 696:94–121
7. Karagozian AR (2010) Transverse jets and their control. Prog. Energy Combust. Sci. 36:531–553
8. Mahesh K (2013) The Interaction of Jets with Crossflow. Annu. Rev. Fluid Mech. 45:379–407
9. Monokrousos A, Åkervik E, Brandt L, Henningson DS (2010) Global three-dimensional optimal disturbances in the Blasius boundary-layer flow using time-steppers. J. Fluid Mech. 650:181–214
10. Peplinski, A., Schlatter, P., Henningson D.S.: Stability Tools for the Spectral-Element Code Nek5000; Application to Jet-in-Crossflow. ICOSAHOM'12, Gammarth, Tunisia, to appear (2013).
11. Peplinski, A., Schlatter, P., Henningson D.S.: Investigations of stability and transition of a jet in crossflow using DNS. DLES 9, Dresden, Germany, to appear (2014).
12. Rolshoven S (2000) A mechanism of transition to torbulence in a three-dimensional boundary layer: Tech.Rep, École Polytechnique
13. Schlatter P, Bagheri S, Henningson DS (2011) Self-sustained global oscillations in a jet in crossflow. Theor. Comput. Fluid Dyn. 25:129–146
14. Schmid PJ, Henningson DS (2011) Stability and transition in shear flows. Springer, New York

Some Challenging Studies on Shock Wave Boundary Layer Interactions Using Advanced Flow Diagnostics

K. Kontis, H. Zare-Behtash and E. Erdem

Abstract Those working in the field of diagnostics continuously find new ways to visualise and quantify complicated flows in ways that were probably at some time thought to be impractical. These include either optimisation of already well-established techniques such as Schlieren with the development of higher resolution and faster cameras, or the invention of new methods by the synergy between different disciplines, such as pressure sensitive paints which bring together physics, chemistry and fluids. Ideally most of these diagnostic methods have a low parasitic profile or are completely non-intrusive. The present article paper gives a brief overview of some challenging investigations on shock boundary layer interactions using these flow diagnostic methods. A case study on axisymmetric transitional interactions at Mach 5 is also presented.

1 Introduction

Even though airflow is invisible, it is evident from the movements of tree leaves and branches all around us. We all remember the recent volcanic eruption in Iceland that caused havoc to the airline industry. Everyone remembers from the weather forecasts on TV or the newspapers how the volcanic plumes followed the air currents down to Europe and lingered in some parts longer than others. This is a natural example of flow visualisation where the smoke and debris from the volcanic ash showed the path which the air particles followed. Other well-known examples can be the swirls we see around obstacles in water, or the heat we see rising from the ground on a hot day. Therefore, we encounter various flow diagnostic methods in our everyday life.

Using the same methods found in nature, or just by using the principle laws of nature, we are able to have in our arsenal a variety of flow measurement techniques capable of revealing different properties of the flow ranging from pressures and temperatures to densities and velocities [1, 2].

K. Kontis (✉) · H. Zare-Behtash · E. Erdem
Aero-Physics Laboratory, School of Engineering, University of Glasgow, Scotland, UK
e-mail: kostas.kontis@glasgow.ac.uk
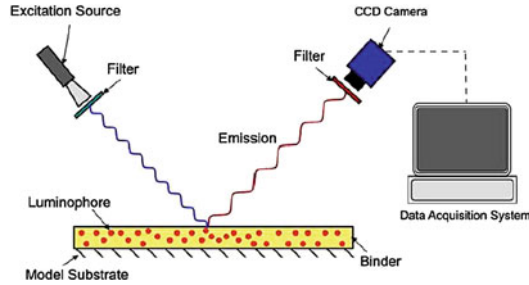
Fig. 1 Elements of a typical PSP system

Within the Aero-Physics Laboratory at The University of Glasgow, using the knowledge and know-how gained through experience alongside the state of the art facilities and equipment, we are host to a range of advanced diagnostic capabilities. The present paper provides an overview for measuring the pressures and temperatures using the relatively new pressure and temperature sensitive paint methods as well as the more familiar particle image velocimetry technique. Using in-house examples, we aim to provide better insight into the abilities of these techniques.

2 Pressure-Sensitive Paints

Pressure-sensitive paints (PSP) are a relatively new method of obtaining global and non-intrusive surface pressures [3, 4]. A typical PSP contains oxygen-sensitive photoluminescent molecules called luminophores suspended in a polymer binder. When light of a certain wavelength, λ, is shined on the PSP, the photons energise these luminophores and the luminophores are said to have become excited. Naturally, these excited molecules desire to return to their equilibrium ground state. The excited molecules do this either by emitting light at a higher wavelength or by transferring the absorbed energy through collision with an oxygen molecule, a process called oxygen quenching. Oxygen quenching results in a decrease in intensity of the emitted light from the photoluminescent molecules [5]. By using a selection of appropriate filters, depending on the type of luminophores used, the light emitted from the PSP can be isolated from the light used to excite the paint [6]. Figure 1 shows a typical PSP system.

There is a linear relationship between air pressure and oxygen concentration, hence, as air pressure increases the intensity of the emitted light from the PSP, I, reduces [7]. To eliminate surface non-uniformities of the PSP, when it is applied to a model surface, the intensity at a given pressure is divided by a reference intensity, Iref. Figure 2 shows how the change in pressure causes a change in intensity emitted as well as the uniform distribution due to dividing each image by that of the reference case, which is taken as vacuum in the current example.

To convert the intensity images into pressure a PSP sample is calibrated within a pressure/temperature controlled environment. This type of calibration is known as

1.0 bar 1.3 bar 1.6 bar 1.9 bar 2.2 bar 2.5 bar 2.8 bar
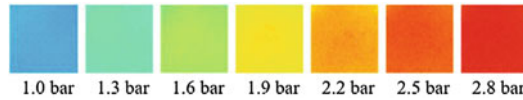
Fig. 2 Variation of PSP intensity with pressure

Fig. 3 Stern-Volmer plot
with curve fit for a typical PSP
formulation [4]
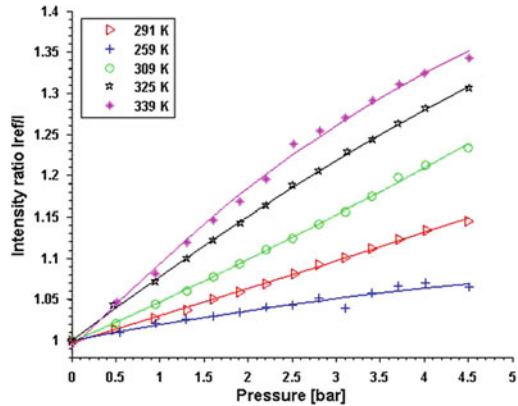
a-priori calibration. Figure 3 shows a typical plot of the variation of PSP intensity
with pressure at different temperatures which is known as a Stern-Volmer plot. In
the figure I corresponds to the intensity at a known pressure, Iref is the intensity at
the reference case, P is the pressure which is varied and Pref relates to the pressure
of the reference state.

The relationship between luminescent intensity and pressure is given by a poly-
nomial curve fit of the experimental data given in Fig. 3. The coefficients A(T), B(T),
and C(T) are determined from the polynomial curve fit. PSP calibration can also take
place in-situ whilst performing an experiment. This is carried out using pressure taps
to record the pressure at different locations along the model and the pressure at these
locations is related to the paint intensity at the immediate vicinity of the tapping.
Performing in-situ calibration reduces the effect of temperature changes along the
model since the emitted intensity is already corrected for this effect. Another advan-
tage of in-situ calibration is that because the same setup is used for both calibration
and to conduct the experiments, any changes in calibration setup that might result in
variations in the calibration curve such as the location of the camera relative to the
light source for example are eradicated [8].

Ruthenium(III) bathophenanthroline perchlorate (Ru(III) bathphen) is another
luminophores which demonstrated significant oxygen sensitivity [9]. It is excited at
475 nm (blue) and emits luminescent at 586 nm (red). Figure 4 shows the Schlieren
and corresponding PSP map of the flow through a convergent nozzle at different
inlet pressures. The visual comparison between the two techniques shows that at
first glance PSP is capable of capturing the flow features well. The flow shear layer
generated between the emerging fluid and the ambient, the compression of the flow
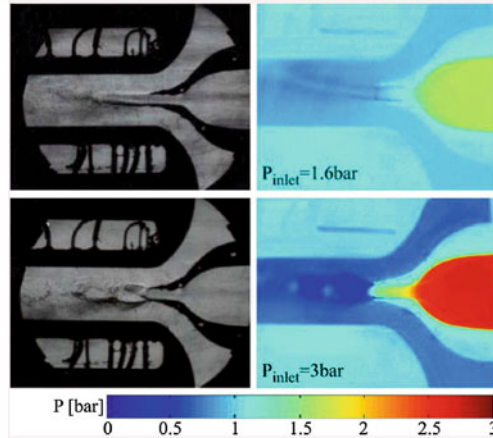
Fig. 4 Schlieren and PSP of flow through a convergent nozzle [4]

entering the area convergence along with the subsequent acceleration through the uniform area channel, and the diamond shock structures created as the flow expands are all readily identifiable.

Before applying PSP to a model usually a base coat is first applied. The base coat not only provides a uniform surface on the model but can also affect the PSP performance [10]. A white base coat is typically used, which acts as a scattering layer for both exciting and emitted photons, enhancing the PSP emitted intensity [11].

The comparison between the pressure measured by PSP and that of Kulite pressure transducers, shown in Fig. 5 for three different inlet pressures, revealed an approximate 4 % difference between the two methods. The profiles show that by increasing the inlet pressure the size of the shock cells increases with a greater pressure drop and subsequent increase through this train. Without prior knowledge of the size and location of the shock cells it would be extremely difficult to position the transducer tappings to perform measurements.

The Ruthenium luminophore can also be used in the transonic regime. Shock boundary layer interaction (SBLI) is an extremely complex and important phenomenon. SBLI plays a crucial role in the design of wing and tailplane junctions with the aircraft fuselage, supersonic engine inlets, and deflected control surfaces of high-speed vehicles. Figure 6 shows the study conducted to examine the control effectiveness of dimples on the glancing shock wave turbulent boundary interaction produced by a hemi-cylindrically blunted fin at $M = 0.8$.

The dimples appear to affect the local flowfield around the leading edge and alter the effective geometry of the leading edge. The effect of the dimples in altering the flowfield is highly dependent on their orientation relative to the model leading edge, leading to a nonsymmetrical flow. Their existence causes changes in shock strength and size over the model. The overall uncertainty of the PSP analysis was calculated at 5 %. One of the challenges of obtaining high resolution and accurate PSP results
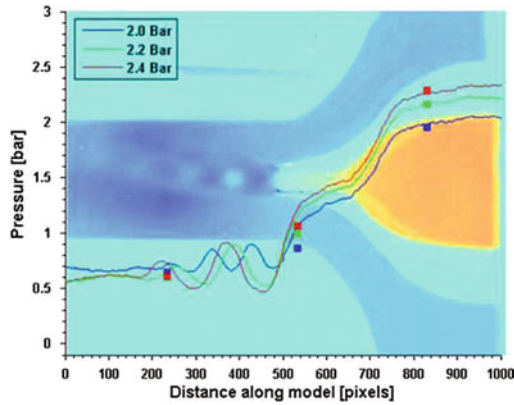
Fig. 5 PSP profiles along model centreline at various inlet pressures and comparison with pressure tappings [4]

is the signal obtained from the paint, that is, the intensity emitted. To obtain a strong signal to noise ratio (SNR) often multiple images of the flow are captured and then summed together. Care must be taken with this procedure when studying unsteady features. Because a summation of images is used to obtain the pressure map, naturally we are looking at a time-averaged image of the pressure rather than the instantaneous values. However, when the frequency of the unsteadiness is lower than the image acquisition time, PSP can provide an accurate description of the flowfield.

2.1 Anodized Aluminium Pressure Sensitive Paints

The development of anodized aluminium pressure sensitive paints (AA-PSP) was driven by the need to have a fast response time to be able to capture flow unsteadiness [13–18]. The procedure of calibration and pressure measurements using AA-PSP is identical to polymer based PSPs. What differentiates AA-PSP and polymer PSP is the substrate [19, 20]. In conventional polymer based PSP the model is usually coated
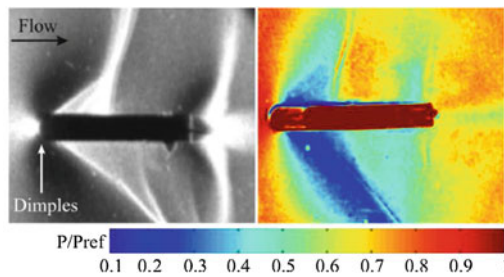
Fig. 6 Schlieren and PSP at M = 0.8 of a blunt fin with dimples [12]
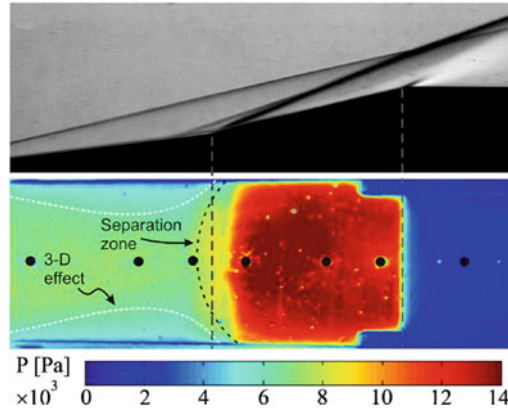
Fig. 7 Schlieren and AA-PSP of a double ramp in M=5 flow at −4° incidence [21]

with a base paint and the PSP is applied over it, in AA-PSP however, as the name implies the model which is made from aluminium is exposed to an electrochemical process which completely alters the surface texture of the model. This process creates micro pores on the model surface. The creation of these micro pores leads to an increased surface area where the luminophores can be adsorbed. More surface areas leads to a greater chance of collision between the oxygen molecules in the surrounding air and the luminophores molecules. The main drawback of AA-PSP is the low signal level emitted from the paint. This can be compensated by either using a powerful illuminations source or having a sensitive camera. Figure 7 shows AA-PSP applied to a double ramp in hypersonic flow at M=5 placed with a 4° incidence. The AA-PSP correlates well with the Schlieren image, showing the region of flow separation before the second ramp, the compressed flow over the second ramp and the expansion of the flow over the uniform area at the rear of the model. It is also captures the three-dimensional spillage effect which occurs over the first ramp.

A classic and fundamental problem in aerodynamics is the complex flow over truncated cones shown in Fig. 8. The complexity of these shapes/models means it is very difficult to cover them with pressure tappings, which alter their geometry, or if numerous taps are used can be quite an expensive experiment.

Using AA-PSP the pressure distribution over the entire model can be obtained in a single run, revealing flow structures that would otherwise be difficult to trace or find without a pre-knowledge of their existence and properties. Of course once the pressure map is obtained, using mathematical models one can obtain flow streamlines or pressure contours similar.
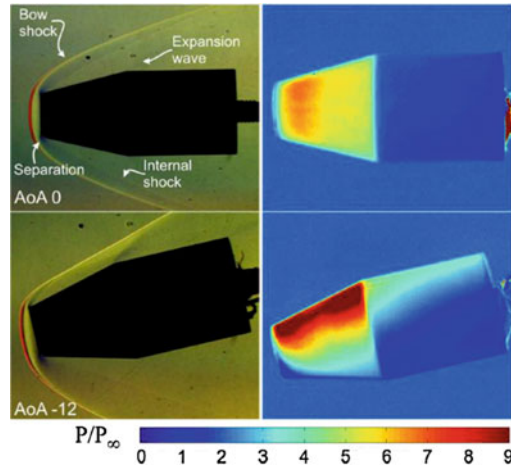
Fig. 8 Colour Schlieren and AA-PSP of a truncated cone in M = 5 at different incidence angles [22]

3 Axisymmetric Transitional Shock-Wave Boundary Layer Interactions at Mach 5

When shock waves interact with boundary layers developing on solid surfaces Shock Wave Boundary Layer Interactions (SWBLIs) form, which embed a series of complicated flow phenomena. SWBLI can induce separation which causes loss of a control surface effectiveness, drop of an air intake efficiency and it may be the origin of large scale fluctuations such as air-intake buzz, buffeting or fluctuating side loads in separated propulsive nozzles. The subsequent reattachment of the separated shear layer on a nearby surface gives rise to local heat transfer rates which can be far in excess of those of an attached boundary layer. Most of the work done in this field over the years has been focused on fully developed turbulent flows since most practical applications were at transonic and low supersonic speeds at altitudes where Reynolds numbers are large and turbulent boundary layer flows are encountered. With the decrease of altitude, there is a rise in Reynolds number so that transition, which first occurs far downstream penetrates into the SWBLI region. Therefore transitional SWBLIs, in which the incoming boundary layer is in a transitional state (natural transition), or in which transition is induced within the interaction itself (triggered transition), appear to be even more unsteady and could have greater adverse effects, and yet have received little attention. The present experimental study focusses on this problem with an impinging shock wave including both transition mechanisms; natural and triggered transition. The methodology involves high-speed wind tunnel testing at Mach 5 with an axisymmetric hollow model.
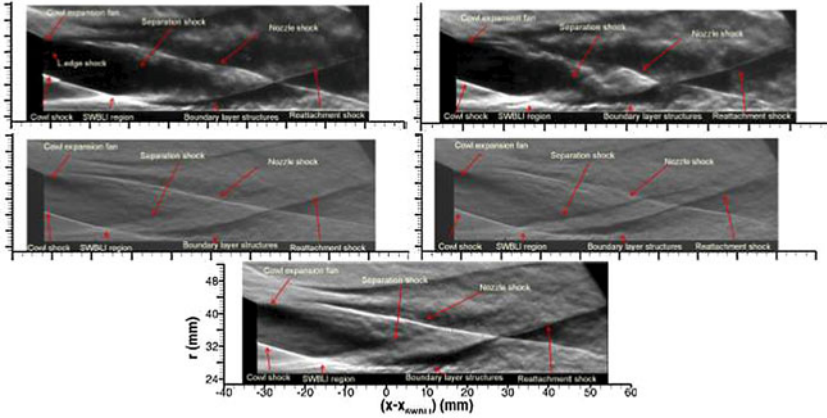
Fig. 9 Schlieren visualisation of the flowfield at the interaction region for SWBLI@90 mm, SWBLI@190 mm, SWBLI@200 mm, SWBLI@220 mm and SWBLI@255 mm cases in descending order [23]

3.1 Results

The results of the experimental campaign include schlieren photography, QIRT (Quantitative Infra-Red Thermography), PSP, particle image velocimetry (PIV), and wall pressure measurements. Figure 9 shows spark schlieren visualisation of the flowfield with different SWBLI positions. The horizontal axis is shifted with respect to SWBLI location. The following structures can be observed clearly; centrebody leading edge shock (only visualised in SWBLI@90 mm case), impinging cowl shock, cowl expansion fan and the shear layer at the cowl trailing edge, upstream separation region (upstream of the shock impingement location) with the separation shock, expansion wave on top of the separation region, the reattachment shock, and finally the nozzle shock. In the downstream of the SWBLI region the boundary layer structures are oscillatory and the turbulent in nature. In general as the intermittency is increased, the boundary layer becomes more turbulent and the skin friction coefficient rises. Hence, it becomes more resistant to the adverse pressure gradient imposed by the impinging shock, which would result a relatively smaller SWBLI region.

Figure 10 (top left) shows Stanton number profiles over the centreline of the centrebody for all the cases. For each case, i.e. SWBLI@90, 190, 200, 220 and 255 mm, the data from the tests without the cowl are also plotted. In addition theoretical laminar and turbulent distributions of heat flux and Stanton number over a flat plate using reference temperature method are included. The agreement between the experiments and the theory is good in terms of laminar and turbulent heat flux distributions. The transition region is found to be broad, starting from around 150 mm and ending nearly at 300 mm. Figure 10 (top right) shows azimuthal Stanton number distributions on max heat flux lines. SWBLI@90 mm shows oscillatory behaviour around the circumference, the reason for that might be the presence of streamwise vortices.
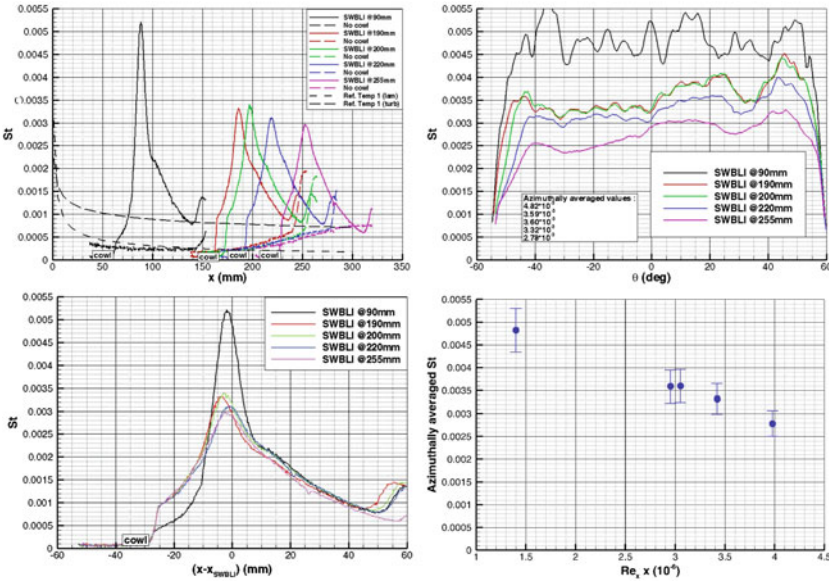
Fig. 10 *Top left* centreline Stanton number distributions for all cases with theoretical laminar and turbulent estimates [23]

SWBLI@190 and 200 mm cases also exhibit oscillatory behaviour but smaller in peaks and troughs. Figure 10 (bottom left) shows the shifted Stanton number distributions over centreline of the centrebody. The horizontal axis is shifted with respect to SWBLI location, i.e. SWBLI location becomes zero. The heat flux rise due to the SWBLI is overlapping on top of each other for SWBLI@190, 200, 220 and 255 cases up to 15 mm upstream of inviscid SWBLI position, afterwards it starts to deviate. The rise is more aggressive for SWBLI@190 and 200 mm cases compared to SWBLI@220 and 255 mm cases. Downstream of heat transfer peak profiles start to overlap around 20 mm downstream of the origin. Smaller rise in profiles at around 50 mm downstream of origin is due to the influence of the nozzle shock. SWBLI@90 mm case has a bigger heat flux peak and steeper rise due to the fact that the boundary layer is undergoing transition to turbulence (triggered transition) throughout the SWBLI region. Figure 10 (bottom right) also shows the azimuthally averaged Stanton number values (between −45 and 45° azimuthal angles) at maximum heat flux lines against Reynolds number based on inviscid position of the impinging shock. The error bars do not represent the experimental uncertainties but manifest the variation of heat flux across the circumference between −45 and 45° (from min to max). Nominally laminar values are found to be biggest and the highest intermittency values are the smallest.

Figure 11 (left) shows shifted non-dimensional wall pressure distributions over the centrebody. The horizontal axis is shifted with respect to inviscid SWBLI location, i.e. SWBLI location becomes zero. The pressure rise due to the SWBLI is ovelapping

Fig. 11 *Left* non-dimensional wall pressure distribution over the centrebody for all cases, *right* non-dimensional wall pressure distribution over the centrebody deduced from PSP for all cases [23]

Fig. 12 *Top* ensemble-averaged velocity magnitude (m/s), *bottom* zoomed in area into SWBLI region [23]
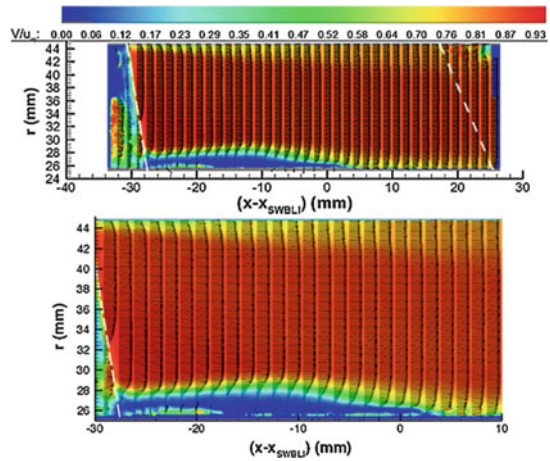
on top of each other for SWBLI@190, 200, 220 and 255 mm cases. SWBLI@90 mm case has a steeper rise on the other hand. However due to the discrete nature of the tappings, the peak of the pressure rise for SWBLI@90 mm case can not be observed. The maximum non-dimensional pressure value is found to be around 5.8. This value is found to be greater than the value of 4.55 found using double regular reflection of 7°. The non-dimensional pressure values are found to be accurate within 4 %. Figure 11 (right) shows the behaviour of non-dimensional wall pressure distributions over the centrebody deduced from PSP. The pressure rise due to the SWBLI is ovelapping on top of each other for SWBLI@190, 200 and 220 mm cases. SWBLI@90 mm case has an abrupt rise whereas SWBLI@255 mm case has a gradual behaviour. The locations for the pressure peaks are found to lie between 3 and 8 mm downstream of the inviscid position of the impinging shock. The most downstream position of the pressure peak is observed for SWBLI@255 mm case.

Figure 12 shows two component particle image velocimetry measurements at the centerline for SWBLI@90 mm. It is evident how the flow above the SWBLI region

turns towards the all and becomes parallel to it. The SWBLI has a height of approximately 4 mm and a length of 18 mm downstream of the inviscid position of the impinging shock. Although compared to the PSP method PIV is a more established technique [24–28], nonetheless, it can be quite challenging when applied to high Mach number flows [29, 30]. Issues such as tracer particle diameter, particle distribution, laser power, and image resolution are some of the properties that must be adequately addressed in order to capture accurate data. A successful PIV campaign provides unparalleled insights into flow physics, such as that demonstrated by Fig. 12.

4 Conclusions

PSP has been applied to a wide range of high speed flows with different characteristics which reveal the techniques' advantages and disadvantages. The technique provide good qualitative information on flow features and the behaviour of the flow. PSP has shown that it can provide accurate measurements at low-speed all the way up to the hypersonic regime. The type of luminophore used plays an important role on the performance of a PSP, some luminophores are more sensitive to pressure changes whilst others have a greater range of operations. The second component to consider when performing PSP experiments is the substrate or the means of applying the PSP to the model surface. This will depend on the sensitivity, response time and signal intensity required by the experimental conditions.

A case study of a transitional Shock Wave Boundary Layer Interaction (SWBLI) at Mach 5 is also presented. Various flow diagnostics were utilised to map the complex flowfield such as schlieren photography, QIRT (Quantitative Infra-Red Thermography), PSP, PIV, and pressure tappings. Time-averaged heat transfer peak was found to occur around the reattachment point. For SWBLI@90 mm case the separation induces transition and the heat transfer and pressure peaks were found to be the highest. For the cases with natural transition with different intermittency levels, where incoming boundary layer is in state of transition, the magnitude of peaks initially started to increase from SWBLI@190 mm case reaching a maximum for SWBLI@200 mm case.

References

1. Mercer C (2003) Optical metrology for fluids, combustion and solids. Kluwer Academic Publishers, Dordrecht
2. Yang W-J (1989) Handbook of flow visualization. Taylor & Francis, London
3. Bell JH, Schairer ET, Hand LA, Mehta RD (2001) Surface pressure measurements using luminescent coatings. Annu Rev Fluid Mech 33:155–206
4. Zare-Behtash H, Gongora-Orozco N, Kontis K, Holder SJ (2009) Application of novel pressure-sensitive paint formulations for the surface flow mapping of high-speed jets. Exp Thermal Fluid Sci 33:852–864
5. Liu T, Sullivan JP (2004) Pressure and temperature sensitive paints. Springer, Berlin
6. Gongora-Orozco N, Zare-Behtash H, Kontis K (2009) Effects of filters on the performance and characteristics of pressure-sensitive paints. Meas Sci Technol 20: 077004 (6pp)
7. Mosharov V, Radchenko V, Fonov S (1998) Luminescent pressure sensors in aerodynamic experiments. Central Aerodynamic Institute (TsAGI)

8. Quinn MK, Gongora-Orozco N, Kontis K, Ireland P (2011) Application of pressure-sensitive paint to low-speed flow around a u-bend of strong curvature. In: 8th Pacific symposium on flow visualization and image processing, Russia
9. Hubner JP, Carrol BF, Schanze KS, Ji HF (2000) Pressure-sensitive paint measurements in a shock tube. Exp Fluids 28:21–28
10. Schairer ET (2002) Optimum thickness of pressure-sensitive paint for unsteady measurements. AIAA 40(11):2312–2318
11. McLachlan BG, Bell JH, Park H, Kennelly RA, Schreiner JA, Smith SC, Strong JM (1995) Pressure-sensitive paint measurements on a supersonic high-sweep oblique wing model. J Aircr 32(2):217–227
12. Kontis K, Lada C, Zare-Behtash H (2008) Effect of dimples on glancing shock wave turbulent boundary layer interactions. Shock Waves 17:323–335
13. Sakaue H, Sullivan JP (2001) Time response of anodized aluminium pressure-sensitive paint. AIAA 39(10):1944–1949
14. Sakaue H, Gregory JW, Sullivan JP, Raghu S (2002) Porous pressure-sensitive paint for characterizing unsteady flowfields. AIAA 40(6):1094–1098
15. Asai K, Nakakita K, Kameda M, Teduka K (2001) Recent topics in fast-responding pressure-sensitive paint technology at national aerospace laboratory. In: Instrumentation in aerospace simulation facilities, 19th international congress on ICIASF, pp 25–36
16. Sakamura Y, Matsumoto M, Suzuki T (2005) High frame-rate imaging of surface pressure distribution using a porous pressure-sensitive paint. Meas Sci Technol 16:759–765
17. Baron AE, Danielson JDS, Gouterman M, Wan JR, Callis JB, McLachlan B (1993) Submillisecond response times of oxygen-quenched luminescent coatings. Rev Sci Instrum 64(12):3394–3402
18. Gongora-Orozco N, Zare-Behtash H, Kontis K (2010) Global unsteady pressure-sensitive paint measurements of a moving shock wave using thin-layer chromatography. Measurement 43:152–155
19. Ishiguro Y, Nagai H, Asai K, Nakakita K (2007) Visualization of hypersonic compression corner flows using temperature- and pressure-sensitive paints. In: 45th AIAA aerospace sciences meeting and exhibit, Reno, AIAA, 2007, vol 118
20. Liu T, Campbell BT, Sullivan JP (1995) Fluorescent paint for measurement of heat transfer in shock—turbulent boundary layer interaction. Exp Thermal Fluid Sci 10:101–112
21. Yang L, Zare-Behtash H, Erdem E, Kontis K (2012) Application of AA-PSP to hypersonic flows: the double ramp model. Sens Actuators, B 161:100–107
22. Yang L, Erdem E, Zare-Behtash H, Kontis K, Saravanan S (2012) Pressure-sensitive paint on a truncated cone in hypersonic flow at incidences. Int J Heat Fluid Flow 37:9–21
23. Erdem E, Murray N, Steeland J, Kontis K (2013) Experiments on transitional shock wave boundary layer interactions at Mach 5. Exp Fluids. doi:10.1007/s00348-013-1598-z
24. Raffel M, Willert CE, Kompenhans J (1998) Particle image velocimetry. Springer, Berlin
25. Melling A (1997) Tracer particles and seeding for particle image velocimetry. Meas Sci Technol 8:1406–1416
26. Hain R, Kahler CJ (2007) Fundamentals of multiframe particle image velocimetry (PIV). Exp Fluids 42(4):575–587
27. Gongora-Orozco N, Zare-Behtash H, Kontis K (2010) Particle image velocimetry studies on shock wave diffraction with freestream flow. In: 48th AIAA aerospace sciences meeting including the new horizons forum and aerospace exposition, Orlando, AIAA 2010, vol 876
28. Zare-Behtash H, Gongora-Orozco N, Kontis K (2009) Global visualization and quantification of compressible vortex loops. J Vis 12(3):233–240
29. Zare-Behtash H, Kontis K, Takayama K (2008) Compressible vortex loop studies in a shock tube with various exit geometries. In: 46th AIAA aerospace sciences meeting and exhibit, Reno, AIAA 2008, vol 362
30. Zare-Behtash H, Kontis K, Gongora-Orozco N, Takayama K (2010) Shock wave induced vortex loops emanating from nozzles with singular corners. Exp Fluids 49(5):1005–1019

Part II
Separated Flow Over Airfoils: Fundamental Instability Mechanisms

Investigation of Coherent Structures and Dynamics Using POD and DMD of a Separated Airfoil Subjected to ZNMF Jet Forcing

N. A. Buchmann, V. Kitsios, C. Atkinson and J. Soria

Abstract Proper Orthogonal Decomposition (POD) and Dynamic Mode Decomposition (DMD) are applied to the unsteady separated flow field over a NACA-0015 airfoil with periodic zero-net-mass-flux (ZNMF) jet forcing at the leading edge at an angle of attack $\alpha = 18^o$ and chord based Reynolds number of $Re = 3 \times 10^4$. This study presents experimental data for the forced flow case and recovers the dominant coherent structures and temporal characteristics that describe the evolution of the velocity perturbation. The dominant frequencies are identified by the DMD eigenvalues and the corresponding spatial modes are compared to the dominant POD modes.

1 Introduction

One of the primary aims of flow control is to prevent boundary layer separation and to extend the effective operational range of engineering devices such as diffusers, compressors, turbines and airfoils. In the case of airfoils, periodic excitation has been shown to delay separation and hence increase lift over a wide range of Reynolds numbers and angles of attack (AoA) [2, 6]. The present experimental flow configuration is a NACA-0015 airfoil with zero-net-mass flux (ZNMF)

N. A. Buchmann (✉) · V. Kitsios · C. Atkinson · J. Soria
Laboratory of Turbulence Research in Aerospace and Combustion,
Monash University, Melbourne, VIC 3141, Australia
e-mail: nicolas.buchmann@monash.edu

N. A. Buchmann
Institute of Fluid Mechanics and Aerodynamics, Bundeswehr University Munich,
85577 Neubiberg, Germany

J. Soria
Department of Aeronautical Engineering, King Abdulaziz University,
Jeddah, United Kindom of Saudi Arabia
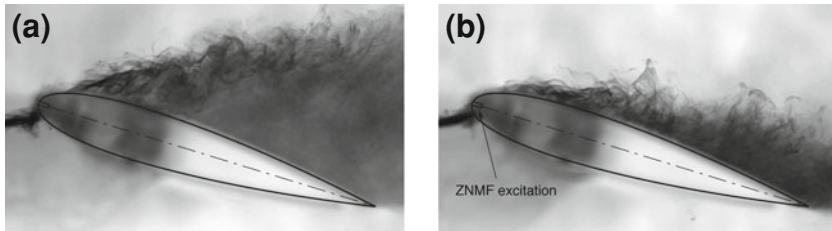
Fig. 1 Dye flow visualisation [7] of a NACA-0015 airfoil, Re $= 3 \cdot 10^4$, $\alpha = 18^\circ$: **a** unforced case; **b** ZNMF jet forcing at the leading edge, $f^+ = 1.3$, $c_\mu = 0.0014$

jet forcing through a 2D slot at the leading edge and chord based Reynolds Re $\equiv U_\infty c/\nu = 3 \times 10^4$, $U_\infty = 260\,\text{mm/s}$, $c = 100\,\text{mm}$ and 18° AoA. The experiments are conducted in a horizontal water tunnel using high repetition Particle Image Velocimetry to measure the time-resolved two-component, two-dimensional velocity fields at mid-span. In the absence of forcing, laminar flow separation occurs at the leading edge as shown in Fig. 1a, while ZNMF jet forcing at the leading edge with a non-dimensional frequency $f^+ = fc/U_\infty = 1.3$ and momentum blowing coefficient $c_\mu = 0.0014$ results in a time-averaged reattachment of the flow (Fig. 1b). A detailed description of the experiments, including dimensionless parameters is available in [1, 7] and a Large Eddy simulation of the unforced base flow in [4].

The focus of the present study is to characterise the structure and dynamics of the ZNMF jet forcing by computing the modes of the Proper Orthogonal Decomposition (POD) and the Dynamic Mode Decomposition (DMD) form the experimental data. The general mathematical approach for computing the POD and DMD is outlined in the first part, which is then followed by a discussion of the modes that are representative of the structure and dynamics of the leading edge ZNMF jet forcing.

2 Mode Decomposition Methods

POD and DMD decompose the flow field into temporal and spatial modes to provide a lower-order representation of the complex time-dependent flow field. The POD is a generalised set of orthogonal basis functions for a given series of time-resolved or statistically independent observations (i.e. snapshots) and the reconstructed modes are an energy-weighted representation of the coherent flow structures. The DMD presents a linear approximation of a time-resolved non-linear process and contains information pertaining to the stability, frequency and growth rate of this process. For a detailed description of the POD we refer to [5] while the present implementation of the DMD algorithm follows that of [3].

The instantaneous velocity field $\mathbf{u}(\mathbf{x}, t)$ at time t and position $\mathbf{x}$ is decomposed into its time-averaged mean $\bar{\mathbf{u}}(\mathbf{x})$ and its fluctuating component $\mathbf{u}'(\mathbf{x}, t)$. The discrete fluctuating flow field, consisting of $N+1$ snapshots, is arranged in the snapshot matrix

$\mathbf{A} = [\mathbf{u}'(\mathbf{x}, t_1), \ldots, \mathbf{u}'(\mathbf{x}, t_N)]$. The POD represents this snapshot matrix such that

$$\mathbf{A} = \mathbf{U}\mathbf{V}^T, \tag{1}$$

where $\mathbf{V}$ are the temporal modes, $\mathbf{U}$ the spatial modes, and the subscript ^{T} the transpose matrix operation. The POD modes are obtained by solving the eigenvalue problem

$$\mathbf{C}\mathbf{V} = \Sigma^2\mathbf{V}, \tag{2}$$

where the eigenvectors $\mathbf{V}$ of the correlation matrix $\mathbf{C} = \mathbf{A}^T\mathbf{A}/N$ are the temporal modes and the eigenvalues Σ^2 the modal energies. The spatial modes are calculated by $\mathbf{U} = \mathbf{A}\mathbf{V}\Sigma^{-2}/N$ and the POD modes have orthogonality properties $\mathbf{U}^T\mathbf{U} = \mathbf{I}$ and $\mathbf{V}^T\mathbf{V}/N = \Sigma^2$.

In the Dynamic Mode Decomposition the non-linear evolution of the fluctuating velocity field is approximated by [3]:

$$\dot{\mathbf{u}}'(\mathbf{x}, t) = \mathbf{M}\mathbf{u}'(\mathbf{x}, t) + \mathbf{f}(\mathbf{x}, t), \tag{3}$$

where $\dot{\mathbf{u}}'(\mathbf{x}, t)$ is the time derivative of $\mathbf{u}'(\mathbf{x}, t)$, $\mathbf{M}$ a deterministic time invariant linear operator, and $\mathbf{f}(\mathbf{x}, t)$ the stochastic residual error of the linear approximation. Using a temporal harmonic approximation for the fluctuations of the form $u'(x, t) = \hat{\mathbf{u}}(\mathbf{x})Ke^{-i\Omega}$ and neglecting the stochastic component expression (3) reduces to the following eigenvalue problem,

$$-i\Omega\hat{\mathbf{u}}(\mathbf{x}) = \mathbf{M}\hat{\mathbf{u}}(\mathbf{x}), \tag{4}$$

where $\lambda = -i\Omega$ are the eigenvalues and $\hat{\mathbf{u}}(\mathbf{x})$ the eigenvectors or spatial modes of $\mathbf{M}$. The temporal modes are given by $\hat{v}(t) = Ke^{-i\Omega t}$, where K is a scaling constant.

The DMD eigenvalue problem (4) can be solved by projecting the matrix $\mathbf{M}$ onto the POD modes. Defining a time-shifted snapshot matrix $\mathbf{A}_2 = [\mathbf{u}'(\mathbf{x}, t_2), \ldots, \mathbf{u}'(\mathbf{x}, t_{N+1})]$ the matrix $\mathbf{M}$ satisfies

$$\dot{\mathbf{A}} = (\mathbf{A}_2 - \mathbf{A})/\Delta t = \mathbf{M}\mathbf{A}, \tag{5}$$

where $(\mathbf{A}_2 - \mathbf{A})/\Delta t$ is the first order approximation of the time derivative. Substituting the POD decomposition (1) into (5), post-multiplying by $\mathbf{V}\Sigma^{-2}/N$, pre-multiplying by $\mathbf{U}^T$, and using the POD orthogonality properties returns

$$(\mathbf{U}^T\mathbf{A}_2\mathbf{V}\Sigma^{-2}/N - \mathbf{I})/\Delta t = \mathbf{U}^T\mathbf{M}\mathbf{U} \equiv \check{\mathbf{M}}. \tag{6}$$

The leading dimensions of $\mathbf{M}$ are the number of snapshots N times the size of the spatial field $\mathbf{x}$, which reduces significantly to the leading dimensions of $\check{\mathbf{M}}$, which are the number of POD modes used in the projection (N_m). Instead of solving the eigenvalue problem (4) one can now solve for $\check{\mathbf{M}}$, which has eigenvalues λ and eigenvector $\mathbf{Z}$. If all POD modes are used in the projection, the eigenvalues of $\check{\mathbf{M}}$
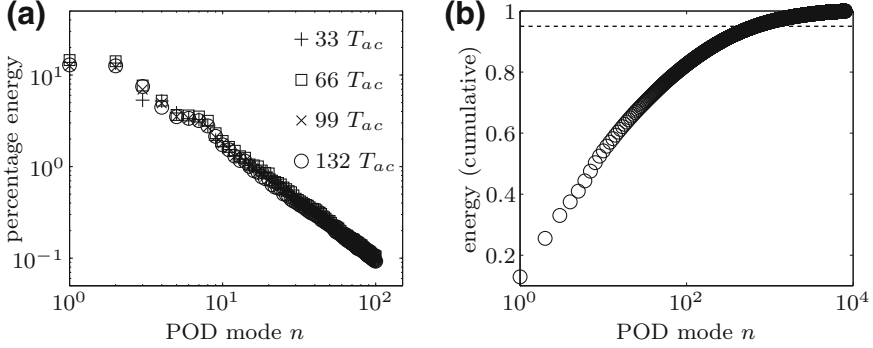
Fig. 2 (*left*) POD percentage energy of the first 100 modes for time periods $T = 33$, 66, 99 and 132 T_{ac}; (*right*) cumulative modal energy ($T = 132 \, T_{ac}$)

are equivalent to the eigenvalues of **M**. The eigenvectors of **M** however, are given by $\hat{\mathbf{u}} = \mathbf{UZ}$, where the matrix **Z** essentially determines the combination of spatial POD modes that is required to reconstruct the DMD modes. Using similar arguments one can determine the adjoint spatial modes $\hat{\mathbf{u}}_{adj}$ of $\check{\mathbf{M}}$ and using the biorthogonal property $\hat{\mathbf{u}}^{T*}\hat{\mathbf{u}} = \mathbf{I}$, where $*$ denotes the complex conjugate operation, the temporal DMD modes are given by $\hat{\mathbf{v}} = A^T \hat{\mathbf{u}}_{adj}$.

3 Results

In the following the above approach is applied to the separated shear layer subjected to ZNMF jet forcing with frequency $f_{ac}^+ = 1.3$. First, the convergence of the mode decomposition is tested by examining the POD eigenvalues for different snapshots periods $T = 33$, 66, 99 and 132 actuation periods T_{ac}, where one actuation period consists of approximately 61 instantaneous snapshots with temporal separation $\Delta t^+ = 0.0135$ (i.e. $5 \, \mu s$). The resulting POD energy spectra are shown in Fig. 2a, which converge after approximately 66 actuation cycles with 95 % of the fluctuating energy captured in the first 10 % of the modes (Fig. 2b).

For demonstration purpose, the DMD modes are computed for $T = 33 \, T_{ac}$ by projecting Eq. (6) onto the first 2000 POD modes, which capture 100 % of the POD energy. The resulting eigenvalues are illustrated in Fig. 3a in form of the unit circle where $\mu \equiv \mu_r + i \mu_i = 1 - i \Omega \Delta t$. These are equivalent to the eigenvalues of the linear propagator $\mathbf{M} \Delta T + \mathbf{I}$ and, which by definition are the eigenvalues of **M**. All of the eigenvalues fall either on or within the unit cycle indicating that these modes are either on a limit cycle or decaying. Using the adjoint DMD modes the amplitude of each mode is determined and the modal energy calculated as $\Sigma_{DMD}^2 = \hat{\mathbf{v}}^{T*}\hat{\mathbf{v}}_{adj}$. This energy is plotted against the frequency of each mode $f = -\arctan(\mu_i/\mu_r)/\Delta t$ in Fig. 3b. The energy spectrum shows a number of distinct peaks that correspond to the
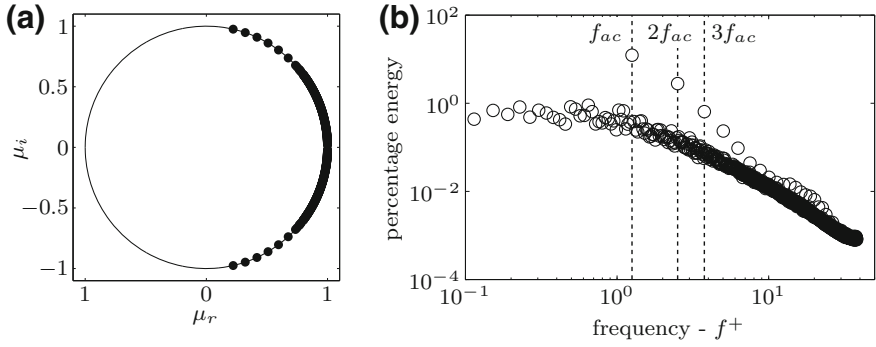
Fig. 3 (*left*) DMD unit circle; (*right*) DMD modal percentage energy versus frequency
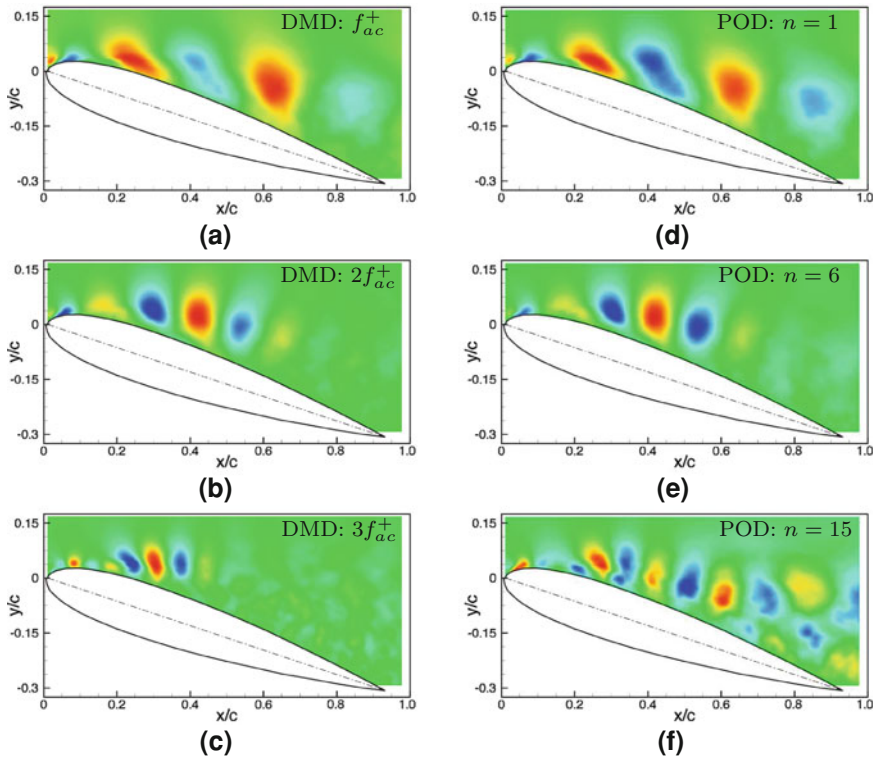
Fig. 4 (**a-c**) Spatial DMD modes at the fundamental and harmonic forcing frequency; (**d-e**) selected POD modes with similar spatial structure compared to the DMD modes. Shown are iso-contours of the vertical velocity component with the color map adjusted for better visualisation

fundamental forcing frequency $f_{ac}^+ = 1.3$ and its harmonics. The dominant spatial DMD modes at the fundamental forcing frequency and its first two harmonics are shown in Fig. 4 by means of iso-contours of the coherent vertical velocity component. The dominant modes illustrate an organised train of coherent spanwise vortices of alternating rotation that originates at the point of actuation near the airfoil leading edge. The spatial frequency of the coherent vortices increases for higher harmonics, but at the same time their amplitudes weakens in streamwise direction. The flow fields associated with the imaginary modes have similar structures, yet offset in space and time. Selected POD modes with similar spatial structure are also shown in Fig. 4 and at least the lower modes (i.e. $m = 1, 6$) exhibit good spatial coherence with the dominant DMD modes. The DMD and POD modes also reveal similar spatial structures compared to the phase-averaged velocity fields in [1].

4 Concluding Remarks

The present work has demonstrated a mean of determining the dynamic modes of a non-linear system via a POD projection of the governing linear operator. DMD and POD modes, for a nominally separate flow forced at the leading edge of a NACA-0015 airfoil have been presented to illustrate the dynamics and coherence associated with this forcing. It should be noted that for periodic flows, such as here, the DMD modes coincide with the Fourier modes. However, the resolved DMD frequencies are not predetermined by the sampling interval Δt^+ and the sampling time T, yet are still subjected to the Nyquist limit.

References

1. Buchmann NA, Atkinson C, Soria J (2013) Influence of ZNMF jet flow control on the spatio-temporal flow structure over a NACA-0015 airfoil. Exp Fluids 54:1485
2. Greenblatt D, Wygnanski IJ (2000) The control of flow separation by periodic excitation. Prog Aerosp Sci 36:487–545
3. Hasselmann K (1988) PIPs and POPs: The reduction of complex dynamical systems using principle interaction and oscillating patterns. J Geophys Res 93(D9):11015–11021
4. Kitsios V, Cordier L, Bonnet J-P, Ooi A, Soria J (2011) On the coherent structures and stability properties of a leading-edge separated aerofoil with turbulent recirculation. J Fluid Mech 683:395–416
5. Kostas J, Soria J, Chong MS (2005) A comparison between snapshot pod analysis of piv velocity and vorticity data. Exp Fluids 38:146–160
6. Seifert A, Greenblatt D, Wygnanski IJ (2004) Active separation control: an overview of Reynolds and Mach numbers effects. Aerosp Sci Technol 8:569–582
7. Tuck A, Soria J (2008) Separation control on a NACA 0015 airfoil using a 2D micro ZNMF jet. Aircr Eng Aerosp Technol 80(2):175–180

Recovery of the Koopman Modes of a Leading-Edge Separated Aerofoil Flow via a Proper Orthogonal Decomposition Rank Reduction

V. Kitsios, N. A. Buchmann, C. Atkinson, J. S. Frederiksen and J. Soria

Abstract Koopman modes are presented for a leading edge separated aerofoil flow with turbulent recirculation. The specific flow configuration is a NACA 0015 aerofoil at an angle of attack of 18° and a chord based Reynolds number of 3×10^4. This decomposition approximates the evolution of a nonlinear system by a linear operator, the eigenvectors of which represent the spatial form of the fluctuations, and the eigenvalues represent the associated temporal frequencies and growth rates. Proper orthogonal decomposition (POD) modes are used to create a reduced rank linear operator from which the Koopman modes are determined. The sensitivity to the number of POD modes used in the rank reduction is assessed. The dominant frequencies identified by the Koopman eigenvalues coincide with the dominant frequencies determined from a Fourier analysis of probe histories.

V. Kitsios (✉) · C. Atkinson · J. Soria
Department of Mechanical and Aerospace Engineering, Laboratory for Turbulence Research
in Aerospace and Combustion, Monash University, Clayton, VIC 3800, Australia
e-mail: vassili.kitsios@monash.edu

C. Atkinson
e-mail: callum.atkinson@monash.edu

N. A. Buchmann
Institut für Strömungsmechanik und Aerodynamik LRT-7, Fakultät für Luft-und
Raumfahrttechnik, Universität der Bundeswehr, Munich, Germany
e-mail: nicolas.buchmann@unibw.de

J. S. Frederiksen
Centre for Australian Weather and Climate Research, CSIRO Marine and Atmospheric
Research, 107–121 Station Street, Aspendale, VIC 3195, Australia
e-mail: jorgen.frederiksen@csiro.au

J. Soria
Department of Aeronautical Engineering, King Abdulaziz University, Jeddah,
Kingdom of Saudi Arabia
e-mail: julio.soria@monash.edu

1 Introduction

In many engineering systems flow separation leads to drastic reductions in performance. The study of separation is therefore of utmost importance both for understanding the physical processes and for developing practical active and passive flow control devises. The flow studied within, is a leading edge separated NACA 0015 aerofoil with turbulent recirculation. It is at an angle of attack of $AoA = 18°$ and with a chord based Reynolds number of $Re \equiv u_\infty c/\nu = 3 \times 10^4$, where ν is the kinematic viscosity, c the chord length, and u_∞ the freestream velocity. This configuration was studied using large eddy simulation (LES) in [4, 5], which demonstrated good agreement with the mean velocity field and Reynolds stresses experimentally measured using particle image velocimetry in [1, 9]. Of particularly interest is the leading edge region, as excitation of the flow near the uncontrolled separation point produces large spatial growth rates [5], and hence requires a lower excitation amplitude for a given level of lift enhancement [8].

Within, the dynamics are characterised by Koopman modes generated from the LES fields of [5]. We outline the approach for calculating the Koopman modes, then present these modes at both the leading edge and throughout the flow domain.

2 Mathematical Approach

Koopman modes were introduced to geophysical fluid mechanics in [3], with a detailed review presented in [10], and further discussion on the Koopman operator in [6, 7]. Here we follow the derivation of [2]. In any case the approach uses observations of a general nonlinear system to construct a linear operator that best represents the evolution of the system, with the eigenvectors of the linear operator the modes of interest. However, the linear operator becomes prohibitively large for large data sets with many spatial points. We alleviate this problem by projecting the Koopman eigenvalue problem onto a set of proper orthogonal decomposition (POD) modes.

We first present the POD decomposition, then the Koopman eigenvalue problem projected onto the POD modes. To facilitate this discussion we define the snapshot matrix $\mathbf{A}$. The instantaneous vector $\mathbf{u}(\mathbf{x}, t)$, at time t and position $\mathbf{x}$, is decomposed into its time averaged mean $\overline{\mathbf{u}}(\mathbf{x})$ and its fluctuating component $\mathbf{u}'(\mathbf{x}, t)$. The matrix $\mathbf{A}$ contains the fluctuating components, with $\mathbf{u}'(\mathbf{x}, t_1)$ at all points in space in the first column through to $\mathbf{u}'(\mathbf{x}, t_{N+1})$ in the final column.

A POD represents the snapshot matrix by $\mathbf{A} = \mathbf{U}\mathbf{V}^T$, where the temporal modes are the columns of $\mathbf{V}$, the spatial modes are the columns of $\mathbf{U}$, and the superscript ^{T} represents the matrix transpose operation. The POD temporal modes are the eigenvectors of the correlation matrix $\mathbf{C} = \mathbf{A}^T \mathbf{w} \mathbf{A}/N$, where $\mathbf{w}$ contains the cell volumes along the diagonal. The eigenvalues of $\mathbf{C}$ are the POD modal energies contained in the diagonal elements of the matrix $\mathbf{\Sigma}^2$. Note the matrix $\mathbf{\Sigma}$ contains the singular

values of $\mathbf{A}$. The spatial modes are calculated by $\mathbf{U} = \mathbf{A}\mathbf{V}\boldsymbol{\Sigma}^{-2}/N$. The POD modes have orthogonality properties $\mathbf{U}^T\mathbf{w}\mathbf{U} = \mathbf{I}$ and $\mathbf{V}^T\mathbf{V}/N = \boldsymbol{\Sigma}^2$.

In the Koopman decomposition a non-linear system is approximated by

$$\dot{\mathbf{u}}'(\mathbf{x}, t) = \mathbf{M}\mathbf{u}'(\mathbf{x}, t) + \mathbf{f}(\mathbf{x}, t), \tag{1}$$

where $\dot{\mathbf{u}}'$ is the time derivative of $\mathbf{u}'$, with $\mathbf{M}$ a time invariant linear operator, and $\mathbf{f}(\mathbf{x}, t)$ represents the residual error in the linear approximation. The eigenvectors of $\mathbf{M}$ are the Koopman modes. The estimate of $\mathbf{M}$ that minimises the error $\mathbf{f}(\mathbf{x}, t)$ is

$$\mathbf{M} = [\langle \mathbf{u}'(\mathbf{x}, t + \Delta t)\mathbf{u}'^T(\mathbf{x}, t)\rangle \langle \mathbf{u}'(\mathbf{x}, t)\mathbf{u}'^T(\mathbf{x}, t)\rangle^{-1} - \mathbf{I}]/\Delta t, \tag{2}$$

where the angular brackets denote time averaging, and the state time derivative is approximated as $\dot{\mathbf{u}}'(\mathbf{x}, t) \approx [\mathbf{u}'(\mathbf{x}, t + \Delta t) - \mathbf{u}'(\mathbf{x}, t)]/\Delta t$, with Δt the time between snapshots.

To reduce the size of the eigenvalue problem, the matrix $\mathbf{M}$ is projected onto the POD modes. We define the matrix $\mathbf{A}_2$, for which the first column contains snapshot 2 and the final column contains snapshot $N + 2$. The matrix $\mathbf{M}$ then satisfies

$$\dot{\mathbf{A}} = (\mathbf{A}_2 - \mathbf{A})/\Delta t = \mathbf{M}\mathbf{A}. \tag{3}$$

We then substitute the POD decomposition $\mathbf{A} = \mathbf{U}\mathbf{V}^T$ into (3), post-multiply by $\mathbf{V}\boldsymbol{\Sigma}^{-2}/N$, pre-multiply by $\mathbf{U}^T\mathbf{w}$, and use the POD orthogonality properties to return

$$\left(\mathbf{U}^T\mathbf{w}\mathbf{A}_2\mathbf{V}\boldsymbol{\Sigma}^{-2}/N - \mathbf{I}\right)/\Delta t = \mathbf{U}^T\mathbf{w}\mathbf{M}\mathbf{U} \equiv \check{\mathbf{M}}. \tag{4}$$

The leading dimension of $\mathbf{M}$ is the number of points times the number of flow variables, which has been significantly reduced to the leading dimension of $\check{\mathbf{M}}$ equal to the number of POD modes used in the projection (N_m). We denote the complex eigenvectors of $\check{\mathbf{M}}$ as being contained in the columns of the matrix $\mathbf{Z}$, and the complex eigenvalues by $-i\Omega$. When all POD modes are used in the projection, the eigenvalues of $\check{\mathbf{M}}$ are equivalent to the eigenvalues of $\mathbf{M}$. The eigenvectors of $\mathbf{M}$ are given by $\hat{\mathbf{u}} = \mathbf{U}\mathbf{Z}$, where the matrix $\mathbf{Z}$ essentially determines the combination of spatial POD modes required to reconstruct the Koopman modes. One can work through similar arguments to determine the adjoint Koopman modes $\hat{\mathbf{u}}_{adj}$. The direct and adjoint Koopman modes form a biorthogonal set.

3 Results

The above approach is now used to extract Koopman modes initially focussed at the leading edge region, and then throughout the flow domain. From this point forward all quantities are nondimensionalised by c and u_∞, unless units are specified.
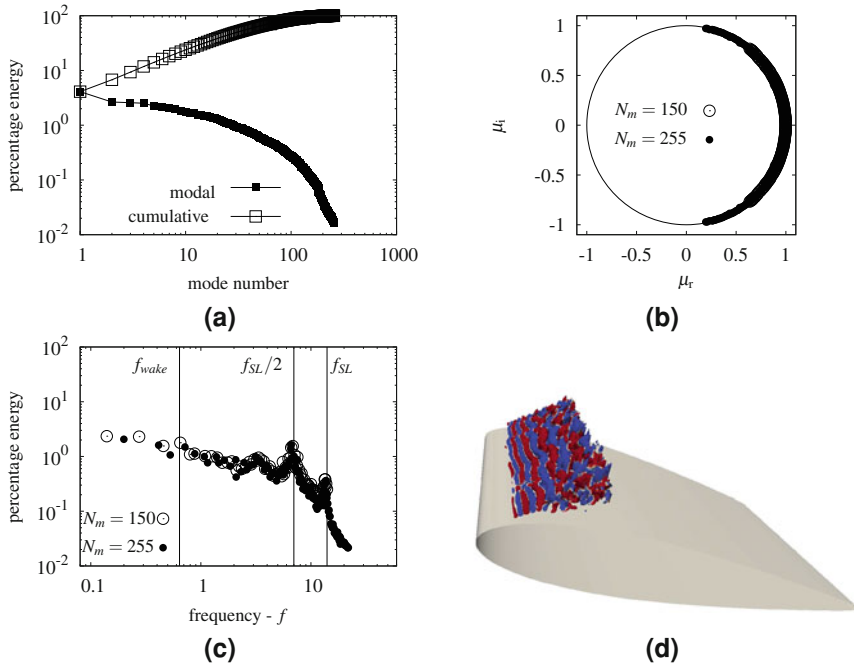
Fig. 1 Koopman modes in the leading edge domain determined from a POD rank reduction. **a** POD percentage modal and cummulative energies. For various POD truncation levels N_m: **b** unit circle; and **c** Koopman modal percentage energies verses frequency. **d** Iso-surfaces of the Q criteria coloured by spanwise vorticity (positive—*red*, negative—*blue*) for the real component of the Koopman spatial mode with $f = f_{SL} = 14$

In the leading edge region, the shear layer is the dominant physical phenomenon. At the point of separation the dominant vortex structures had a temporal period of approximately 0.08 [5]. A POD was created over 77 of these periods with $\Delta t = 0.01$. The POD modal energies are illustrated in Fig. 1a. We project the Koopman linear operator onto all 255 of the POD modes capturing 100 % of the energy, and also the first 150 modes capturing 95 %. The resulting eigenvalues are illustrated in Fig. 1b. Here we present the eigenvalues in the typical unit circle form where $\mu \equiv \mu_r + i\mu_i = 1 - i\Omega\Delta t$, which is equivalent to the eigenvalues of the propagator $\mathbf{M}\Delta t + \mathbf{I}$. Note the eigenvectors of $\mathbf{M}\Delta t + \mathbf{I}$ are the same as the eigenvectors of $\mathbf{M}$. All of the eigenvalues are either on the unit circle (or within it) indicating that these modes are in a limit cycle (or decaying). The energy in each Koopman mode is given by the diagonal elements of the matrix $\mathbf{Z}_{\mathbf{adj}}^{T*} \mathbf{\Sigma} \mathbf{Z}$. This energy is plotted against the frequency of each mode $f = -\arctan(\mu_i/\mu_r)/\Delta t$ in Fig. 1c. There are distinct peaks in energy at both $f_{SL} = 14$ and also its subharmonic $f_{SL}/2$. The latter is more energetic as the energy is integrated over the entire volume, and the subharmonic structures are further downstream from separation, and physically larger. In Fig. 1d we show the spatial form of the mode with $f = f_{SL}$ by iso-surfaces of the second invariant
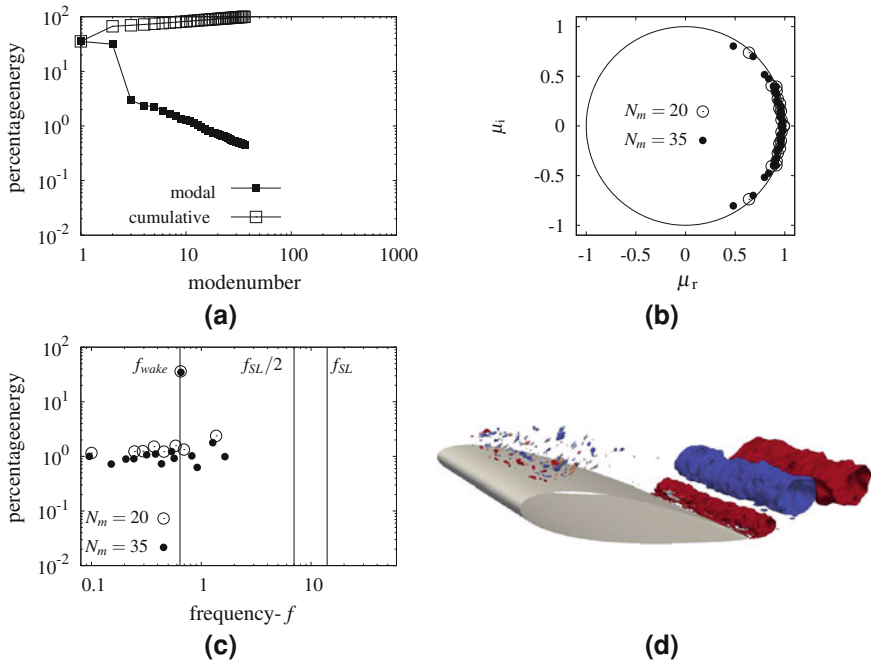
Fig. 2 Koopman modes throughout the flow domain determined from a POD rank reduction. **a** POD percentage modal and cummulative energies. For various POD truncation levels N_m: **b** unit circle; and **c** Koopman modal percentage energies verses frequency. **d** Iso-surfaces of the Q criteria coloured by spanwise vorticity (positive—*red*, negative—*blue*) for the real component of the Koopman spatial mode with $f = f_{wake} = 0.64$. To facilitate a direct comparison each plot has the same scale as the associated plots in Fig. 1

of the real velocity gradient tensor (Q) coloured by spanwise vorticity. This illustrates an organised train of spanwise structures of alternating rotation originating at the point of separation. Vortices in the associated imaginary velocity field have similar structure but offset in space downstream.

The only vortex structure present throughout the entire flow domain is the bluff body shedding, which has a frequency of $f_{wake} = 0.64$ and associated period $1/f_{wake} = 1.56$ [5]. A POD was created over 32 shedding cycles with approximately 16 snapshots per cycle ($\Delta t = 0.1$). The POD modal energies are illustrated in Fig. 2a. The first 2 modes represent the bluff body shedding and capture 69 % of the energy. We then project the Koopman linear operator onto all 35 of the POD modes capturing 100 % of the energy, and also the first 20 modes capturing 91 %. The resulting eigenvalues are illustrating in Fig. 2b with all modes either stable or on the limit cycle. The energy in each mode is then plotted against frequency in Fig. 2c, indicating a distinct peak at the bluff body shedding frequency of $f_{wake} = 0.64$, with all other modes lower in energy by two orders of magnitude. The shear layer frequencies are not captured as the Δt between the snapshots is not small enough.

Figure 2d illustrates the spatial form of this dominant mode, by the Q iso-surfaces of the real velocity field coloured by spanwise vorticity. This shows large coherent spanwise structures representative of the bluff body shedding. Again vortices in the associated imaginary velocity field have a similar yet offset structure.

4 Concluding Remarks

We have demonstrated a means of determining Koopman modes via a POD rank reduction of the governing linear operator. Koopman modes representative of the dynamics at the leading edge and throughout the flow domain have been illustrated. At these truncation levels the Koopman eigenvalues and modal energies are found to be only weakly dependent on the number of POD modes used in the decomposition. These modes could potentially be used for the development of reduced order models for real time model based flow control.

References

1. Buchmann N, Atkinson C, Soria J (2013) Influence of ZNMF jet flow control on the spatio-temporal flow structures over a NACA-0015 airfoil. Exp Fluids 54:1485–1498
2. Frederiksen JS, Branstator G (2005) Seasonal variability of teleconnection patterns. J Atmos Sci 62:1346–1365
3. Hasselmann K (1988) PIPs and POPs: the reduction of complex dynamical system susing principal interaction and oscillation patterns. J Geophys Res 93:11015–11021
4. Kitsios V (2010) Recovery of fluid mechanical modes in unsteady separated flows. PhD thesis, The University of Melbourne and Université de Poitiers
5. Kitsios V, Cordier L, Bonnet J-P, Ooi A, Soria J (2011) On the coherent structures and stability properties of a leading edge separated airfoil with turbulent recirculation. J Fluid Mech 683:395–416
6. Mezić I (2005) Spectral properties of dynamical systems, model reduction and decompositions. Nonlinear Dyn 41:309–325
7. Rowley CW, Mezić I, Bagheri S, Schlatter P, Henningson DS (2009) Spectral analysis of nonlinear flows. J Fluid Mech 641:115–127
8. Smith D, Amitay M, Kibens V, Parekh D, Glezer A (1998) Modification of lifting body aero-dynamics using synthetic jet actuators. AIAA-98-0209
9. Tuck A, Soria J (2008) Separation control on a NACA 0015 airfoil using a 2D micro ZNMF jet. Air Eng Aero Tech 80(2):175–180
10. von Storch H, Burger G, Schnur R, von Storch J-S (1995) Principal oscillation patterns: a review. J Clim 8:377–390

Effect of the Trailing Edge Geometry on the Unsteadiness of the Flow Around a Stalled NACA 0015 Airfoil

Wei He, Francisco Gómez, Daniel Rodríguez and Vassilis Theofilis

Abstract The effect on the flow unsteadiness on a NACA 0015 airfoil at Reynolds number $Re = 200$ and Angle of Attack $AoA = 18°$ is investigated numerically. Four different geometries based on the NACA 0015 airfoil and with trailing-edge modifications are compared. Long-time integration of the incompressible two-dimensional Navier-Stokes equations shows that the recovered flow field is steady independently of the trailing-edge geometry.

1 Introduction

With increasing angle of attack, flow separation in thick airfoils (those in which the thickness-to-chord ratio $\geq$ 15 %) occurs first at the trailing edge, and subsequently moves up-chord towards the leading edge ultimately causing what is called trailing-edge stall [1]. For thinner airfoils, e.g. NACA 0012, separation occurs near the leading edge just downstream of the suction peak, leading to a completely different stall behavior [2]. In their study of the flow instability of a stalled NACA 0015 airfoil, Kitsios et al. [3] concluded that the flow at Reynolds number $Re = 200$ and Angle of Attack $AoA = 18°$ computed by means of time-accurate two-dimensional simulation is steady, but able to develop three-dimensional instabilities [4]. Brehm and Fasel [5] attempted to reproduce these results, but found in their 2D simulations that, under the same conditions, the flow developed self-sustained oscillations, and

W. He (✉) · D. Rodríguez · V. Theofilis
School of Aeronautics, Universidad Politécnica de Madrid, Plaza. Cardenal Cisneros 3,
28040 Madrid, Spain
e-mail: wei@torroja.dmt.upm.es

F. Gómez
Department of Mechanical and Aerospace Engineering, Monash University, Melbourne,
VIC 3800, Australia

Fig. 1 Different trailing-edge geometries
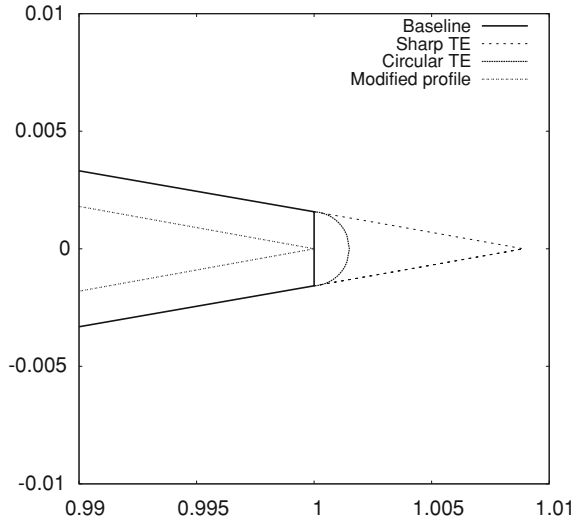
argued that the code used in Kitsios et al. would had too much numerical dissipation if the results were grid-independent.

Another potential cause for this discrepancy is related to the precise definition of the trailing-edge geometry. Different closures to the trailing edge are typically adopted during the meshing process prior to numerical simulations, which on occasions modify the original geometry towards an idealized one, affecting the flow instability properties. In particular, the trailing edges of NACA-family airfoils present a rectangular shape instead of closing into a single point. In simulations, it is usually convenient to modify the trailing-edge so that the pressure and lee sides end in a common point. This paper employs a different simulation code from that in Kitsios et al., and studies whether the particular geometry of the trailing edge alters significantly the instability behaviour of the flow around the NACA 0015, addressing the controversy reported by Brehm and Fasel.

2 Geometry of Trailing Edge

Figure 1 depicts the four different trailing-edge geometries based on the NACA 0015 airfoil considered. The "Baseline" NACA 0015 case has a non-zero trailing-edge thickness, with a thickness relative to the chord of 0.315 %. The NACA 0015 airfoil is described by the function

$$y = \pm 0.75 \left(0.2969\sqrt{x} - 0.1260x - 0.3516x^2 + 0.2843x^3 - 0.1015x^4 \right), \ x \in [0, 1]. \tag{1}$$

The second airfoil, referred to as "sharp TE", is the same as the baseline but replaces the trailing edge with the parabolic function

$$y = \pm \left(-0.3503313x^2 + 0.5268143x - 0.1749080 \right), \; x \in [1, 1.0089]. \quad (2)$$

The third geometry replaces the trailing edge with a circular edge of diameter $R \approx$ 0.001576875 in the baseline profile. The arc center coordinate are (0.9999923125, 0).

As opposed to the previous geometries, the equation describing the airfoil has been modified for the last case. The fourth coefficient in the polynomial is altered slightly in order to have zero thickness at the trailing edge:

$$y = \pm 0.75 \left(0.2969\sqrt{x} - 0.1260x - 0.3516x^2 + 0.2843x^3 - 0.1036x^4 \right), \; x \in [0, 1]. \quad (3)$$

This "Modified airfoil" has a bigger leading edge radius and the position of the maximum thickness is displaced downstream, but the overall modifications are very small.

3 Numerical Simulation Setup

Incompressible viscous flow is governed by the Navier-Stokes (NS) equations,

$$\frac{\partial \mathbf{U}}{\partial t} + \mathbf{U} \cdot \nabla \mathbf{U} = -\nabla P + \frac{1}{Re} \nabla^2 \mathbf{U} \quad (4)$$

and the equation of continuity,

$$\nabla \cdot \mathbf{U} = 0 \quad (5)$$

where $\mathbf{U}(x, y, t)$ and $P(x, y, t)$ are dimensionless velocity and pressure of the fluid, and Re is the Reynolds number. Two-dimensional incompressible transient laminar flow governed by NS equations are solved by OpenFOAM. OpenFOAM is an open-source finite volume method solver. The quality of the code has been demonstrated by some authors [6, 7]. The code uses a second-order Crank-Nicholson method for time marching and PISO algorithm to couple velocity and pressure. The grid and computational domain for the sharp trailing-edge geometry are shown in Fig. 2a. An O-mesh topology is used, that is divided internally into several blocks to generate an structured grid. The outer boundary of the domain has a radius of 20 chords. Figure 2b shows a zoom in mesh near the boundary layer.

Boundary conditions adequate for external incompressible viscous flow are used. No-slip boundary condition $\mathbf{U} = \mathbf{0}$ is imposed at the solid walls. Inlet and outlet boundaries type are switched by the sign of the flux as

$$\begin{cases} \cos(\mathbf{n} \cdot \mathbf{U}) \geq 0, & \text{inlet}, \\ \cos(\mathbf{n} \cdot \mathbf{U}) < 0, & \text{outlet}. \end{cases} \quad (6)$$

(a)   **(b)**
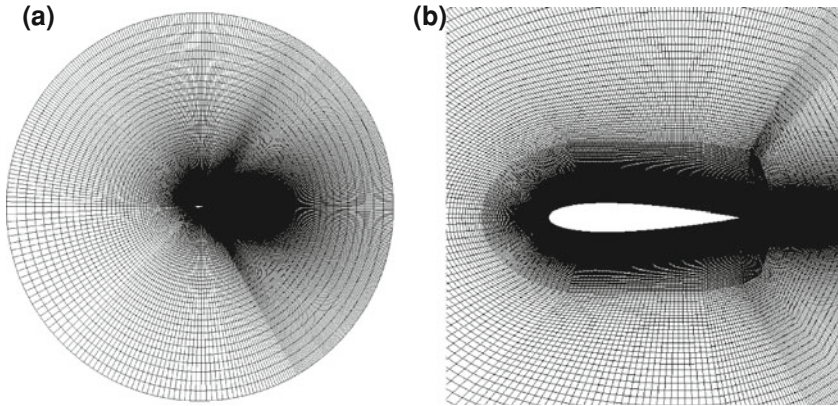
Fig. 2 Grid of NACA 0015, extend trailing edge

Table 1 Three different grid sizes for the sharp trailing-edge airfoil

Mesh	$N_C \times N_R$	Grid points	C_d	$GCI_{j+1,j}(\%)$
Fine	260×212	$\sim 5.5 \times 10^4$	0.404166	0.09
Medium	194×150	$\sim 2.9 \times 10^4$	0.404270	0.23
Coarse	143×107	$\sim 1.5 \times 10^4$	0.404523	–

N_R is the number of radial points and N_C is the number of circumferential points

$\mathbf{U} = constant$ and $\partial_n P = 0$ are imposed on inlet boundary. For outlet boundary, its boundary condition is $\partial_n \mathbf{U} = 0$ and $P = 0$, respectively.

4 Results

In order to estimate the grid independence of the results, the grid convergence index (GCI) is calculated. Following Roache [8], GCI represents a simple method for uniform reporting of grid-convergence studies without any restriction to integer refinement. This index is defined as $GCI_{j+1,j} = 300 \times |f_{j+1} - f_j/f_j (l^n - 1)|$, where f_j is any chosen value in the jth point of the grid. The GCI is based on the generalized Richardson extrapolation which involves comparison of discrete solutions at two different grid spacings. Table 1 shows the grid information for the sharp trailing-edge geometry at three different grid size levels. The residual of the discretized NS equations is employed to study the convergence of the solutions. It is defined as $Res = |C_c - C_t|$, where C_c and C_t denote the converged and time dependent values (e. g. drag or velocity), respectively. The value of $GCI_{2,3}$ based on drag coefficient (C_d) is small enough to prove that medium mesh is closed to the grid independent solution.
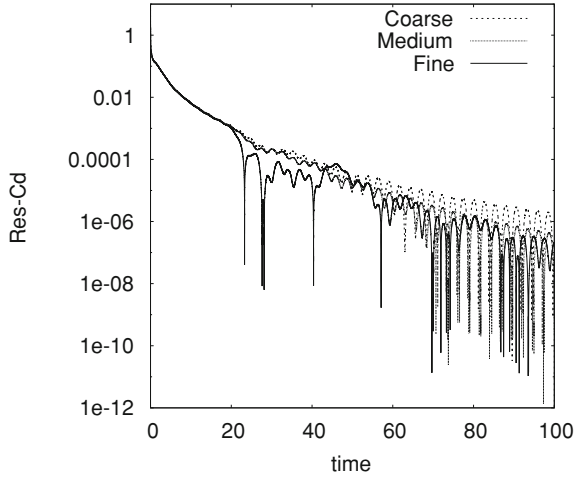
Fig. 3 Convergence history of C_d for three grids
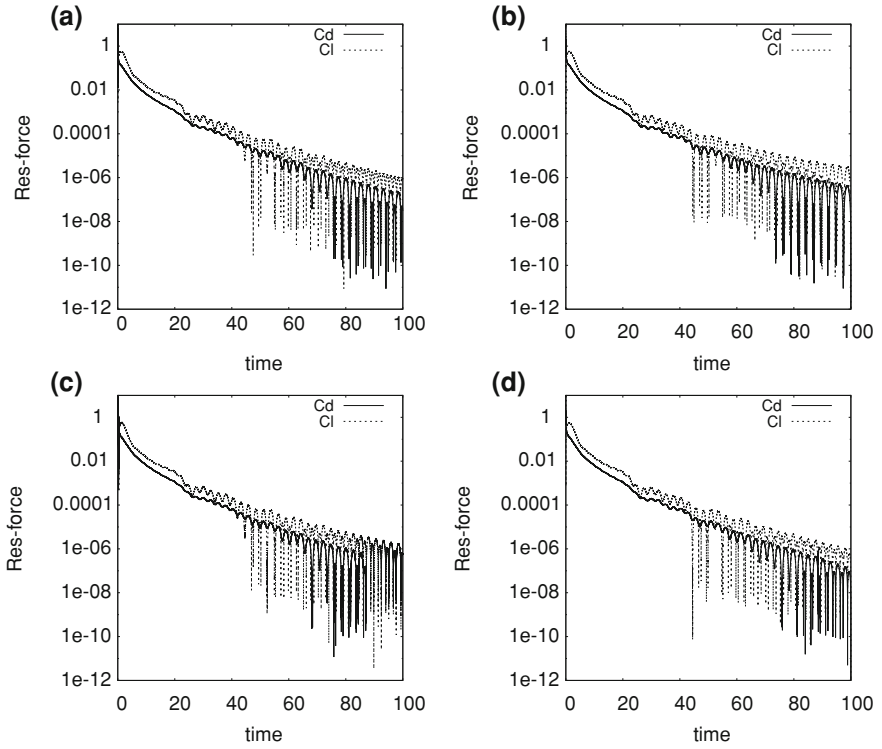
Fig. 4 Convergence history of the residual of C_d and C_l for the four geometries

Figure 3 shows the convergence history of the drag coefficient ($Res - C_d$) for the three mesh sizes. The temporal decay slope of $Res - C_d$ in medium and fine grids are nearly coincident. Following the GCI values based $Res - C_d$, with the aim of reducing computational resources, the medium meshes have been used to perform the remaining numerical simulations. The C_d and C_l residuals for the four different geometries are shown in Fig. 4. The results for the four cases show the damping in amplitude of oscillations towards a steady flow, independently of the trailing-edge geometry.

5 Conclusion

Two-dimensional simulations were carried out considering a NACA 0015 airfoil and three geometry modifications affecting the trailing edge. The time histories of the drag coefficient for each case show that, independently of the geometric details of the trailing edge, the flow around a NACA 0015 at 18° of angle of attack and Reynolds number based on chord and free-stream velocity equal to 200, computed by 2D simulations, is steady. This indicates the absence, under these conditions, of self-excited two-dimensional flow instabilities.

References

1. MacCullough G, Gault D (1951) Examples of three representative types of airfoil-section stall at low speed. NACA TN 2502
2. Jones BM (1934) Stalling. J R Aero Soc 38:747–770
3. Kitsios V, Rodríguez D, Theofilis V, Ooi A, Soria J (2009) Biglobal stability analysis in curvilinear coordinates of massively separated lifting bodies. J Comp Phys 228:7181–7196
4. Rodríguez D, Theofilis V (2011) On the origin of stall cells on airfoils. Theor Comput Fluid Dyn 25:105–117
5. Brehm C, Fasel HF (2011) Biglobal stability analysis as an initial value problem for a stalled airfoil. In: Proceedings of the 41th AIAA fluid dynamics conference and exhibit, AIAA, Honolulu, Hawaii, pp 2011–3569
6. Bohorquez P, Sanmiguel-Rojas E, Sevilla A, Jimenez-Gonzalez JI, Martinez-Bazan C (2011) Stability and dynamics of the laminar wake past a slender blunt-based axisymmetric body. J Fluid Mech 676:110–144
7. Kunkelmann C, Stephan P (2009) CFD simulation of boiling flows using the volume-of-fluid method within openfoam. Numer Heat Transfer, Part A 56:631–646
8. Roache PJ (1997) Quantification of uncertainty in computational fluid dynamics. Annu Rev Fluid Mech 29:123–160

The Role of Laminar Separation Bubbles on the FX 63-137 Airfoil

Abhijit Mitra and O. N. Ramesh

Abstract Low Reynolds number airfoils are prone to be adversely affected by the presence of laminar separation bubbles (LSB). But at relatively high Reynolds number (based on the chord of the airfoil) in the range of 100,000–200,000, suppression of LSB, by a boundary layer trip, caused the performance of the airfoil to deteriorate further. In this particular case boundary layer trip does not result in an overall drag reduction due to suppression of the laminar separation bubble, as conventional wisdom would have suggested. The trip causes the turbulent boundary layer to separate early, at relatively high angles of attack, and augmenting the form drag.

1 Introduction

Laminar separation bubbles (LSB) are almost always linked to the degradation of the performance of low Reynolds number airfoils. A steady laminar boundary layer on an airfoil is prone to flow separation as it encounters an adverse pressure gradient. The separated shear layer is inviscidly unstable because of the presence of a single or even multiple inflection points in the velocity profile. As a matter of fact, the velocity profile becomes inflectional even upstream of the separation point causing the Tollmien-Schlichting waves to amplify upstream of the laminar separation point as observed by Diwan and Ramesh [1]. The laminar shear layer quickly transitions into turbulent shear layer, and the ensuing turbulence transports momentum towards the wall to enable the flow to reattach itself back onto the airfoil surface, resulting in a recirculating flow within the separation and reattachment points.

A. Mitra (✉) · O. N. Ramesh
Indian Institute of Science, Bangalore, India
e-mail: abhijit@aero.iisc.ernet.in

O. N. Ramesh
e-mail: onr@aero.iisc.ernet.in

At very low Reynolds number, based on the chord, the flow does not seem to reattach back onto the surface after it has separated from a laminar state, thus preventing the formation of the LSB. For Reynolds number greater than 60,000, one can expect the formation of LSB and at these Reynolds numbers the length of the LSB could be about 30–50 % of the chord. LSB can be classified as long and short bubbles depending on how much the coefficient of pressure distribution along the surface of the airfoil deviates from the inviscid one. Long bubble has a global effect on the flow field and affecting the coefficient of pressure distribution for most of the chord, whereas short bubbles merely act as a trip which helps the flow to quickly break-down into turbulence.

FX 63-137 is a 13.7 % thick airfoil and it is considered to be relatively a thick airfoil at these Reynolds numbers. As expected, the stall characteristics of this airfoil is predominantly that of a typical trailing edge stall as described aptly by McCullough and Gault [2]. At stalling angles turbulent separation kicks in and it moves progressively upstream as the angle of attack (AoA) is increased. The trailing edge stall is characterised by a very rounded C_L versus AoA curve and the loss of lift and increase of the drag is smooth, as described by McCullough and Gault. All the above characteristics were observed in the present experiment.

In the literature, for moderately high Reynolds numbers (in the range of 100,000–200,000), LSB had been reported as something undesirable and held responsible for the augmentation of drag in the system (for Reynolds number of 100,000 or more). Selig, Donovan and Fraser [3] reported that it is due to the presence of LSB that there is an increase in drag (referred to as bubble drag) contributed by the LSB. Their experiments were performed for Reynolds number of greater than 100,000 (primarily 300,000). They concluded that the drag due to LSB is considerable and deteriorates the performance of the airfoil, not only at these Reynolds numbers, but also at lower Reynolds numbers of around 50,000.

Very recent Particle Image Velocimetry (PIV) studies of McArthur [4] over airfoils indicated otherwise. McArthur found that the drag increase at moderate lift coefficients was due to simple laminar separation with no immediate transition to turbulence and no reattachment at a Reynolds number of 60,000. The subsequent drag decrease at higher angle of attack (AoA) is caused by the formation of an LSB which is supported by the PIV measurements. This fact is in distinction with the observation stated just above at Reynolds numbers of 100,000–200,000.

In the present work, the effect of laminar separation bubble on the drag coefficient C_d and several other parameters have been studied. For Reynolds number range of 100,000–200,000 we have performed experiments whereas for the smaller Reynolds number range of 30,000–60,000 our conclusions are purely based on calculations made with the Xfoil code (and validated against the experiments of Mc Arthur at those Reynolds numbers).We find that LSB is actually not detrimental as far as the performance of the airfoil is concerned in the Reynolds number range of 100,000–200,000, for angles of attack ranging from 0 to 12° (stalling angle) . This observation is in contradistinction to the results of Selig et.al. On the other hand, in the Reynolds number range of 30,000– 60,000, the presence of LSB is found to reduce the drag (as compared to the tripped case when there is no LSB) for angles of attack larger than

Fig. 1 FX 63-137

11° (i.e. in the post stall regime); for angles of attack less than 11° the tripped case results in a lower drag as compared to the untripped case. These trends are consistent with the experimental results of McArthur.

2 Experimental Details

The airfoil that is considered for the present study is FX 63-137 and is shown in Fig. 1.

In the present work, measurements for Reynolds number range of 100,000–200,000, were taken on clean (untripped) airfoils. The LSB was subsequently suppressed by placing a trip wire, of 400 microns lateral dimensions at the leading edge of the aerofoil.

All the experiments were carried out in a closed circuit wind tunnel with the test section cross-section of 1×1 m. The airfoil's chord lengths was 0.25 m with a span of 1 m. The Reynolds numbers based on the chord were 100,000 and 200,000. The measurements consisted of surface pressure distribution and wake traverse.

The pressure measurements were performed using a projection manometer with a least count of 0.1 mm of alcohol.

3 Results and Discussions

The coefficient of pressure, C_p distribution curve for the clean airfoil (FX 63-137) for AoA = 0° is shown in Fig. 2, which is also being compared with the Xfoil results. The match of the C_p curve is quite satisfactory. The difference of the reattachment point, predicted by Xfoil, from the experiments can be advocated to the fact that the transition model used by the viscous code might not be exactly simulating the conditions exactly in this case. The e^N transition model is incorporated in Xfoil, where $N_{crit} = 9$. Drela [5] had assumed, as it is generally seen, the N_{crit} for wind tunnels is about 9. The dead air region is accompanied by a pressure plateau in the C_p versus x/c curve, which can be clearly observed from the C_p curve shown in Fig. 2.

To check the relative importance of LSB, it is suppressed by a boundary layer trip placed near the leading edge of the airfoil. The C_d values for the tripped airfoil is always higher than the untripped counterpart as shown in Fig. 3. Since the bubbles at these Reynolds numbers are weaker, the suppression of the LSB does not cause the pressure distribution to vary much from the distribution of pressure for the clean airfoil. Thereby, the coefficient of lift is fairly the same for both the cases (tripped
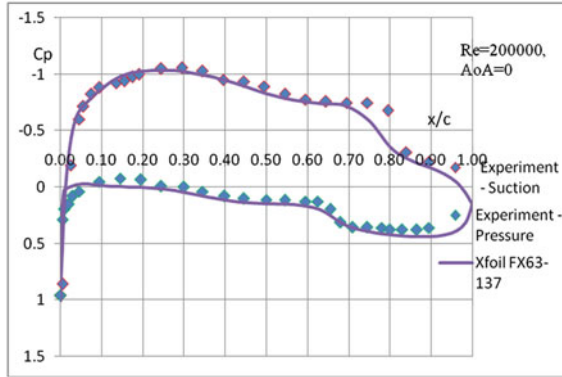
Fig. 2 The pressure distribution at Re = 200, 000 and AoA = 0°
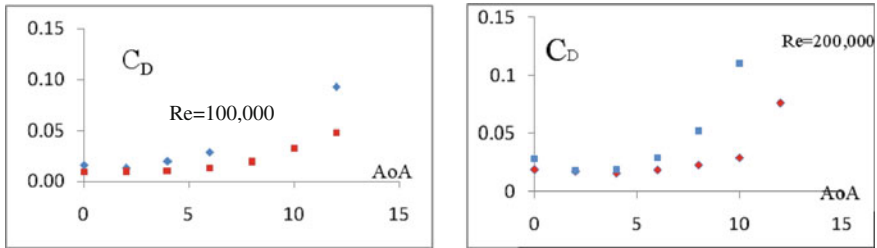
Fig. 3 Drag coefficient variation with angle of attack at chord Re = 100,000 and 200,000 for clean and tripped FX 63-137

as well as clean airfoil) for moderate angles of attack (until turbulent separation sets in).

The fact that the LSB is suppressed for the tripped airfoil and the flow is turbulently attached for most of the airfoil surface for moderate angles of attack, indicates that the rise in the coefficient of drag is actually due the augmentation of the skin friction drag due to turbulent attached flow (in the tripped case). Whereas, for the clean airfoil the LSB at these Reynolds numbers (where the LSB is relatively weak) just act as a placeholder and a switch for the flow to transition to turbulence late, reducing the wetted area of the turbulent attached flow thereby possibly explaining the increase of the coefficient of drag in the tripped airfoil case. Passive suppression of the LSB does not help improving the performance at Re = 2×10^5 and 10^5 and it seems that LSB formation is a favorable phenomena at these Reynolds number.

At higher angles of attack, the LSB is seen to shrink in size and minimally affect the coefficient of lift of the airfoil when compared to the inviscid C_L. At these angles of attack the LSB can justifiably be called as a short bubble. But when the bubble (at these angles of attack) is suppressed, it causes the drag to go up about two folds but, not affecting the lift much. If one sees broadly, a short LSB and the trip have got an operational similarity in the fact that both make the flow transition from a laminar
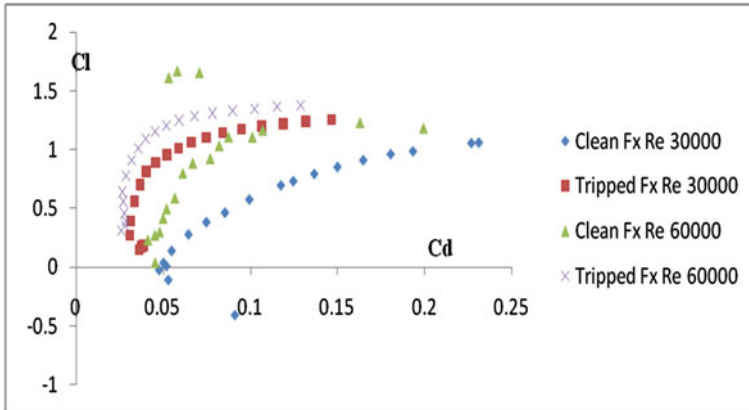
Fig. 4 Computed using Xfoil [4]. Cd is considerably lower at Re $= 60,000$ when compared to Re $= 30,000$

state to a turbulent one. So, given this, one can infer that a small LSB is very efficient in making the flow go from a laminar state to a turbulent one than a passively placed boundary layer trip at the leading edge of the airfoil. A small LSB seems to be a very efficient switch for the oncoming attached laminar flow to transit to an attached turbulent flow.

Flows at low Reynolds numbers of about 30,000 and 60,000 seems to behave differently. Separation for most of the angles of attack considered is open. For Reynolds number of 60,000, the laminar separation bubble forms at an angle of attack of 11°. And the formation of the LSB causes a sharp drop in the value of the coefficient of drag indicating LSB as something that is not unfavourable even at these Reynolds numbers. But, the fact is the flow finds it difficult to reattach itself once it has laminarly separated at these Reynolds numbers and moderate angles of attack. Suppression of LSB at these Reynolds numbers (around 30,000) causes something exactly opposite to the case of Re $= 200,000$ and 100,000. The performance of the airfoil improves by the fact that the drag decreases when LSB is suppressed. Figure 4 shows the drag polars at these Reynolds number.

Figure 5 shows the apportioned C_D values and its variation with angle of attack at Reynolds number of 60,000. The dominant drag component being the pressure drag, the boundary layer trip seems to work for most of the angles of attack as it is successful in keeping the flow attached for a longer downstream extent consequently bringing down the pressure drag. The important thing to note here is what happens at AoA of 11°–13°. The C_D for untripped airfoil is lower than the tripped airfoil and it is at these AoAs that the formation of LSB is observed [4].
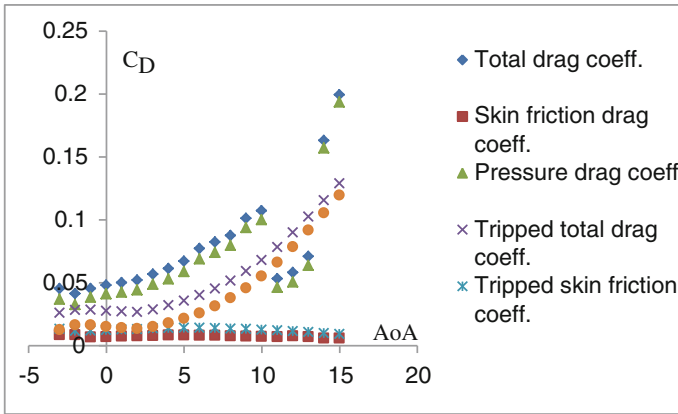
Fig. 5 Computed using Xfoil [4]. C_D versus AoA at Re $= 60,000$

4 Conclusion

The formation of LSB, at Reynolds numbers of about 50,000, improves the performance of the airfoil in comparison to fully separated flow, which is distinctly evident from the present calculations and also supported by McArthur's measurements. The trip improves the performance but, when the Re is increased (thus weakening the LSB), suppression of LSB with a trip wire placed near the leading edge of the airfoil does not seem to improve the performance, on the contrary the C_D shoots up while the C_L is not much affected. Formation of LSB might be a very efficient switch for the flow to become turbulent from a laminar state at moderately higher Reynolds numbers of 100,000–200,000, without affecting the performance of the airfoil a great deal.

Suppression of weak LSB causes deterioration of the aerodynamic performance of the airfoil. This is in contrast to the conventional wisdom according to which LSB is thought to be always detrimental from the perspective of aerodynamic efficiency. Here, on the contrary, it was found that suppression of the weak LSB at Re $= 200,000$, causes the C_D to rise. At higher angles of attack, the form drag due to the turbulent separation might play an important role.

References

1. Diwan SS, Ramesh ON (2009) On the origin of inflectional instability of a laminar separation bubble. J Fluid Mech 629:263–298
2. McCoullough GB, Gault DE (1951) Examples of three representative type of airfoil section stallat low speed, TN 2502
3. Selig MS, Donovan JF, Fraser DB (1989) Airfoils at Low Speeds, Soartech 8. SoarTech Publications, Virginia Beach
4. McArthur J (2008) Aerodynamics of wings at low Reynolds number: boundary layer separation and reattachment. Ph.D. dissertation, University of Southern California
5. Xfoil 6.7 (2008) Subsonic airfoil development system, Drela, MIT

Part III
Separated Flow Control of Airfoils

Evaluation Criteria and Performance Comparison of Actuators

Avraham ("Avi") Seifert

Abstract Active flow control (AFC) relies on actuators' control authority as a primary enabling technology for flow manipulation. The requirements of the actuation systems are revisited and tools for *critical* evaluation of actuators are offered. The application in mind is boundary layer separation control. To be accepted by industry, system efficiency should always be assessed, not only the improvement in aerodynamic performance. Clearly there are additional considerations. A few performance based criteria for comparing different actuation concepts are offered, considering the actuation power and system weight. Relevant recent separation control data are compared and discussed.

1 Background and Motivation

Unsteady flow control using periodic excitation and utilizing flow instability [1] has the potential of surpassing the invested energy to perform AFC. The feasibility of increasing the efficiency and simplifying flow related systems (e.g., airplanes, heavy vehicles, wind turbines) is appealing from commercial and environmental aspects. Mature actuators with sufficient control authority and wide bandwidth are essential in a closed-loop AFC system. This manuscript does not attempt to review the state-of-the-art (e.g., see [2]) actuation techniques. Over the last decade, periodic zero-mass-flux (ZMF) excitation proved to be a versatile tool for AFC. Clearly, it is more effective than steady blowing and simpler to generate than steady suction. When generated by Piezo-fluidic actuators [2], it is flight proven [3] and its bandwidth is suitable for a wide range of feedback control applications [4]. Effective yet more robust actuators are sought after. The recent introduction of the steady Suction and Oscillatory Blowing (SaOB) actuator [5] concept to AFC and the use of similar

A. Seifert (✉)

School of Mechanical Engineering, Tel-Aviv University, 69778 Tel-Aviv, Israel

e-mail: Seifert@eng.tau.ac.il

no-moving parts oscillators [6] have the potential to be both effective at higher speeds and overall efficient. The 3D SaOB generated actuation has recently been used in several experiments [4, 7–10] over a very wide range of incompressible Reynolds number and proven to be energy efficient. In the following we present the comparison criteria.

2 Actuation System Comparison Criteria

A prerequisite for comparing actuation systems is identifying clear operational criteria. Even the output to be compared is difficult to identify. The fluidic output can be a local or a global velocity fluctuation, unsteady momentum injection or mass removal, force, vorticity flux, thermal pulse, sound generation and more. The independent parameters could be size, weight, energy consumption, cost, maintenance, robustness, reliability, bandwidth, compatibility and complexity. A possible measure of an actuator input–output relations could be its thrust multiplied by its peak velocity, in space and time, measured in still air, divided by the input power (electric or fluidic). Therefore, we suggest using the ***mechanical conversion efficiency*** defined as:

$$\eta \equiv F_a U_p / P_a \tag{1}$$

An estimate of the overall energy efficiency (considering the signal generation and amplification system) should be provided along with additional system component weight, based on current technology. Thrust, if not measured, could be estimated by the ejected fluid momentum. In [11] an excellent actuator performance evaluation is described. An actuator robustness and efficiency performance parameter, termed ***Overall Figure of Merit*** is defined as:

$$OFM \equiv F_a^2 U_p / W_a P_a \tag{2}$$

In Eqs. 1 and 2, W_a is the total weight of the actuation system or of the actuator alone, P_a is the total actuation system power consumption or the power delivered to the actuator, U_p is the peak, typical actuator output velocity and F_a is the thrust generated by the actuator when operating in still fluid. The actuator thrust could be replaced by: $F_a \approx C\rho A_a U_p^2$, where A_a is a cross section from which excitation is affected (e.g., cross section of a slot, suction hole diameter, wall jet thickness times width, etc.). Scaling arguments should be provided to guide the evaluation of the constant C. Its value is typically 0.25–0.5. Besides the actuator operation in still fluid, its effect on the controlled flow should be quantified. The (***first) Aerodynamic Figure of Merit*** (*AFM1*) for boundary layer separation control was defined already in [7]:

$$AFM1 \equiv \frac{U_\infty L_c / (U_\infty D_c + P_a)}{(L/D)_b} \tag{3}$$

In Eq. 3, L is the lift, D is the drag, the subscript "b" refers to *baseline* uncontrolled conditions, the subscript "c" refers to *controlled*. It should be indicated if form or total drag was measured and how and also if total system power consumption or only actuator power is reported. In [7] it was shown that AFM1 ≈ 1.4 was obtained by 3D actuation using surface mounted Piezo operated "benders". The 2nd *Aerodynamic Figure of Merit (AFM2)*, where the weight of the actuator (W_a) is taken off the lift of the controlled case while weight savings due to AFC (W_s) are added to lift:

$$AFM2 \equiv \frac{U_\infty (L_c - W_a + W_s)/(U_\infty D_c + P)}{(L/D)_b} \tag{4}$$

This approach is justified because in certain applications the AFC system replaces or at least reduces the weight of an existing system, e.g., simplified high-lift system [12], so $W_a - W_s$ is the net weight change which could be negative.

In [8] we defined a figure of merit, suitable for wind turbines, in the form:

$$AFM3 \equiv \frac{[(L - D) \cdot U_\infty]_c - 2 \cdot P_a}{[(L - D) \cdot U_\infty]_b} \tag{5}$$

Following [8], in [4] AFM3 values of up to 1.6 were measured. Finally, for drag reduction purposes, the 4th AFM can be defined in the form:

$$AFM4 \equiv \frac{U_\infty D_c + P_a}{U_\infty D_b} \tag{6}$$

In [9] and [10] the authors measured AFM4 ≈ 1.2 for circular cylinder at $Re = 1 - 2 \times 10^5$ and for an axis-symmetric body at Re range of $1 - 5 \times 10^6$. In [13], 7 % drag reduction over a circular cylinder at $Re = 15,000$ using pulsed DBD plasma actuation were measured. While the power saving was 700 times the fluidic power input, when accounting for the electric power, the AFM4 was 0.5.

For numerical studies (e.g., of drag reduction), where the actuation power consumption cannot be evaluated, one should calculate the maximum allowable actuation input power to achieve $AFM4 > 1$ and from it arrive at the minimum required actuation mechanical efficiency. By combining Eqs. 1 and 6:

$$\eta_{\min} \equiv A_a/A_m \left(U_p/U_\infty \right)^3 1/\Delta C_d \tag{7}$$

where A_m is the model reference area, A_a is the cross section from which actuation is applied. Also note that the reciprocal of the drag reduction dictates the minimum actuation η, according which an actuation system can be chosen. The main new actuation concept that became popular during the time that passed since [14] are fluidic oscillators. For this the reader is referred to a recent review [6]. The actuator used in [9, 10] is described in detail in [5].

Fig. 1 Actuator mechanical conversion efficiency (Eq. 1) plotted versus the peak actuation velocity. Note the log scale
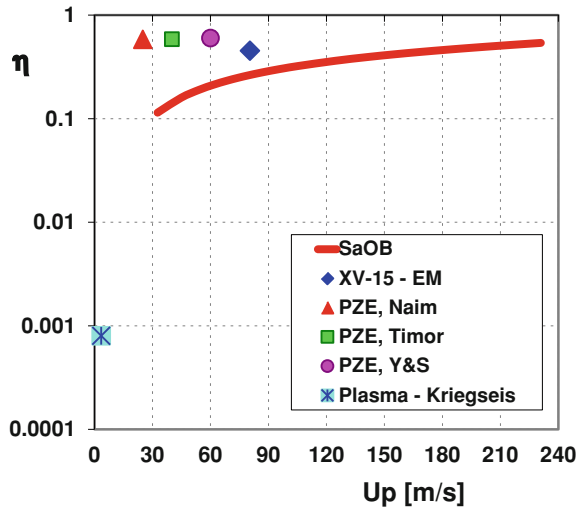
3 Actuation Systems Performance Comparison

A detailed comparison of different actuation systems, based on the criteria suggested above is revisited, following [14]. Very little data is available for the calculations of the performance criteria suggested above. Only through private communication were we able to obtain sufficient information for comparing TAU developed actuators with the actuators used for the flight tests of the XV-15 [15]. Further information that is provided below is from the recent paper by Kriegseis et al. [11] and based on conservative evaluations by the author. The actuator conversion efficiency from input energy to mechanical output energy is shown in Fig. 1. It is plotted versus the peak typical velocity each actuator can produce. It can be seen that while TAU Piezo-fluidic actuators have roughly 60 % efficiency, the XV-15 electromagnetic actuators have efficiency of about 50 %. The SaOB actuator [5] starts at $\eta \approx 0.1$ for low exit velocities and its η increases to about 60 % for near sonic exit speeds, due to weakening Reynolds number effects. It is interesting to note that the peak efficiency of standard BDB plasma actuators is lower than 0.1 % [11] reached at $U_p \approx 3$ m/s. The Overall Figure of Merit (*OFM,* Eq. 2) compares the actuator performance as it is operated in still air, taking its fluidic output, its weight and power consumption into account, according to Eq. 2.

As presented in Fig. 2, for the actuators used during the XV-15 fight tests and at the flight test conditions, the *OFM* = 0.014 with U_p = 80.4 m/s. Comparing this number to TAU developed Piezo-fluidic actuators results in *OFM* = 0.052 (for U_p = 20m/s, [16]) and *OFM* = 0.107 (for U_p = 40 m/s, [17]). For the compact actuator used in [18, 19] (U_p = 60 m/s), the *OFM* = 0.295.

Note the different peak slot velocities in the above comparisons. An estimation of the OFM for standard DBD plasma actuators such as those used in [11, 20, 21], results

Fig. 2 Actuator OFM (Eq. 2) plotted versus the peak actuation velocity for a few actuation devices. Note the log scale
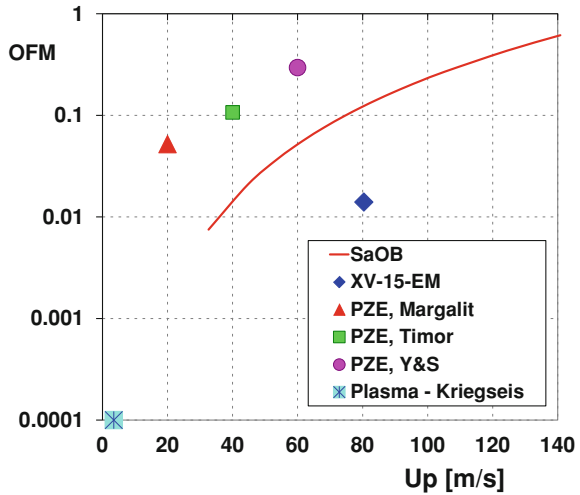
in OFM $< 1.0 \times 10^{-4}$. This was evaluated for $Up = 3.5$ m/s, a region of influence extending 1 mm above the electrode, a total actuator weight of about 0.04 N/meter and steady-state operation, neglecting the weight of the cables connecting the electrodes to the electric circuits. Aerodynamic Figures of Merit were available only in a few TAU and collaborator publications, where values above unity were reported [4, 7–10].

4 Summary, Conclusions and Recommendations

A critical review of current actuation technology was conducted. At least six criteria for evaluating and comparing actuators and their impact on the flow have been proposed, focusing on boundary layer separation control. It is emphasized that AFC experiments should include not only local but integral fluidic and energetic characterization of the actuators and actuation system as a whole. Considerations such as weight, volume, cost, reliability, time response, bandwidth and compatibility should also be addressed. From the actuation concepts on which sufficient information is available, it is clear that Piezo-fluidic technology is significantly superior to electromagnetic and two-three orders of magnitude more efficient than plasma actuators in imparting momentum. Fluidic oscillators, especially in combination with steady suction are effective and efficient, with near sonic exit velocities capability. The SaOB and TAU Piezo-fluidic actuators were the only to report greater than unity aerodynamic figures of merit in separation control experiments to date, still in laboratory experiments. Field, energy efficient AFC demonstrations are on-going.

References

1. Seifert A, Darabi A, Wygnanski I (1996) Delay of airfoil stall by periodic excitation. J Aircraft 33(4):691–699
2. Cattafesta LN, Sheplak M (2011) Actuators for active flow control. Ann Rev Flu Mech 43:247–272
3. Seifert A, David S, Fono I, Stalnov O, Dayan I (2010) Roll control via active flow control: from concept to flight. AIAA J Aircraft 47(3):864–874
4. Troshin V, Seifert A (2013) High-performance wind turbine airfoil using distributed closed-loop flow control system. Exp Fluids 54:1443
5. Arwatz G, Fono I, Seifert A (2008) Suction and oscillatory blowing actuator modeling and validation. AIAA J 40(5):1007–1017
6. Gregory J, Tomac MN (2013) A review of fluidic oscillator development. AIAA paper 2013–2474.
7. Seifert A, Eliahu S, Greenblatt D, Wygnanski I (1998) Use of piezoelectric actuators for airfoil separation control (tn). AIAA J 36(8):1535–1537
8. Stalnov O, Kribus A, Seifert A (2010) Evaluation of active flow control applied to wind turbine blade section. AIP J Sustain Renew, Energy 2.
9. Shtendel T, Seifert A (2014) Three-dimensional aspects of bluff-body drag reduction by active flow control. Int J Heat Flow 109–127
10. Wilson J, Schatzmann D, Arad A, Shtendel T, Seifert A (2013) Suction and pulsed-blowing flow control applied to an axisymmetric body. AIAA J (Posted online on 6 Aug 2013).
11. Kriegseis J, Duchmann A, Tropea C, Grundmann S (2013) On the classification of dielectric barrier discharge plasma actuators: a comprehensive performance evaluation study. J Appl Phys 114:053301
12. Shepshelovich M, Koss D, Wygnanski I, Seifert A (1989) An experimental evaluation of a low-Reynolds number high-lift airfoil with vanishingly small pitching moment. AIAA paper 1989–538.
13. Jukes TN, Choi KS (2009) Long lasting modifications to vortex shedding using a short plasma excitation. PRL 102:254501
14. Seifert A (2007) Closed-loop AFC system: actuators. In: King R (ed) Springer, Berlin, vol 95. ISBN 10 3-540-71438-3.
15. Nagib HM, Kiedaisch JW, Wygnanski IJ, Stalker AD, Wood T, McVeigh MA (2005) First-in-flight full-scale application of active flow control: the XV-15 tiltrotor download reduction. RTO-MP-AVT-111.
16. Margalit S, Greenblatt D, Seifert A, Wygnanski I (2004) Delta wing stall and roll control using segmented piezoelectric fluidic actuators. AIAA J Aircraft.
17. Timor I, Ben-Hamou E, Guy Y, Seifert A (2007) Maneuvering aspects and 3d effects of active airfoil flow control. Turbul Combust 78:429–443
18. Yehoshua T, Seifert A (2006) Active boundary layer tripping using oscillatory vorticity generator. Aerosp Sci Technol 10(3):175–180
19. Yehoshua T, Seifert A (2006) Boundary condition effects on the evolution of a train of vortex pairs in still air. Aeronaut J 110(1109):397–417
20. Labergue A, leger L, Moreau E, Touchard G (2005) Effect of a plasma actuator on an airflow along an inclined wall-P.I.V. and wall pressure measurements. J Electrostat. In: 10th International conference on electrostatics, Espool/Helsinki Finland, 15–17 June 2005.
21. Post ML, Corke TC (2004) Separation control on high angle of attack airfoil using plasma actuators. AIAA J 42(11):2177–2182

Flow Control on Gö 387 Airfoil by Using Nanosecond Pulse Plasma Actuator

Kentaro Kato and Christian Breitsamter

Abstract Airfoil flow separation control using a plasma actuator driven by repetitive nanosecond pulse voltage was experimentally investigated. The pressure distribution on the airfoil surface was measured by means of a liquid manometer. The lift coefficient was computed by integrating the pressure distribution and the effects of the input voltage amplitude and repetitive frequency were evaluated. The results show the lift is increased in two ranges of angle of attack. The first range corresponds to the pre-stall and stall angle of attack. In this range the flow is steady and the lift is increased regardless of the frequency. Strong hysteresis effect is also observed. The second range corresponds to the post-stall angle of attack. In this range the flow is unsteady and the lift increment is heavily dependent on the amplitude and frequency. Characteristic pressure distribution and shift of the separation point, which was estimated from the pressure gradient, are also reported.

1 Introduction

Unsteady flow separation control with periodic excitation has been achieved by various active actuator devices [2]. Among the different devices, the dielectric barrier discharge plasma actuator (DBD-PA) has been intensively investigated because of some prominent aspects: the simple structure illustrated in Fig. 1 and high bandwidth. From these aspects, DBD-PAs are expected to be applied to various flow controls with a broad range of geometries and time scales.

K. Kato (✉) · C. Breitsamter
Lehrstuhl für Aerodynamik und Strömungsmechanik,
Technische Universität München, Boltzmannstr. 15, 85748,
Garching bei München, Germany
e-mail: Kentaro.Kato@aer.mw.tum.de

C. Breitsamter
e-mail: Christian.Breitsamter@aer.mw.tum.de

Fig. 1 DBD-PA consists of a pair of electrodes separated by dielectric layer. The exposed electrode is excited by the high voltage (HV)
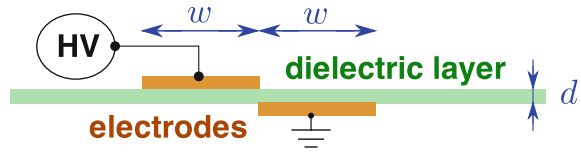
Two different mechanisms for the effect of DBD-PAs are known: the electrohydrodynamic and the thermal effect. The first plays a main role in operation with alternating-current voltage. The generated plasma induces the wall jet near the actuator surface. The velocity of the wall jet is typically up to a few meter per second [1, 4]. Therefore, the application has been limited to the low-speed flow regime. The thermal effect becomes dominant for the operation with nanosecond pulse (NS) voltage. The energy of the discharge is rapidly converted to heat [3, 6, 7]. For the thermal mechanism, a wider range of applications is expected.

Despite the potential of the thermal effect, the effect of the voltage signal parameters on the control authority for a certain flow application has not been fully cleared yet. Detailed investigations are required from the application perspective.

The objective of the present work is to evaluate the effects of NS plasma actuation on separation phenomena. Special interest is on the effects of the input voltage parameters on the control authority. Flow control on a Gö 387 airfoil was selected as test case. The pressure distribution on the airfoil is measured by means of a liquid manometer to avoid electromagnetic interference effect. The measurements are conducted under the conditions of different repetitive frequencies f and amplitudes V_{pp} of the pulse voltage. The obtained pressure coefficients and lift coefficients are compared at various angles of attack α.

2 Experimental Method

The measurements were carried out in the Göttingen type wind tunnel facility B of the Institute of Aerodynamics and Fluid Mechanics at Technische Universität München. Dimensions of the open test section were $1.2\,m \times 1.55\,m$.

A Gö 387 airfoil model with a chord length of $C = 100\,mm$ and a span of $b = 500\,mm$ was used. The model was made from lacquer coated metal. The airfoil is equipped with 27 static pressure taps at the mid-span section.

The pressure distribution was measured by a liquid manometer consisting of multiple tubes. Colored alcohol in each tube freely moves depending on the corresponding static pressure p at the pressure tap. For the sake of convenience, the pressure was calculated by means of a photogrammetric technique.

In order to obtain the pressure distribution, two separated plasma actuators were used which do not cover the pressure taps as shown in Fig. 2. The length of the electrodes of each actuator is 197.5 mm, thus covering 79 % of the wing span. The actuator was mounted on the upper airfoil surface so that the interface of two electrodes was located at $x/C = 0.05$. It should be noted that the plasma layer was generated not only over the covered electrode but also on the upstream side of

Fig. 2 Two separated actuator configurations: the photo was taken from the upstream side. The plasma layer can be observed as the *bright purple lines* on the leading edge. Thin end disks with 300 mm diameter were attached at the wing tips of the *rectangular wing* in order to limit the three dimensional flow effects. The tufts were removed during the pressure measurement
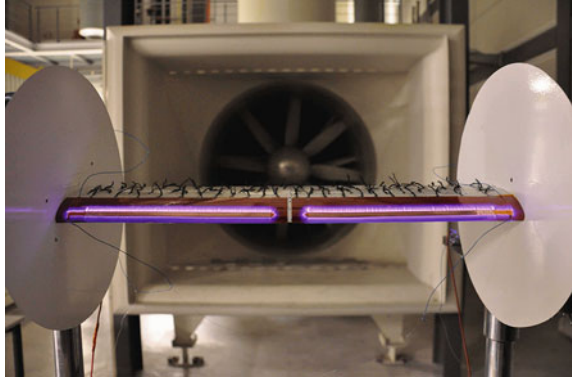
the exposed electrode as shown in Fig. 2, due to the conductive model surface. The actuator was connected to the power source FPG 20-1MC2 made by FID GmbH. Copper tape (3M,1181 with a width of $w = 6$ mm) and dielectric Kapton tape (3M, 5413) were used as materials. The dielectric layer consisted of 8 Kapton layers with a total thickness of $d = 0.56$ mm. The thickness generated a discontinuity on the airfoil surface and increased the radius of the leading edge. The present results, however, provide comparison between ON and OFF operation as well as among the various operation conditions with different V_{pp} and f.

In order to investigate the effects of V_{pp} and f, the static pressure was measured in the following order. First, the measurement without operation was conducted as the baseline. Second, twelve operations with different voltage amplitudes ($V_{pp} = 5$, 10, 20 kV) and frequencies ($f = 0.1, 0.2, 0.5, 1$ kHz) were applied. The effect of the actuation was evaluated by comparing the controlled case with the baseline case. For each operation condition, 30 samples of the resulting pressure distribution were acquired. This procedure was repeated with changing α for the two different Reynolds number conditions: $Re \equiv C U_\infty / \nu = 1.6$ and 2.3×10^5; the corresponding freestream velocities are $U_\infty \approx 26$ and 37 m/s, respectively.

For the evaluation, the lift coefficient C_L was calculated as shown below,

$$C_L \approx \frac{\int_0^C (p_l - p_u) dx \cos \alpha}{\frac{\rho U_\infty^2}{2} C} \tag{1}$$

where p_l and p_u are the pressure at a chordwise location x on the lower and upper surface, respectively. ρ denotes density of the air. In the present study, the term "lift coefficient" is used to denote this component due to the pressure.

3 Results and Discussions

Averaged lift coefficients $\overline{C_L}$ are shown in Fig. 3 for the different operation conditions. In the angle of attack range of $17.8° \leq \alpha \leq 23.8°$ for $Re = 1.6 \times 10^5$ and $\alpha \approx 24.8°$ for $Re = 2.3 \times 10^5$, the lift increases regardless of V_{pp} and f. In addition, the flow
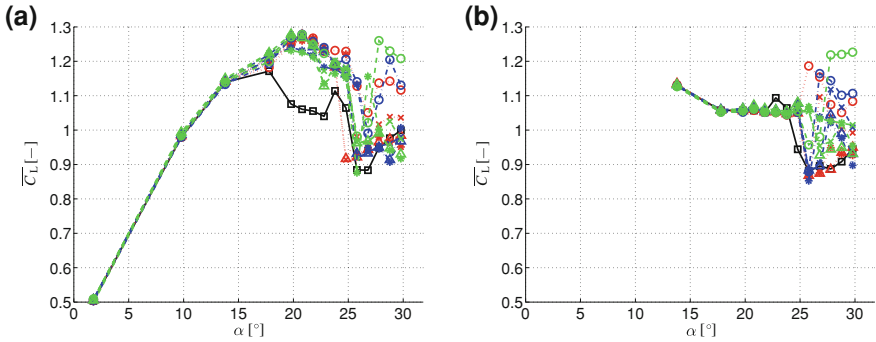
Fig. 3 Averaged lift coefficient $\overline{C_L}$ with the different operating conditions for two Reynolds numbers: *Solid line* with *squares* indicates the baseline. The *dotted*, *dashed-dotted* and *dashed lines* indicate the different voltage amplitudes $V_{pp} = 5, 10, 20$ kV. The markers (*circle, cross, triangle and asterisk*) indicate the operation frequencies $f = 0.1, 0.2, 0.5, 1$ kHz; **a** $Re = 1.6 \times 10^5$, **b** $Re = 2.3 \times 10^5$

is steady and the strong hysteresis effect is observed in these ranges: The lift is still increased even after the actuation is stopped (Mode 1). At a higher angle of attack, the flow is highly fluctuating and no hysteresis effect is observed. For some operation conditions, however, the lift is increased (Mode 2).

In order to clarify the complex trend for Mode 2, the increments of the lift coefficients ΔC_L are plotted in Fig. 4. It indicates that some preference frequencies can exist: $f = 0.1, 1$ kHz ($F^+ \equiv f\,C/U_\infty = 0.4,\ 3.8$) for $Re = 1.6 \times 10^5$ and $f = 0.1, 0.2$ kHz ($F^+ = 0.3,\ 0.5$) for $Re = 2.3 \times 10^5$. For these frequencies increasing V_{pp} seems to shift the range of α, where the increase in lift is achieved to higher α rather than to increase the maximum value of ΔC_L. That is, an optimal V_{pp} exists for some frequency ranges depending on α.

The dependency of V_{pp} can be explained in terms of the excitation area: The plasma layer on the upstream side of the exposed electrode is propagated further upstream by increasing V_{pp}. The extended plasma layer can work most effectively at a higher α, where the separation also occurs at a further upstream location.

These two modes and the characteristics (hysteresis, frequency dependency, unsteadiness) are also observed by other researchers [5]. According to their work, Mode 1 is caused by active transition tripping. Mode 2 is related to the spanwise coherent vortices. The present results indicate the qualitative agreement.

The pressure coefficient C_p is shown in Fig. 5 as local information. The square indicates the estimated separation point x_{sp} based on the pressure gradient. The bands at $x/C = 0.03$–0.00 (on the lower side), 0.05–0.10 (on the upper side) highlight where the plasma is generated.

Figure 5a indicates that the increase in lift for Mode 1 is mainly caused by amplifying the suction peak. For Mode 2, the pattern of the pressure distribution can be classified into two groups according to α. The first group is observed near the stall regime. As shown in Fig. 5b, the pressure distribution on the upper surface and
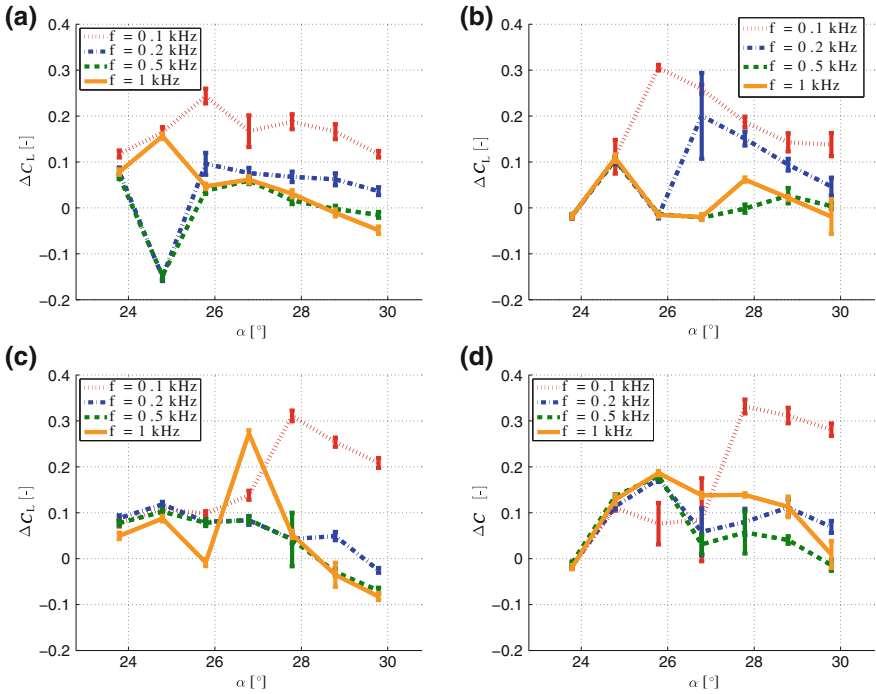
Fig. 4 Increment of the lift coefficient ΔC_L with the different operations for the different Reynolds number conditions: the error bars indicate the root mean square of 30 samples; **a** $Re = 1.6 \times 10^5$, $V_{pp} = 5$ kV, **b** $Re = 2.3 \times 10^5$, $V_{pp} = 5$kV, **c** $Re = 1.6 \times 10^5$, $V_{pp} = 20$kV, **d** $Re = 2.3 \times 10^5$, $V_{pp} = 20$kV
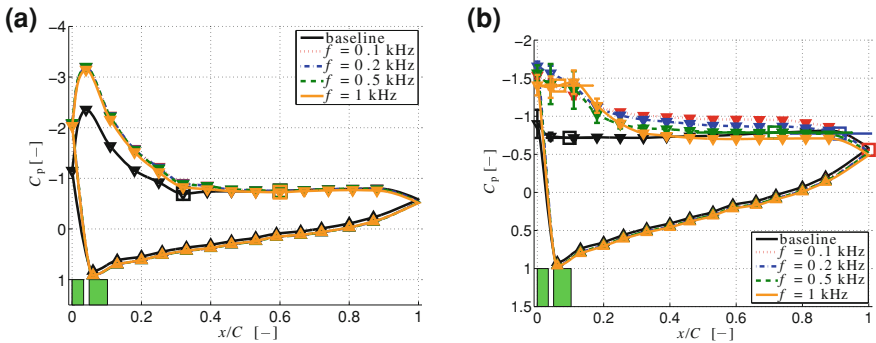
Fig. 5 Typical pressure distributions: the *horizontal* and *vertical* error bars indicate the root mean square of 30 samples. **a** Mode 1: $Re = 1.6 \times 10^5$, $\alpha = 20.8°$, $V_{pp} = 10$kV, **b** Mode 2: $Re = 2.3 \times 10^5$, $\alpha = 27.8°$, $V_{pp} = 10$kV with shift of x_{sp}

x_{sp} were affected depending on both V_{pp} and f. The second group is observed at the higher α. In this region, x_{sp} is fixed at the leading edge although the pressure distribution is not shown here. However, the actuation shifts the pressure on the entire upper surface and increases the lift coefficient. In this condition, the plasma actuation seems to manipulate the detached vortices rather than the separation.

4 Concluding Remarks

Flow manipulation on a Gö 387 airfoil by nanosecond pulse dielectric barrier discharge (NS DBD) has been investigated for Reynolds numbers of $1.6–2.3 \times 10^5$. The parameter study for the amplitude and repetitive frequency of input voltage indicates the different manners of the control authority depending on the angle of attack. The analyses for the lift coefficient and separation point imply that the characteristics are associated with the various flow phenomena. It is expected that NS DBD is able to manipulate transition, separation and detached vortices. Concentrating on the high angle of attack regime, both frequency and voltage amplitude are important factors to manipulate the separation and detached vortices.

References

1. Forte M, Jolibois J, Pons J, Moreau E, Touchard G, Cazalens M (2007) Optimization of a dielectric barrier discharge actuator by stationary and non-stationary measurements of the induced flow velocity: application to airflow control. Exp Fluids 43(6):917–928
2. Greenblatt D, Wygnanski I (2000) The control of flow separation by periodic excitation. Prog Aerosp Sci 36(7):487–545
3. Little J (2010) High-lift airfoil separation control with dielectric barrier discharge plasma actuators. PhD thesis, The Ohio State University.
4. Macheret S, Shneider M, Miles R (2004) Magnetohydrodynamic and electrohydrodynamic control of hypersonic flows of weakly ionized plasmas. AIAA J 42(7):1378–1387
5. Rethmel C, Little J, Takashima K, Sinha A, Adamovich I, Samimy M (2011) Flow separation control over an airfoil with nanosecond pulse driven dbd plasma actuators. In: 49th AIAA aerospace sciences meeting including the new horizons forum and aerospace exposition, Orlando, Florida.
6. Starikovskii A, Nikipelov A, Nudnova M, Roupassov D (2009) Sdbd plasma actuator with nanosecond pulse-periodic discharge. Plasma Sources Sci Technol 18:015–034
7. Takashima K, Zuzeek Y, Lempert W, Adamovich I (2011) Characterization of a surface dielectric barrier discharge plasma sustained by repetitive nanosecond pulses. Plasma Sources Sci Technol 20:009–055

Progress Toward Closed Loop Control of a Flow Around an Airfoil with Coanda Blowing

Yosef El Sayed Mohamed and Richard Semaan

Abstract Progress toward developing a closed loop control of flow around an airfoil with a Coanda flap is presented. Two loop components were addressed and analysed for the reference no-blowing case: the estimator and its input signal. For the estimator, a Proper Orthogonal Decomposition (POD) Galerkin model based on unsteady Reynolds averaged Navier-Stocks (uRANS) data was evaluated. To compensate for the unresolved dissipative scales in uRANS and for truncation error, the POD Galerkin model was calibrated by introducing an eddy viscosity term. The calibrated POD Galerkin model succeeded in replicating the time coefficients of the first two modes but failed to replicate the higher modes. The sensor location over the flap was optimized using modified Linear Stochastic Estimation (mLSE). With an optimal sensor placement it was possible to determine the state of the flow more accurately than for the same number of evenly spaced sensors.

1 Introduction

Closed-loop flow control is a fast growing research field aimed at altering or controlling the state of a flow. It is found in many fluid mechanics applications, such as boundary layer transition control and drag reduction behind a cylinder. Despite its numerous advantages, closed-loop control has not been widely used in aerodynamic applications. One possible application is the Coanda flap, where a jet is blown tangentially over the surface of a specially designed flap upper surface. This concept with an open loop control has been previously researched at the institute of

Y. El Sayed Mohamed (✉) · R. Semaan
Institut für Strömunsmechanik, Technische Universität Braunschweig,
Hermann-Blenk-Str. 37, 38108 Braunschweig, Germany
e-mail: y.el-sayed-m@tu-braunschweig.de

R. Semaan
e-mail: r.semaan@tu-braunschweig.de

fluid mechanics [1]. This paper presents our initial efforts to "close the loop" and consequently further increase the lift gain. Two elements of the control loop were addressed: the estimator and its input signal.

The estimator is usually a simplified model of the flow. It should be simple enough to be used in real time while being able to capture the complexity of the natural and actuated flow. Proper Orthogonal Decomposition (POD) based Galerkin models produce a low-order system of ordinary differential equations that captures the flow physics, thus fulfilling those requirements. Such models have been extensively studied, and were shown capable of representing and controlling several flow problems [2].

To accurately determine the current state of the flow, the estimator requires an adequate input signal, which is usually provided by surface sensors. The processing power required and the reaction time of the system is directly proportional to the number of sensors. Through clever placement of the sensors at locations, the number of sensors required could be reduced. Several approaches are found in the literature, such as Mokhasi and Rempfer [3], and Stanlov et al. [4]. In this study, the sensor placement utilizes the modified Linear Stochastic Estimation (mLSE) to predict the time coefficients to compare with the reference values. The mLSE assumes that a correlation exists between the pressure signal of several sensors on the surface of the airfoil, and the computed POD time coefficients.

2 Theory

Reduced order models of the flow sacrifice physical accuracy for a reduction in complexity and therefore smaller computation costs. The details of POD Galerkin model are described by Noack et al. [5] among others, and are well known. The snapshot method introduced by Sirovich [6] is used to calculate the POD modes from temporally discrete numerical data. The POD Galerkin model is produced by substituting the POD velocity field expansion into the Navier-Stocks equations and projecting the resulting equations onto the subspace spanned by the POD modes. This yields a series of ordinary differential equations that model the development of the time coefficients and hence the state of the entire flow field

$$\frac{d}{dt}a_i = \nu \cdot \nu_T \sum_{j=0}^{N} l_{ij}a_j + \sum_{j=0}^{N}\sum_{k=0}^{N} q_{ijk}a_j a_k, \quad i = 1, \ldots, n \tag{1}$$

where N is the number of considered modes and ν is the flow viscosity. The linear part of the Eq. (3) is the dissipative term, whereas the quadratic part is the convective term. Both terms are computed a priori using $l_{ij} = (\vec{\phi}_i, \Delta\vec{\phi}_j)_\Omega$, and $q_{ijk} = (\vec{\phi}_i, \nabla \cdot [\vec{\phi}_i\vec{\phi}_k])_\Omega$. For most practical cases the pressure term is neglected [7].

The Galerkin time coefficients obtained using uRANS simulations, such as in the current study, tend to divert from the POD ones, since uRANS simulations fail

to resolve the dissipative scales, and due to the finite number of modes used to generate the model. A common approach is to calibrate the model by multiplying the linear viscous term with an eddy viscosity ν_T, as shown in Eq. (1). This and other calibration techniques are detailed in Cordier et al. [7], the simplest of which is based on minimizing the least square error,

$$Error = \left(\frac{1}{M} \sum_{k=1}^{M} \sum_{i=1}^{N} \left(a_i^P(t_k) - a_i^G(t_k) \right)^2 \right), \tag{2}$$

where a^P and a^G are the POD and Gakerkin time coefficients respectively, and M is the number of snapshots.

Another approach to estimate the time coefficient uses stochastic estimation. The mLSE method [8] adopted in this study, assumes that the statistical information contained within the two-point correlation R_{ij} could be combined with instantaneous information to estimate the flow field. Assuming that the input signal from the airfoil surface is a pressure signal, the estimated time coefficients can be computed as

$$\tilde{a}_n(t) = A_{ni} P_i(t), \tag{3}$$

where $\tilde{a}_m$ are the estimated mLSE time coefficients and p_i are the pressure values. The vector A_{ni} is determined by solving the following equations,

$$\begin{bmatrix} < p_1 p_1 > & \cdots & < p_q p_1 > \\ \vdots & \ddots & \vdots \\ < p_1 p_q > & \cdots & < p_q p_q > \end{bmatrix} \begin{bmatrix} A_{ni} \\ \vdots \\ A_{nq} \end{bmatrix} = \begin{bmatrix} < a_1 p_1 > \\ \vdots \\ < a_n p_q > \end{bmatrix} \tag{4}$$

over a learning period of q number of snapshots, where a_n are the POD time coefficients and p_i are the pressure signals over the learning period.

3 Numerical Setup and Reference Case

The flow was simulated over a 2D FNG airfoil at zero angle of attack equipped with a droop-nose and a specially designed Coanda flap at landing configuration. The airfoil had a chord length of 1m, and a flap deflection angle of 65°. The selected reference case was the no-blowing configuration, where the flow over the flap is fully separated. The numerical grid was a combination of structured mesh around the airfoil to resolve the boundary layer, and unstructured mesh in the far field, with total of 2.3×10^5 nodes. The grid extended 50 chord lengths in every direction. The boundary layer was resolved in the grid down to a dimensionless wall distance (y_+) of 1.

Fig. 1 Optimal locations of
five sensors on the flap, shown
in *red*
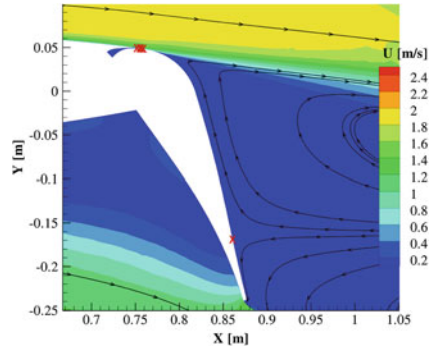
Fig. 2 A comparison
between the first
two POD time
coefficients and the same
calibrated Galerkin time
coefficients
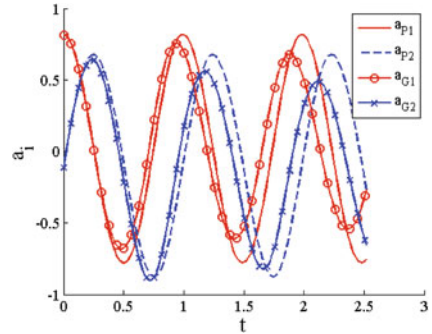
The unsteady Reynolds average Navier-Stokes (uRANS) simulations were carried
out for zero angle of attack using Fluent flow solver with shear stress transport (SST)
k-ω model. Since the numerical simulations will be validated by a water tunnel
experiment, the Reynolds number was set at an equivalent value of Re = 1.5 million.

4 Results

The estimator has to be based on a model which is able to predict the development of
the system's state. In this study only the first four POD modes were considered, which
captured about 98 % of the total kinetic energy. By solving Eq. (1) over the desired
time range, the four Galerkin time coefficients were obtained. The error (Eq. 2)
between the estimated and computed time coefficients was minimized using a simple
golden section calibration scheme, which acted on the eddy viscosity term. The
calibrated results for the first two modes are shown in Fig. 2, where the coefficients
are now in better agreement. The minimum of the error function was reached at an
eddy viscosity value of 2,724.8.

The range of possible sensor locations was confined to the upper surface of the flap.
The upper surface was divided by 384 grid points, at which the computed pressure

Fig. 3 Comparison between
the optimized sensor error
and the error of evenly spaced
sensors
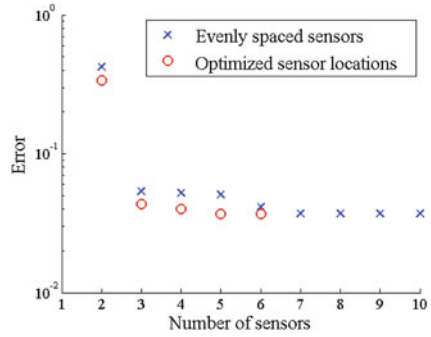
Table 1 Minimum error for a
number of optimized sensors,
and the reduction in
considered the surface grid
points

No. of sensors	Reduction factor	Error [$1/s^2$]
2	1	0.33552
3	3	0.04330
4	10	0.04035
4 HR	5	0.03997
5	10	0.03671
6	20	0.03696

values could be used in the mLSE to simulate a sensor. For any given constellation
of sensors, the error was computed using Eq. (2), where the Galerkin time coefficient
was substituted with the estimated mLSE time coefficients.

Using brute force optimization better sensor locations were found for a given
number of sensors. The error distribution is symmetrical and produces the highest
error when the sensors coincide. The minimum error was achieved for the two sensors
at the flap shoulder. With increasing number of sensors the processing costs for a brute
force optimization increased drastically, and a reduction in the number of considered
sensor locations was needed. Table 1 lists the error for a given number of optimized
sensors, and the resolution reduction factor used.

The four sensor case was repeated with twice the surface resolution, to gauge its
sensitivity. With increasing surface resolution, the optimized sensor positions moved
only slightly with respect to the lower resolution case, and with a slight decrease in
error. This case, as shown in Fig. 1, also exhibits an optimal sensor located at the
middle of the flap. The number of considered sensor locations had to be reduced
further for the cases with five and six sensors, it led to a slight increase in error
between the two cases, as seen in Table 1. The error for the optimized sensor locations
is compared to the error for the evenly spaced sensors in Fig. 3. There is a significant
reduction in error for the optimized cases in comparison to the evenly spaced ones,
for a given number of sensors. Overall there is an error reduction with an increasing
number of sensors. This is expected as the dominant flow structures (with the highest
energy content) are already captured with the first 3 sensors.

5 Conclusion

A reduced order model has been generated for the estimator based on uRANS data, and calibrated using a golden section scheme. The calibrated POD Galerkin model shows some promising results. While it was able to capture the first two modes after calibration, it failed to perform as well with the following modes. This was expected because of the unresolved dissipative scales from the uRANS simulation, and due to the mode truncation error. Using Large Eddy Simulation (LES) or Detached Eddy Simulation (DES) to build this model, which resolve the flow down to smaller scales, would solve this issue. An effort that is currently pursued.

A brute force optimization was performed to determine the optimal sensor locations over the airfoil flap. The optimization minimised the error between the predicted mLSE time coefficients and the reference POD ones. It was shown that increasing the number of sensors will reduce the error. This error reduction, however, asymptotes with further increase of sensors since the dominant structured could be already captured with a limited number. The required number of sensors to achieve a certain level of accuracy was shown to be less with the optimized sensor locations compared to the evenly spaced ones. For the above mentioned flow conditions, optimization of the sensor locations favoured positions around the edge of the separation. For cases with more than three sensors, an optimal sensors location inside the separation was found. The complete closed-loop control system requires development under real world conditions, and will be tested in a water tunnel experiment, and with the different estimator models and sensor combinations.

References

1. Pfingsten KC, Radespiel R (2009) Experimental and numerical investigations of a circulation control airfoil. In: 47th AIAA aerospace science meeting, Orlando.
2. Bergmann M, Cordier L, Brancher JP (2005) Optimal rotary control of the cylinder wake using proper orthogonal decomposition reduced-order model. Phys Fluids 17:097101
3. Mokhasi P, Rempfer D (2004) Optimized sensor placement for urban flow measurement. Phys Fluids 16(5)
4. Stalnov O, Palei V, Fono I, Cohen K, Seifert A (2007) Experimental estimation of a D-shaped cylinder wake using body-mounted sensors. Exp fluids 42(4):531–542
5. Noack BR, Afanasiev K, Morzynski M, Tadmor G, Thiele F (2003) A hierarchy of low-dimensional models for the transient and post-transient cylinder wake. J Fluid Mech 497:335–363 (Cambridge University Press).
6. Sirovich L (1987) Turbulence and the dynamics of coherent structures. Q Appl Math Vil XLV(3):561–590.
7. Cordier L, Abou El Majd B, Favier J (2010) Calibration of POD reduced order models using Tikonov regularization. Int J Numer Methods Fluids 63:269–296
8. Ausseur J (2007) Application of low-dimensional techniques for closed-loop-control of turbulent flows. Ph.D. dissertation, Department of Mechanical and Aerospace Engineering. Syracuse University, Syracuse, NY.

Distributed Closed-Loop Lift Control for Performance Recovery of a Thick Turbulent Airfoil

Victor Troshin and Avraham ("Avi") Seifert

Abstract The experiment was aimed at recovering performance of a thick, turbine blade airfoil degraded due to poor surface quality at Reynolds number of around 500,000. A closed-loop system that controls lift is presented. We used up to three rows of "synthetic jets" coupled with an array of time resolved hot film and pressure sensors to estimate the separation location and lift. Using an amplitude distribution algorithm it was possible to recover the clean turbine blade performance and change the blades lift force as desired over a range of working conditions.

1 Introduction

Degraded surface quality of large wind turbines promotes boundary layer transition, leading to premature boundary layer separation which in turn adversely affects turbine' performance. Active control of flow separation is known to be capable of manipulating boundary layer separation [4]. Currently closed-loop lift control system is presented [7]. We have chosen Piezo-fluidic actuators [1, 2, 5, 8] , due to their compact design, flexibility in operation, reliability, durability and especially their low power consumption. Efficient operation requires not only proper positioning of the actuators but also real-time knowledge of the separation location, the effect actuators interactions and on the performance to be controlled. This complex task can be achieved only with distributed sensing and actuation, state estimation and suitable control algorithm. Two methods were currently considered for monitoring the boundary layer state: measuring the local pressure variations at a high rate [3] and

V. Troshin (✉) · A. Seifert (✉)
Meadow Aerodynamics Laboratory, School of Mechanical Engineering,
Faculty of Engineering, Tel Aviv University, Tel Aviv, Israel
e-mail: victortrn@gmail.com

A. Seifert
e-mail: seifert@eng.tau.ac.il

Fig. 1 Actuator slots, sensor, and roughness locations on the contour of the 31 % thick airfoil. "HF" indicates hot film sensors; "Press" indicates pressure sensors
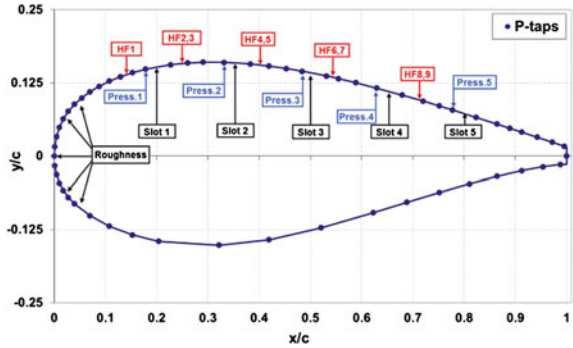
measuring the shear-stress fluctuations [6] at 5 points each along the upper surface of the airfoil.

2 Experimental Setup

A 31 % thick, AH-W-93-300 airfoil with a chord length of 480 mm (Fig. 1) was tested in the Knapp-Meadow low speed tunnel. Five possible locations for actuators are available, into which three pre-calibrated Piezo-fluidic actuators were used at $x/c = 0.35$, 0.50 and 0.65. Each actuator row consists of 13 actuators operated at π phase shift. The exit slots are 44 by 0.8 mm; the spacing between each pair of actuator slots in a row was 1 mm. The excitation is ejected downstream, 30° to the local surface tangent. The airfoil is equipped with 94 pressure taps connected to multi-channel pressure scanner, PSI[TM] model ESP-8,400[TM], with a full scale of 10 in. of water. Distributed roughness in the form of 5 by 5 mm "bugs" were located near the leading edge between $x/c = 0.05$ on the upper and lower surfaces in order to simulate degraded surface quality.

Two kinds of unsteady sensors were placed on the airfoil surface for real time "state" monitoring. Nine uncalibrated hot-film (HF) sensors, operated at constant voltage mode, were placed at five locations (Fig. 1). Five unsteady pressure sensors, located under the upper surface, and connected via short (20 mm) tubes to the upper surface, via 0.5 mm (internal diameter) tubes. The pressure sensors' bandwidth, as installed, was found to be flat at the relevant range (up to 1 kHz).

The experiments were performed in the closed-loop, low speed, low turbulence Knapp-Meadow wind tunnel. Test section width is 609 mm, so three dimensional effects at high incidence, separated flow are expected to be present. The large test section height (1.5 m) assures minimal interference with the floor and ceiling. No correction to any of these effects is applied. Lift, moment and pressure-drag are calculated from the airfoil surface pressures. The total drag is calculated by wake total and static pressures using a vertically traversed rake with 60 pressure ports, connected to the tunnel pressure scanner using Betz formula.
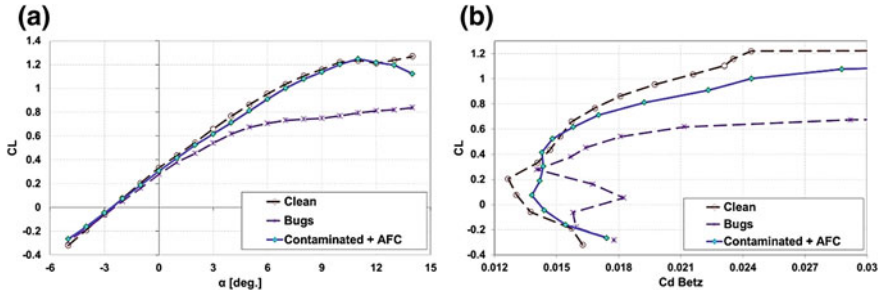
Fig. 2 The effect of contamination ("Bugs") and its control via AFC on the lift (**a**) and drag (**b**) at chord Reynolds number Re $= 0.5 \times 10^6$

3 Results

The effect of surface quality degradation on the airfoil performance and its recovery by open-loop AFC was first demonstrated.

The airfoil lift and drag data are shown in Fig. 2a, b, respectively, for Reynolds number of 0.5×10^6 and for clean, rough (termed "Bugs"), and rough-controlled states (termed "contaminated + AFC"). It can be seen that lift is significantly reduced and drag is significantly increased with degraded leading edge surface quality, compared to the "clean" airfoil. Activating actuator rows located at x/c = 0.35 and at x/c = 0.50, with C$\mu \approx 0.04$ and Strouhal of 41, re-establishes the "clean" lift and almost restores the drag of the airfoil. The energetic efficiency of this AFC application will be discussed later in the paper.

At the next stage of the experiment, 5 hot films and 5 unsteady pressure sensors positioned on the upper surface of the airfoil were used for state estimation. An indication of the boundary layer separation was obtained using the spectra of the hot-films data according to [6]. The low frequencies (large scale flow structures) are more dominant in separated flow then in the attached regions. Therefore, by comparing the sensor low to high frequency variance ratio (termed FVR) to a specified threshold, it is possible to determine the flow state (separated or attached) in the region of each sensor. The cutoff frequency (between low and high frequencies) was chosen based on chord Strouhal number $S_t = 4.5$. The validated mean (with pressures) separation location is then used in lift force estimation and actuation amplitude distribution algorithm. The lift was estimated from dynamic data acquired by the pressure sensors to provide a feedback for the closed-loop control system as outlined below. The averaged pressure coefficient ($\overline{C_p}$) was defined as the weighted average of the five local unsteady pressure sensors' readings (P_i), normalized by the dynamic pressure (q obtained by an additional unsteady pressure sensor) as:

$$\overline{C_p} = \frac{1}{q} \cdot \sum_{i=1}^{5} (C_i \cdot P_i) / \sum_{i=1}^{5} C_i. \tag{1}$$

Fig. 3 Validation of C_L estimation from five unsteady pressure sensors data. An incidence angle scans at $Re = 0.4 \times 10^6 - 0.6 \times 10^6$ range. All actuator slots active with the same amplitude in a range of 24–96 RMS [VAC]
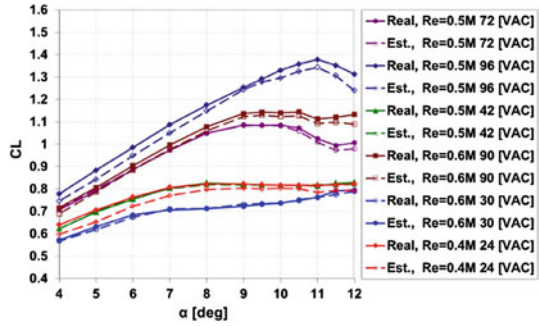
In Eq. (1), C_i is defined as the ratio of separation location to ith sensor's location.

Several tests were performed in order to determine the correlation between the averaged pressure and the lift coefficients. Those tests included a Reynolds number scan in the range of 400k–600k, excitation amplitude scans from 0 to 96 VAC, and incidence angles scan in a range of $4°-12°$. It was found that in the examined range of parameters, the Reynolds number is a very weak parameter. As a result, a linear correlation between the averaged pressure coefficient, the incidence angle (α [deg], quite weak dependence too), and the lift coefficient (C_L) variation was obtained. The best fitted correlation is:

$$C_L = -199.0 \cdot \overline{C_p} + 0.04432 \cdot \alpha - 0.7377 \tag{2}$$

In Fig. 3 the comparison of the estimated and measured lift (dashed and solid lines, respectively) versus α for a few Reynolds numbers and excitation amplitudes are presented. It can clearly be seen that the lift estimation is in very good agreement with the measured lift for the design point (Re $= 0.5 \times 10^6 \alpha = 9°$) and degrades slightly with the "distance" from the design point. However, the lift is predicted quite well, even at post stall.

The final step of this study was to design and implement a robust closed-loop lift controller. The closed-loop system block diagram is presented in Fig. 4. A feedback based on the separation location and C_L estimation algorithm (Eq. 2) was included, i.e., blocks "FVR" and "CL calc." respectively (Fig. 4). The difference between CL set-point and its estimation was fed into the PID controller as input. The output of the controller, "Max Amp", (maximum allowed amplitude), was fed into the "Amplitude Distributor" block. In addition, the current separation point was fed into this block for purpose of calculating the amplitudes, provided to the three actuator rows. Those amplitudes are proportional to the distance of the actuator from the separation location—higher excitation amplitudes were provided to the slots which are closer to the separation point. Thereafter, the set-point tracking and disturbance rejection tests showed that the system is quite robust to disturbance rejecting.

One of the possible advantages of closed- over open-loop AFC is the ability to adapt the control parameters to the changing flow "state" and minimize the energy expenditure. To examine the energetic efficiency aspect, the aerodynamic performance
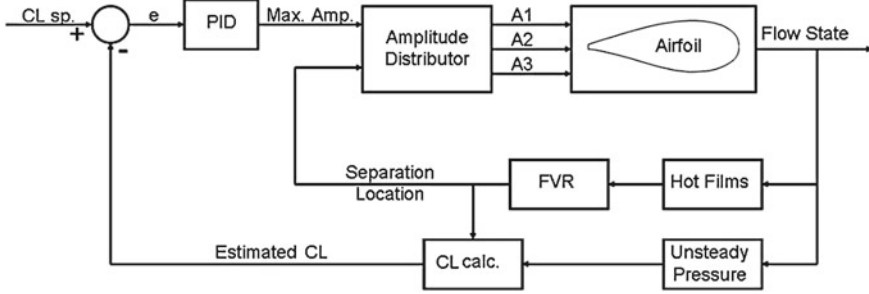
Fig. 4 The block diagram of the closed-loop lift AFC system

Fig. 5 Overall system efficiency (AFM3) for the cases presented in Fig. 2 compared to the closed-loop configuration. Re $= 0.5 \times 10^6$
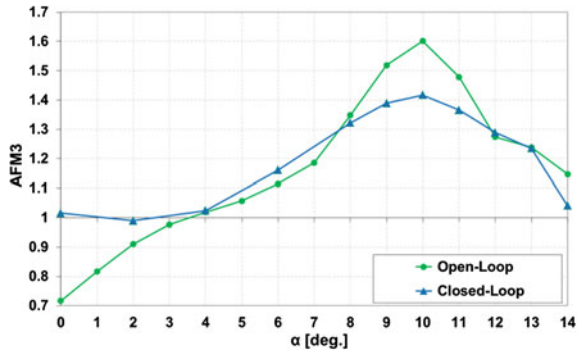
of the closed-loop AFC system was compared to the performance of the open-loop configuration of Fig. 2. For this purpose similar airfoil performance was achieved by the closed-loop configuration and energetic efficiency of the approaches were compared using an aerodynamic figure of merit (AFM3) [9]. Values of AFM3 > 1 means that it is energy efficient to introduce power to the actuators because the energy harvesting capability of the airfoil will increase, when accounting for the power spent on AFC.

From Fig. 5 it can be noticed that the highest efficiency is reached at $\alpha = 10°$, when only two actuator rows are operated in open-loop. However, when the angle of attack is changed, this set-up loses its superior efficiency. In contrast, in the closed-loop configuration at low incidence angles the efficiency improves due to using only the required power. Therefore, AFM3 for CLAFC is always equal or higher than unity, at a relevant range of incidence angles. Moreover, the incidence averaged efficiency of the closed-loop system is slightly higher than in the open-loop case at the current parameters.

Definitely, this system does not provide the most efficient amplitude combination. For example, the open-loop is 20 % more efficient at $\alpha = 10°$, this is only a set-point issue. Further improving the efficiency of the closed-loop system could be obtained by reconsidering the amplitude distribution algorithm.

4 Conclusions

The main objectives of the study were: Recovery of the airfoil's degraded performance due to premature laminar-turbulent transition by AFC, real-time flow state estimation using surface mounted sensors, and, closed-loop lift control in an unsteady environment. Indeed, the performance of a contaminated airfoil intended for the root section of a wind turbine blade can be fully recovered and its energy harvesting capability is expected to be increased by up to 60 % (compared to the contaminated state, or fully recovered to the clean state) using AFC, but only over a narrow incidence range. However, to be efficient over a wide range of unknown and unsteady conditions, closed-loop AFC is required. It was demonstrated that the flow state can be estimated using a small number of sensors distributed on the upper surface of the airfoil. The separation location was estimated by un-calibrated hot-film sensor array in real-time, based on the spectral content of the signals with no cross-actuator information transfer. The static responses of the unsteady pressure sensor array were compared to that of the lift response and enabled real-time lift estimation with high fidelity. Eventually a closed-loop PID lift control system was designed, tuned and implemented. It uses the estimated lift, by the pressure sensors, as a feedback and the three actuator rows for control authority. The system energetic efficiency was also considered. It was found that the closed-loop system is more efficient then the open-loop system, when the entire operational incidence angles range is considered. This is because the system reduces or even nullifies the power input to the actuators according to the measured flow state and specified lift. In future studies we plan to use larger number of actuators operating over a range of Reynolds numbers and incidence angles and improve the energy distribution and close-loop algorithms to increase the efficiency of the active flow control systems over a whole blade in field tests.

References

1. Cattafesta LN, Garg S, Shukla D (2001) Development of piezoelectric actuators for active flow control. AIAA J 39:1562–1568
2. Glezer A, Amitay M (2002) Synthetic jets. Annu Rev Fluid Mech 34:503–529
3. Kumar V, Alvi FS (2009) Toward understanding and optimizing separation control using microjets. AIAA J 47:2544–2557
4. Seifert A, Darabi A, Wyganski I (1996) Delay of airfoil stall by periodic excitation. J Aircr 33:8
5. Seifert A, Eliahu S, Greenblatt D, Wygnanski I (1998) Use of piezoelectric actuators for airfoil separation control. AIAA J 36:1535–1537
6. Seifert A Melton LT (2006) Control and identification of turbulent boundary layer separation. In: IUTAM symposium on one hundred years of boundary layer research. (ed.), Springer, Heidelberg, pp 199–208
7. Troshin V, Seifert A (2013) Performance recovery of a thick turbulent airfoil using a distributed closed-loop flow control system. Exp Fluids 54:1–19
8. Seifert (2007) Closed-loop active flow control systems: actuators. In: King R (ed) Active flow control-NNFM. NNFM, vol. 95, Springer, Heidelberg, pp 69–84
9. Stalnov O, Kribus A, Seifert A (2010) Evaluation of active flow control applied to wind turbine blade section. J Renew Sustain Energy 2:063101

Part IV
Analysis of Separated Supersonic Flow Instabilities

Proper Orthogonal Decomposition and Dynamic Mode Decomposition of Under-Expanded Free-Jets with Varying Nozzle Pressure Ratios

Paul Stegeman, Andrew Ooi and Julio Soria

Abstract This paper provides an overview of the progress made in a study of the coherent structures of feedback loops found in under-expanded free-jets. In order to gain a better understanding of the topology and dynamics of these structures the proper-orthogonal decomposition (POD) and dynamic mode decomposition (DMD) techniques will be applied to high resolution numerical datasets. We consider a purely convergent under-expanded free jet with nozzle pressure ratios $NPR = \{2.2, 2.6\}$ and a nozzle lip thickness $t_n/d = 1/3$ where $d = 15$ mm is the nozzle diameter. The analysis has shown that DMD is more capable than POD in extracting the structure of instabilities from small datasets which correspond well to the experimental observations.

1 Introduction

Acoustic feedback in under-expanded free-jets has been a topic of research over the last five decades with a global summary provided in [8]. It is understood that the feedback loop is due to large scale coherent structures present in the shear layer interacting with the core shock cells and that the attenuation of these structures may significantly reduce the broadband and discreet (Screech) noise generated. However the details of the dynamics of these large scale structures and the significant changes that occur due to a change in the jets nozzle pressure ratio (*NPR*) are still not well

P. Stegeman (✉) · J. Soria
Laboratory for Turbulence Research in Aerospace and Combustion,
Department of Mechanical and Aerospace Engineering, Monash University, Melbourne, VIC 3800, Australia
e-mail: paul.stegeman@monash.edu

A. Ooi
Department of Mechanical Engineering, University of Melbourne,
Parkville, VIC 3052, Australia

understood. In order to gain a better understanding of the topology and dynamics of these structures the Proper-orthogonal decomposition (POD) and dynamic mode decomposition (DMD) techniques will be applied to high resolution numerical datasets.

From prior acoustic and schlieren experiments of under-expanded jets with circular nozzles numerous instability modes have been observed in the screech phenomena [6]. The dominant modes are the axisymmetric instability (toroidal), lateral instability (azimuthal variation) and a helical instability with the transitions occurring respectively with increasing *NPR*. In this study we consider a purely convergent under-expanded free jet with nozzle pressure ratios $NPR = \{2.2, 2.6\}$ and a nozzle lip thickness $t_n/d = 1/3$ where $d = 15$ mm is the nozzle diameter. These were chosen to match the experimental setup of Mitchell [4] and were found to exhibit both axisymmetric and lateral instabilities.

2 Numerical Dataset

The free-jet dataset used in this study is the result of a three dimensional hybrid large-eddy simulation on a non-uniform structured cylindrical grid. For spatial differentiation the hybrid solver employs a sixth order central nite difference scheme for smooth regions and a fifth order weighted essentially non-oscillatory scheme with local Lax-Friedrichs ux splitting in discontinuous regions. Temporal integration is performed using a fourth order five step Runge-Kutta scheme. The sub-grid scale terms were computed using Germanos dynamic model with the adjustments made by Lilly [3].

The domain consists of approximately 16.4 million nodes with the spatial extent of 30d downstream and 15d the radial direction. Locally one-dimensional inviscid compressible boundary conditions defined in [5] are used for the adiabatic nozzle wall and outflow regions. Sponge regions are employed near the outflow boundary were the flow field is forced to a self similar incompressible jet solution that has been determined *a priori*. The jet inlet velocity profile was modeled using the hyperbolic-tangent function found in [1] while the temperature profile was determined using the Crocco-Busemann relationship [7].

As of this paper the $NPR = 2.2$ and $NPR = 2.6$ cases have completed approximately 100,000 and 50,000 time steps or $t/t_0 = 100$ and $t/t_0 = 50$ turn-over times respectively where $t_0 = d/u_j$ and u_j is the nozzle exit velocity (≈ 310 m/s). Snapshots of two axial-radial planes perpendicular to each other have been recorded every 50 time steps with $\Delta t/t_0 = 0.048$ for the purpose of the POD and DMD analysis.

3 Mean Field Results

A plot of the temporal mean axial velocity may be found in Fig. 1. The average shock spacing for the $NPR = 2.2$ and $NPR = 2.6$ cases are 0.57d and 0.84d respectively. For all cases the mean velocity fields near the nozzle (<4d) have converged, however
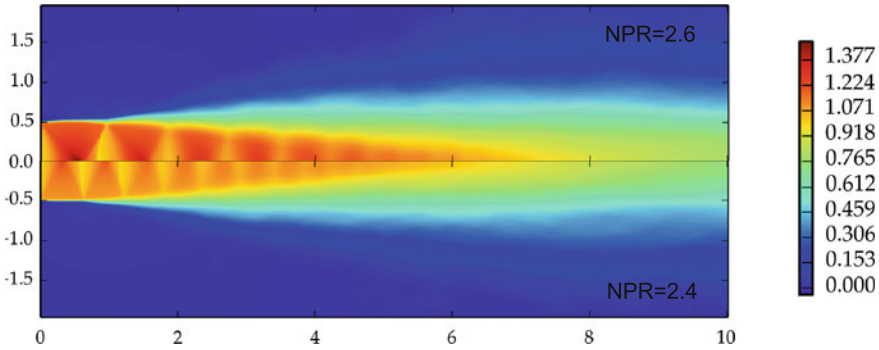
Fig. 1 Mean axial velocity for both cases

at greater distances (>4d) from the nozzle the radial and azimuthal velocities still contain spurious fluctuations with magnitudes of the order of 5 % of the unsteady values. This is likely due to the shedding of turbulent eddies from the core jet region at which point their residence time is significantly increased due to the large drop in their advection speed. Based on the rate of convergence in these regions an extra 100,000–200,000 steps will be required for each case to reduce the residuals to <0.1 %.

4 Proper Orthogonal Decomposition and Dynamic Mode Decomposition

The proper orthogonal decomposition (POD) technique is used to calculate a set of orthogonal basis functions of a ensemble dataset where the energy content of each mode is maximized. POD produces a set of spatial and temporal modes along with a corresponding modal energy. In contrast dynamic mode decomposition (DMD) calculates the Koopman modes describing the transient linear components of a non-linear flow field. DMD produces a set of spatial modes with corresponding eigenvalues describing the temporal frequencies and growth/decay rates associated with each mode. The algorithm used for determining the POD and DMD modes is outlined in [2] however in this study no rank reduction is performed in the DMD analysis. POD requires an ensemble dataset of statistically independent snapshots where the DMD technique requires an ensemble time-series dataset. A POD analysis therefore requires data from a much larger time interval than DMD which significantly increases the computational costs of generating the numerical datasets.

The POD modes have not converged for either case and the first few spatial modes exhibit none of the expected structures. This is probably due to the lack of a large number of statistically independent snapshots in the current dataset which is estimated to be approximately 100 for the $NPR = 2.2$ case and 50 for the $NPR = 2.6$ case. In the POD of an under-expanded free-jet completed by Mitchell using planar particle

Fig. 2 $NPR = 2.2$ DMD pre-multiplied spectra
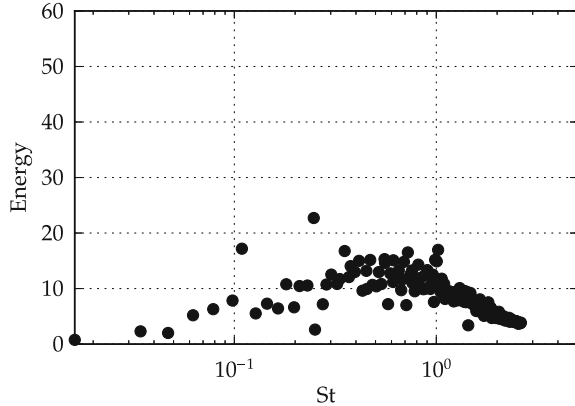
image velocimetry measurements the required number of statistically independent snapshots to reach converged POD modes was on the order of 1,000 [4]. DMD however, exhibited reasonable convergence in the higher frequencies ($St > 0.4$) for both cases.

DMD spectra for $NPR = 2.2$ may be seen in Fig. 2 with peaks occurring at Strouhal numbers of 0.11, 0.25, 0.36, 0.72 and 1.02. The spatial eigenvectors for the $St = 0.11$, $St = 0.25$ and $St = 0.36$ cases exhibit no global structure which may be due to the lack of convergence in the lower frequencies. The spatial eigenvectors at $St = 0.72$ and $St = 1.02$ represent the structures of lateral and axisymmetric instabilities respectively. The real component of the spatial structures for the lateral mode may be seen in Fig. 3. As can be seen the lateral vortex structure is well defined near the nozzle but is significantly distorted in regions further downstream. This is probably due to the use of a temporal mean that has not converged in these regions and is expected to become clearer with more snapshots. Neither of these modes' eigenvalues are growing or decaying as expected and correspond with the acoustic measurements of Mitchell in which the $NPR = 2.2$ case showed the presence of both lateral and axisymmetric instabilities [4].

DMD spectra for $NPR = 2.6$ may be seen in Fig. 4 with peaks occurring at Strouhal numbers of 0.40, 0.52, 1.03 and 1.84. The spatial eigenvectors for the $St = 0.40$ case exhibits no global structure in a similar manner to the low frequency modes in the $NPR = 2.2$ case. The spatial eigenvector for the $St = 0.52$ mode represents a lateral instability with a corresponding harmonic at $St = 1.03$, neither of which are growing or decaying. The modes compare well with Mitchell's acoustic measurements in which the $NPR = 2.6$ case exhibited a strong lateral instability [4]. However, the spatial eigenvector of the $St = 1.84$ mode exhibits an unexpected small scale helical like instability that does not seem to be present in the experimental data. Further analysis must be undertaken to determine the reason for this discrepancy.

Fig. 3 $NPR = 2.2$ lateral-mode ($St = 0.7$) axial velocity (*left*) and radial velocity (*right*)
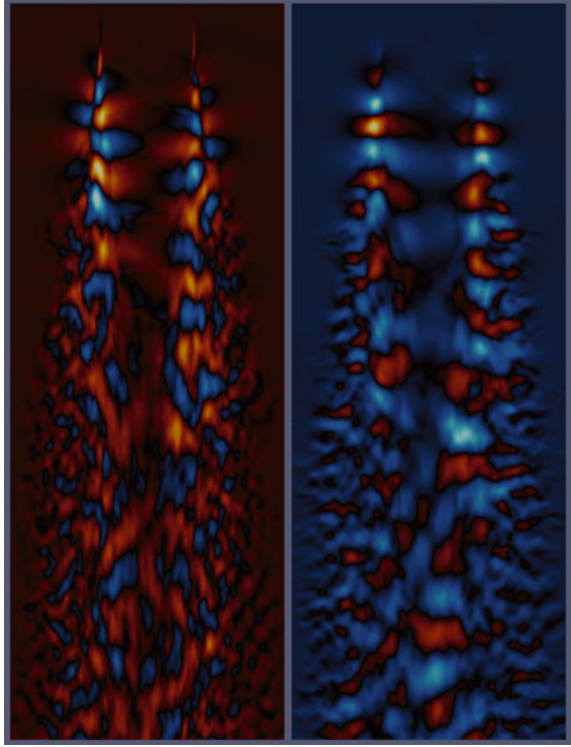
Fig. 4 $NPR = 2.6$ DMD pre-multiplied spectra
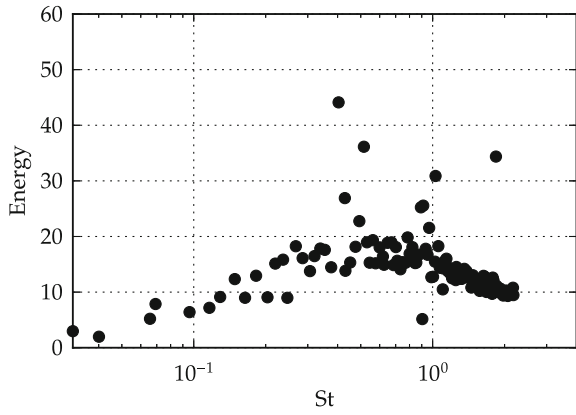
5 Summary

An overview of the current state of an analysis of feedback instabilities in under-expanded supersonic free jets using proper orthogonal decomposition and dynamic mode decomposition has been provided. The analysis has shown that DMD is more capable than POD in extracting the structure of instabilities from small datasets which correspond well to the experimental observations of Mitchell.

References

1. Bodony D, Lele S (2005) On using large-eddy simulation for the prediction of noise from cold and heated turbulent jets. Phys Fluids 17:85–103
2. Kitsios V, Buchmann NA, Atkinson CA, Frederiksen JS, Soria J (2013) Recovery of the koopman modes of a leading-edge separated airfoil flow via a proper orthogonal decomposition rank reduction. In: Instability and control of massively separated flows, Prato, Italy.
3. Lilly D (1992) A proposed modification of the germano subgrid-scale closure method. Phys Fluids 4:633
4. Mitchell D (2013) Aeroacoustic feedback loops in underexpanded supersonic jet flows. PhD thesis, Department of Mechanical and Aerospace Engineering, Monash University.
5. Poinsot T (1992) Boundary conditions for direct simulations of compressible viscous flows. J Comput Phys 99:352
6. Raman G (1999) Supersonic jet screech: half-century from powell to the present. J Sound Vib 225(3):543–571
7. Schlichting H, Gersten K (2000) Boundary layer theory. Springer.
8. Tam CKW (1995) Supersonic jet noise. Annu Rev Fluid Mech 27:17–43

Instability Study of the Wake Behind a Discrete Roughness Element in a Hypersonic Boundary-Layer

P. Paredes, N. De Tullio, N. D. Sandham and V. Theofilis

Abstract The linear instability induced by an isolated roughness element in a boundary-layer at Mach 6 has been analysed through spatial BiGlobal and three-dimensional parabolised (PSE-3D) stability analyses. It is important to understand transition in this flow regime since the process can be slower than in incompressible flow and is critical to prediction of local heat loads on next-generation flight vehicles. The results show that the roughness element, with a height of the order of the boundary-layer displacement thickness, generates an convectively unstable wake where different instability modes develop. Furthermore, at this high Mach number, boundary-layer modes develop at high frequencies and are also covered here. Important discrepancies are observed between BiGlobal and PSE-3D predictions, mainly for the roughness-induced wake modes. Results are in qualitative agreement with a full Navier-Stokes receptivity study of the same flow.

P. Paredes (✉) · V. Theofilis
School of Aeronautics, Universidad Politécnica de Madrid,
Pza. Cardenal Cisneros 3, 28040 Madrid, Spain
e-mail: pedro.paredes@upm.es

V. Theofilis
e-mail: vassilios.theofilis@upm.es

N. De Tullio
Department of Mathematics, Imperial College London,
South Kensington Campus, London SW7 2AZ, UK
e-mail: n.de-tullio@imperial.ac.uk

N. D. Sandham
Aeronautics and Astronautics, Faculty of Engineering and the Environment,
University of Southampton, Southampton SO17 1BJ, UK
e-mail: n.sandham@soton.ac.uk

1 Introduction

Experimental observations indicate that the dominant laminar-turbulent transition mechanisms in boundary-layers can be greatly modified by the presence of localised or distributed roughness, leading to a significant acceleration of the transition process both in noisy and in quiet environments. Over the years, a number of possible scenarios have been postulated to explain these observations. However, despite the numerous research efforts, the underlying physical mechanisms responsible for roughness-induced transition are only partly understood. Consequently high-speed vehicle design still relies on empirical transition-prediction criteria [1]. A deeper understanding of the effects of roughness on the stability of boundary-layers is thus urgently needed since it is particularly important for high-speed applications, where transition to turbulence leads to a significant increase of both the skin-friction and the wall heat-transfer, with obvious implications for the design of high-speed vehicles.

Three-dimensional roughness elements often induce subcritical disturbance amplification, leading to a "bypass"-like laminar-turbulent transition. The flow behind small three-dimensional localised roughness elements is characterised by the presence of counter-rotating streamwise vortices, which through the "lift-up" effect can potentially lead to strong algebraic growth of boundary-layer streaks and breakdown to turbulence both in incompressible [2] and compressible [3, 4] boundary-layers.

Recently, Wheaton and Schneider [5] have carried out a set of experiments on roughness-induced transition at $M = 6$, reporting the first quantitative measurements of the roughness wake instability at hypersonic speeds. For the same Mach number, direct numerical simulations [6, 7] show that the roughness wake can sustain the growth of a number of different instability modes, the relative importance of which seems to depend on the specific flow conditions considered.

In the wake flow behind an isolated three-dimensional roughness element, a predominant spatial direction exists along which the mean flow properties vary slowly, while the flow varies rapidly in the crossflow directions. These properties are taken into account in the derivation of the three-dimensional parabolised stability equations (PSE-3D), which represent the most efficient simplified approach for the solution of the instability problem of such flows. In an analogous manner to the extension of the Orr-Sommerfeld and Squire equations to the conventional PSE [8], the BiGlobal analysis equations are extended to the PSE-3D analysis. The linear PSE-3D methodology, formulated in the compressible flow regime by De Tullio et al. [9], assumes the existence of two scales along the streamwise spatial direction: a slow one, on which the base state varies, and a fast one, along which linear and nonlinear wave-like perturbations develop. In the latter work, the independently performed Navier-Stokes (NS), spatial BiGlobal and PSE-3D stability results are in excellent agreement with each other, validating the use of simplified theories for roughness-induced transition involving wake instabilities.

In this work we study the linear stage of the laminar-turbulent transition process induced by a sharp-edged isolated roughness element embedded in a Mach 6 boundary-layer. The linear instability of the flow is investigated through spatial

BiGlobal and linear PSE-3D stability analyses upon the laminar base state recovered by direct numerical simulations. In Sect. 2 we present the problem formulation, while the theoretical and numerical aspects used are described in [9, 10]. A discussion of the results obtained is provided in Sect. 3 and the paper ends with some conclusions in Sect. 4.

2 Problem Formulation

The equations governing the motion of a Newtonian fluid with viscosity μ are obtained by imposing conservation of mass, momentum and energy. Sutherland's law is used for the calculation of the dynamic viscosity. Dimensionless parameters which define the problem are the Reynolds number Re, the Mach number M and the Prandtl number Pr, which is considered to be constant and equal to $Pr = 0.72$. The reference values are taken at the free stream, while the reference length is the displacement thickness of the laminar boundary-layer at the computational domain inflow, δ_0^*.

This work focuses on the linear instability of the wake induced by the isolated roughness element. The study includes the effects of one roughness element with nondimensional height $h = 1$. The roughness element has length $L = 6.0$ and same width. The Reynolds number is $Re_{\delta_0^*} = 8,200$ and the Mach number is $M = 6$. The walls are considered no-slip and isothermal with $T_w = T_{ad} = 7.022$, where T_{ad} is the laminar adiabatic-wall temperature. The roughness Reynolds number is $Re_h = 331$ [3].

The analysis of flow stability monitors the development, in time and space, of small-amplitude perturbations superposed upon a given flow through the solution of the linearised Navier-Stokes equations. Linearisation of the equations of motion is performed around a laminar steady flow, denoted as "base flow", $q_b(x, y, z)$, upon which "small-amplitude perturbations", $\tilde{q}(x, y, z, t)$, develop; see [11] for more details. In this work, the linear stability of the flow, solution of DNS simulations of De Tullio and Sandham [6], is investigated through simplified stability theories, specifically PSE-3D and spatial BiGlobal analyses.

3 Results

The laminar base flow is calculated using full NS simulations. The roughness element induces two regions of 3D separated flow, located immediately upstream and downstream of it. The wake of the roughness element is convectively unstable for the condition studied here. A pair of counter-rotating streamwise vortices form at the edges of the roughness element, inducing lift-up of low momentum fluid from the near wall region and give rise to a low velocity streak. Figure 1 shows shaded contours of $u_s = [(\partial u_b/\partial y)^2 + (\partial u_b/\partial z)^2]^{1/2}$ at three different streamwise positions. Note that the shape of the low velocity streak changes significantly along the streamwise extent of the computational domain, suggesting that non-parallel flow effects
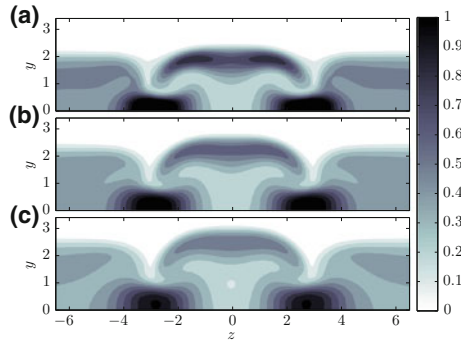
Fig. 1 Contours of u_s in crossflow planes at $x = 79.6$, 113.2 and 142.6 for **a**, **b** and **c** respectively, showing the localised shear generated by the roughness-induced counter-rotating vortices
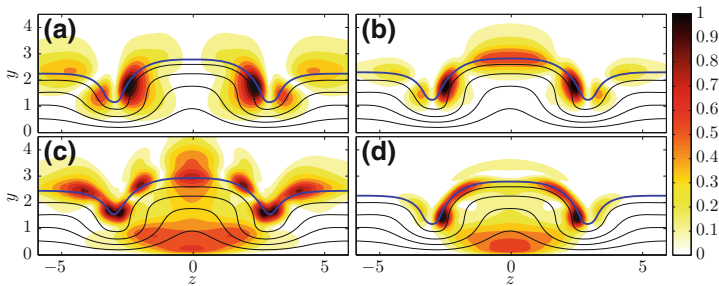
Fig. 2 Leading roughness-induced wake mode normalized modulus of streamwise velocity eigenfunctions at different frequencies for $x = 142.6$ recovered by spatial BiGlobal analysis. **a** for $F = 0.02$ (sinuous mode) and **b**, **c** and **d** for $F = 0.06$, $F = 0.12$ and $F = 0.14$ respectively (varicose modes). The *black* isolines correspond to $u_b = (0 : 0.2 : 0.8)$ and the *thicker blue lines* indicate the critical layers ($u_b = c_{ph}$, where c_{ph} is the phase speed of the instability modes)

might play an important role in the determination of the stability characteristics of the wake.

Here, the u-velocity amplitude functions of the dominant wake modes obtained from the BiGlobal eigenvalue analysis at $x = 142.6$ are shown in Fig. 2 for $F = 0.02$, 0.06, 0.12 and 0.14. For $F = 0.02$, the shape function peaks near the lateral shear layer and the instability mode manifests itself as a sinuous deformation of the low velocity streak. The modes having $F \geq 0.06$ grow in the two lateral shear layer and lead to a varicose streak mode. These shape functions compare very well with those recovered by full NS simulations [6] for the same set of frequencies and streamwise position.

A more complete picture of the modes taking part in the instability of the wake is observed in Fig. 3, which shows the spatial BiGlobal eigenspectrum obtained for $F = 0.14$ at $x = 142.6$ and the discrete unstable eigenfunctions. In Fig. 3a the observed amplification of the Mack mode in the surrounding boundary-layer is in agreement with the full NS predictions [6]. Furthermore, a second unstable
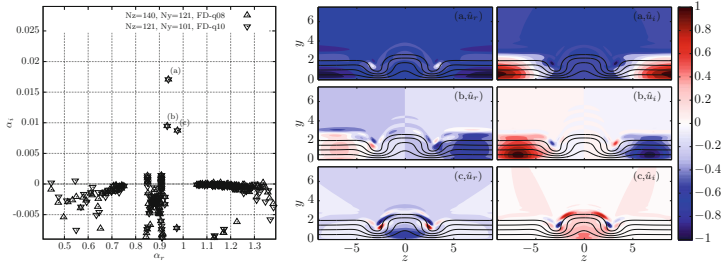
Fig. 3 Spatial BiGlobal spectrum, with letters in parentheses referring to subsequent figures, and contours of streamwise velocity eigenfunctions. The isolines correspond to $u_b = (0 : 0.2 : 0.8)$. The spectrum and eigenfunctions were obtained for $F = 0.14$ at $x = 142.6$

Fig. 4 Disturbance growth-rates at different streamwise positions for $F = 0.14$, being $-\alpha_i$ for spatial BiGlobal (*SBG*) and σ_K for PSE-3D, differentiating for the leading roughness-induced wake mode (*WM*) and the leading Mack mode (*MM*)
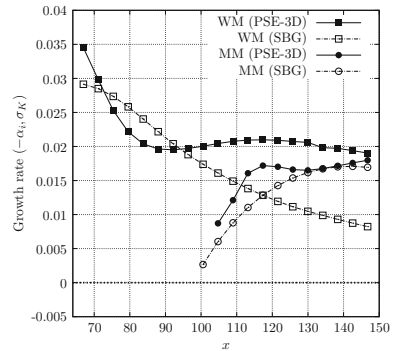
mode peaks in the lateral boundary-layer with lower amplification rate, showing an antisymmetric shape function about the roughness mid-plane as can be seen in Fig. 3b. Finally, the streamwise velocity eigenfunction of the unstable varicose wake mode is shown in Fig. 3c.

Having identified the structure of the modes dominating the wake instability, PSE-3D simulations are carried out to determine their growth-rates. The frequency is set to $F = 0.14$ since it corresponds to the maximum linear growth rate [6]. Figure 4 compares the growth-rates of the dominant modes extracted from the PSE-3D and BiGlobal results at different streamwise locations. The PSE-3D effective growth-rates are defined as $\sigma_k = -\alpha_i + 1/2\, d(\ln K)/dx$ in order to account for the residual slow variation of disturbance kinetic energy ($K = \int_y \int_z \rho_b (\hat{u}^2 + \hat{v}^2 + \hat{w}^2)\, dy\, dz$) with x. In fact, regarding the changes of the roughness-induced wake along x, strong discrepancies are found between PSE-3D and BiGlobal predictions for the varicose wake mode. In the other hand, the growth rate results for the second Mack mode differ less. It is important to notice the very good prediction of the PSE-3D effective growth rate comparing with the DNS results of [6], where the amplification slope of the most amplified mode, namely the growth rate, is nearly constant ≈ 0.021 for $80 \leq x \leq 147$ and the averaged effective growth rate along the same domain is $\sigma_K = 0.0203$.

4 Conclusions

The laminar-turbulent transition induced by a sharp-edged quadrilateral isolated roughness element at Mach number $M = 6$ was investigated, focusing on the linear instability of the roughness-modified steady base flow. The main contributions of the present work are an analysis of the linear instability of the convectively unstable wake generated behind the roughness element through spatial BiGlobal stability and PSE-3D simulations. The application of these different methods to the same problem allows the effect of multiple modes and flow nonparallelism to be separated out. Mack modes are found to grow slower and in a smaller region of instability than roughness-induced wake modes. Varicose instability modes were found to be the most unstable, which is also observed in full NS simulations [6]. Furthermore, the results are found in a qualitatively good agreement with the same NS simulations. The shape functions and growth-rates of the most unstable modes extracted from the DNS data are in close agreement with the two-dimensional eigenfunctions obtained from the BiGlobal stability analysis and the growth-rates obtained from the PSE-3D simulations, respectively.

References

1. Reda DC (2002) Review and synthesis of roughness-dominated transition correlations for reentry vehicles. J Spacecraft Rockets 39(2):161–167
2. Rizzetta DP, Visbal MR (2007) Direct numerical simulations of flow past an array of distributed roughness elements. AIAA J 45(8):1967–1976
3. Redford JA, Sandham ND, Roberts GT (2010) Compressibility effects on boundary-layer transition induced by an isolated roughness element. AIAA J 48(12):2818–2830
4. Bernardini M, Pirozzoli S, Orlandi P (2012) Compressibility effects on roughness-induced boundary layer transition. Int J Heat Fluid Fl 35:45–51
5. Wheaton BM, Schneider SP (2012) Roughness-induced instability in a hypersonic laminar boundary layer. AIAA J 5(6):1245–1256
6. De Tullio N, Sandham ND (2012) Direct numerical simulations of roughness receptivity and transitional shock-wave/boundary-layer interactions. RTO-MP-AVT-200. Art. 22, NATO
7. Choudhari M, Li F, Chang CL, Norris A, Edwards J (2013) Wake instabilities behind discrete roughness elements in high speed boundary layers. AIAA 2013–0081
8. Herbert T (1997) Parabolized Stability Equations. Ann Rev Fluid Mech 29:245–283
9. De Tullio N, Paredes P, Sandham N, Theofilis V (2013) Roughness-induced instability and breakdown to turbulence in a supersonic boundary-layer. J Fluid Mech 735:613–646
10. Paredes P, Hermanns M, Le Clainche S, Theofilis V (2013) Order 10^4 speedup in global linear instability analysis using matrix formation. Comput Meth Appl M 253:287–304
11. Theofilis V (2011) Global linear instability. Annu Rev Fluid Mech 43:319–352

Global Instability in Shock Wave Laminar Boundary-Layer Interaction

F. Guiho, F. Alizard and J.-Ch. Robinet

Abstract The linear global stability of an interaction between an oblique shock wave and a laminar boundary layer is carried out for various oblique shock angles. It is illustrated that such a flow acts as a noise amplifier. The least temporally damped global modes are classified into three main categories, low, medium and high frequencies. The high frequencies are localized into the attached boundary layer, the medium frequencies are associated with Kelvin–Helmholtz like structures along the shear layer and convective waves in the separated flow downstream whereas the low frequencies are driven by the interaction zone. In particular, a low frequency mode emerges which is scaled by the interaction length and the freestream velocity.

1 Introduction

Shock-wave/boundary-layer interactions (SWBLI) have important applications in a wide range of industrial problems, such as high speed flight occurring on aircraft, space/launch vehicles and projectiles. In particular, these interaction phenomena is a prior interest for supersonic/hypersonic flows where aerodynamic heating is a major factor [3]. The generation of shock waves by various surfaces of a vehicle or aircraft engine and the impingement of those shocks on other surfaces can greatly amplify the local heat transfer. When shock wave interacts with a laminar boundary layer, the experiments have shown that, for a sufficiently large pressure gradient amplitude, the boundary-layer becomes turbulent. It strongly modifies the interaction zone as well as its dynamics yielding to a reduced separated zone. Transition mechanisms are poorly known. However, in the presence of a low environmental noise or low upstream

---

F. Guiho · J.-Ch. Robinet (✉)
DynFluid Laboratory, Arts et Métiers ParisTech, 151, Bd. de l'Hôpital, 75013 Paris, France
e-mail: Jean-christophe.ROBINET@ensam.eu

F. Guiho · F. Alizard
DynFluid Laboratory, CNAM, 151, Bd. de l'Hôpital, 75013 Paris, France

disturbances, linear stability analysis can provide a good approximation of the
position of laminar-turbulent transition (see for instance the e^N method) [7]. In
addition, when the interaction zone is higher, one may also trigger self-sustained
low-frequency oscillations or three-dimensionality [6]. This specific dynamics can
not be captured by a local linear stability analysis, a global analysis is thus required.

In this paper, the linear global stability of a two-dimensional interaction between
an oblique shock wave and a laminar boundary-layer on a flat plate is carried out. In
particular, it will be further examine whether such a flow may act as a resonator or
a noise amplifier when it is subjected to two-dimensional perturbations. In addition,
the global modes which are involved in the space-time dynamics will be highlighted.

2 Governing Equations and Numerical Methods

The present approaches are based on the standard small perturbation technique. The
instantaneous flow is decomposed into base flow and unsteady perturbations:

$$\mathbf{q}(x, y, t) = \mathbf{Q}_b(x, y) + \mathbf{q}'(x, y, t) \qquad (1)$$

where $\mathbf{Q}_b = (\rho_b, \rho_b U_b, \rho_b V_b, \rho_b E_b)^T$. The decomposition (1) is introduced into
compressible Navier–Stokes equations. The base flow $\mathbf{Q}_b$ is supposed to be an
equilibrium solution of the 2-D compressible Navier–Stokes equations. The result-
ing equations are further simplified by considering that the perturbation is infin-
itesimal, i.e. the nonlinear fluctuating terms are neglected. Finally, compressible
Navier–Stokes equations are transformed into a linear partial differential equations
$\partial \mathbf{q}'/\partial t = \mathscr{A} \mathbf{q}'$ where $\mathbf{q}'$ represents the conservative variables for the perturbation.
Let-us introduce the following decomposition $\mathbf{q}' = \hat{\mathbf{q}}_k(\mathbf{x}) e^{-i \Omega_k t}$ where the couple
$(\hat{\mathbf{q}}_k, \Omega_k)$ is the so-called global mode and is a solution of large eigenvalue prob-
lem. The space and time behaviour of each global mode are governed by $\hat{\mathbf{q}}_k$ (the
eigenfunction) and Ω_k (the complex circular frequency) respectively.

The numerical method implemented in CFD DynFluid PHOENIX solver is based on
the finite-volume approach and on a cell centered discretization. Roe flux difference
splitting scheme are employed to obtain advective fluxes at the cell interface. The
MUSCL approach extends the spatial accuracy to third order. For viscous terms, a
central difference method is used. For unsteady computations, the dual time stepping
method is used, the derivative with respect to the physical time is discretized by a
second-order formula. For more details about the numerical methods, see [4].

To obtain an equilibrium state of the compressible Navier–Stokes equations, the
dual-time is turned off with a large CFL number with respect to the fully implicit
method.
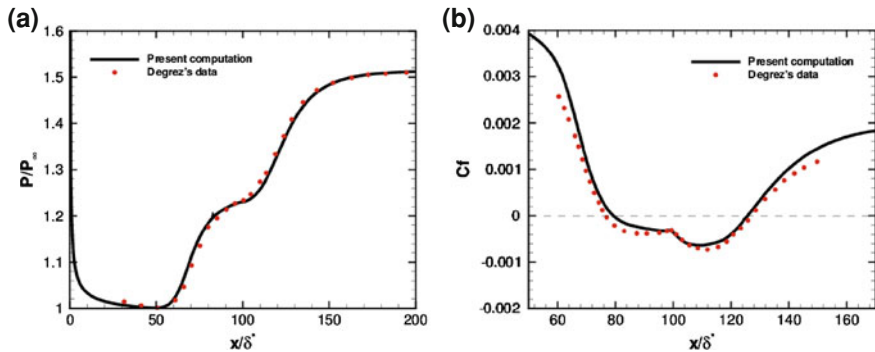
Fig. 1 Base flow characteristics for $\theta = 30.8^{\circ}$, $Re_{\delta^{\star}} = 886$. Comparison between numerical solution and Degrez's experiment **a** $P_{(x)}/P_{\infty}$ **b** $C_f(x)$

To perform a global stability analysis, the eigenvalues of the Jacobian matrix $\mathscr{A}$ are computed with a time-stepper approach, see [1]. The Arnoldi algorithm implemented into the temporal loop of PHOENIX code is used to obtain the most unstable modes, see [4].

3 Base Flow

The configuration studied is similar as the case of Degrez et al. described in [2]. An oblique shock wave, whose the angle of the shock relative to the horizontal axis is referred as θ hereafter, is made to impinge on the flat plate laminar boundary layer at $M_{\infty} = 2.15$ by enforcing at the inlet boundary discontinuous conditions that satisfy the Rankine–Hugoniot relations. In addition, the stagnation pressure is fixed at 12,300 Pa. Nonreflecting boundary conditions are enforced at the freestream and downstream boundaries. Finally, Dirichlet boundary conditions for both the velocity components and the temperature are prescribed at the adiabatic wall.

A preliminary computation is performed by considering a laminar boundary layer without impinging shock. Hence, δ^* is the displacement thickness taken at the theoretical location where the shock impinges the boundary layer, U_{∞}, ρ_{∞} and μ_{∞}, are the velocity, the density and the molecular viscosity at the freestream.In the next, the Reynolds number based on the previous quantities is fixed to $Re_{\delta^*} = 886$. After having reached a stationary state for the laminar boundary layer, the shock is introduced at the inflow condition. Hereafter, we consider four-different values for $\theta = 30.8^{\circ}$, 31.2°, 31.6° and 32° while holding the Reynolds number and the Mach number constants. Finally, we note L_{sep} and L_{int} the separation and the interaction length respectively.

The computational domain $\mathscr{D}$ extends from $\left[x_0/\delta^{\star}; x_n/\delta^{\star}\right] \times \left[y_0/\delta^{\star}; y_n/\delta^{\star}\right] = [0; 400] \times [0; 250]$ in the streamwise and wall-normal directions respectively. Figure 1a, b show comparisons between the base flow obtained by the PHOENIX
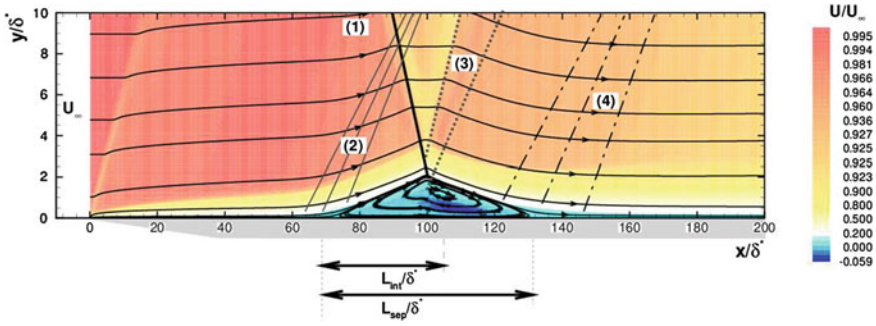
Fig. 2 Base flow characteristics for $\theta = 30.8^o$, $Re_{\delta^\star} = 886$. Iso-lines of streamwise velocity $U(x, y)$, streamlines and some characteristic phenomena: **1** incident shockwave; **2** separated waves; **3** expansion waves; **4** reattachment waves

Fig. 3 Eigenspectrum for Degrez's case, $\theta = 30.8^o$ and $Re_{\delta^\star} = 886$. $St = \Omega_r L_{int}/(2\pi U_\infty)$
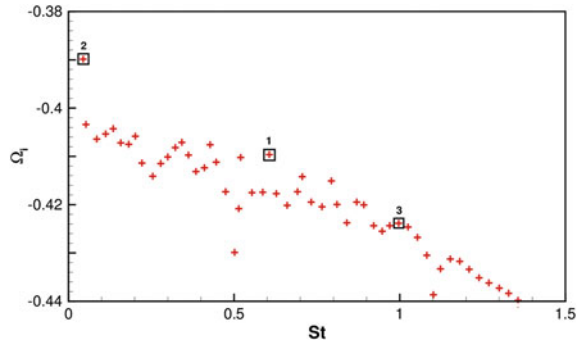
code and data from the experiments of Degrez et al. [2] for $\theta = 30.8^o$. Both the wall pressure distribution (Fig. 1a) and the friction coefficient (Fig. 1b) exhibit a good agreement with the experimental results. As an example, we plot the streamwise velocity for $\theta = 30.8$ in Fig. 2.

4 Global Stability Analysis

4.1 Stability for the Shock Wave Angle $\theta = 30.8$

As shown in Fig. 3, all the global modes are damped temporally which is consistent with the experiment of Degrez et al. [2] where none global unsteadiness is observed. Such a flow acts therefore as a noise amplifier.

The modes labelled 1, 2, 3, medium, low and high frequencies respectively, are shown in Fig. 4a, b and c. All these modes are associated with convective waves which are travelling along the shear layer in the separated zone and the attached boundary

(a) Mode labelled 1 in Fig. 3.

(b) Mode labelled 2

(c) Mode labelled 3
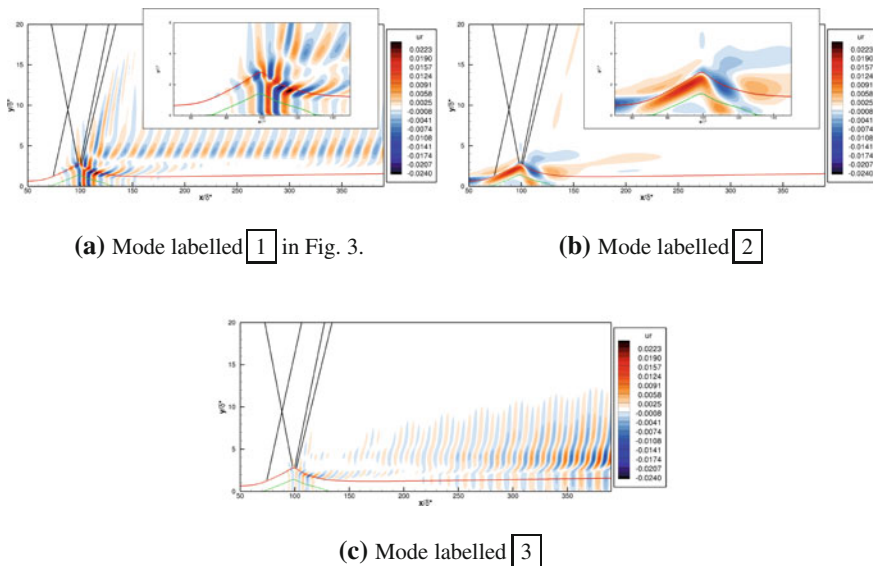
Fig. 4 Eigenfunctions for $\theta = 30.8^{\circ}$, $Re_{\delta^{\star}} = 886$. The streamwise component is shown

layer. In particular, lower the frequency is, more the spatial support of the global mode is localized inside the interaction region. Finally, the medium frequencies are clearly associated with Kelvin–Helmholtz like structures along the shear layer which emits Mach wave radiation in the vicinity of the impingement of the incident shock.

One may precise that the convergence of our results have been carefully checked by carrying out the global stability analysis with a large computational box which extends up to $400\delta^{\star}$ and a coarse mesh, where 20 grid points per wavelength are used for the mode labelled 3 for instance.

4.2 Influence of the Shock Wave Angle

When the incident angle increases, the interaction becomes stronger, causing an increase in the recirculation zone (not shown here for the sake of conciseness). The spectrum for $\theta = 30.8$, 31.2, 31.6 and 32 are shown in Fig. 5. Because all the modes are damped temporally for all the shock angles which are considered, the present shock wave-laminar boundary layer interaction is clearly identified as a noise amplifier. Hence, our global stability analysis further confirms the DNS results of Pagella et al. [5]. In addition, it is interesting to remark that a low frequency mode emerges for all equilibrium states (labelled as 2 in Fig. 3). When rescaled by the interaction length L_{int} and the freestream velocity U_{∞}, the corresponding frequency is seen to be almost constant around $S_t \approx 0.05$.
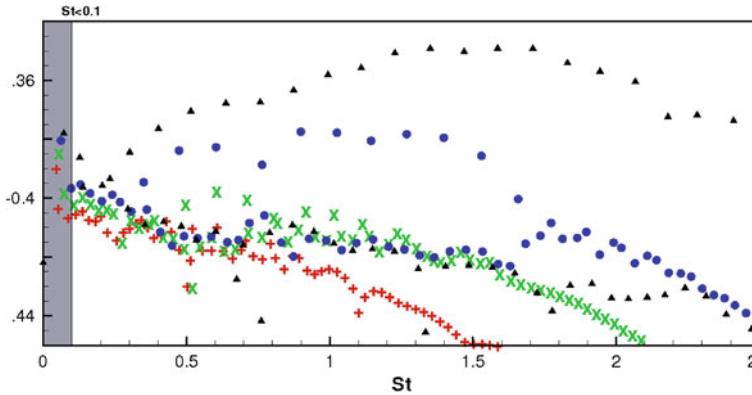
Fig. 5 Eigenspectrum for various shock angles θ $(30.8^{\circ}(+), 31.2^{\circ}(\times), 31.6^{\circ}(\bullet), 32.0^{\circ}(\blacktriangle)]. Re_{\delta^{\star}} = 886$

5 Conclusion

The linear global stability analysis of the interaction between an oblique shock wave and a laminar boundary-layer confirms that such a flow acts as a noise amplifier, even for large shock wave angles. The global modes exhibit a Kelvin–Helmholtz like structure developing in the shear-layer. The lower frequency modes are mainly localized in the interaction zone. Finally, a low frequency mode strongly localized in the interaction zone and scaled by the interaction length and the freestream velocity emerges which may provides new insight about the low frequencies unsteadiness observed in the turbulent regime.

References

1. Bagheri S, Akervik E, Brandt L, Henningson DS (2009) Matrix-free methods for the stability and control of boundary layer. AIAA J 47(5):1057–1068
2. Degrez G, Boccadoro CH, Wendt JF (1987) The interaction of an oblique shock wave with a laminar boundary layer revisited. an experimental and numerical study. J Fluid Mech 177: 247–263.
3. Délery J, Marvin JG (1986) Shock-wave boundary layer interactions. Technical report, AGAR-Dograph
4. Guiho F, Alizard F, Robinet J-C (2013) Global stability analysis with compressible cfd solver. AIAA Paper-2013-2620.
5. Pagella A, Rist U, Wagner S (2002) Numerical investigations of small-amplitude disturbances in a boundary layer impinging shock wave at ma = 4.8. Phys Fluids 14(7):2088–2101
6. Robinet J-Ch (2007) Bifurcations in shock wave / laminar boundary layer interaction: global instability approach. J Fluid Mech 578:67–94
7. Tullio N, Sandham ND (2012) Transitional shock-wave/boundary layer interaction behind a roughness element. In: Kontis K (ed) 28th International symposium on shock waves. Springer, Heidelberg, pp 439–445

Part V
TriGlobal Instabilities in Incompressible Separated Flows

The Role of Spanwise Forcing on Vortex Shedding Suppression in a Flow Past a Cylinder

G. Rocco and S. J. Sherwin

Abstract Controlling the wake vortex dynamics of bluff bodies efficiently is a fundamental problem in many applications. Earlier direct numerical simulations (Darekar and Sherwin) of three-dimensional bluff bodies demonstrated that the introduction of a spanwise waviness at both the leading and trailing surfaces suppresses the vortex shedding and reduces the amplitude of the fluctuating aerodynamic forces. Under this motivation, starting from a fully developed shedding, a sufficiently high spanwise forcing is introduced on the surface of the cylinder, in the regions where separation effects occur, resulting in the stabilisation of the near wake in a time-independent state, similar to the effect of a sinusoidal stagnation surface. Stability analysis of the linearised Navier-Stokes equations was then performed on the three-dimensional flows to investigate the role of the spanwise modulation on the absolute instability associated with the von Kármán street.

1 Introduction

Controlling vortex shedding is an important problem in many engineering applications due to the relevant amount of drag, vibrations and noise that it generates. Several techniques aimed at suppressing the von Kárman street in two-dimensional wakes, have been studied; these methods can be classified in two categories respectively: two-dimensional and three-dimensional controls. Two-dimensional controls are characterised by a constant control input in the spanwise direction; this type of control has been extensively studied and some examples are the end plate, base bleed [2, 10], splitter plates, secondary small cylinders. Three-dimensional control

G. Rocco (✉) · S. J. Sherwin
Department of Aeronautics, Imperial College London, London SW7 2AZ, UK
e-mail: g.rocco10@imperial.ac.uk

S. J. Sherwin
e-mail: s.sherwin@imperial.ac.uk

techniques present instead a variation of the actuation property in the spanwise direction; some examples are the segmented trailing edge, the wavy trailing edge, the wavy stagnation face [4], the spanwise-periodic blowing/suction [7] and a small vertical tab. A more exhaustive overview of the techniques used to control the vortex shedding, and the relative references, can be found in Choi et al. [3]. Despite the potential efficiency of 3D techniques, the physical mechanisms underlying the suppression of the vortex shedding remains poorly understood. Hwang et al. [6] presented the first explanation of the most relevant phenomena by means of the linear stability analysis. It was found that the application of a spanwise waviness to a flow past a bluff body is able to stabilise the near-wake absolute instabilities; the flow was assumed to be parallel and the Monkewitz model was used to describe the profile of the wake. However, real configurations may be strongly non-parallel and this might significantly affect the dynamics of the absolute instabilities, as the authors point out. Therefore, the complex structure of the wake associated with a bluff body subject to three-dimensional control methods leads us to a question: how do the three-dimensional modifications of the base flow affect the stabilisation of the global instabilities? In the present study the attention is focused on the suppression of the vortex shedding in a flow past a cylinder at $Re = 60$, above the onset of the vortex shedding, using two different types of spanwise forcing. The effect of the the role of spanwise modulation on the absolute instability was then investigated by computing the fully three-dimensional global mode.

2 Three-Dimensional Base Flow

The spatial discretisation of the three-dimensional Navier-Stokes equations was performed using a quasi-3D method; in the spanwise direction a Fourier spectral method was used, while a spectral/hp element method was adopted in the streamwise and transverse directions. The time-integration of the equations was performed using a stiffly stable splitting scheme [8].

The suppression of vortex-shedding was achieved by 3D distributed forcing applied to two slots, respectively at the top and bottom surface of the cylinder. The forcing is the product of two components: $F_{st}(x, y)$ and $F_{sp}(z)$, where F_{st} is a gaussian function with a standard deviation $\zeta_{st} = 0.1$, mapped on to the surface of the cylinder and centred at about 20° from the transverse direction just before the separation points of the boundary layer. Concerning the spanwise forcing F_{sp}, two different functions were applied: a sinusoidal $F_{sp}^{(1)}$ and a gaussian one $F_{sp}^{(2)}$; a schematic representation of the model is given in Fig. 1.

$$F_{st} = \exp\left[-\left(\frac{\arctan^2\left(\frac{x}{|y|}\right) + \frac{\pi}{9}}{2\zeta_{st}^2}\right)\right] \tag{1}$$

Fig. 1 Sketch of distributed forcing. Two gaussian forcing functions F_{st}, centred at $\theta = \pm 20°$ with respect to the vertical axis y, are applied in the xy plane. In-phase sinusoidal functions or gaussian functions are instead applied along the span
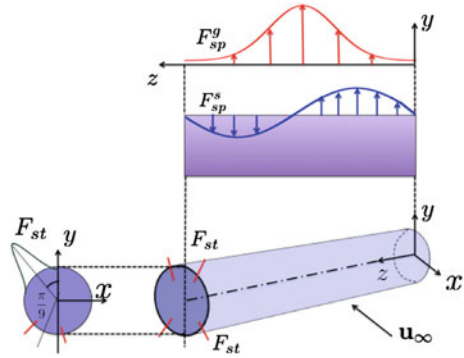
$$F_{sp}^{(1)} = \sin\left(\frac{2\pi}{\lambda_z}z\right) \tag{2}$$

$$F_{sp}^{(2)} = \exp\left[-\left(\frac{z - \frac{L_z}{2}}{2\zeta_{sp}}\right)^2\right] \tag{3}$$

Equation (1) express the streamwise forcing F_{st}, while Eq. (2) the sinusoidal $F_{sp}^{(1)}$ and gaussian $F_{sp}^{(2)}$ spanwise forcing respectively; λ_z represents the forcing wave-length, while ζ_{sp} the width of the Gaussian function. These two functions have been normalised such that the integral of the forcing over the domain is constant, so the same amount of energy is introduced into the system. The role of these two parameters has been been investigated assuming an amplitude of the forcing $A = 0.1u_\infty$, which was verified to lead to a complete stabilisation of the vortex shedding, in accordance with Kim and Choi [7]. The optimal wave-length for the sinusoidal forcing is around $\lambda_D \simeq 5$, with a drag reduction of about 20 %, resembling the studies of Darekar and Sherwin [4] and Kim and Choi [7] (Fig. 2a) . The effect of ζ_{sp} is reported instead in Fig. 2b; a decrease of the standard deviation results in a more efficient drag reduction. This behaviour is related to the increasing steepness of the gaussian function and a consequent larger amount of spanwise/transverse vorticity is introduced in the system. These additional components of the vorticity are responsible for preventing the rolling-up of the three-dimensional shear layers into the vortex street, as described by Darekar and Sherwin [4]. Figure 3 shows the temporal change of ω_x/ω_z and ω_y/ω_z in the point $(x, y, z) = (0, 0.7, 1.8)$, where z corresponds to the inflection point and y is within the shear layer. It can be seen that both these components grow in time and the gaussian forcing is generally more efficient. The sinusoidal forcing introduces in fact an amount of streamwise and transverse vorticity that is about 20 % less than the gaussian forcing. This issue is reflected in the critical value of the amplitude able to suppress the vortex shedding, which is almost double for the sinusoidal forcing ($A_{cr} = 0.23$) with respect to the gaussian forcing ($A_{cr} = 0.12$). For this reason, the following sections will only discuss the gaussian forcing.
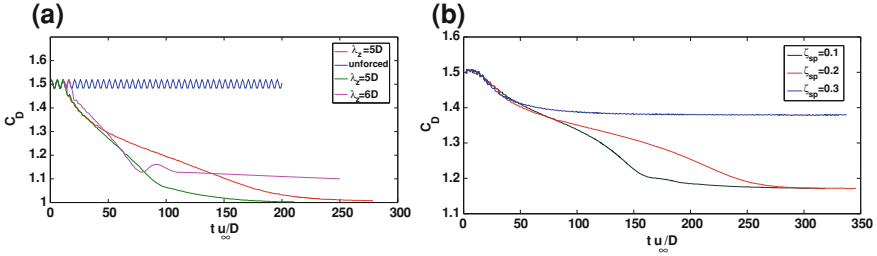
Fig. 2 Variation of the drag coefficient with the wave-length λ_D (sinusoidal forcing **a**) and the standard deviation ζ_{sp} (gaussian forcing **b**)
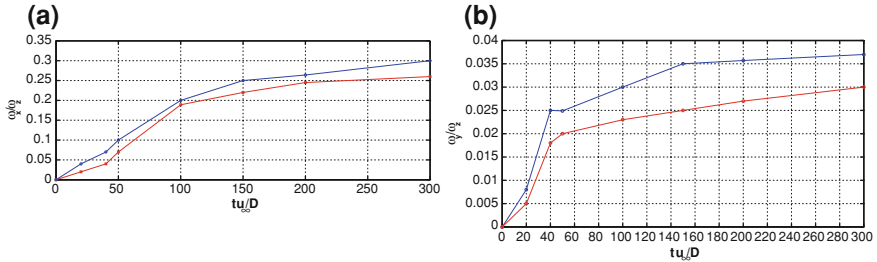
Fig. 3 Time evolution of: **a** the streamwise and **b** transverse vorticity. *Blue lines* represent the gaussian forcing, *red lines* the sinusoidal one
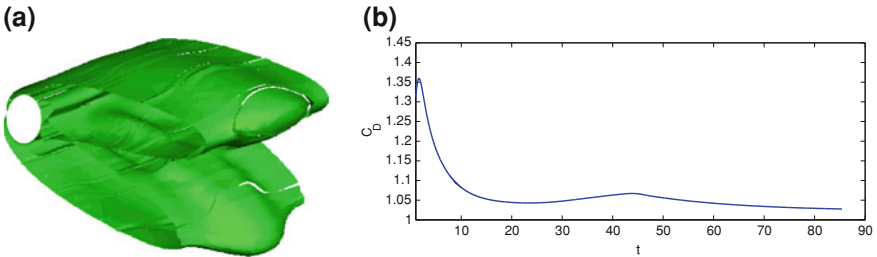
Fig. 4 **a** Wake topology at $tU_\infty/D = 100$. **b** Time evolution of the drag coefficient

In Fig. 4a the profile of the vortical structures is shown using the Q-criterion. The vortex shedding has been completely suppressed using a gaussian spanwise forcing at the critical amplitude $A = 0.12$. It can be seen that the iso-surface is symmetrical with respect to the centreline with both vertical and horizontal connection. The drag coefficient is subject to a reduction of 22 %, while the Strouhal frequency and the lift coefficients are zero, pointing out the steadiness of the near-wake (Fig. 4b).
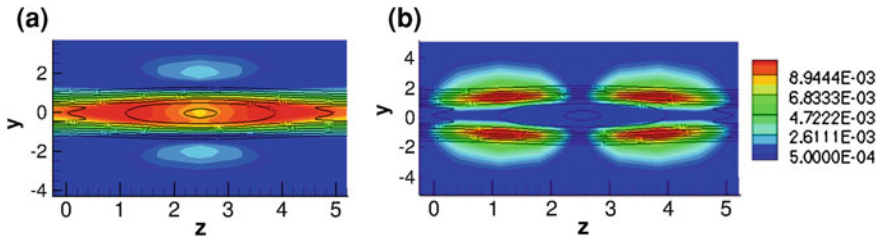
Fig. 5 **a** Transverse perturbation $|v|/|v_{max}|$. **b** Spanwise perturbation $|w|/|w_{max}|$

3 Fully Three-Dimensional Direct Stability Analysis

An insight into the mechanisms that lead to the suppression of the vortex shedding can be obtained by means of the hydrodynamic stability analysis. The distributed forcing on the surface of the cylinder has a prominent effect on the near-wake region, which was seen to be particularly sensitive to a force-velocity coupling [5]. Due to the variation of the flow in in all the spatial directions, a fully three-dimensional global stability analysis, often referred to as TriGlobal [9], is the appropriate approach to studying the dynamics of the instabilities. The stability of the problem was investigated by computing the eigenmodes of the Navier-Stokes equations linearised around the suppressed regime. An Arnoldi algorithm [1] was applied to calculate the eigenvalue and eigenvector of the system. The temporal growth rate is given by the imaginary part of the eigenvalue $\Im(\lambda_i)$, the frequency by the real part $\Re(\lambda_i)$. When the critical forcing amplitude was applied in order to stabilise the wake, the flow was found to be absolutely stable and the decay rate of order -3×10^{-4}, comparable with the value of a subcritical flow at $Re = 30$. An additional increase of the amplitude showed a further decrease of the decay rate despite the topology of the eigenmode did not change significantly. This decrease was observed to saturate when the amplitude of the forcing was about 30 % above the critical value. Figure 4 shows the profile of the eigenmode when $A = 1.3A_{cr}$ and the decay rate was found to be 3×10^{-5}. The structure of the mode is located close to the cylinder ($0.5D < x < 5D$) highlighting the crucial role of the perturbations in this region. A cross-streamwise section at $x = 1$ is considered, where the perturbations were found to be most intense. The mode is located in a relatively narrow spanwise range ($1 < z < 4$) in the region just above and below the cylinder. These regions are located at the same transverse location where the forcing was applied, where the perturbations are able to disrupt the vortex shedding. The normalised magnitude of the transverse and spanwise components of the mode have an important role in the dynamics of the transport of vorticity perturbations and their structures are reported in Fig. 5a and b. It can be seen that the transverse perturbation velocity is more intense at $y = 0$ and its intensity is more pronounced in the region where the base flow velocity is slower, in accordance with Hwang et al. [6]. The spanwise perturbation velocity is instead more intense at the

extremities of the domain ($z = L/4$ and $z = 3/4L$) and in the region just above and below the cylinder, similar to the transverse component.

4 Conclusion

The present work investigated the effect of two different types of spanwise forcing to study the effect on the suppression of the vortex shedding in a flow past a cylinder at $Re = 60$. The gaussian forcing was found to be more efficient than the sinusoidal, in accordance with previous studies. This results in a noteworthy reduction of the drag, about 20 %. Direct stability analysis allowed us to study the mechanism behind the suppression and the flow was confirmed to be absolutely stable with a decay rate similar to a flow at $Re = 30$. The eigenmode is located downstream from the cylinder, relatively close to the bluff body, up to about $5D$. The transverse component is more intense close to the axis $y = 0$ where the base flow is slower. The spanwise component is more intense at $z = L_z/4$ and $z = 3/4L_z$, following the profile of the base flow. No variation in the shape of the mode was detected using amplitudes over the critical value at this Reynolds number, although this is not necessarily expected to be valid at higher values.

References

1. Barkley D, Blackburn HM, Sherwin SJ (2008) Direct optimal growth analysis for time-stepper. Int J Numer Meth Fluids 57:1435–1458
2. Bearman PW (1967) The effect of base bleed on the flow behind a two-dimensional model with a blunt trailing edge. Aeronaut Q 18:207–224
3. Choi H, Jeon WP, Kim J (2007) Control of flow over a bluff body. Ann Rev Fluid Mech 40:113–139
4. Darekar RM, Sherwin SJ (2001) Flow past a square-section cylinder with wavy stagnation face. J Fluid Mech 426:263–295
5. Giannetti F, Luchini P (2007) Structural sensitivity of the first instability of the cylinder wake. J Fluid Mech 581:167–197
6. Hwang Y, Kim J, Choi H (2013) Stabilization of absolute instability in spanwise wavy two-dimensional wakes. J Fluid Mech 727:346–378
7. Kim J, Choi H (2005) Distributed forcing of flow over circular cylinder. Phys Fluids 17 :033103
8. Karniadakis GE, Israeli M, Orszag SA (1991) High-order splitting methods for the incompressible Navier-Stokes equations. J Comp Phys 97:414–443
9. Theofilis V (2011) Global linear Instability. Ann Rev Fluid Mech 43:319–352
10. Wood CJ (1964) The effect of base bleed on a periodic wake. J R Aeronaut Soc 68:477–482

Three-Dimensional Transition of the Flow Past a Cylinder Fitted with Helical Strakes

F. Gómez, J. Hermida, R. Gómez, V. Theofilis, B. S. Carmo and J. R. Meneghini

Abstract Helical strakes are the most employed devices to mitigate or suppress vortex-induced vibrations of circular cylinders. Although several investigations have been performed in order to predict the performance of these devices, proving its efficiency in specific configurations, little is understood regarding the physical mechanisms leading to the efficiency of these devices. Direct Numerical Simulation and three-dimensional global (TriGlobal) analysis of the flow around a cylinder fitted with helical strakes is performed at low Reynolds number in order to identify and understand more deeply the flow instabilities and physical mechanisms that mitigate and suppress the spanwise-correlated vortex-shedding.

1 Introduction

Helical strakes are surface protrusions placed as helices in the spanwise direction around the surface of cylindrical structures. The geometry of the strakes is shown in Fig. 1 and is characterized by the number of strakes n_s, the strake pitch p, the strake height h and the cylinder diameter d. These helical strakes are the devices most employed in order to affect the separation lines and separated shear layers and

F. Gómez (✉)
Department of Mechanical and Aerospace Engineering, Monash University,
Melbourne, VIC 3800, Australia
e-mail: francisco.gomez-carrasco@monash.edu

J. Hermida · R. Gómez
National Institute of Aerospace Technology INTA, Carretera de Ajalvir,
km. 4. Torrejón de Ardoz, E-28250 Madrid, Spain

V. Theofilis
School of Aeronautics, Universidad Politécnica de Madrid, Madrid, Spain

B. S. Carmo · J. R. Meneghini
Department of Mechanical Engineering NDF-POLI, University of Sao Paulo, Sao Paulo, Brazil
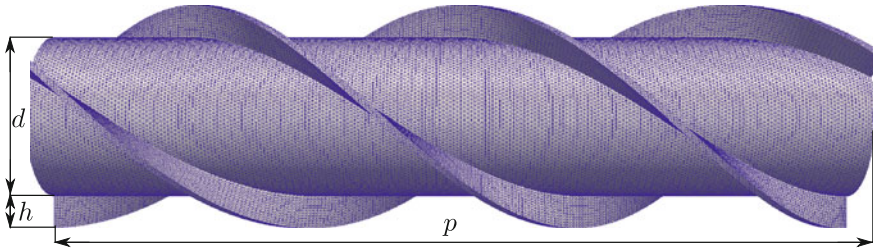
Fig. 1 Geometry and mesh of the cylinder fitted with helical strakes created by using a cylindrical mesh with helical splines. Current geometry with $n_s = 3$, $h = 0.2d$, $d = 1$ and $p = 5d$

thus mitigate or altogether suppress spanwise-correlated vortex shedding in a wide range of Reynolds numbers. Interest in these devices arises on account of the multiple applications associated with cylinder wake manipulation, especially in the context of vortex-induced vibrations (VIV) of drilling risers. In particularly, in a VIV context, strong interest exists on account of the fact that such vibrations can induce structural damages due to fatigue failures.

Several experiments have been performed in the past in order to predict the performance of helical strakes. Zdravkovich [1] was the first to present a review of the state-of-the-art in the use of different devices in the mitigation of vortex shedding, proving the efficiency of the three helical strakes (THS) configuration. Additional recent experiments showing the effectiveness of the THS in specific configurations have been carried out by Korkischko and Meneghini [2, 3], Zhou et al. [4] and references therein.

From a global instability analysis point of view, extensive research has been done for the bare cylinder case. As an example of the application of the Global (and Floquet) instability analysis, Barkley and Henderson [5] employed this theory to study the stability of the cylinder wake, successfully reporting for first time the two three-dimensional secondary instability modes existent at low Reynolds that were identified in earlier transition experiments [6]. This finding was an important breakthrough in the quest of understanding the sequence of instabilities leading to a turbulent wake. An overview of this theory may be found in the work of Theofilis [7] while Gómez et al. [8] recently presented an assessment of progresses and challenges of the theory.

However, despite the extensive studies on the bare cylinder wake, no work is known to date that deals with the effect on the strakes on the different bifurcations of the wake flow past the cylinder. Questions are open in this context:

- Is the primary instability onset the result of a local or a global bifurcation?
- Does a global mode exist with a unique frequency or are there different vortex shedding modes, operative at different locations with different shedding frequencies?

The goal of the present work is to address these open questions by performing Direct Numerical Simulation and TriGlobal stability analysis to the flow around

Fig. 2 Employed domain for
the simulation of flow past
a cylinder fitted with helical
strakes
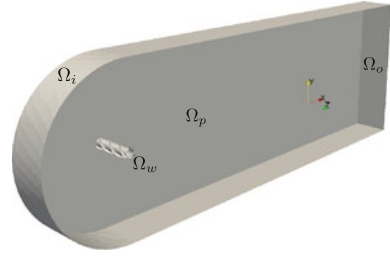
a cylinder fitted with helical strakes in order to understand more deeply the flow
instabilities and physical mechanisms identified in the literature that mitigate and
suppress the spanwise-correlated vortex shedding.

2 Problem Formulation

The flow past a cylinder fitted with helical strakes is described by the three-
dimensional and dimensionless Navier–Stokes equations of a viscous, incompress-
ible fluid with the Reynolds number defined as $Re = U_\infty d/\nu$, being U_∞ the free
stream velocity, d the cylinder diameter, ν the kinematic viscosity. As sketched in
Fig. 2, the boundary condition are inlet for boundary Ω_i, periodic boundary condi-
tions for the domain sides Ω_p, no-slip for the cylinder with strakes Ω_w and outlet
for the rear part of the domain Ω_o, that follow:

$$\begin{aligned}
\mathbf{u}(x, y, z) &= (1, 0, 0), & \frac{\partial p(x,y,z)}{\partial \mathbf{n}} &= 0 & \text{on } \Omega_i \\
\mathbf{u} &= (0, 0, 0), & \frac{\partial p(x,y,z)}{\partial \mathbf{n}} &= 0 & \text{on } \Omega_w \\
\mathbf{u}(x, y, 0) &= \mathbf{u}(x, y, 5), & p(x, y, 0) &= p(x, y, 5) & \text{on } \Omega_p \\
\frac{\partial \mathbf{u}}{\partial \mathbf{n}} &= 0, & p(x, y, z) &= 0 & \text{on } \Omega_o.
\end{aligned}$$

A grid refinement study based on a generalized Richardson extrapolation method
[9] has been employed and the Direct Numerical Simulation have been performed
using the transient incompressible solver of the Navier–Stokes equations of the open-
source finite-volume code OpenFOAM. This solver employs a PISO [10] (Pressure
Implicit with Splitting of Operators) velocity-pressure coupling approach to solve
the Navier–Stokes equations. A GAMG (Geometric Algebraic Multi Grid) iterative
method is used for the solution of the pressure equation while the momentum equa-
tions are solved using a preconditioned bi-conjugate gradient. Linear interpolation
is used for the volume flux calculations and the equations are advanced in time using
a Crank-Nicolson scheme.

Attention needs to be be paid to the efficient solution of the global instabil-
ity eigenvalue problem. Because of the three dimensional nature of the helical
strakes no homogeneous spatial directions exist and, hence, no assumptions can
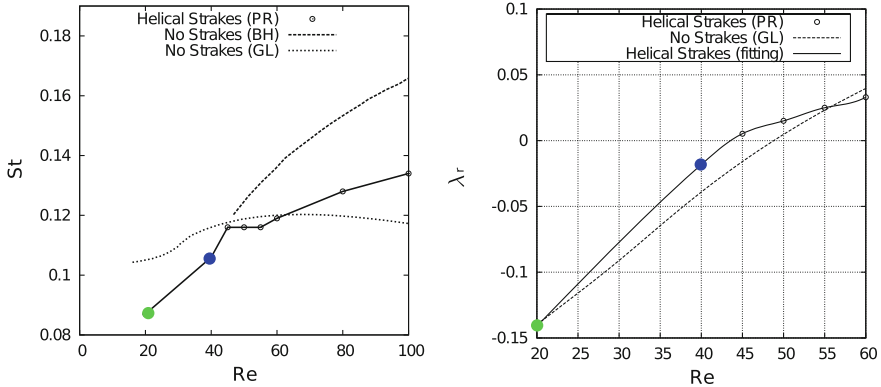
Fig. 3 (*left*) Comparison of *St* number between the straked cylinder and the bare cylinder. (*right*) Comparison of λ damping/growth ratio between the straked cylinder and the bare cylinder. (PR) Present results (BH) Barkley and Henderson [5] (GL) Giannetti and Luchini [12]. *Green circle $Re = 20$ $\lambda = -0.14$, $St = 0.087$. Blue circle $Re = 40$ $\lambda = -0.017$, $St = 0.105$*

be made on the shape of the eigenfunctions and a rather challenging TriGlobal eigenvalue problem must be solved. The stability analysis in the present work is carried out using a Jacobian-free Newton–Krylov time-stepping algorithm in order to deal with the massive computational requirements of the TriGlobal problem in an efficient way. Details about the complete stability analysis method can be found in Gómez et al. [11].

3 Results

Complete fully three-dimensional time-resolved Direct Numerical Simulations have been performed from $Re = 20$ to $Re = 100$ employing the solver described in the previous section. Comparisons have been made against the flow of a bare cylinder with the same pitch $p = 5d$ as the straked cylinder. In order to extract the flow features from the Direct Numerical Simulation results, an implementation of the nonlinear least-squares (NLLS) Marquardt-Levenberg algorithm in conjunction with the residual algorithm developed by Theofilis [7] has been used. This least-squares fitting permits the identification of the linear regime of the growth of the leading eigenmodes before the corresponding linear saturation.

Figure 3 (*left*) shows the results of this fitting for the *St* number from $Re = 20$ to $Re = 100$ and its comparison with the bare cylinder based on the results of Barkley and Henderson [5] and Giannetti and Luchini [12]. The discrepancy of the bare cylinder results beyond the bifurcation at $Re = 47$ is explained by the different analysis carried out by the authors. Giannetti and Luchini provide the *St* of a unstable steady state solution while Barkley and Henderson [5] provide the *St* of the saturated
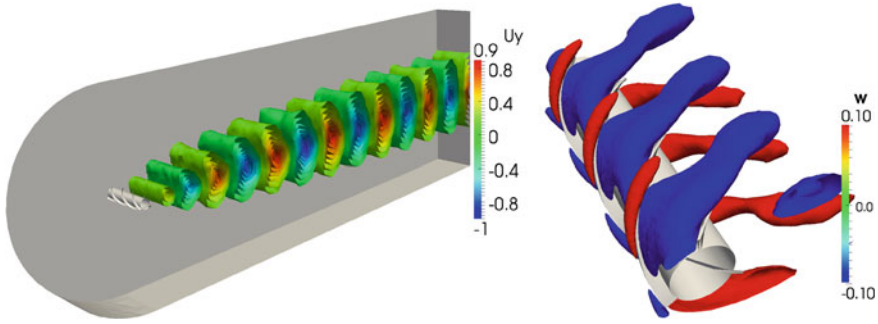
Fig. 4 *Left* $y-$velocity component of the leading (damped) eigenmode of the straked cylinder at Reynolds number $Re = 40$. *Right* isosurfaces of spanwise velocity $w = \pm 0.1$ at $Re = 100$

base flow. Analogously, the present results for the straked cylinder are those of the stable steady or periodic base flow. Three different zones can be inferred from Fig. 3: a large slope until $Re \sim 40$, a band with constant $St = 0.116$ until $Re \sim 55$ and a slow increase in St number beyond $Re \sim 55$. Figure 3 (*right*) shows the comparison of λ damping/growth ratio between the straked cylinder and the bare cylinder. It can be seen that the leading eigenmode of the straked cylinder flow crosses the real axis at $Re_1 \sim 43$ which is a smaller critical Re than that of the flow around a cylinder without strakes. Beyond this Re_1 the leading eigenmode grows and saturates the flow into an oscillatory flow with $St = 0.116$ as the Direct Numerical Simulation results show.

In order to understand more deeply this first bifurcation of the flow, a Global Stability Analysis have been carried out at $Re = 20$ and $Re = 40$. A Krylov subspace dimension $m = 20$ and an integration time of $\tau = 10$ have been required to accurately capture the first eigenmode. The eigenvalues associated with the leading global modes of the flow recovered with the present methodology are represented in Fig. 3 by a green circle and a blue circle respectively. Figure 4 (*left*) shows the real part of the $y-$velocity component eigenfunction of the leading (damped) global eigenmode of the straked cylinder at $Re = 40$, which corresponds to a complex eigenvalue with a damping ratio of $\lambda = 0.017$ and a Strouhal number $St = 0.105$, which are in perfect agreement with the results from the Direct Numerical Simulations This eigenfunction is similar to the classic Von Kármán vortex street, however it is completely three-dimensional, as vortex shed from the upper part and bottom part of the cylinder have spanwise velocity component in opposite directions. Because of the existence of this global mode, it is stated that the flow undergoes a Hopf bifurcation and no local shedding is produced. Figure 4 (*right*) shows the isosurface of spanwise velocity with a magnitude 10 % of the free-stream velocity at $Re = 100$ in order to present this three-dimensionality more clearly. The three-dimensional effects induced by the strakes vanish at a distance $x \sim 3d$ because of the high dissipation at this Reynolds number.

4 Conclusions

An analysis of the dynamics of the wake of a cylinder fitted with helical strakes has been carried out by means of Direct Numerical Simulation and TriGlobal instability analysis. It has been found that the first bifurcation of the flow past a straked cylinder is of Hopf type and occurs at $Re \sim 43$. The flow becomes periodic in a similar fashion to the Von Karman street but with a three-dimensional wake in which consecutive vortex are shed with opposite spanwise velocity.

References

1. Zdravkovich M (1981) Review and classification of various aerodynamic and hydrodinamic means for suppressing vortex shedding. J Wind Eng Ind Aerodyn 7:145–189
2. Korkischko I, Meneghini J (2010) Experimental investigation of flow-induced vibration on isolated and tandem circular cylinders fitted with strakes. J Fluids Struct 26(4):611–625
3. Korskischko I, Meneghini J (2011) Volumetric reconstruction of the mean flow around circular cylinder fitted with strakes. Exp Fluids 51:1109–1122
4. Zhou T, Razali S, Hao Z, Cheng L (2011) On the study of vortex-induced vibration of a cylinder with helical strakes. J Fluids Struct 27:903–917
5. Barkley D, Henderson RD (1996) Three-dimensional Floquet stability analysis of the wake of a circular cylinder. J Fluid Mech 322:215
6. Williamsom C (1996) Vortex dynamics in the cylinder wake. Ann Rev Fluid Mech 28:477
7. Theofilis V (2011) Global linear instability. Ann Rev Fluid Mech 43:319–352
8. Gómez F, LeClainche S, Paredes P, Hermanns M, Theofilis V (2012) Global linear instability at the dawn of its fourth decade: recent progress and remaining challenges. AIAA J 50(12):2731–2743
9. Roache P (1994) Perspective: a method for uniform reporting of grid refinement studies. J Fluids Eng 116:405
10. Ferziger J, Peric M (2001) Computational methods for fluid dynamics. Springer, Berlin
11. Gomez F, Gomez R, Theofilis V (2013) On three-dimensional global linear instability analysis of flows with standard aerodynamics codes. Aerosp Sci Technol 32(1):223–234
12. Giannetti F, Luchini P (2007) Structural sensitivity of the first instability of the cylinder wake. J Fluid Mech 581:167

Comparison Between the Koopman Modes for the Flow Around Circular Cylinder and Circular Cylinder Fitted with Helical Strakes

Cesar M. Freire, Julio R. Meneghini, Rafael S. Gioria and Gustavo R. S. Assi

Abstract The helical strake is a device commonly employed for vortex-induced vibration attenuation or suppression. It works by changing and affecting the flow patterns around a circular cylinder and, thereby, reducing the interaction of the shear layers formed in this massive separated type of flow. In this paper the wake of vortices generated by a bare circular cylinder is compared to the wake generated by a circular cylinder fitted with helical strake with pitch equal to ten cylinder diameters and height equal to 0.2 of the cylinder diameter. Besides the analysis of the measured velocity field, a Koopman decomposition is made and the most energetic modes obtained for each condition are compared. The Reynolds number for the visualizations is Re = 10,000.

1 Introduction

The vortex-induced vibration phenomenon (VIV) can be found in several engineering applications. In most of them, the cyclic loads caused by the vortex shedding accumulate fatigue damage, reducing the lifespan of the structure undergoing VIV. The oscillations observed due to the vortex shedding process amplify the drag and lift coefficients when comparing to same parameters measured for fixed cylinders,

C. M. Freire (✉) · J. R. Meneghini · R. S. Gioria · G. R. S. Assi
Fluid Dynamics Research Group (NDF), Escola Politécnica, University of São Paulo
(EPUSP), São Paulo, Brazil
e-mail: cmfreire87@gmail.com

J. R. Meneghini
e-mail: jmeneg@usp.br

R. S. Gioria
e-mail: rafaelgioria@usp.br

G. R. S. Assi
e-mail: g.assi@usp.br

but even when VIV is not occurring, structures submitted to vortex shedding are accumulating fatigue damage.

In order to suppress the vortex formation and shedding, and then VIV, different techniques can be used. Those techniques can be classified as passive, active or mixed, depending on the energy requirements for its operation. Helical strakes appear in the group of the passive techniques. This kind of suppressor consists of a group of helical protrusions, usually three, which affect the flow past the cylinder. The use of helical strakes makes it more difficult for the shear layers to interact, weakens the generated vortices and also enhances three-dimensionalities to the flow, disrupting the spanwise correlation.

In the present study the wake of vortices generated by a bare circular cylinder and a cylinder fitted with helical strakes are compared from the point of view of flow decomposition techniques. The comparison is made using the streamwise u and cross-flow v velocity fields acquired with particle image velocimetry (PIV) in the region behind the fixed cylinders. The decomposition technique employed is the Dynamic Mode Decomposition (DMD), proposed by [5]. According to [4], the DMD numerical procedure provides an approximation to the Koopman modes.

Given the expected periodicity of the flow under analysis, as the current velocity is kept constant and the bluff bodies used to generate the vortices wakes are fixed, Fourier Decomposition could also have been applied. However, the DMD method is additionally capable of handling transiency, and was therefore chosen. Proper ortogonal decomposition (POD) was not chosen because we are interested in modes classified by their frequencies. A comprehensive review about flow decomposition techniques is presented by [3].

2 Experimental Procedure

The flow visualizations presented in this work were conducted in the water channel facility of the Fluid and Dynamics Research Group (NDF) at the University of São Paulo. The water channel has a 0.7 m wide, 0.8 m deep and 7.5 m long test section and can operate with low turbulence level (lower than 2 %) up to 1 m/s. The walls and floor of the water channel are made of glass in order to allow flow visualizations.

The flow was seeded with polyamide particles with average diameter of 11 µm. These particles were illuminated by a (Quantel Twins) double-cavity pulsed Nd:YAG laser with wavelength of 532 nm. Two Imager Pro X 2 Megapixel cameras with two Nikon (AF Nikkor f/1.4D) lenses of 50 mm focal length were used to record 345 pairs of snapshots with acquisition frequency of 14.8 Hz.

The cylinders were made of acrylic and have 32 mm of external diameter D. The straked cylinder was constructed by attaching three rigid rubber tapes in a helical pattern around an acrylic cylinder, as described in [2]. The helical strake geometry used in this work has height equal to 0.20 D and pitch 10 D. This geometry was selected because it suppresses VIV in isolated cylinders, as shown in [2]. Both bare

Fig. 1 For each value of $N_{\text{snapshots}}$ a different ϕ_m (last vector of the series) and r were obtained. The convergence criteria was adopted to be the ratio between the norms of r and ϕ_m, as presented in Fig. 1. As it can be seen in this plot, despite minor oscillations in $||r||/||\phi_m||$, the relative error decreases when $N_{\text{snapshots}}$ is increased thus all snapshots were used
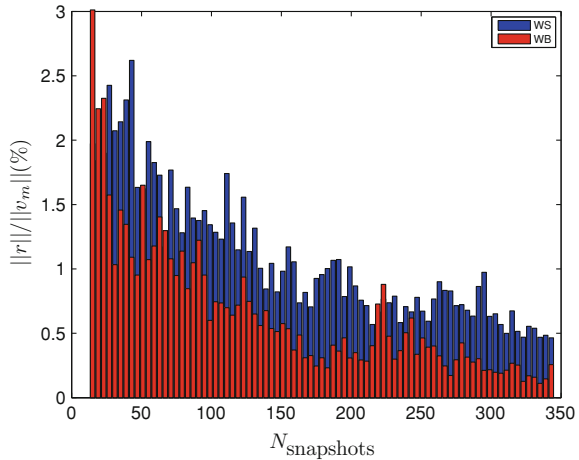
and straked cylinders were painted with black matte dye in order to diminish the influence of the laser beams reflection in the images recording.

The flow around both the fixed bare and straked cylinder were recorded for Reynolds number Re = 10,000.

For the visualizations, the cylinders were mounted vertically and fixed by their upper extremity. The lower tip touches the water channel floor. The water level L_w used in the experiments were 700 mm, so the aspect ratio was above $L_w/D = 21$. The illuminated plane was placed in the middle of the test section which is 350 mm above the water channel floor. For the cylinder fitted with strakes, the selected plane was one of the helical strakes aligned to the flow direction, as illustrated in Fig. 3e, f. It is important to highlight that the flows are expected to present significant three-dimensionalities and the study of different planes would bring additional information about the flow. In this first paper the authors focused the analysis in the major differences between the two compared wakes and, for brevity, only one plane was presented.

3 Wake Comparisons

The numerical procedure employed to obtain the DMD modes, as an approximation for the Koopman modes, follows [4, 5]. The formulation is not described in this paper for brevity. The DMD results on modes ψ_k with an associate eigenvalue λ_k. Both the streamwise u and cross flow v velocity fields, measured by PIV, were combined in a single velocity field $\phi = \{u; v\}$ which was used in the decomposition.

A convergence analysis, presented in Fig. 1, was conducted by measuring the norm of the residue vector $||r||$ (Eq. 1). Due to the camera storage limitation, for each PIV acquisition a sequence of 345 snapshots was recorded. The acquisition

(a)

(b)
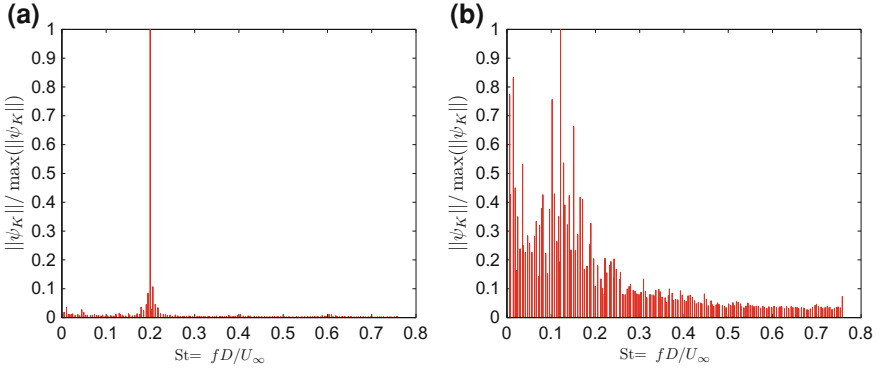
Fig. 2 Normalized norm of each mode plotted against the non-dimensional frequency. (**a**) WB, (**b**) WS

frequency was 14.8 Hz. For the bare cylinder the vortex shedding frequency, considering the vortex shedding was close to 2 Hz, so each cycle is represented by 7 snapshots approximately. The main goal of this convergence analysis was to quantify the residue norm and to verify how many snapshots $N_{\text{snapshots}}$ would be necessary to best characterize the flow.

$$r = \phi_m - \sum_{n=1}^{N_{\text{snapshots}}-1} c_n \phi_n. \tag{1}$$

The wake of vortices generated by the flow past a fixed and bare circular cylinder will be treated as the Wake of the Bare cylinder, or simply WB. The wake of vortices generated by the flow past the fixed cylinder fitted with strakes will be named as the Wake behind the Straked cylinder, or just WS.

Figure 2 compares the energy profile for each wake. The jth mode energy was quantified by the norm eigenvector $||\psi_j||$ and then normalized by the most energetic oscillatory mode $||\psi_2||$. The most energetic mode ($||\psi_1||$) represents, for both the presented wakes, the mean velocity field and have energy levels orders of magnitude higher then the oscillating modes. As the purpose of this paper was to compare the flow fluctuations and not its mean value, the mean fields were not considered in the analysis and the second mode was used as a reference to normalize the energy leves.

For the WB, Fig. 2a depicts a dominant mode with St = 0.2. In contrast to this dominant behavior, Fig. 2b does not present just one dominant peak, but a group of modes with similar energy levels.

The real and imaginary parts of the eigenvalues λ_j found for both wakes are depicted in Fig. 3a, d. Both wakes have their most energetic mode, represented by a blue dot, lying on real axis. Those modes are the mean velocity field for each wake. The second and third most energetic modes are represented by red dots. It is important to keep in mind that the second and the third modes have the same
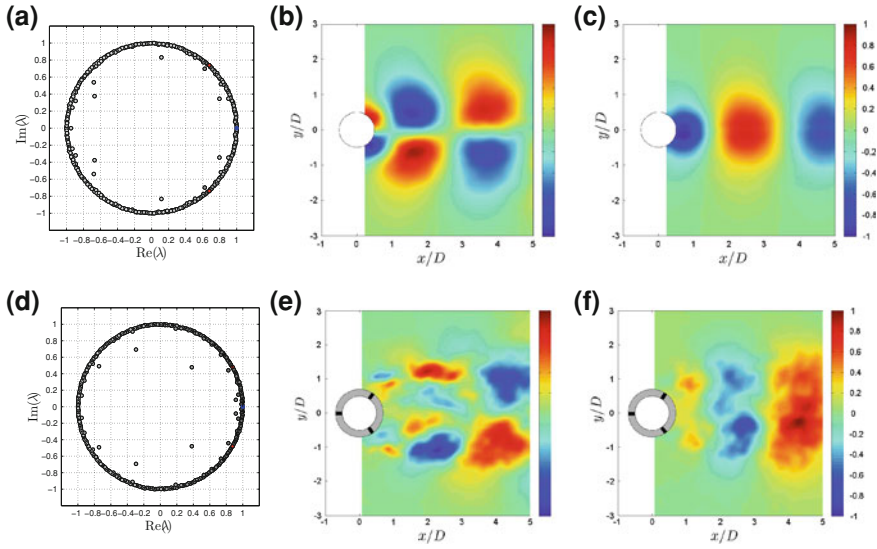
Fig. 3 Real and imaginary part of λ_j (**a**) and (**d**). Real part of the most energetic periodic mode for the in-line direction (**b**) and (**e**). Real part of the most energetic periodic mode for the transverse direction (**c**) and (**f**). First row stands for WB and second row for WS

norm, since the third mode is the complex conjugate of the second mode. The grey dots represent the other modes. The color indicates the norm of each mode divided by the norm of the second most energetic mode. Darker dots represent modes with more energy. For the WB the most energetic modes lie close to the red dot, whilst for the WS there is no concentration and the most energetic modes are scattered in the unity circle. Both unity circles depicted in Fig. 3a, d have inner points. As this is an experimental study, the analyzed fields include turbulent velocity deviations and experimental errors. Since both effects are not part of any mode, they appear as spurious modes. In contrast to the dominant modes, during the convergence analysis presented previously, it could be seen that these inner points depend on $N_{\text{snapshots}}$. Nevertheless, the number of snapshots taken is sufficient to identify the most energetic modes and their frequencies, accomplishing the purpose of this study.

Figure 3b, c illustrate the real part of the in-line and transverse components of the velocity field for non-constant most energetic mode in WB and Fig. 3e, f show the real part of the in-line and transverse components of the velocity field for WS. Comparing the in-line and transverse components of each mode, one can see that while WB presents a smoother topography, WS presents irregularities.

4 Conclusions

Using the Koopman/DMD decomposition, two different wake of vortices were compared. More than a simple visual comparison of different velocity fields measured by PIV, the decomposition allowed a more comprehensive comparison taking into account the energy distribution and also the topology of the most energetic modes obtained from a group of more than three hundred snapshots. This technique can cope with experimental uncertainties and turbulence effects.

The wake formed behind the fixed and bare cylinder presented a very strong and dominant mode for Strouhal number St = 0.2. On the other hand, no dominant mode was found in the wake generated in the flow past the fixed cylinder fitted with strakes. For this second kind of wake, several different modes with similar energy levels and with close frequencies were found. As the modes found for WS have non-correlated frequencies and similar energy levels they may sometimes interact constructively and sometimes destructively during each cycle leading the fluid system to a non-periodic behavior.

An improvement of the analysis conducted in this paper could be achieved employing the optimized DMD, proposed by [1]. This optimized decomposition could help to grouping some of the multiple modes found in the WS and highlight the existence dominant modes. As this is an ongoing research, this result is expected for a future work.

References

1. Duke D, Soria J, Honnery D (2012) An error analysis of the dynamic mode decomposition. Exp Fluids 52:529–542
2. Korkischko I, Meneghini JR (2010) Experimental investigation of flow-induced vibration on isolated and tandem circular cylindes fitted with strakes. J Fluid Struct 26:611–625
3. Mezic I (2013) Analysis of fluid flows via spectral properties of the Koopman operator. Ann Rev Fluid Mech 45:357–378
4. Rowley CW, Mezic I, Bagheri S, Schlatter P, Henningson DS (2009) Spectral analysis of non-linear flows. J Fluid Mech 641:115–127
5. Schmid PJ (2010) Dynamic mode decomposition of numerical and experimental data. J Fluid Mech 656:5–28

Influence of the Shape
on the Roughness-Induced Transition

J.-Ch. Loiseau, S. Cherubini, J.-Ch. Robinet and E. Leriche

Abstract Global instability analysis of the three-dimensional flow past two roughness elements of different shape, namely a cylinder and a bump, is presented. In both cases, the eigenspectrum is made of modes characterised by a varicose symmetry and localised mostly in the zones of large base flow shear. The primary instability exhibited is the same in both cases and consists in an isolated unstable mode probably related to streaks instability. For the cylinder however, a whole branch of modes is in addition destabilised as the Reynolds number is further increased.

1 Introduction

Delaying transition in spatially developing boundary layer flows has been a long time challenge. For small amplitude disturbances and supercritical Reynolds numbers, the linear stability theory predicts the slow transition process due to the generation, amplification and secondary instability of Tollmien-Schlichting (TS) waves. It has been shown recently in Ref. [1] that those TS waves can be stabilised by streamwise streaks. In this experimental work, sub-optimal streaks have been created using a periodic array of cylindrical roughness elements. Despite the stabilising effect of the streaks on the TS waves, the flow may undergo transition to turbulence right downstream the roughness elements provided the streaks are strong enough. This roughness-induced transition has been extensively investigated experimentally by different authors [2–4]. For cylindrical roughness elements, in the early 60's, most of the results available back then have been reviewed in Ref. [5] into one transition

J.-Ch. Loiseau (✉) · S. Cherubini · J.-Ch. Robinet
Laboratoire DynFluid, Arts et Métiers ParisTech, 151, Bd. de l'Hopital, 75013 Paris, France
e-mail: loiseau.jc@gmail.com

E. Leriche
Laboratoire de Mécanique de Lille, Université Lille-1, Boulevard Paul Langevin,
59655 Villeneuve d'Ascq, France

diagram, thus giving an empirical criterion for transition. However, fewer studies have been carried out on smooth roughness elements, and the influence of the shape of the roughness on the destabilisation process has not yet been investigated in detail. Though the mechanism responsible for transition to turbulence in the flow past a 3D roughness element is not yet fully understood, it is believed that it is due to an instability of the streaks induced by the roughness elements. Thus, in order to investigate the origin of unsteadiness, a global instability analysis of the three-dimensional flow past a sharp-edged and a smooth roughness element is performed.

2 Problem Formulation

The aim of the present work is to investigate the influence of the shape of the rough-ness element on the streaks generation further downstream along with their possible global instability. Two different kinds of roughness elements having aspect ratio $d/k = 2$ (where d is the diameter and k is the maximum height of the roughness), both mounted on a flat plate, have thus been considered: a cylindrical roughness ele-ment, and a smoother one defined by a cubic cosine function, $h(r) = k \cos^3(\pi r/d)$, r being the distance from the centre of the bump on the $x - z$ plane.

The flow past these roughness elements is studied using the 3D incompressible Navier-Stokes (NS) equations, non-dimensionalised with respect to the maximum height k of the roughness and the free-stream velocity U_∞; therefore, the Reynolds number is defined as $Re = U_\infty k/\nu$, ν being the kinematic viscosity. The compu-tational domain extends from $x = -15$ to $x = 90$ in the streamwise direction, has a spanwise extent of $L_z = 16$ and wall-normal dimension $L_y = 50$ such that the global stability results are almost independent of the domain size. The Blasius veloc-ity profile prescribed at the inlet ($x = -15$) is chosen such that, in the absence of the roughness element, one would have a theoretical Blasius boundary layer thickness of $\delta_{99} = 2$ at $x = 0$, i.e. the location of the roughness element.

The behaviour of an infinitesimal perturbation $\mathbf{q} = (\mathbf{u}, p)^T$ superposed to a 3D steady state $\mathbf{Q} = (\mathbf{U}, P)^T$ has been studied using a global stability analysis. The steady base flows have been computed using the selective frequency damping (SFD) approach introduced in Ref. [6]. The following boundary conditions have been applied: at the inlet, the Blasius boundary layer velocity profile is imposed for the streamwise and wall-normal components of the velocity, whereas its spanwise component is set to zero. At the outlet, a standard outflow boundary condition is used. In the spanwise direction, periodic boundary conditions are imposed for the three components of the velocity. At the upper boundary, the streamwise component has been set equal to U_∞, and a Neumann condition on the wall-normal direction has been imposed for the wall-normal and spanwise components of the velocity. Finally, a no-slip condition is imposed on the flat plate and the roughness element's walls.

Once the base flow has been computed, the NS equations are linearised around such a steady state, leading to a problem of the following type:

$$\frac{\partial \mathbf{u}}{\partial t} = A\mathbf{u},\tag{1}$$

which is subject to the same boundary conditions as previously except regarding the inflow and the upper boundaries where a zero-velocity condition is prescribed. To perform a global stability analysis, one has to compute the eigenvalues of the Jacobian matrix A, which is a hard computational task due to the large number of degrees of freedom involved. Thus, a time-stepper approach as introduced in Refs. [7, 8] has been used, which avoids the explicit storage of A and direct computation of its eigenvalues.

All of the calculations were performed using the code Nek5000 [9]. Spatial discretisation is done by a spectral elements method with Legendre polynomials of order $N = 8$. The convective terms are advanced in time using an extrapolation of order 3, whereas the viscous terms use a backward differentiation of order 3 as well.

3 Results and Discussion

Figure 1 shows base flows obtained at $Re = 1,000$ for both roughness elements considered. An upstream and a downstream reversed flow region are shown in the right frames of Fig. 1 by the $U = 0$ isosurface (blue). In the left frames, the streaks induced by the roughness elements, being defined as the deviation of the base flows from the Blasius velocity profile U_B as in Ref. [4], are plotted. These flows share similar features: five streaks can be observed, two positive (red) and three negative (green) ones. These are induced by the presence of strong horseshoe vortices wrapped around the roughness elements, whose legs transport the low and high-momentum flow upwards and downwards in the boundary layer. These counter-rotating vortices induce the two outer pairs of streaks, whereas the central low-speed one is due to the streamwise velocity deficit induced by the roughness element.

Though their main structure is similar, some differences are found between the two flow fields. Indeed, for the case of the bump: (i) the separation zone is smaller than for the cylinder; (ii) the horseshoe vortex wrapping around the roughness element is much more spanwise-localised, its legs being weaker and closer one to the other; (iii) the streaks are weaker and quickly fade away downstream of the roughness element, whereas for the cylinder they appear to sustain on a much longer streamwise extent.

The eigenspectra obtained for the cylinder case at $Re = 800$ and $Re = 1,000$ are provided in Fig. 2a, b, respectively. At $Re = 800$, one can observe a single isolated eigenvalue lying almost on the neutral axis. Slightly increasing the Reynolds number drives the most unstable mode to move towards the upper-half complex plane, so that the flow becomes globally unstable at $Re_{cr} \approx 805$. Further increasing the Reynolds number yields a whole branch of eigenvalues to move in the upper-half complex plane, as shown in Fig. 2b for $Re = 1,000$.

Regarding the bump, a similar behaviour has been found. Figure 2c shows the eigenspectrum obtained for $Re = 800$. As previously, a single isolated mode
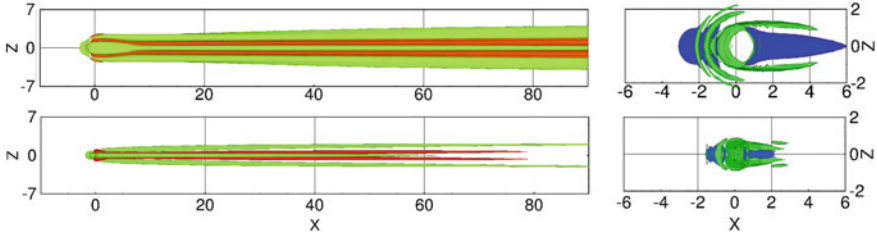
Fig. 1 Base flows computed at $Re = 1,000$ in the presence of a cylinder (*top*) and a bump (*bottom*). The *left frames* show positive (*red*) and negative (*green*) surfaces of $U_{st} = U - U_B$, with $U_{st} = \pm 0.1$ (*top*) and $U_{st} = \pm 0.05$ (*bottom*); the *right frames* show isosurfaces of the $U = 0$ contour (*blue*), highlighting the separation zone, and the Q-criterion (*green*, for $Q = 0.1$)
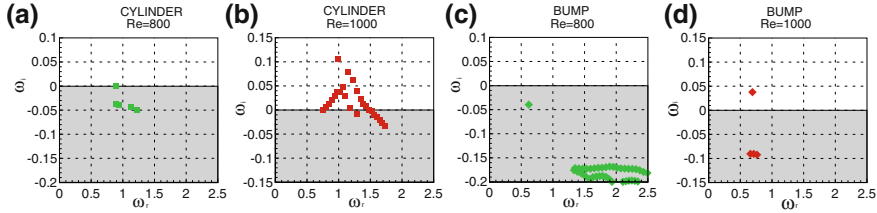
Fig. 2 Eigenspectra obtained for the flow past a cylinder with $Re = 800$ (**a**) and $Re = 1,000$ (**b**), and for the flow past a bump with $Re = 800$ (**c**) and $Re = 1,000$ (**d**)

is observed within the lower-half complex plane. When the Reynolds number is increased this eigenvalue moves upwards, reaching the upper-half of the complex plane at $Re_{cr} \approx 891$ as shown on Fig. 2d.

As to get some insights on the instability mechanisms, the shape of the two unstable global modes is closely looked at. Figure 3 provides the streamwise component of the velocity for the most unstable eigenmode obtained at $Re = 1,000$ for the cylinder case (left) and the bump one (right). These global modes are both characterised by streamwise alternated patches of positive/negative velocity developing mostly along the central low-speed streak, showing a symmetry with respect to the $z = 0$ plane. For the cylindrical element, the wave packet is placed well downstream of the roughness element, in a region where the streaks are well-developed and quasi-parallel. On the other hand, in the bump case, the most unstable eigenmode is placed closer to the roughness element which is concordant with the weaker streaks and gradients induced by the bump as well as their smaller streamwise extent.

The location and structure of the spatial support of the most unstable modes with respect to the base flow streaks at $Re = 1,000$ are shown in Fig. 4a, b for both cases, respectively. For the cylinder case, the streamwise velocity contours of the eigenvector (shaded contours) and of the base flow (solid lines) are provided in the $x = 25$ plane. The strong deformation of the $U = const$ contours indicates the large amplitude of the streaks. The zones of maximum amplitude of the eigenvector are localised on the flanks and the top of the streaks, where the spanwise and wall-normal

Fig. 3 Streamwise velocity component of the most unstable mode obtained at $Re = 1,000$ for the cylindrical roughness element (**a**) and the smooth one (**b**)
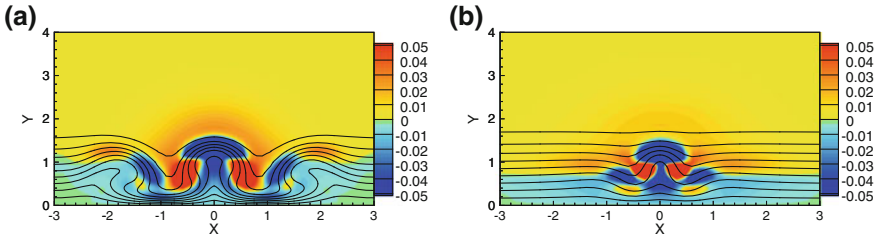
Fig. 4 Shaded contours of the streamwise component of the most unstable mode for the cylindrical roughness element in the plane $x = 25$ (**a**) and the cubic-cosine-shaped one at $x = 15$ (**b**) with $Re = 1,000$. The solid lines are the base-flow streamwise velocity contours in the range [0.1, 0.9]

shears are the largest. A similar behaviour is observed for the bump case, as shown in Fig. 4b. As indicated by the deformation of the $U = const$ contours in the $x = 15$ plane, the streaks are weaker and much more localised in the spanwise direction. The spatial structure of the eigenvector is similar to the one recovered for the cylinder, showing a mushroom-shaped disturbance on top of the central low-speed streak, with maximum velocity values located in the zones of maximum base-flow shear. However, the spatial support of the mode is much more compact in the spanwise direction.

These locations seem to indicate that these unstable global modes might be linked to a streak instability similar to the one recovered for parallel optimal streaks in Ref. [10] and that the instability mechanism might be related to the transport of the base flow shear by the perturbation. It is noteworthy that, for parallel streaks, the primary instability is of sinuous type, whereas in the present case it is of varicose type. However, one must note that for thinner roughness elements (not presented here) similar sinuous instabilities have also been recovered. The present results also confirm that, for large roughness elements, varicose perturbations are the most dangerous ones, as also highlighted by a global transient growth analysis in Ref. [11].

4 Conclusion

The flows past two roughness elements, a cylindrical and a cubic-cosine one, have been investigated. The cylindrical roughness element induces strong streaks which appear to be well sustained in the streamwise direction, whereas in the bump case

the streaks are weaker and eventually fade away. In both cases, a global stability analysis of the three-dimensional steady base flow has been carried out. In all of the cases considered, the spectra are composed by modes characterised by a varicose symmetry, mostly localised in the zones of large base flow shear and related to an instability of the quasi-parallel streaks. Finally, the critical Reynolds number being higher for the smooth bump than for the cylindrical roughness element might be related to the weaker amplitude of the induced streaks in the former case.

References

1. Fransson JHM, Talamelli A, Brandt L, Cossu C (2006) Delaying transition to turbulence by a passive mechanism. Phys Rev Lett 96(6):064501
2. Tani I, Komoda H, Komatsu Y, Iuchi M (1962) Boundary-layer transition by isolated roughness. Technical report, p 375.
3. White EB (2002) Transient growth of stationary disturbances in a flat plate boundary layer. Phys Fluids 14(12):4429
4. Choudhari M, Fischer P (2005) Roughness-induced transient growth. In: 35th AIAA fluid dynamics conference and exhibit, Toronto, Ontario Canada, AIAA-2005-4765.
5. von Doenhoff AE (1961) The effect of distributed surface roughness on laminar flow and flow control. Pergamon Press, NY Lachmann edition
6. Akervik E, Brandt L, Henningson DS, Hoepffner J, Marxen O, Schlatter P (2006) Steady solutions of the Navier-Stokes equations by selective frequency damping. Phys Fluids 18:068102
7. Edwards W, Tuckerman L, Friesner R, Sorensen D (1994) Krylov methods for the incompressible Navier-Stokes equations. J Comput Phys 110(1):82–102
8. Bagheri S, Akervik E, Brandt L, Henningson DS (2009) Matrix-Free methods for the stability and control of boundary layer. AIAA J 47(5):1057–1068
9. Fischer PF, Lottes JW, Kerkemeier SG (2008) Nek5000 Web page. http://nek5000.mcs.anl.gov
10. Andersson P, Brandt L, Bottaro A, Henningson DS (2001) On the breakdown of boundary layer streaks. J Fluid Mech 428:29–60
11. Cherubini S, De Tullio M, De Palma P, Pascazio G (2013) Transient growth in the flow past a three-dimensional smooth roughness element. J Fluid Mech 724:642–670

Part VI
Axisymmetric Separated Flows and Their Control

Tomo-PIV Measurements of Flow Around A Slender Body at High Angles of Attack

S. Alzahrani, S. Hafez, K. A. Juhany and I. M. AlQadi

Abstract Detailed measurements and analysis of temporal and spatial scales inherent in the unsteady asymmetric wake vortex flow generated by a slender axisymmetric body at high angle of attack are performed. Tomographic Particle Image Velocimetry measurements are carried out at 40° angle of attack and Reynolds number ranges from 1.0×10^4 to 4.5×10^4. Results show the presence of two main asymmetric counter rotating vortices. The Reynolds numbers affect the configuration of these vortices where vortex flipping occurred at the lowest Reynolds number investigated. Time-averaged vorticity contours and instantaneous streamlines are presented. Time-averaged vorticity suffered from the expected smoothing of details that have short duration. Instantaneous flow field data such as streamlines shows possible interaction between the main vortices and model attached vortices. Also, the core of the two main vortices can be seen to be affected by the presence of multiple vortex filaments.

1 Introduction

Understanding the physics of flows has been a key to many breakthroughs in the development of aerospace vehicles and technologies. Flow control is one of these developing technologies that emerged as a result of enhanced knowledge of fundamental fluid dynamics. Areas of flow control applications include (but are not limited to) circulation control, vortex flow control, separation and wake control,

S. Alzhrani · S. Hafez · K. A. Juhany (✉) · I. M. AlQadi
King Abdulaziz University, P.O. Box 80204, Jeddah 21589, Saudi Arabia
e-mail: khalid@kau.edu.sa

S. Hafez
e-mail: shafaz@kau.edu.sa

S. Alzhrani
e-mail: soalzahrani@kau.edu.sa

I. M. AlQadi
e-mail: ialqadi@kau.edu.sa

drag reduction, and noise reduction. One of the many complex problems in fluid mechanics is that of the development of side force on slender axisymmetric bodies at high angle of attack, α, which is the angle between the body axis and the direction of the freestream velocity, U_∞. Flow over slender bodies at different angles of attack exhibits the development of two modes of wake-vortex, either symmetric or asymmetric. The asymmetric mode presents a control problem for aircraft and missiles at high angles of attack. The side force generates a yawing moments that cannot be overcome by control surfaces. Studies towards the control of the behavior of the wake vortex are the first step to devise a control mechanism for active control at high angles of attack when traditional control surfaces become ineffective. Flow around slender axisymmetric bodies resembles a simple representation of flow around aircraft, missiles or similar platforms. Operational conditions may require these bodies to encounter incoming flows at high angles of attack. Different flow regimes were identified with typical flow characteristics [1]. At low angle of attack, $\alpha < 15°$, a wake vortex system is formed in the base flow while the flow over the body is mainly attached. At intermediate angles of attack, $15° < \alpha < 30°$, a pair of counter rotating vortices emerges and develops with a possible further breakdown, vortex burst. At increasing angle of attack, $30° < \alpha < 65°$, the flow over the slender body will develop into a system of asymmetric vortex flow patterns. Bridges [2] provided a comprehensive experimental and numerical review regarding the problem of asymmetric wake vortex flow. Previous studies showed that disturbances introduced at the tip of the body will propagate and grow downstream causing vortices to separate from the body. Possible causes of vortex asymmetry at high α have been suggested to be either inviscid hydrodynamic instability of symmetrically separated vortices or asymmetric flow separation and/or asymmetric flow reattachment on each side of the body. Xueying and Yankui [3] experimented with various active and passive forebody vortex flow control techniques that include forebody strakes, helical trips, unsteady bleed, micro blowing to name a few. The effectiveness of these techniques proved limited in application with high angle of attack. Deng et al. [4] reviewed vortex flow evolution after tip perturbation and how the asymmetric vortices are developed with the increase of Reynolds number, Re_D. The Reynolds numbers primarily influence the boundary layer separation over a body and then indirectly influence the vortex wake and corresponding side forces on bodies. Emphasis was placed on the importance of employing artificial tip perturbation to achieve repeatability of experimental results. Bernhardt and Williams [5] addressed the Reynolds number effects on the asymmetric vortex control at low Reynolds numbers. The Reynolds numbers were limited to the range of 6.2×10^3 to 3.0×10^4. They investigated the response and behavior of the asymmetric vortex to tip perturbation by suction and bleeding. It implied that at lower Reynolds numbers, the vortex flow was absolutely unstable, so there existed a bi-stable state for the asymmetric vortex flow where even for the same tip perturbation state, two steady solutions existed for the flow.

Peiqing and Xueying [6] carried out aerodynamic force measurements and wake flow visualizations over slender bodies (cone cylinder, elliptic-nose cylinder). The experimental results showed that at angles of attack (30°–40°), the flow is unsteady and the signal of side forces contains wide ranges of amplitudes and frequencies. The

unsteadiness phenomena include low-frequency asymmetry related vortex flipping, moderate frequency Von Karman vortex shedding and higher shear layer fluctuations.

The present project is concerned mainly with the study of the flow around slender shaped bodies at angle of attack that can exhibits asymmetric vortex wake flow. Detailed instantaneous three dimensional velocity fields will be investigated by using optical measurement technique, Tomographic Particle Image Velocimetry (Tomo-PIV). The measurements will focus on the development of the wake vortex system and its interaction with the slender model leading to flow separation. The effects of Reynolds number will be investigated as well.

2 Experimental Facility and Setup

Measurements and experimental investigations are carried out at the low speed wind tunnel of the Aeronautical Engineering Department at King Abdulaziz University. The facility is an open return blower wind tunnel of working section 50×70 cm in cross section. The length of the working section is 380 cm and the tunnel's maximum speed is 40 m/s. Flow qualifications tests are conducted at 90 cm upstream of the model employed. Mean flow velocity variations are ± 0.2 % or better over the velocity range of 4m/s to 20m/s. Streamwise turbulence intensity level of 0.05 % is measured. Fast Fourier Transform, FFT, performed on the recorded velocity signals showed normal spectra without any noticeable spikes or low frequency energy content. Streamwise surface pressure measurements taken with the test model at maximum angle of attack are found to be within 0.05 % along most of the measuring domain.

2.1 Measurements and Experimental Techniques

Measurements are carried out around a slender cylindrical tangent ogive model with slenderness ratio of 3.5 and overall length 10 times the base diameter, D, 35 mm. The model is attached to a model support mechanism that allows changing the angle of attack externally. The instantaneous measurement of the three-dimensional velocity field is of a special interest to the problem investigated as it reveals the topology of unsteady coherent flow structures. Moreover, three dimensional measurements are relevant for the investigation where the flow does not exhibit specific symmetry planes or axes and several planar measurements are required for a sufficient characterization. The Tomographic Particle Image Velocimetry, Tomo-PIV, method is a relatively new extension of the PIV measurement technique with the specific ability to determine three-dimensional velocity vectors fields [7]. The principle of Tomo-PIV is based on the calculation of the velocity vectors field in a flow from the displacement of imaged tracer particles on two subsequently captured images of the region of interest. With a planar stereoscopic PIV set-up it is possible to determine instantaneous velocity vectors fields with all three components in a two dimensional plane (2D-3C). Furthermore, Tomo-PIV enables the determination of an instantaneous velocity
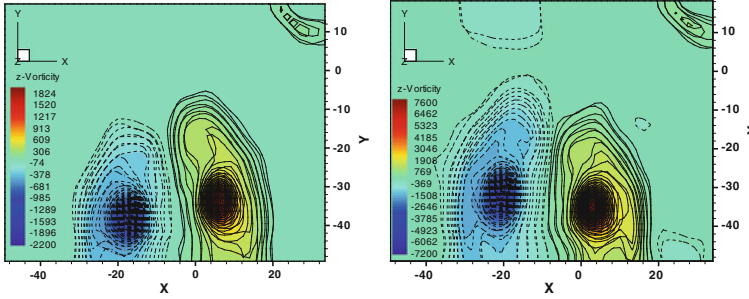
Fig. 1 Averaged vorticity contours in X-Y plane, $left: Re_D = 1.0 \times 10^4$, $right: Re_D = 4.5 \times 10^4$

vectors volume (3D-3C). The Tomo-PIV system used in this study is supplied by LaVision GmbH. The system consists of four high speed cameras with zoom lenses, a laser with optical mirror and particle generator for seeding. DaVis 8 software is used for recording and analyzing the data. The cameras are FlowMaster FM HSS6 and the laser is Litron LDY 304. The system had been installed and checked before using in the present study. Al Zahrani [8] provided a detailed account regarding calibration, data recording and analysis relevant to the system and software employed.

3 Results and Discussion

Tomo-PIV measurements are conducted at two nominal freestream velocities, U_∞, 5 and 20 m/s with the corresponding Reynolds numbers, Re_D, are 1.0×10^4 to 4.5×10^4 respectively. Tests are carried out with the model at fixed angle of attack, $\alpha = 40°$, and at a longitudinal distance along the model axis, L/D = 6, from the model vertex. The measurements volume is perpendicular to the main flow direction, not the model axis of symmetry. The measurements volume domain is about 80 mm in x-direction, 70 mm in y-direction and 6 mm in the streamwise direction (z). The x-y plane is the transverse plane with y is the height and x is the width. The four cameras and the laser are synchronized at 1 kHz as a repetition rate. The recording time for each run is about 2 sec which is limited by the onboard storage capacity of the cameras. Captured images are subsequently transferred for storage and further processing. Typical time for data transfer is about 40 min. The instantaneous and time-averaged three velocity components are calculated for the two nominal freestream velocities considered. Averaged vorticity along z-axis is deduced and plotted in Fig. 1. These plots represent the most downstream sub-volume with a thickness of 1.5 mm.

Averaged vorticity contours as shown in Fig. 1 provide information about two main vortical fields with similar features and strength. The presence of two major asymmetric vortices is clear and its elongated shape is a result of the orientation of the measuring volume with respect to the vortex core. The averaged vorticity contours show a change of vortex asymmetry position, vortex flipping, with the increases of Reynolds number.
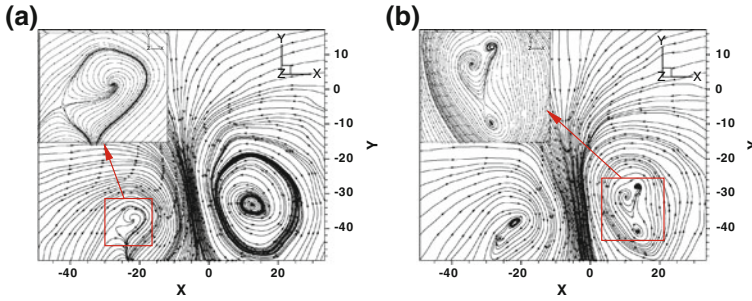
Fig. 2 Instantaneous streamlines at $Re_D = 1.0 \times 10^4$ at two different time instances, *left*:(**a**) and *right*:(**b**)

One of the main advantages of the Tomo-PIV is the ability to capture instantaneous images for the 3D flow field. The following are few features that are smoothed out by the averaging process and require further analysis. Figure 2a shows possible interaction between the left hand side main vortex and the test model. Figure 2b shows a multiple vortex filaments within the main right hand side vortex. Direction of theses vortices are the same as the main vortex. The instantaneous images clearly show that the wake vortex is a dynamic interaction of vortex filaments of yet partially recognized origin. Vortex filaments of once rolled vortex sheets appears to interact with the neighbouring vortex, in addition to either vortex instability that originate from the body or further downstream within the vortex, i.e. an instability of the main vortex. Such questions are currently under investigation.

4 Conclusions and Recommendations

The flow around a tangent ogive cylindrical model at $\alpha = 40°$ over a range of Re_D from 1.0×10^4 to 4.5×10^4 had been investigated experimentally using Tomo-PIV. Initially, the wind tunnel employed in the present study was modified and thoroughly inspected for its quality to measure the complex wake vortex flow investigated. Two main asymmetric counter rotating vortices are profound at all Reynolds number within the region covered by the Tomo-PIV system. The increase in Reynolds number promotes vortex flipping of the asymmetric vortex wake. Instantaneous flow field data shows possible interaction between the two main vortices and the test model. Multiple vortex filaments, up to three, that rotates with main vortex had been identified. Their origin could be the same vortex sheets responsible for the formation of the main neighboring vortex. Further effort will be directed to achieve time resolved Tomo-PIV measurements while investigating different planes to follow the vortex core, its development and the interaction with the model.

References

1. Ericsson LE, Reding JP (1991) Asymmetric flow separation and vortex shedding on bodies of revolution. Tactical Missile Aerodyn: Gen Topics, Prog Astronaut Aeronaut, AIAA J 141: 391-452.
2. Bridges DH (2006) The asymmetric wake problem: Asking the right question, AIAA paper 2006–3553, 36th AIAA fluid dynamics conference and exhibit. CA, Jun, San Francisco, USA
3. Xueying D, Yankui W (2004) Asymmetric vortices flow over slender body and its active control at high angle of attack. Acta Mech Sin 20(6):567–579
4. Deng XY, Tian W, Ma BF, Wang YK (2008) Recent progress on the study of asymmetric vortex flow over slender bodies. Acta Mech Sin 24:475–487
5. Bernhardt JE, Williams DR (1993) Effect of Reynolds number on vortex asymmetry about slender bodies. Phys Fluids 5(2):291–293
6. Peiqing L, Xueying D (2003) Experimental investigation of aerodynamic characteristics on slender bodies at high angles of attack. CASI 49(1):31–40
7. Elsinga GE, Scarano F, Wieneke B, van Oudheusden BW (2006) Tomographic particle image velocimetry. Exp Fluids 41:933–947
8. AlZahrani S (2013) Experimental study of wake vortex flow at high angles of attack. M.Sc thesis, King Abdulaziz university, Saudi Arabia.

Open-Loop Control of a Turbulent Axisymmetric Wake

Anthony R. Oxlade, Jonathan F. Morrison and Georgios Rigas

Abstract A high-frequency periodic jet, issuing parallel to the freestream from immediately below the point of separation, is used to force the turbulent wake of a bluff axisymmetric body. It is shown that, at the optimum jet forcing frequency and momentum flux coefficient, the time-averaged area-weighted base pressure increases by as much as 33 %. A detailed investigation of the effects of forcing is made using modal decomposition of pressure fluctuations on the base of the model and phase-locked two-component PIV. The high-frequency jet creates a row of closely spaced vortices, immediately adjacent to which are regions of large irrotational dissipation on each side. These shear layers inhibit the entrainment of fluid. The resulting pressure recovery is proportional to the strength of the vortices produced by the jet, and is accompanied by a broadband suppression of base pressure fluctuations associated with **all** modes. The optimum forcing frequency, at which amplification of the shear layer approaches unity gain, is roughly five times the shear-layer frequency.

1 Introduction

We report a novel phenomenon in which a high-frequency jet is used to increase the base pressure of a bluff body. Pulsed-jet blowing is applied to the near-wake of an axisymmetric body with its axis aligned with the free-stream direction. Turbulent separation occurs at a sharp trailing edge, immediately beneath which there is a small annular slit through which the jet emerges parallel to the free stream [14, 16, 17]. See Fig. 1. The pulsed jet is of zero net-mass flux [5], although

A. R. Oxlade · J. F. Morrison (✉) · G. Rigas
Department of Aeronautics, Imperial College London, London, UK
e-mail: j.morrison@imperial.ac.uk

A. R. Oxlade
e-mail: anthony.oxlade@imperial.ac.uk

G. Rigas
e-mail: g.rigas10@imperial.ac.uk
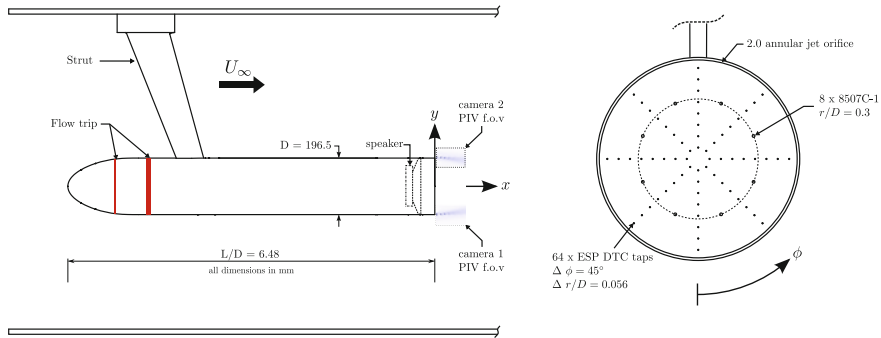
Fig. 1 Schematic of the experimental setup. Each view is independently to scale

crucially, the nonlinear coupling between the jet and the wake requires there to be a finite, jet-induced momentum flux appearing as a change in pressure drag on the body.

Ideas from stability theory may be used in the context of turbulent wake flows where there is a sufficient scale separation between the large organised structures and the small scales; then the growth of large-scale turbulent structures in a wake may be described as the propagation of instability waves about an inviscidly unstable mean shear flow [4, 6, 11]. The concepts of absolute and convective instability [8, 9] provide insight into wake behaviour. At sufficiently high Reynolds numbers, an absolute instability appears as a global vortex-shedding mode. Alternatively, convectively unstable shear layers rely on spatial amplification of external perturbations. Here we show that a global instability can be controlled indirectly from a location where the separating boundary layer is convectively unstable and receptive to "extrinsic" disturbances [7].

2 Experimental Setup

Figure 1 shows a schematic of the model which is mounted in a closed-circuit wind tunnel, with a contraction ratio of 4.92:1. Its blockage is 1.8 % and the free-stream turbulence intensity is less than 0.1 %. A PID controller with a set-point variation of less than 0.2 % is used to maintain the free-stream velocity, $U_\infty = 15\,\text{m s}^{-1}$. The model has diameter $D = 196.5$ mm and length $L = 6.48D$ ($Re_D = 1.88 \times 10^5$, $Re_\theta = 2{,}050$, respectively, Reynolds number based on body diameter and momentum thickness at separation). A high-fidelity speaker mounted inside the model is used to generate a pulsed jet of variable frequency and amplitude. The jet issues in the free-stream direction from a 2.0 mm annular slit, located 1.0 mm below the trailing edge. The jet velocity was calibrated with a single hot wire against speaker-chamber pressure, the amplitude of which was also maintained constant using a PID controller, with a set-point variation for the speaker-chamber pressure of less than 0.15 %. The model base is instrumented with 64 static pressure tappings and 11 Endevco 8507C-1 transducers which were sampled at, respectively, 225 Hz and 40 kHz. Phase-locked

two-component PIV measurements were made immediately downstream of the jet orifice on the upper and lower separating shear layers simultaneously. A conservative estimate of the PIV spatial resolution, the -3 dB cut-off wavelength of the measurement, $\lambda_c = 0.7$ mm [15].

3 Results

The boundary layer separating from an axisymmetric body is subject to a shear-layer instability which gives rise to several mode shapes through a selective amplification of disturbances; individual modes were identified using an azimuthal Fourier decomposition of the fluctuating pressure measured by the eight transducers located at $r/D = 0.3$ with separation $\Delta\phi = 45°$ (Fig. 1). For a cross correlation $R(\phi, t)$, the spectral density per mode, m, is given by

$$\Phi_m(f) = \frac{1}{(2\pi)^2} \int_0^\infty \int_0^{2\pi} R(\phi, t) e^{\mp i 2\pi (m\Delta\phi + ft)} d\phi \, dt, \tag{1}$$

where integration of the spectral energy $f\Phi_m(f)$ with respect to frequency, f, gives the mean-square pressure fluctuation for each mode.

$$\overline{p_m^2} = \int_0^\infty f\Phi_m(f) d(\log f). \tag{2}$$

Ho and Huerre [6] performed a linear stability analysis of an initially laminar, plane mixing layer to show that maximum amplification occurs at a momentum thickness based Strouhal number, $St_\theta = 0.016$. Owing to their inclination to the radial direction, both helical structures and inclined vortex rings introduce an azimuthal phase variation. However, nearly all of the energy appears at much lower frequencies: the axisymmetric "bubble pumping" ($m = 0$) mode and the helical, anti-symmetric ($m = \pm 1$) global instability appear at $St_D \approx 0.05$ and 0.2, respectively [2]. Monkewitz [13] conducted a linear stability analysis for a family of axisymmetric wake (parallel flow) profiles: he showed that the helical mode is absolutely unstable and noted that the helical vortex structure is most clearly observed somewhat downstream of the body, typically near the rear stagnation point [2]. The present results (Fig. 2) also show evidence of very low-frequency energy in the wake, with an azimuthal wavenumber $m = \pm 1$ and period of about 8 s ($St_D \approx 0.0017$). This random rotation of the wake structure has also been observed in sphere wakes [10, 12]. The energy at this frequency is significant, and the slight imbalance between $m = \pm 1$ modes indicates a bias in the direction of rotation due to the boundary conditions. It is also worth noting that the peak for the $m = \pm 2$ modes occurs at $St_D \approx 0.008$, not far from the subharmonic of the $m = \pm 1$ modes. This suggests some form of coupling between anti-symmetric modes, possibly vortex pairing.
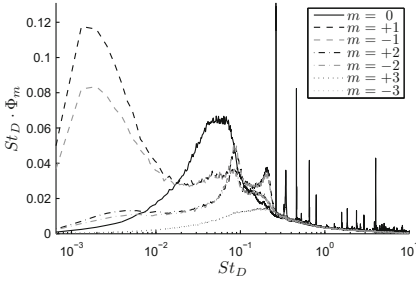
Fig. 2 Modal decomposition of base pressure spectral density at $r/D = 0.3$
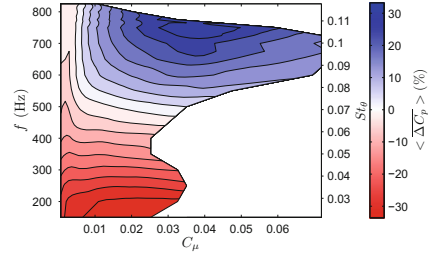
Fig. 3 Change in base pressure coefficient as a function C_μ and St_θ

Figure 3 shows the change due to forcing of mean base-pressure coefficient, $\langle \overline{\Delta C_p} \rangle$ (an area-weighted and temporal average, where $C_p = \frac{p - p_\infty}{0.5 \rho U_\infty^2}$) as a function of forcing amplitude and frequency, expressed as a percentage of the unforced case. The forcing amplitude is represented by a momentum flux coefficient, $C_\mu = \frac{u_j^2 A_j}{U_\infty^2 A}$, where u_j is the amplitude of the jet perturbation, A_j is the area of the jet orifice, and A is the area of the base of the model. There are two key features. At $St_\theta \leq 0.08$, there is a region in which the forcing reduces the base pressure due to strong shear-layer amplification, with a maximum at $St_\theta \approx 0.021$: this is close to the value of Zaman and Hussain [18]. For the present experiment, $D/\theta = 92$, so that turbulence may be regarded as 'small' compared to the large structure. This phenomenon is well understood [6] as shown in related work [16, 17]. At higher forcing frequencies, there is an increase in pressure: this effect does not appear to have been noticed previously. Figure 4 shows the attenuation of mean-square pressure fluctuations for each mode shape, normalised by the baseline case, as a function of forcing amplitude at $St_\theta = 0.10$. As C_μ increases, $\overline{p^2}_m$ decreases. The suppression of energy occurs across all modes and is a broadband attenuation below the shear-layer frequency.

4 Discussion and Conclusions

An explanation of this phenomenon is provided in Fig. 5 which shows that, for this unoptimised geometry, there is a maximum pressure recovery of 33 % at $C_\mu = 0.04$ and $St_\theta = 0.10$, that is at about five times the shear-layer frequency. Figure 5 also shows that the maximum pressure coincides with the maximum vorticity of the primary vortex created by the jet, $|\omega_z| D/U_\infty$, which increases with forcing amplitude up to $C_\mu \approx 0.04$. At higher forcing amplitudes the primary vortex breaks down into multiple structures reducing the effect. There is a strong correlation between the pressure recovery and the vorticity of the primary vortex.

The jet efflux produces a pair of counter-rotating, concentric vortex rings, the outer one with vorticity of opposite sign to that of the boundary layer. Their cancellation
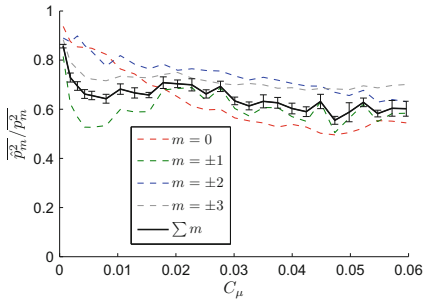
Fig. 4 Change of mean-square pressure for each mode shape as a function of forcing amplitude, C_μ, at $St_\theta = 0.10$, $r/D = 0.3$
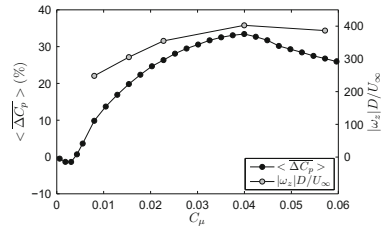
Fig. 5 Change of average base pressure and maximum vorticty of the jet vortex, ω_z, with C_μ. Forcing at $St_\theta = 0.10$
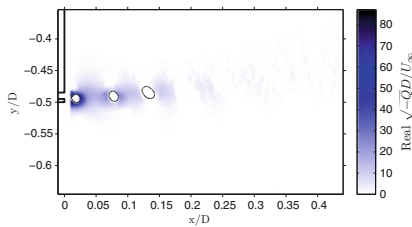
Fig. 6 Phase average of real (λ_{cr}) and imaginary (λ_{ci}) eigenvalues of second invariant of strain rate at the optimum forcing condition ($St_\theta = 0.10$, $C_\mu = 0.04$). λ_{cr}: shaded area. Closed contour level denotes $\lambda_{ci} > 800$
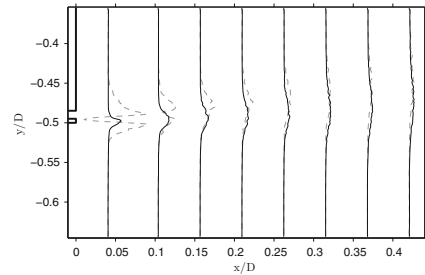
Fig. 7 Comparison of second invariant, $-2Q = \dfrac{\partial u_i}{\partial x_j} \dfrac{\partial u_j}{\partial x_i}$ ($St_\theta = 0.10$, $C_\mu = 0.04$). *Lines*: *solid line* unforced; *dashed line* forced

leaves the inner vortex ring with vorticity of the same sign as that of the boundary layer. Figure 6 shows real (shear) and imaginary (swirl) eigenvalues of the strain rate, $\sqrt{-Q} = \lambda_{cr} \pm i\lambda_{ci}$, where Q is the second invariant of the strain rate. Discrete vortices are clearly identified for $\lambda_{ci} > 800$, while shaded areas clearly identify significant regions of irrotational shear around each vortex, the regions of largest shear appearing for the primary vortex closest to the orifice. The Poisson equation for pressure fluctuations may be written in the form [3],

$$-2Q = \frac{\partial u_i}{\partial x_j} \frac{\partial u_j}{\partial x_i} = -\frac{\nabla^2 p}{\rho} = e_{ij} e_{ji} - \frac{1}{2}\omega_i^2. \tag{3}$$

Loosely, the first term of the right-hand side may be taken to represent stagnation points in the instantaneous streamline pattern, or "eddy collisions", leading to a positive pressure. The second term indicates eddy rotation ("spin") implying a rapidly

rotating eddy with negative pressure near the axis of rotation. The form of the right-hand side is not unique [1], yet Fig. 6 shows that, for the forced flow, the distinction is unambiguous, and that the sign of Q (in two-dimensions, identical to the discriminant of opposite sign) is sufficient to separate these regions, Fig. 7. It appears that the mechanism by which pressure at the base of the body may be raised is due to a discrete row of vortices of large enstrophy bounded on each side by a shear layer of large irrotational dissipation. The latter are responsible for the reduction in entrainment and therefore drag on the body. This novel effect is generic in the sense that we have also been able to demonstrate it for turbulent separation from a bluff body of rectangular cross section as well as that from a backward facing step.

References

1. Adrian RJ (1982) Comment on a note on Poisson's equation for pressure in a turbulent flow. Phys Fluids 25:577
2. Berger E, Scholz D, Schumm M (1990) Coherent vortex structures in the wake of a sphere and a circular disk at rest and under forced vibrations. J Fluids Struct 4:231–257
3. Bradshaw P, Koh YM (1981) A note on Poisson's equation for pressure in a turbulent flow. Phys Fluids 24:777
4. Gaster M, Kit E, Wygnanski I (1985) Large-scale structures in a forced turbulent mixing layer. J Fluid Mech 150:23–39
5. Glezer A, Amitay M (2002) Synthetic jets. Annu Rev Fluid Mech 34:503–529
6. Ho C-M, Huerre P (1984) Perturbed free shear layers. Annu Rev Fluid Mech 463:365–424
7. Huerre P (2000) Open shear flow instabilities. In: Batchelor GK, Moffatt HK, Worster MG (eds) Perspectives in fluid dynamics. Cambridge University Press, Cambridge
8. Huerre P, Monkewitz PA (1985) Absolute and convective instabilities in free shear layers. J Fluid Mech 159:151–168
9. Huerre P, Monkewitz PA (1990) Local and global instabilities in spatially developing flows. Annu Rev Fluid Mech 22:473–537
10. Miau JJ, Leu TS, Liu TW, Chou JH (1997) On vortex shedding behind a circular disk. Exp Fluids 23:225–233
11. Michalke A (1965) On spatially growing disturbances in an inviscid shear layer. J Fluid Mech 23:521–544
12. Mittal R, Wilson JJ (2001) Symmetry properties of the transitional sphere wake. AIAA 40(3)
13. Monkewitz PA (1988) A note on vortex shedding from axisymmetric bluff bodies. J Fluid Mech 192:561–575
14. Oxlade AR (2013) High-frequency periodic jet forcing of a turbulent axisymmetric wake. PhD dissertation, Imperial College, Department of Aeronautics.
15. Oxlade AR, Valente PC, Ganapathisubramani B, Morrison JF (2012) Denoising of time-resolved PIV for accurate measurement of turbulence spectra and reduced error in derivatives. Exp Fluids 53:1561–1575
16. Qubain A (2009) Active control of a turbulent bluff body wake. PhD dissertation, Imperial College, Department of Aeronautics.
17. Qubain A, Morrison JF (2009) Active control of an axisymmetric turbulent wake. In KATnet II conference on key aerodynamic technologies, Bremen, 12–14, May 2009
18. Zaman KBMQ, Hussain AKMF (1981) Turbulence suppression in free shear flows by controlled excitation. J Fluid Mech 103:133–159

Stability and Coherent Structures in the Wake of Axisymmetric Bluff Bodies

Georgios Rigas, Aimee S. Morgans and Jonathan F. Morrison

Abstract The coherent structures observed in the turbulent wake of axisymmetric bluff bodies are investigated. Concepts from hydrodynamic stability are used to derive low-dimensional mathematical models based on a weakly nonlinear analysis of the governing Navier-Stokes equations that describe the temporal amplitude evolution of the coherent structures in the near wake. Forced experiments applying axisymmetric pulsed-jet blowing on the base of the body are performed to validate the models. Very good quantitative agreement between model predictions and experiments is obtained, showing for the first time that Landau-type models are capable of describing the dynamic behavior of a three-dimensional turbulent wake.

1 Introduction

We present experimental evidence that the initial instabilities observed in laminar flows behind axisymmetric bluff bodies persist in the turbulent regime and, in both cases, manifest as coherent flow structures. Treating these structures as organized waves, we derive dynamic models from a weakly nonlinear analysis of the governing Navier-Stokes equations which capture accurately the complex response of the coherent structures to external forcing. We validate the models by applying pulsed-jet blowing on the base of an axisymmetric body.

The transition of the stable laminar flow to a turbulent state in axisymmetric-body wakes follows a two-stage scenario: a steady bifurcation of a $m = +1$ mode followed

G. Rigas (✉) · A. Morgans · J. Morrison
Department of Aeronautics, Imperial College London, London, UK
e-mail: g.rigas@imperial.ac.uk

A. Morgans
e-mail: a.morgans@imperial.ac.uk

J. Morrison
e-mail: j.morrison@imperial.ac.uk
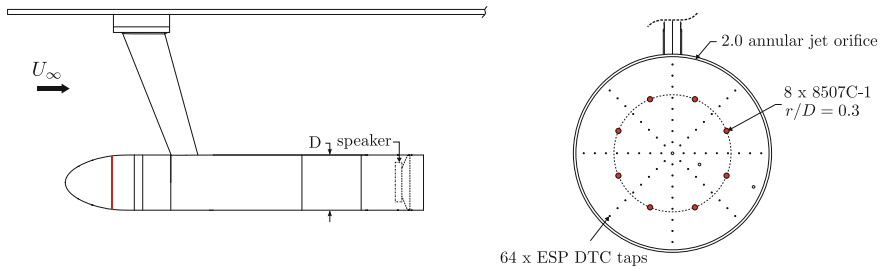
Fig. 1 Schematic of the experimental setup. Actuator and sensors are shown

by an unsteady bifurcation giving rise to oscillatory behavior with $m = \pm 1$, as shown in DNS simulations [1] , at Re $= 100 - 400$. Here m is the azimuthal wavenumber of the unstable waves. The flow field after the initial bifurcation is characterised by loss of axial symmetry, but with reflectional symmetry about a longitudinal plane with an arbitrary orientation, resulting in a constant nonzero force applied normal to the base. The second bifurcation gives rise to the periodic shedding of vortex structures with opposite sign, known as vortex shedding. In this regime, the average force remains nonzero but its amplitude is periodically varying at the frequency of the vortex shedding. Increasing the Reynolds number, the symmetries of the flow are lost due to random variations of the vortex shedding angle [7].

In the laminar regime, simple low-dimensional models have been proposed based on a weakly nonlinear analysis of the Navier-Stokes equations [5] and on theory of mode interactions in the presence of $O(2)$ symmetry [2]. These models are three coupled Stuart-Landau equations capturing the amplitude evolution of the global modes close to the threshold of the bifurcations. Recently, Sipp [6] studied the effect of a harmonic body force on a cavity flow, with a single unstable mode, and showed how this force enters the weakly nonlinear equations describing the amplitude of the global mode. In the present study, we extend the weakly nonlinear analysis to a three-dimensional bluff-body flow at high Reynolds numbers, where the separating boundary layer is turbulent. We include explicitly the effect of forcing in the models.

2 Experimental Setup

The experiments were performed using an axisymmetric bluff body with an elliptic nose, shown schematically in Fig. 1. The model is mounted in a closed-circuit wind tunnel, with a contraction ratio of 9:1. Its blockage is 3.6 % and the free-stream turbulence intensity is less than 0.05 %. A PID controller with a set-point variation of less than 0.2 % is used to maintain the free-stream velocity, $U_\infty = 15 \, \text{ms}^{-1}$ ($Re_D = 1.88 \times 10^5$, $Re_\theta = 2,050$, respectively, based on diameter and boundary layer momentum thickness at separation). A high-fidelity speaker mounted inside the model is used to generate an axisymmetric ($m = 0$) pulsed jet of variable frequency and amplitude, when driven by a harmonic voltage signal. The jet issues in the freestream direction from a 2.0 mm annular slit, located 1.0 mm below the trailing

Fig. 2 PSD of the azimuthally decomposed pressure fluctuations measured on the base of the axisymmetric body for the unforced flow
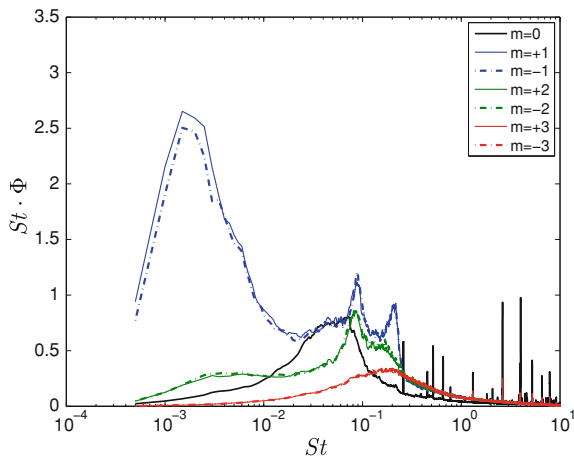
edge. Sensing is achieved with 64 static pressure tappings and 8 Endevco 8507C transducers which were sampled at, respectively, 225 Hz and 40 kHz.

3 Results

The premultiplied spectrum of the base-pressure fluctuations, decomposed spatially into azimuthal modes, is shown in Fig. 2. Frequencies are non-dimensionalised with the diameter of the body and the freestream velocity ($St = fD/U_\infty$). Despite the fact that the flow is turbulent, and turbulent flows are known to exhibit a wide range of temporal and spatial scales, the wake is clearly sustaining coherent structures among them. The peak at $St \approx 0.2$ is associated with the global oscillatory mode of the wake—shedding of vortices with azimuthal wavenumber $m = \pm 1$. It is consistent with previous experimental observations from bodies of similar geometry [3]. Instantaneous snapshots of the pressure distribution on the base indicate that the wake is characterised by reflectional symmetry. The very low frequency peak at ($St \approx 0.002$, $m = \pm 1$) corresponds to a random rotation of the symmetry plane, as it will be shown below, and could be linked to the loss of axisymmetry due to the steady bifurcation.

Insight to the forces exerted on the body and their link to the instabilities of the turbulent wake is given by the Centre-of-Force (CoF), calculated from the area-weighted pressure and defined on the Cartesian coordinate system of the base as $\mathbf{R}_{cart} = \left(1/\int \overline{P_i} dA\right) \int P_i \mathbf{x} dA$. The probability density of the CoF is plotted in Fig. 3 and shows that the most probable location of it lies on a circle centered on the base of the body. Further information on the dynamic behaviour of the coherent structures can be provided by examining the spectra of the CoF, but now transformed to polar coordinates, $\mathbf{R}_{polar} = (R_r, R_\theta)$. The CoF oscillates in the radial direction at the frequency of the vortex shedding, $St \approx 0.2$, as shown in Fig. 4. In the same framework, the spectral content of the angular component shows clearly that the low frequency oscillation at $St \approx 0.002$ is a rotation around the axis of the body.

Fig. 3 PDF of center of aerodynamic force on the base of the body (Cartesian coordinates)
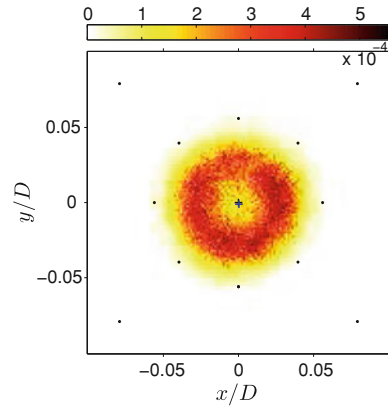
Fig. 4 PSD of center of aerodynamic force on the base of the body (polar coordinates)
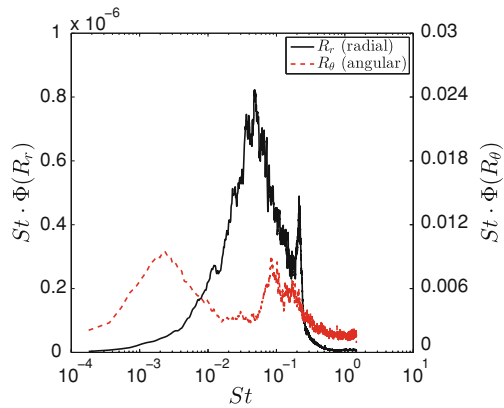
Having identified the predominant modes present in the natural flow, the effect on these of flow forcing using axisymmetric pulsed-jet actuation is now considered. As expected in a linear framework, the flow responds at the forcing wavenumber, $m_f = 0$, and frequency ω_f. However, a pronounced change is also observed in the amplitude of the $|m| = 1$ global mode, near $St = 0.2$, highlighting the nonlinear coupling between axisymmetric forcing and the global mode. The steady-state response of the $|m| = 1$ global mode to axisymmetric harmonic forcing over different frequencies is shown in Fig. 5.

A strong subharmonic resonance in the response occurs when the forcing is close to twice the global mode frequency, $St \approx 0.4$. Near this forcing frequency, the frequency of the global mode "locks-in" to one-half the forcing frequency. The lock-in region depends on the forcing amplitude; increasing amplitude results in a wider lock-in region. "Lock-in" phenomena point to nonlinear oscillator behaviour forcing past a suspected global-mode frequency or its rational multiples [4].

Fig. 5 Amplitude and frequency response of the vortex shedding mode ($m = \pm 1$, $St \approx 0.2$) to axisymmetric forcing ($m_f = 0$, St_f) for two forcing amplitudes
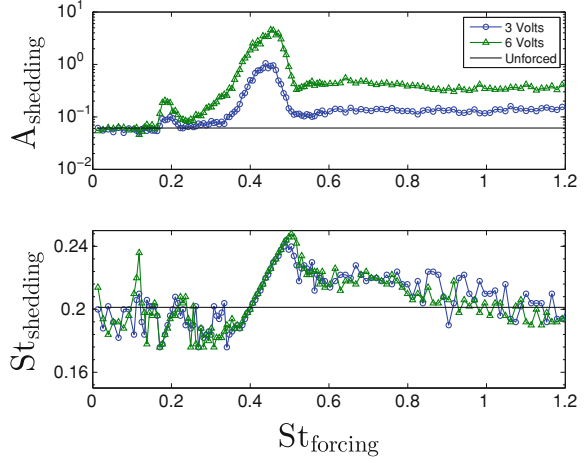
4 Modelling and Conclusions

In view of the observation that the near-wake turbulent flow, $\mathbf{q} = (\mathbf{u}, p)$, contains structures of widely varying scales, we consider a model employing scale subdivision with the large scales accounting for the coherent structures $\tilde{\mathbf{q}}$ and the small scales involving the incoherent background $\mathbf{q}'$:

$$\mathbf{q}(\mathbf{x}, t) = \mathbf{q_0}(\mathbf{x}) + \tilde{\mathbf{q}}(\mathbf{x}, t) + \mathbf{q}'(\mathbf{x}, t), \tag{1}$$

where $\mathbf{q_0}$ is the laminar base flow at Re_c. The governing equations for the turbulent flow can be written as

$$\partial_t \mathbf{u} + \mathbf{u} \cdot \nabla \mathbf{u} = -\nabla p + \mathrm{Re_T}^{-1} \nabla^2 \mathbf{u} \quad \text{and} \quad \nabla \cdot \mathbf{u} = 0. \tag{2}$$

Here, $\mathrm{Re_T} = (U_\infty D)/\nu_T$, where ν_T is the turbulent eddy viscosity modelling the incoherent field. Introducing a *fast* time scale t and a *slow* time scale $t_1 = \varepsilon t$, where ε is a small parameter, the flow field can be expanded as

$$\mathbf{q}(t, t_1) = \mathbf{q_0} + \sqrt{\varepsilon}^1 \tilde{\mathbf{q}}_1(t, t_1) + \sqrt{\varepsilon}^2 \tilde{\mathbf{q}}_2(t, t_1) + \sqrt{\varepsilon}^3 \tilde{\mathbf{q}}_3(t, t_1) + \cdots \tag{3}$$

Assuming $\mathrm{Re_T}^{-1} = \mathrm{Re}_c^{-1} - \varepsilon$, we introduce (3) into (2), and equating coefficients of the nth power of $\sqrt{\varepsilon}$ to zero, a series of equations is obtained at various orders [5, 6]. At order $\sqrt{\varepsilon}^3$, we obtain a Landau-like equation describing the (complex) amplitude evolution of the global shedding mode ($m = \pm 1$, $St \approx 0.2$) of the following form:

$$\frac{dA_\pm}{dt} = \lambda A_\pm + (\kappa + \nu)|A_\pm|^2 A_\pm + \mu A_0 A_\pm^*. \tag{4}$$
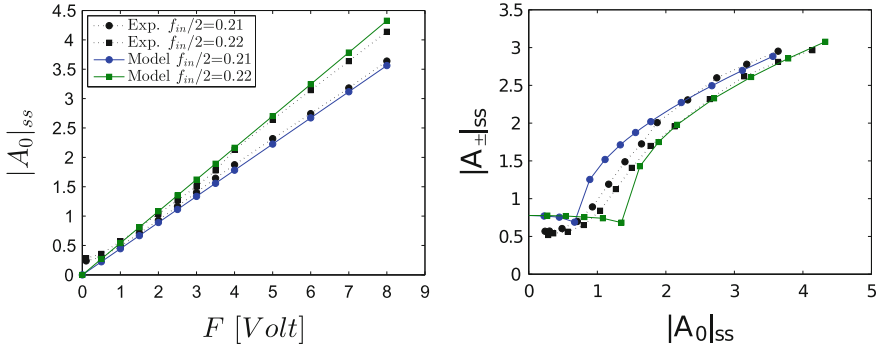
Fig. 6 Comparison of model predictions and experimental measurements for the steady-state amplitude response for two different forcing frequencies. *Left* Axisymmetric perturbation as a function of the actuator driving voltage. *Right* Vortex shedding to axisymmetric perturbation

The last term in Eq. (4) describes the coupling between the complex conjugate of the global mode $A_{\pm}^{*}$ and the axisymmetric perturbation A_0, when forcing is applied resonantly near twice the global mode frequency (parametric subharmonic resonance).

Transient and steady-state data are used to identify the unknown complex coefficients κ, λ, μ, ν of the the amplitude Eq. (4). A linear equation, capturing the actuator dynamics and describing the transfer function between driving voltage, F, and perturbation to the flow, A_0, is also introduced. In Fig. 6 we show the steady-state amplitude response of the actuator and the parametric subharmonic resonance of the global vortex shedding mode due to forcing. Very good agreement between model simulations and experiments is obtained, showing for the first time that Landau-type models are capable of describing the dynamic behavior of a three-dimensional turbulent wake. This set of equations can provide the basis for the design of optimal controllers.

References

1. Bohorquez P, Sanmiguel-Rojas E, Sevilla A, Jiménez-González JI, Martínez-Bazán C (2011) Stability and dynamics of the laminar wake past a slender blunt-based axisymmetric body. J Fluid Mech 676:110–144
2. Fabre D, Auguste F, Magnaudet J (2008) Bifurcations and symmetry breaking in the wake of axisymmetric bodies. Phys Fluids 20:051702
3. Grandemange M, Gohlke M, Parezanović V, Cadot O (2012) On experimental sensitivity analysis of the turbulent wake from an axisymmetric blunt trailing edge. Phys Fluids 24(3):035106
4. Huerre P, Monkewitz PA (1990) Local and global instabilities in spatially developing flows. Annu Rev Fluid Mech 22(1):473–537
5. Meliga P, Chomaz J-M, Sipp D (2009) Global mode interaction and pattern selection in the wake of a disk: a weakly nonlinear expansion. J Fluid Mech 633:159
6. Sipp D (2012) Open-loop control of cavity oscillations with harmonic forcings. J Fluid Mech 1(1):1–30
7. Tomboulides AG, Orszag SA (2000) Numerical investigation of transitional and weak turbulent flow past a sphere. J Fluid Mech 416(1):45–73

Part VII
Separation in Bluff Body Flows

Stability and Control on a Low Aspect Ratio Cantilevered Circular Cylinder

Edward Paisley DeMauro, Chia Min Leong and Michael Amitay

The stability of the near wake of a low aspect ratio cantilevered cylinder, with and without the influence of synthetic jet forcing, was estimated using piecewise two-dimensional inviscid stability analysis. Using a cusp method, the size of the 3-D vortex formation length was estimated. When the synthetic jet was activated it decreased the vortex formation length, altering the spectral content of the near wake, in agreement with experimental measurements. Furthermore, the turbulence intensity within the near wake could be estimated from the eigenfunctions corresponding to the most amplified spatial instability modes.

1 Introduction

The hydrodynamic stability of flow past a 2-D bluff body has been studied extensively in the past; for example, to understand the flow around a 2-D cylinder, giving insight into the onset of transition within the individual flow regions: the boundary layer, the separated shear layer, and the wake [1]. However, in practice, bluff bodies are three-dimensional and the ability to modify the flow field around these bodies can help improve aerodynamic characteristics.

For a cylinder wake, the Rayleigh equation can be utilized successfully with a minimal difference compared to the Orr-Sommerfeld equation [2] since the primary source of instability in the cylinder wake is the existence of inflection points in the velocity profile. Although not strictly representative of physical reality, the use of local stability methods can be advantageous in obtaining useful knowledge of the

E. P. DeMauro · C. M. Leong
Mechanical, Aerospace, Nuclear Engineering, RPI, Troy, NY, USA

M. Amitay (✉)
James L. Decker Endowed Professor of Aerospace Engineering, RPI, 110 8th street
JEC5038, Troy, NY 12180, USA
e-mail: amitam@rpi.edu

flow field through application of the traditional normal mode analysis. Upon applying local theory, the flow can be further described as being absolutely or convectively stable [3].

This paper investigates the changes to the near wake of a cantilevered low aspect ratio circular cylinder induced by a single synthetic jet, complimenting earlier experimental work of DeMauro et al. [4, 5]. The goal is to determine the feasibility of studying stability characteristics within a highly 3-D flow field as a series of piecewise 2-D flow field at various spanwise locations. Attention is also given to the effect of the synthetic jet on the vortex formation region downstream of the cylinder, and the contribution of the synthetic jet to the primary instability.

2 Experimental Setup and Procedure

Experiments were conducted in an open-return low-speed wind tunnel. A finite-span circular cylinder with a diameter, $D = 101.6$ mm was used, where its height to diameter ratio was 3 ($AR = 3$). The coordinate system is shown in Fig. 1, where x, y, and z are the streamwise, cross-stream, and spanwise directions, respectively.

The cylinder was instrumented with a single finite-span synthetic jet located at $z/D = 1.5$. The jet used here had a rectangular exit orifice of length $b = 20.32$ mm and width $h = 1$ mm, where its long axis parallel to the freestream (Fig. 1). Therefore, the jet swept $22°$ along the cylinder surface, centered at $\theta_{jet} = 90°$. The cylinder was placed on a circular fence to isolate the cylinder from the wind tunnel boundary layer.

The synthetic jet was driven at a frequency, $f_{jet} = 2.6$ kHz, resulting in a Strouhal number, $St_{jet} = 14.7$ (two orders of magnitude larger than the cylinder Strouhal number of $St = 0.16$, [6]). Here, the jet strength, relative to the flow, was quantified using momentum coefficient, C_μ, and blowing ratio, C_b, defined as:

$$C_\mu = \frac{\rho_{jet} bh}{\rho_\infty DH} \cdot \frac{1}{TU_\infty^2} \int_0^{T/2} U_{jet}^2(t) dt \qquad (1)$$

$$C_b = \frac{1}{TU_\infty} \int_0^{T/2} U_{jet}(t) dt \qquad (2)$$

where $U_{jet}(t)$ is the velocity of the synthetic jet at its exit plane, ρ_{jet} and ρ_∞ are the density of the synthetic jet and the freestream, respectively, T is the synthetic jet period time, b and h are the width and length, respectively, of the jet orifice, and H is the span of the cylinder. Here, the momentum coefficient and the blowing ratio were $C_\mu = 5.7 \times 10^{-4}$ and $C_b = 0.6$, and the Reynolds number was 116,600.

Stereoscopic Particle Image Velocimetry (SPIV) measurements were taken at the cylinder's near wake ($x/D = 1$, 1.5, 2, 2.5, and 3). In order to increase the spatial
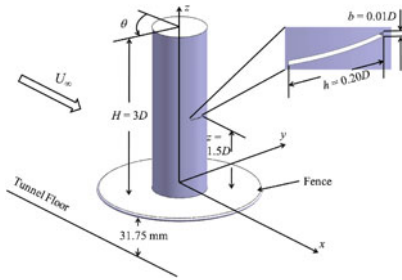
Fig. 1 Experimental setup and primary axes
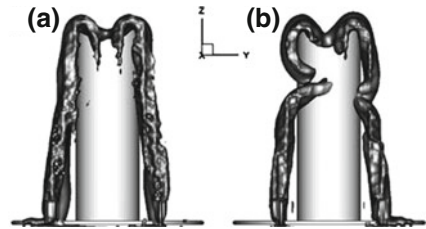
Fig. 2 The time-averaged arch-type vortex structure within the near wake: $\omega_{tot} = 2.5$. **a** Baseline; **b** forced, $\theta_{jet} = 90°$

resolution, each plane was divided into six interrogation windows, which were then combined to provide the entire wake at a given streamwise locations (more details in [4]). In addition, a single hot-wire sensor was used in the near wake to resolve its spectra content.

3 Results

As shown by DeMauro et al. [4], the baseline wake demonstrates large regions of streamwise vorticity, symmetric about the centerline of the cylinder, due to large velocity gradients associated with a non-negligible spanwise velocity component, i.e. downwash. When the synthetic was activated, it modified the streamwise vorticity and altered the power spectra.

In order to appreciate the changes to the arch-type vortex structure, a volumetric reconstruction was performed using measurements taken at 5 streamwise planes. Iso-contours of total vorticity, ω_{tot}, are shown in Fig. 2, where the structure represents the time-averaged, symmetrically-shedding, arch-type vortex. With actuation (Fig. 2b), symmetry is diminished and the structure on the actuated side shows a vortex dislocation (the jet effect is also seen in the unactuated side).

Power spectra, measured at $x/D = 2$ (not shown), indicated that there is a very small difference between the unforced and forced wakes on the unactuated side of the cylinder, in agreement with the structures seen in Fig. 2. Towards the base of the cylinder ($z/D = 1$), the power spectra demonstrates a dominant frequency, $St = 0.155$, which is the shedding frequency of the arch-type vortex (as shown by [6]). On the actuated side, the power spectra shows a small increase in power associated with a frequency of $St = 0.24$, closer to a 2-D value, at $z/D = 2$, which is at the spanwise location of the vortex dislocation.

The primary assumption is that the stability characteristics are driven by inflection points in the time-averaged velocity profiles, and therefore inviscid flow theory could

Table 1 Stability characteristics at 3 streamwise and spanwise locations

z/D	$\beta_{0,r}$	$\beta_{0,i}$	St	z/D	$\beta_{0,r}$	$\beta_{0,i}$	St
$x/D = 1$; *baseline*				$x/D = 1$; *forced*			
1	0.9047	0.4429	0.1440	1	0.9121	0.3986	0.1452
1.5	1.0250	0.3312	0.1631	1.5	1.0070	0.1970	0.1603
2	1.0920	0.2466	0.1738	2	1.2950	0.1714	0.2061
$x/D = 2$; *baseline*				$x/D = 2$; *forced*			
1	0.6479	0.3092	0.1031	1	0.7781	0.2681	0.1238
1.5	0.8712	0.2977	0.1387	1.5	0.9594	0.1522	0.1527
2	1.1850	0.1694	0.1886	2	1.2160	−0.2741	0.1935
$x/D = 3$; *baseline*				$x/D = 3$; *forced*			
1	0.6690	0.0935	0.1065	1	0.8296	−0.0585	0.1320
1.5	0.8746	−0.1855	0.1392	1.5	0.9042	−0.3581	0.1439
2	1.0480	−0.6418	0.1668	2	0.8966	−0.7570	0.1427

be used [2, 7, 8]. Regarding parallel flow, the analysis assumed that the change of the wake width across one wavelength of the disturbance is very small. The final assumption treated the wake as two-dimensional slices at various spanwise locations along the span of the cylinder.

Analysis was carried out using normal modes, where the wavenumber, $\alpha = 2\pi D/\lambda$ and frequency, $\beta = 2\pi f D/U_\infty$ were scaled based on the parameters of the wake. The analysis was performed on the entire wake profile ($y/D \to \pm\infty$) at 3 separate spanwise locations ($z/D = 1, 1.5, 2$) and at 3 streamwise positions ($x/D = 1, 2, 3$) for the baseline and forced cases.

A cusp method [9] was used to map $\alpha = \alpha_r + i\alpha_i$ with $\beta = \beta_r + i * \beta_i$ in order to estimate the value of the pinch point, β_0, where $\beta_{0,r} = 2\pi St$, i.e. the shedding frequency within the velocity profile [9]. Therefore, the velocity profile was determined to be absolutely unstable if an unstable value of α resulted in an unstable value of β (i[.e., $\beta_{0,i} > 0$), and convectively unstable if $\beta_{0,i} < 0$ [9].

Next, absolute versus convective instability in the vortex formation region and shedding frequency is discussed (the results are listed in Table 1 and Fig. 3).

Both the baseline and forced wakes appear to have a 3-D formation region, as seen from the increasingly negative values of $\beta_{0,i}$ along the span of the cylinder. In the baseline wake, the wake becomes convectively unstable at $x/D = 3$, whereas in the forced case the wake becomes convectively unstable at $x/D = 2$, indicating a size reduction of the vortex formation region (in agreement with [5]).

The shedding frequency reported in the literature for a low-aspect ratio cylinder is $St \approx 0.16$ [6]. At $x/D = 1$, within the formation region, the average Strouhal number resulting from the present calculation is $St = 0.1603$, in agreement with both the literature and the measured power spectra. Farther downstream, the agreement is not as good due to the increasing three-dimensionalities within the near wake, suggesting that the quasi 2-D assumption may no longer be valid. In comparison to the baseline case, the forced wake shows increased values for the Strouhal number, $St \approx 0.2$ at

Fig. 3 Comparison of stream-
wise turbulence intensity with
eigenfunctions: $x/D = 1$, z/D
$= $ (a) 1, (b) 1.5, (c) 2; $x/D = 2$,
$z/D = $ (d) 1, (e) 1.5, (f) 2;
$x/D = 3$, $z/D = $ (g) 1, (h) 1.5,
(i) 2
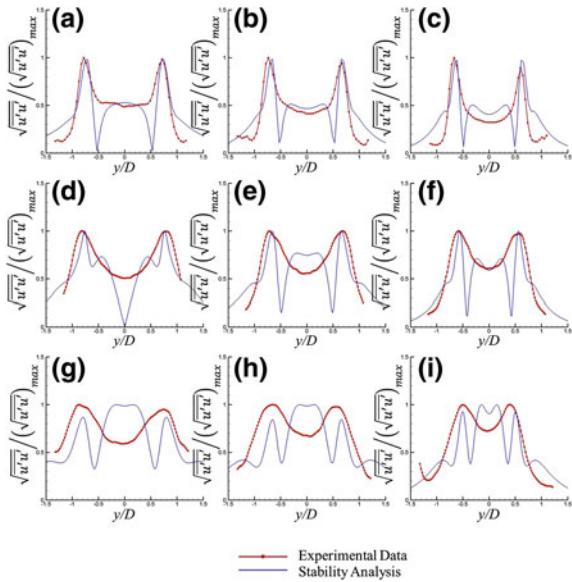
$z/D = 2$ for streamwise locations of $x/D = 1$ and 2, which is due to the narrower wake at this location. This is in good agreement with the experimental power spectra.

In addition, a spatial stability analysis was used to calculate the eigenfunctions corresponding to the most amplified mode only for the streamwise component of the baseline wake. The normalized magnitudes of these eigenfunctions can be seen in Fig. 3 overlaid with measured turbulence intensities.

The streamwise eigenfunctions are in good agreement with the corresponding turbulence intensities. Within the streamwise eigenfunctions, points of discontinuity correspond to locations where the eigenfunction changes sign (i.e., direction since the eigenfunction is a vector), whereas the turbulence intensity is a magnitude composed of all the modes within the flow field. Both the streamwise turbulence intensities and eigenfunctions have symmetric peaks about the centerline of the wake, corresponding to inflection points within the shear layer profile. The agreement demonstrates that the turbulence intensity distribution is dominated by the primary wake instability mode (i.e., the arch-type vortex).

4 Conclusions

Local, two-dimensional, inviscid linear stability analysis was used to estimate the stability characteristics of the near wake of a cantilevered cylinder of low-aspect ratio. Using a *cusp method*, the size of the vortex formation region was estimated assuming that the vortex formation region corresponded to a region of absolute

instability downstream of the cylinder. It was shown mathematically that forcing results in a reduction in the size of the vortex formation region, in agreement with experimental results. Furthermore, using the simplified theory, it was possible to estimate the vortex shedding Strouhal number.

The eigenfunctions corresponding to the most amplified spatial disturbance were also compared to the experimental turbulence intensity. Within the unforced wake, there was good agreement between the turbulence intensities and the eigenfunctions, indicating that the turbulence intensity within the near wake is primarily associated with the arch-type vortex. From these data, it was possible therefore to show that it is possible to achieve reasonable approximation to the highly 3-D wake in terms of vortex formation, shedding frequency, and turbulence intensity, using a piecewise 2-D method. However, in order to improve agreement with experimental and theoretical results, a fully 3-D approach is needed.

References

1. Williamson CHK (1996) Vortex dynamics in the cylinder wake. Annu Rev Fluid Mech 28:477–539
2. Yang X, Zebib A (1989) Absolute and convective instability of a cylinder wake. Phys Fluids A 1(4):689–696
3. Drazin PG (2002) Introduction to hydrodynamic stability. Cambridge University Press, Cambridge
4. DeMauro EP, Leong CM, Amitay M (2012) Modification of the near wake behind a finite-span cylinder by a single synthetic jet. Exp Fluids 53:1963–1978
5. DeMauro EP, Leong CM, Amitay M (2013) Interaction of a synthetic jet with the flow over a low aspect ratio cylinder. Phys Fluids 25:6
6. Sumner D, Heseltine JL, Dansereau OJP (2004) Wake structure of a finite circular cylinder of small aspect ratio. Exp Fluids 37:720–730
7. Hultgren LS, Aggarwal AK (1987) Absolute instability of the gaussian wake profile. Phys Fluids 30(11):3383–3387
8. Thiria B, Wesfreid JE (2007) Stability properties of forced wakes. J Fluid Mech 57:137–161
9. Triantafyllou GS, Triantafyllou MS, Chryssostomidis C (1986) On the formation of the vortex streets behind stationary cylinders. J Fluid Mech 170:461–477

Suction and Oscillatory Blowing Applied to the Rounded Front Edges of a Square Prism

G. Lubinsky and A. Seifert

Abstract An experimental study of a 2D square prism with rounded front edges is described. The purpose of the study is to reduce the aerodynamic drag by Active Flow Control (AFC) of boundary layer separation. Robust and efficient suction and pulsed blowing (SaOB) actuators are installed inside a circular cylinder that forms the upper-front curved edge. In addition and for simplicity, steady suction is applied at the lower-front round edge. The AFC results in significant form-drag reduction, narrower wake and correspondingly an increase in the base pressure.

1 Introduction

Reducing the energy consumption of heavy vehicles is an important issue. Heavy trucks are characterized by massively separated flow which yields high form-drag resulting from low pressure at the rear surface of the vehicle. Nevertheless, not all the potential for drag reduction is at the rear-of the vehicle. The flow could separate from the vehicle's surface just downstream of its frontal face, resulting in higher drag force [1]. The traditional way for preventing boundary layer separation and elevated drag is to assure a large enough radius of the front side edges. This shaping restricts design, manufacturing, visibility distortions and more. Current design methodology significantly limits the functionality of the vehicle, limiting the field of view and reducing the internal volume of the cab. Bridging these contradicting requirements could be achieved by Active Flow Control (AFC), capable of preventing flow separation using highly energy efficient actuators [2]. The use of AFC could relax the stringent design constraints effective nowadays. For the current application, the no moving parts SaOB (Suction and Oscillatory Blowing) actuator, which was proven

G. Lubinsky (✉) · A. Seifert
School of Mechanical Engineering, Faculty of Engineering, Tel Aviv University, Tel Aviv, Israel
e-mail: gadilub@gmail.com

A. Seifert
e-mail: seifert@eng.tau.ac.il
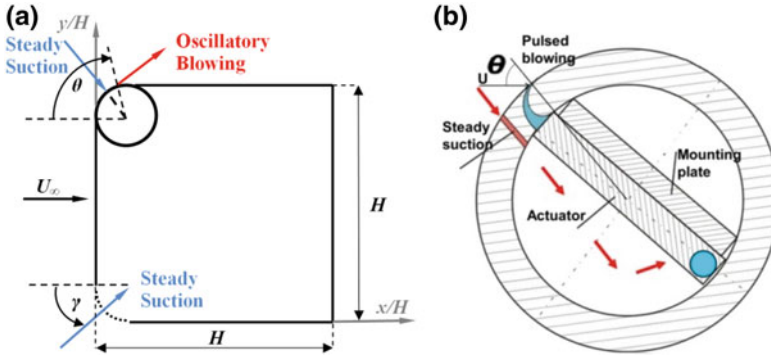
Fig. 1 a A side view sketch of the model. The coordinate system, the PBS angle, θ, and the location of the steady suction of the lower part, γ, are shown as well. The x, y origin is at the intersection of the *x/H* and *y/H* axes. **b** A cross-sectional view of the upper flow control cylinder

to be efficient tool for boundary layer separation control is used [3]. This paper will discuss the aerodynamic effects of flow control on a square prism with rounded front edges using an array of SaOB actuators and steady suction.

2 Experimental Set-Up

Wind tunnel experiments were conducted on a square prism model with equal height and length ($H = 300$ mm) which spans the wind-tunnel test section width (609 mm). The rear edges of the model are sharp, while the front edges are round with radius of $R/H = 0.127$. The model incidence was zero (Fig. 1a). The Reynolds number is 200k ($Re = U_\infty H/\nu$) and the free-stream turbulence level in the tunnel is 0.1–0.2 %. In order to examine the model performance in transitional and turbulent flows, the front side of the model was covered by two strips of Grit #60 roughness which span the entire model and located at the front surface ($0.68 < y/H < 0.85$ and $0.18 < y/H < 0.35$), since turbulent separation is desired.

The lower edge AFC device creates steady suction through arrays of holes. The suction location is altered by taping over the unused holes. The angle between the suction to the free-stream direction is defined as γ (Fig. 1a). The suction holes span 93 % of the part, their diameter is 2.5 mm, with spacing of 5 mm (staggered) and 8.18° (γ direction) between the rows. The sub-pressure is transferred via tubes that are connected to the suction pump. The tubes were connected to a symmetric pressure divider. The mass flow rate, the air density and the sub-atmospheric pressure, were all measured at the entrance (downstream) of the pressure divider.

The upper cylinder (Fig. 1b) combines steady suction and oscillatory blowing [3]. A slot of $h = 2$ mm was left open for the pulsed blowing (named PBS). Over the entire span of the cylinder, located 15° upstream of the PBS, 96 holes of 2 mm diameter were drilled for the suction. The cylinder can rotate around its axis such that, the PBS location along with the suction holes row can be altered. The PBS

angle (θ) is defined as the angle between the free-stream velocity (U_∞) and the PBS location (Fig. 1). The steady suction and pulsed blowing of this AFC device were created by 7 SaOB actuators synchronized in a π phase lag. The pulsed blowing velocities, suction velocity, SaOB array total power consumed were calibrated by Hot Wire (HW) measurements [3].

Pressure taps (diameter 1 mm) were located at the mid span of the model, with smaller spacing near the model's corners. The angle between the pressure taps that are located at lower-front edge to the free-stream direction is defined as γ'. In addition, a wake rake was installed at a distance of 940 mm downstream of the rear surface of the model ($x/H = 4.13$).

3 Discussion of Results

The effect of asymmetric steady suction was tested first. For this condition, the upper cylinder FC exits were located inside the model and the surface between the upper-cylinder to the main model was taped. The lower cylinder suction holes were taped, except for the active suction rows. Figure 2 presents the effect of steady suction for several suction locations and for the Baseline case (where all of the FC exits are covered). Cs is the normalized suction mass flow rate coefficient, calibrated with the tunnel off. The flow on the upper surface, where FC is not applied, is separated just downstream the front edge for all cases (Fig. 2a). As for the lower surface, where FC is activated, the suction changes the flow regime. Observing the Baseline pressure data (Fig. 2c), it seems that the separation takes place at $\gamma' = 57°$.

The separation point is attributed to the location where the pressure gradient abruptly vanishes. According to this information, an analysis of the effect of the suction angle, γ, could be made.

When activating the suction just upstream of the natural separation point ($\gamma = 49°$ and 57°) or downstream of it ($\gamma = 65°$ and 73°), the suction acts to accelerate the flow. As a result, the separation at the lower-front curved edge is delayed to the rear corner of the model. Consequently, both the invert base pressure ($-C_{pb}$) and the front side drag coefficient (C_{df}) decrease (Fig. 2d). For $\gamma = 65°$ and 73° the flow accelerates in a stronger manner so that C_{df} is lower, leading to a lower total drag coefficient. For suction locations $\gamma = 81°$ and 90°, the flow at suction magnitude $C_s = 0.003$ is separated. This is probably since γ is too far downstream of the natural separation point so it requires higher C_s to reattach the flow. On the other hand, for suction at $\gamma = 32°$ and 41°, upstream of the natural separation point, the flow is separated from the model surface, but will reattach further downstream (a separation bubble is formed). Consequently, $-C_{pb}$ decreases relative to the baseline value. Looking further upstream the trend seems to be different. For $\gamma = 16°$ and 24°, the flow separates just downstream of the curved edge so the total drag is high. In contrast, for suction location of $\gamma = 0°$ and 8°, the flow is attached, leading to low value of C_{dp}, but not as low as the other attached flow cases. In order to better understand these observations, the effect of suction magnitude should be discussed.
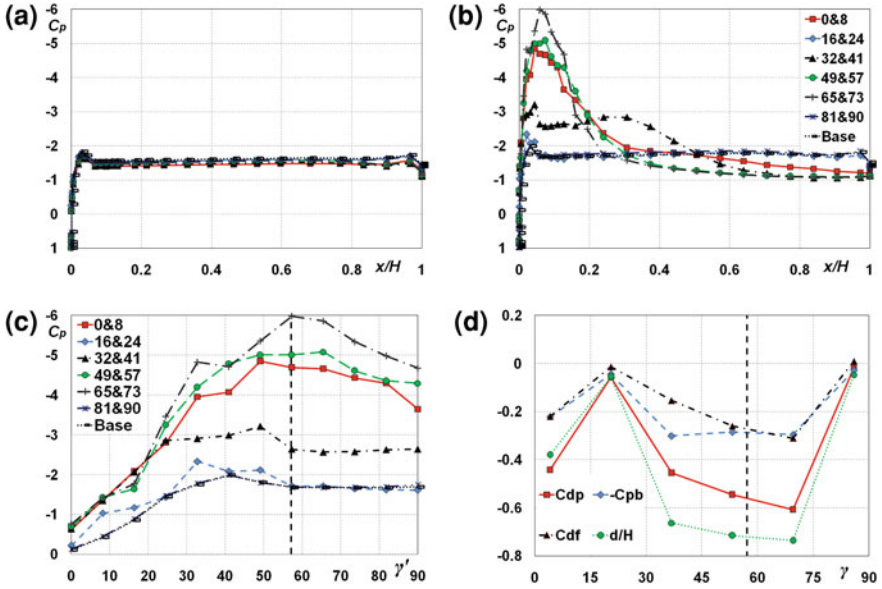
Fig. 2 The effect of steady suction (alone) from the lower-front edge. Suction applied from 2 rows of holes (uniform suction cavity) exposed to the flow. **a** C_p versus x/H of the upper surface, **b** C_p versus x/H of the lower surface. **c** A closer look on the lower front edge pressure distribution: C_p versus γ'. Legend refers to angle, γ (defined in Fig. 1), of suction holes exposed to the flow. **d** The difference between flow integral parameters (see legend) to their baseline values (FC exits are taped) versus the average location of γ. Baseline values are: $C_{dp} = 1.69$; $-C_{pb} = 1.44$; $C_{df} = 0.24$; $d/H = 1.63$. Reynolds number $Re = 200\,k$ Nominal suction coefficient $C_s = 0.003$. The vertical *dashed line* represents the separation point (γ' unit) for the baseline configuration
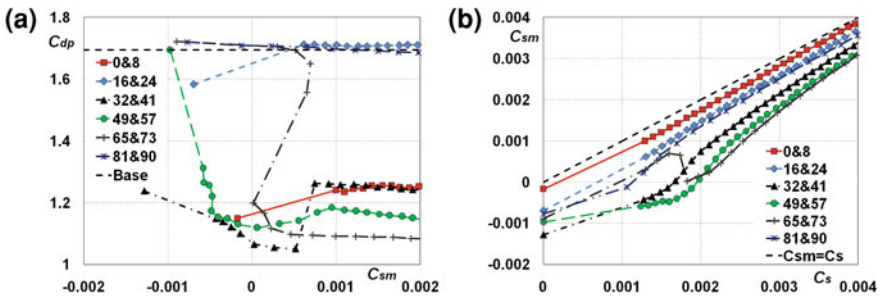
Fig. 3 **a** The pressure drag coefficient, C_{dp}, versus measured suction coefficient, C_{sm}. The *horizontal dashed line* is C_{dp} baseline. **b** Measured suction coefficient C_{sm} (wind ON) versus nominal suction coefficient C_s (when tunnel OFF). $Re = 200\,k$. The exposed suction rows are γ in legend)

Figure 3a presents the effect of measured suction coefficient, C_{sm}, on C_{dp} for several suction locations. Additionally, Fig. 3b provides the relationship between the measured suction coefficient, C_{sm}, to the nominal coefficient, C_s (calibrated for no-
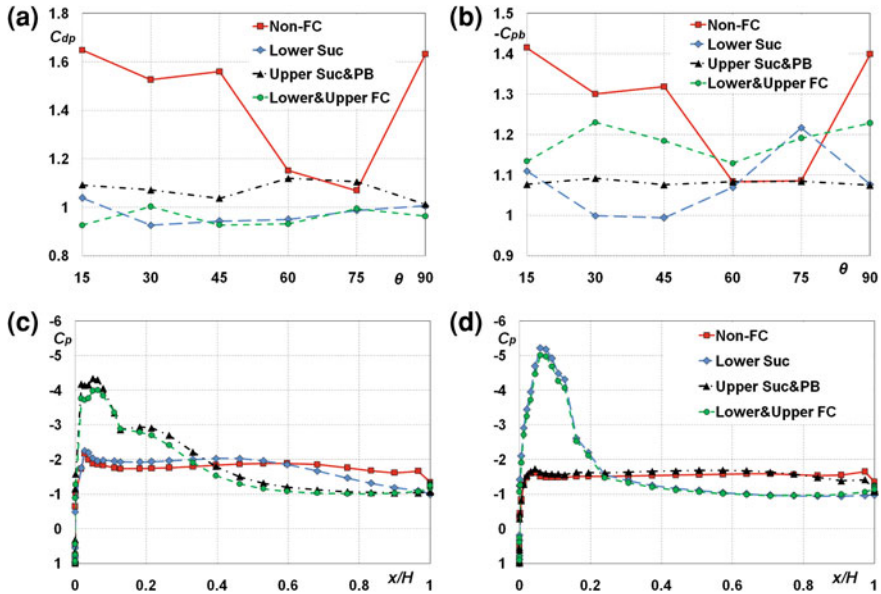
Fig. 4 The effect of several AFC configurations (see legend): Open passive FC exits; *Lower* front-edge suction $C_s = 0.0024$; *Upper* Suc&*PB* $C_\mu = 0.014$ (SaOB suction coefficient $C_s = 0.001$); or both *upper* and *lower* FC. Two *lower* suction rows $\gamma = 65$ and 73° open. The FC are closed ($C_{sm} = 0$ or $C_\mu = 0$) when AFC is not applied. $Re = 200k$: **a** C_{dp} versus PBS angle, θ. **b** C_{pb} versus PBS angle, θ. **c** C_p versus x/H on the upper surface ($\theta = 30°$). **d** C_p versus x/H on the lower surface ($\theta = 30°$)

wind condition). The difference stems from the surface C_p. For zero or low C_s, the measured mass flow rate is negative, meaning that instead of suction, on the average, blowing is created. This can be explained as follows: the FC exits are located at the front curved edge where sub-pressure is created on the external surface. For negative values of C_{sm}, the drag coefficient is not effected where the FC is activated further downstream of the natural separation point (Fig. 3a) and it is identical to the baseline value. For $\gamma = 49°$ and 57°, the suction acts to decrease C_{dp} gradually, just for low C_s values. Apparently, since it is located near the natural separation point. For $\gamma = 65°$ and 73° and 81° and 90°, where suction is applied further downstream of the natural separation point, suction is not effective up to high enough threshold magnitude. The threshold value is sensitive to the suction angle and to the Reynolds number (not shown). For γ which is further up-stream the natural separation point($\gamma = 0°$ and 8° and 16° and 24°), C_{dp} is weakly sensitive to C_s. This finding indicates that the mechanism leading to the above is probably related to transition or enhanced mixing, rather than removing the low momentum fluid from near the wall.

It was expected that combining both upper and lower FC on the two front edges, will act to reduce the drag with respect to one side activation. However, as can be seen from Fig. 4a, individual AFC from upper or lower front edges acts to reduce

C_{dp}, but the combination of both not necessarily yield the optimal drag reduction. Observing the inverted base pressure it can be seen that for most PBS locations, the combination of upper and lower FC have the undesirable effect to increase $-C_{pb}$ in relation to the one side FC (Fig. 4b). On the other hand, it acts to reduce the front drag component, C_{df} (not shown). Therefore, the total effect of this combination is relatively close to one side FC.

When AFC is not applied, the flow is separated just downstream of both the upper and lower front edges (Fig. 4c, d). Both, suction on the lower edge or SaoB actuation on the upper edge, acts to prevent separation where it applied, but does not directly affects the pressure distribution on the opposite edge. When activating FC on both the upper and lower edges, it acts to accelerate the flow for each surface in the same manner as it did for one side activation only. This behavior explains the reduction of C_{df} when both upper and lower AFC are operated since on the average a greater sub-pressure is created on the front edge. However, the inverted base pressure for this case is lower when separation occurs from one of the surfaces only (Fig. 4a), due to the short length of the model.

4 Conclusions

The effects of steady suction, oscillatory blowing and combining both techniques, including the passive effects of FC openings ($C_s = 0$) were studied. Both steady suction and pulsed blowing applied on the front round edge were found to affect the flow significantly. The actuation on the front-edges acts for certain conditions to reduce the drag force by two mechanisms. The direct impact of the FC is to accelerate the flow, leading to a greater sub pressure on the front side. In addition, AFC on the front side has the ability to delay separation and by that to alter the wake. Further study should be focused on AFC on a square model with smaller radius at the front-edges, as well as the energy efficiency of the system.

References

1. Hucho W-H (2002) Aerodynamics of road vehicles. In: Hucho W-H, Ahmed SR (eds) Butterworths, London, Boston.
2. Choi H, Jeon W-P, Kim J (2008) Control of flow over a bluff body. Ann Rev Fluid Mech 40(1):113–139
3. Shtendel T, Seifert A (2012) Drag reduction of bluff body using flow control. In: ISR aero conference, Feb 2012.

Suppression of Vortex-Induced Vibration of a Cylinder Fitted with Free-to-Rotate Parallel and Oblique Plates

G. R. S. Assi, G. S. Franco and M. S. Vestri

Abstract Experiments have been carried out on models of free-to-rotate parallel and oblique plates fitted to a rigid section of circular cylinder to investigate the effect of plate length and oblique angle on the stability of this type of VIV suppressor. Measurements of the dynamic response by trajectories of motion are presented for models with low mass and damping, free to respond in the cross-flow and streamwise directions. It is shown that, depending on a combination of geometric parameters devices might not be able to completely suppress VIV for the whole range of reduced velocities investigated. Plates with larger oblique angles turned to be less stable than parallel plates and induced high-amplitude vibrations for some specific reduced velocities.

1 Introduction and Methodology

This text reports on fundamental studies regarding the dynamic stability of a pair of free-to-rotate (f-t-r) plates acting as suppressors for the vortex-induced vibration (VIV) of a circular cylinder. Motivation comes from the offshore industry of submarine risers, which demands VIV suppressors that are efficient for low mass-damping systems without increasing drag. Suppressors employing parallel plates are already available as viable commercial solutions [7] being employed on offshore drilling risers. It is expected that small variations in the angle between the plates may affect the flow behaviour around the suppressor in order to enhance efficiency of suppression and potentially reduce drag. Nevertheless, an opposite effect may also occur and plates with large oblique angles may produce hydrodynamically unstable systems. It is known that f-t-r suppressors may experience hydrodynamic instabilities that will

G. R. S. Assi (✉) · G. S. Franco · M. S. Vestri
Department of Naval Architecture and Ocean Engineering, University of São Paulo, São Paulo, Brazil
e-mail: g.assi@usp.br
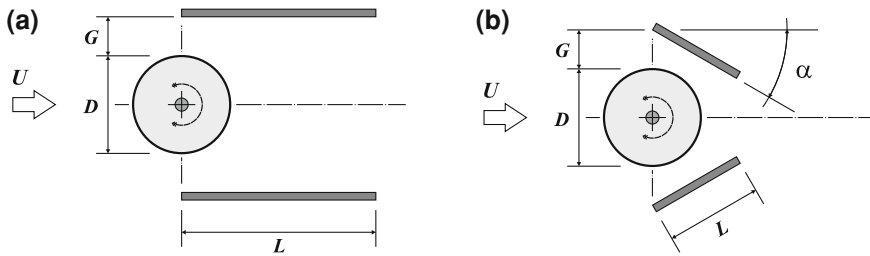
Fig. 1 **a** Parallel plates ($G/D = 0.4$, $\alpha = 0°$) and **b** oblique plates ($G/D = 0.4$, $L/D = 1.0$)

not only cause a substantial increase in drag but also prevent it from suppressing vibrations [1]. Actually, an unstable f-t-r suppressor may induce the structure into more vigorous vibrations excited by a type of flutter mechanism. Studies [1, 2] have shown that the instability of f-t-r suppressors is directly related to the level of rotational resistance encountered in the system as well as geometric parameters such as plate length.

A previous work [4] has investigated if f-t-r parallel plates would be able to find stable configurations and suppress VIV for various plate lengths. In that configuration the leading edge of the plate was practically touching the cylinder wall, creating a chamber of almost stagnant flow downstream of the cylinder and in between the plates. That configuration did not allow any flow to "ventilate" the near wake. The longer the plates, the larger would become the region of stagnant flow. In the present study we want to investigate if a small vent (a gap) between the plates and the cylinder would possibly allow high-speed flow to feed momentum into the near wake creating a more streamlined body, but at the same time disrupting the interaction between the shear layers that generates vortices. Hence we set out to investigate if f-t-r oblique plates are able to find stable configurations and suppress VIV for various plate lengths and oblique angles. Three geometric parameters were varied (Fig. 1) to characterise the suppressors: plate length (L/D), plate oblique angle (α) and the gap (G/D) measured between the leading edge of the plate and the cylinder wall. Plates cannot move in relation to each other, but the pair is free to rotate about the centre of the cylinder.

Theoretically, the gap G/D is directly related to the flow intake into the near wake and especially related to the flow behaviour in the boundary layers. The plate angle α directs momentum inwards, but it is also directly related to strong flow separation that may occur on the outer surface of the plates. Minor variations in both G/D and α would be enough to modify the flow behaviour. Actually, it is not difficult to imagine that an optimum solution to minimise vibration and reduce drag would have a small gap and a minute α. At present we are primarily concerned with the overall stability of the system rather than with optimum proportions, hence our parameters will vary in large steps as follows: $L/D = 0.5$, 1.0, 1.5, 2.0 and $\alpha = 0°$, 10°, 20°, 30°. $G/D = 0.4$ is kept fixed in this report. The investigation was divided into two experiments. In the first experiment with parallel plates (Fig. 1a), $G/D = 0.4$ and

Fig. 2 Reference experiment.
VIV trajectories of motion for
a plain cylinder
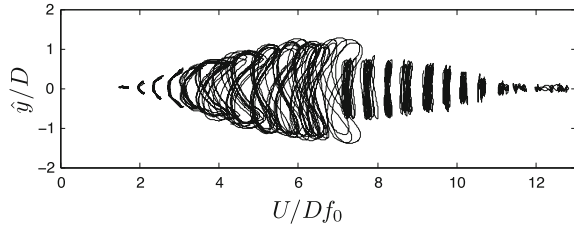
$\alpha = 0°$ were kept constant while plate length L/D was varied in four steps. In the
second experiment with oblique plates (Fig. 1b), $G/D = 0.4$ and $L/D = 1.0$ were
kept constant while plate α was varied in four steps.

Experiments were performed in the circulating water channel of NDF at the University of São Paulo, Brazil. Details about the experimental set-up can be found in
[1]. Models were mounted on a very low damping rig that allowed the cylinder to
freely respond in both cross-flow and streamwise directions. Two pairs of springs
were installed in the x and y axes to set the natural frequencies in both directions of
motion. The springs were chosen to provide the same natural frequency (f_0) measured in air in both the cross-flow and streamwise directions. Mass ratio, defined as
the ratio between the total mass and the mass of displaced fluid, was kept around
$m^* = 2.1$ for all cases. Measured structural damping ratio was $\zeta = 0.20\%$ resulting
in a mass-damping parameter around $m^*\zeta = 0.0042$, kept to the lowest possible
value in order to amplify the amplitude of response (y/D for cross-flow and x/D
for streamwise responses). Experiments were made using a fixed set of springs and
the reduced velocity range covered was between $U/Df_0 = 1.5$ and 13. The only
flow variable changed during the course of the experiments was the flow velocity U,
which alters both the reduced velocity and the Reynolds number between 3,000 and
20,000.

2 Results and Discussion

Dynamic responses are analysed only in terms of trajectories of motion in this report;
for detailed response curves please refer to [3]. Figures 2, 3 and 4 compare samples of
displacement trajectories obtained for the plain cylinder and the suppressors for the
first and second experiments, respectively. Figures show the evolution of trajectories
as reduced velocity is increased in the horizontal axis. The x-displacement axis for
trajectories has been suppressed for clarity, but it has the same scale as the y-axis. A
preliminary experiment was performed with a straight cylinder in order to validate the
set-up and methodology. The general behaviour of the cross-flow response confirms
the typical response for two-degree-of-freedom VIV of a system with the same natural
frequency in both directions, which is in good agreement with other results in the
literature [5, 6].
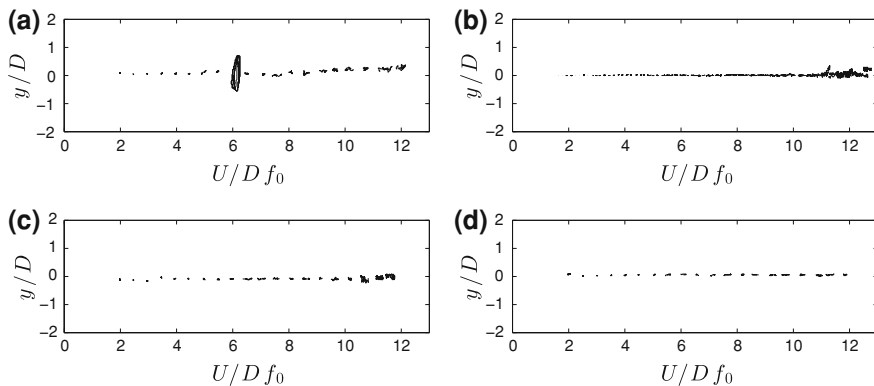
Fig. 3 First experiment. Trajectories of motion for a cylinder with parallel plates varying L/D. **a** $L/D = 0.5, \alpha = 0°$. **b** $L/D = 1.0, \alpha = 0°$. **c** $L/D = 1.5, \alpha = 0°$. **d** $L/D = 2.0, \alpha = 0°$
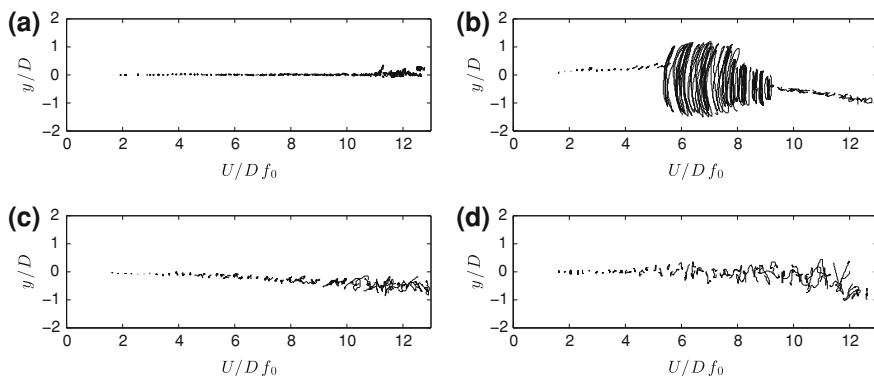
Fig. 4 Second experiment. Trajectories of motion for a cylinder with oblique plates varying α. **a** $L/D = 1.0, \alpha = 0°$. **b** $L/D = 1.0, \alpha = 10°$. **c** $L/D = 1.0, \alpha = 20°$. **d** $L/D = 1.0, \alpha = 30°$

The first experiment involves only parallel plates varying in length L/D. The general behaviour of all f-t-r parallel plates (Fig. 3) shows a remarkable reduction in vibration in both directions for most of the reduced velocity range investigated when compared to a plain cylinder (Fig. 2). All parallel plates were found to be reasonably stable for the whole range of reduced velocities. A distinct behaviour was observed for a parallel plate with $L/D = 0.5$ around reduced velocity 6.0, as seen in Fig. 3a. Most plates were able to practically mitigate vibrations below $y/D = 0.2$ for the whole range of reduced velocities, even during the cross-flow and streamwise resonances. For reduced velocities greater than 10, random vibration associated with turbulence buffeting appeared for all suppressors as well as for the plain cylinder reaching $y/D \approx 0.1$. The increase of random vibration is even more pronounced for the streamwise motion, monotonically building up from reduced velocity 8.0 and reaching $x/D \approx 0.3$ for the maximum flow speed (made clear

by data presented in [3]). Based on the first experiment we cannot affirm that all plates are perfectly stable either, since we have observed some distinct vibration for $L/D = 0.5$. We can only infer that very short plates around $L/D = 0.5$ may be more prone to instability rather than longer ones. There is a possibility that other plates may present unstable regimes as well, especially if plate length is increased beyond $L/D = 2.0$ [1]. At least one question remains open in this matter. Assi et al. [4] showed that their parallel plates with no gap ($G/D = 0.0$) were able to suppress VIV because they inhibited the interaction between the free shear layers, delaying vortex formation and consequent excitation. For a geometry with $G/D = 0.0$ the boundary layers would not separate, but the shear layers would flow along the outer surface of the plate. Now, in the present study with a large gap of $G/D = 0.4$, the flow separates around the cylinder and the free shear layers flow downstream along the inner side of the parallel plates, hence there is no obstruction to the interaction of the shear layers and, in principle, the vortex shedding mechanism could occur confined in between the plates. If vortices are being shed, how is it possible that VIV is suppressed by parallel plates with such a large gap?

The second experiment involves $1D$-long plates varying only α. Figure 4 presents new results for which we found no references in the literature to be compare with. Differently from the first experiment, variation in α showed an interesting effect over the response, especially in the cross-flow movement of the cylinder. The case for $\alpha = 0°$ suppressed vibration below $y/D = 0.1$ for most of the reduced velocity range. The only exception was found for the case for $\alpha = 10°$, illustrated in Fig. 4b, where plates were unable to stabilise and periodic vibrations were registered for a few cycles for reduced velocities between 6.0 and 9.0 reaching almost $y/D = 1.3$. Such vibrations are normally associated with resonant mechanisms such as VIV, but they can also be an effect of a flutter type of excitation due to the rotational movement of the plate. At the same time, streamwise vibration was also increased to $x/D \approx 0.3$ for a shorter resonant range between reduced velocities 6.0 and 7.0. Periodic motion registered in the trajectory plot of Fig. 4b supports the hypothesis of resonant vibration within a limited range of reduced velocity.

Figure 4b, c and d clearly show that the cylinder drifted to one side as flow speed was increased. Oblique plates, especially those with large angles, tend to be more difficult to align themselves with the flow direction, thus stabilising at a small deflected position from the centreline. Similar behaviour has been found for parallel plates longer than $L/D = 1.0$ [4]. Apart from that, all other cases showed vibration that are associated with turbulence buffeting rather than a resonant phenomenon such as VIV. Of course other excitation mechanisms may also be occurring for highly oblique plates. It is not difficult to imagine that large α generate separated flow around the plates and cylinder. The interaction between unstable reattachment bubbles and small scale vortices may be driving the cylinder into a different type of vibration. Almost all trajectory plots of Figs. 3 and 4 show random vibrations for the higher reduced velocities. Figure 4d particularly shows non-periodic vibrations for most of flow speeds.

Here, another question remains to be answered. Minute variations of α may drastically alter the flow behaviour in the region in between the plates. Is there a value

of α (as well as the other geometric parameters) to permit maximum "ventilation" of the near wake, with minimum flow separation around the plates and consequent VIV suppression with drag reduction? We believe PIV and numerical simulations could also provide important information about the flow pattern as a function of α.

3 Conclusion

Although being a fundamental study in laboratory scale, the present investigation may shed some light in the development of new geometries of commercial VIV suppressors. Results showed that plates with a large gap may present hydrodynamically unstable behaviour depending on the other geometric parameters. Nevertheless, most of the plate configurations tested were able to suppress vibrations down to $y/D \approx 0.2$ and $x/D \approx 0.2$ for most of the reduced velocity range, given the level of rotational friction of the system. In summary, we conclude that: (1) The gap between plates and cylinder, supposed to act as a vent, may cause the plate to act as a strong lifting surface detached from the cylinder. (2) Systems may present severe streamwise vibration due to strong flow separation and reattachment on the outer surface of the plates, particularly for larger oblique angles. (3) An undesirable lateral force appeared to act on the system for plates with high oblique angles causing the cylinder to drift to one side. Future work on this topic will focus on PIV analysis to investigate flow behaviour around the system, in the gap and within the near wake region in between the plates. Also, a detailed study presenting variations of all parameters is being prepared and should become available soon.

References

1. Assi GRS, Bearman PW, Kitney N (2009) Low drag solutions for suppressing vortex-induced vibration of circular cylinders. J Fluids Struct 25:666–675
2. Assi GRS, Bearman PW, Kitney N, Tognarelli M (2010) Suppression of wake-induced vibration of tandem cylinders with free-to-rotate control plates. J Fluids Struct 26:1045–1057
3. Assi GRS, Franco GS (2013) Experimental investigation on the stability of parallel and oblique plates as suppressors of vortex-induced vibration. In: The proceedings of OMAE2013, 32nd international conference on Ocean, Offshore and Arctic Engineering, 2013, Nantes, France.
4. Assi GRS, Rodrigues JR, Freire C (2012) The effect of plate length on the behaviour of free-to-rotate VIV suppressors with parallel plates. In: The proceedings of OMAE2012, 31st international conference on Ocean, Offshore and Arctic Engineering, Rio de Janeiro, Brazil.
5. Dahl J, Hover F, Triantafyllou M (2006) Two-degree-of-freedom vortex-induced vibrations using a force assisted apparatus. J Fluids Struct 22:807–818
6. Jauvtis N, Williamson C (2004) The effect of two degrees of freedom on vortex-induced vibration at low mass and damping. J Fluid Mech 509:23–62
7. Taggart S, Tognarelli M (2008) Offshore drilling riser VIV suppression devices? What is available to operators? In: The proceedings of OMAE2008, 27th international conference on Offshore Mechanics and Arctic Engineering, Estoril, Portugal.

Numerical Study of the Flow Around a Circular Cylinder with Dual Parallel Splitter Plates

D. Serson, J. R. Meneghini, B. S. Carmo, E. V. Volpe and G. R. S. Assi

Abstract A simple way to decrease the drag and oscillating lift forces in the flow around a circular cylinder consists of positioning splitter plates in the wake of the flow. In our work, a geometry consisting of two splitter plates placed close to a circular cylinder was studied. The length of the splitter plates is equal to the cylinder diameter and they are positioned in a side by side configuration parallel to the freestream velocity, with their leading-edges aligned with the cylinder center. This flow was studied using two-dimensional direct numerical simulations, with the Spectral Element Method being employed to solve the incompressible Navier-Stokes equations for Reynolds numbers in the range between 100 and 350. The results showed a strong dependence on the Reynolds number, with the splitter plates being more beneficial at the higher values of Reynolds numbers considered.

1 Introduction

In the flow around a circular cylinder, flow separation leads to the formation of two shear layers transporting vorticity with opposite signs. The interaction between these layers causes vortex shedding, significantly increasing the drag force and generating an oscillating lift force that may cause what is known as vortex-induced vibration (VIV). Structures affected by VIV (such as offshore oil production risers and exhaust gas stacks) are subject to fatigue due to these oscillating loads.

D. Serson · J. R. Meneghini (✉) · B. S. Carmo · E. V. Volpe
NDF, Department of Mechanical Engineering, POLI,
University of São Paulo, São Paulo, Brazil
e-mail: jmeneg@usp.br

G. R. S. Assi
NDF, Department of Naval Architecture and Ocean Engineering, POLI,
University of São Paulo, São Paulo, Brazil
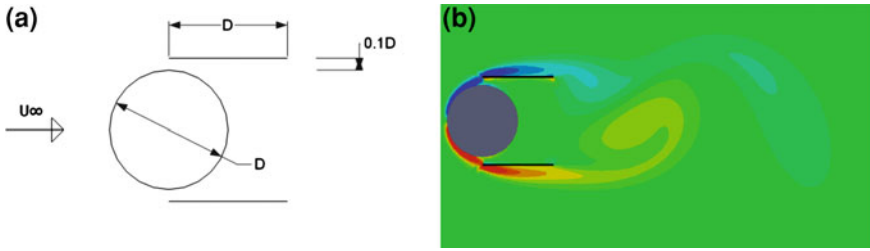
Fig. 1 On the *left*, schematic drawing of the studied geometry. On the *right*, vorticity contours for a simulation with $Re = 200$

A simple way to decrease these forces consists of positioning splitter plates in the wake of the flow. The splitter plates can prevent the interaction between the shear layers, forcing the vortices to form further away from the cylinder, leading to a decrease in the lift and drag forces. The present study focuses on a configuration consisting of two parallel splitter plates of length equal to the cylinder diameter positioned with a small gap to the cylinder surface, as shown in Fig. 1a. Figure 1b presents an example of a numerical result for Reynolds number $Re = 200$ using this configuration.

Most of the works available in the literature related to the use of splitter plates consider a single splitter plate located in the wake centerline, where the geometry can be defined by the splitter plate length L and the gap between the cylinder and the splitter plate g. The first works showing results for this geometry had the objective of validating physical explanations for the vortex shedding phenomenon, using the splitter plate as a method of suppressing the shear layers interaction. Roshko [14] carried out experiments using both attached and detached splitter plates in a circular cylinder wake, concluding that the drag coefficient was reduced for gaps below a critical values. Similar results were obtained by Bearman [5] for a splitter plate near a blunt trailing-edge body, where the base pressure coefficient suffered a sharp increase for $L/h < 1$.

Other experimental studies using a single splitter plate in the wake centerline of a circular cylinder include [1, 7, 9]. More recently, a few numerical studies related to this flow have been developed, including [6, 12, 13].

Unlike the single splitter plate case, the use of a configuration consisting of two parallel splitter plates have received little attention so far. Grimminger [8] performed experiments to study the effect of different types of guide vanes in the drag and vibration of circular cylinders. One of these vanes consisted of a geometry similar to the one analyzed in the present paper, and led to a reduction in the drag and suppressed vortex induced vibration. Assi et al. [2] also considered a similar geometry in a experimental study to verify the viability of several vortex-induced vibration suppressors. Their study was performed at a Reynolds number around 30,000 and used splitter plates longer than the present study, with length $1.5D$, which caused a reduction of 33 % in the drag. Also, [3] studied numerically a configuration with two parallel splitter plates attached to the cylinder at different angular positions,

considering only the range $20 \leq Re \leq 160$. In this last work, the splitter plates were relatively short ($L/D = 0.3$), and its ability to reduce the drag and lift forces was strongly dependent on the Reynolds number and on the angular position of the splitter plates.

From what was presented above, it is clear that the flow around a circular cylinder with two parallel splitter plates has not been intensively studied yet, specially regarding the limited amount of detailed numerical results. This paper presents results of two-dimensional direct numerical simulations for one possible geometric configuration, with the Reynolds number being varied in the range $100 \leq Re \leq 350$. The paper is organized as follow. Section 2 briefly presents the numerical method employed in the simulations. Then, Sect. 3 shows the results and Sect. 4 summarizes the main conclusions of the work.

2 Numerical Method

We consider an incompressible viscous flow, which is governed by the Navier-Stokes equations. These equations can be written in non-dimensional form using the cylinder diameter as the reference length and the free-stream flow speed U_∞ as the reference velocity:

$$\frac{\partial \mathbf{u}}{\partial t} = -(\mathbf{u}.\nabla)\mathbf{u} - \nabla p + \frac{1}{Re}\nabla^2\mathbf{u}, \tag{1}$$

$$\nabla.\mathbf{u} = 0, \tag{2}$$

where $\mathbf{u} \equiv (u, v, w)$ is the velocity field, t is the time, p is the static pressure and Re is the Reynolds number. The pressure is assumed to be scaled by the constant density ρ.

In the simulations, these equations were discretized in the two-dimensional domain following the Spectral/hp method as described in Karniadakis and Sherwin [10], and solved by time integration using the stiffly stable splitting scheme described by Karniadakis et al. [11].

The boundary conditions for the simulations were: on the left, upper and lower boundaries the velocity was set to a unity value in the x direction (inflow condition); on the right boundary, the normal derivative of the velocity was set to zero (outflow condition); and in the cylinder and splitter plates surfaces the velocity was set to zero (wall boundary condition). Some simulations were also performed using a slip-wall boundary condition (zero normal derivative for the tangential velocity and zero normal velocity) on the splitter plates, while keeping the no-slip wall boundary condition for the cylinder surface. This was motivated by a previous study by the authors that showed that this approximation is able to capture the splitter plate effect on the flow for a single splitter plate located at the wake centerline. However, in the present study this type of boundary condition was not able to capture the influence of

the splitter plates accurately, leading to errors around 10 % for the Strouhal number and 20 % for the drag coefficient.

In order to make the results mesh independent and to guarantee their accuracy, several convergence tests were performed following a procedure similar to that of [4]. The goal of these tests was to obtain the required polynomial order of the basis functions and the time step that will lead to simulations with good spatial and temporal resolution, and to define the size of the domain that will make the effects of blockage negligible. The size of the domain was based on a previous study by the authors, extending from -52 to 55 diameters in the stream direction and from -60 to 60 diameters in the crossflow direction. The spatial convergence was guaranteed by running tests with basis functions of increasing polynomial orders for $Re = 200$, until the error (relative to the next simulation) in the forces and in the Strouhal number were below 1 %. Using this criterion, the polynomial order for the simulations was 9. A similar procedure was applied to define a time step of 0.001 non-dimensional units.

3 Results

The two-dimensional simulations were carried out for values of Reynolds numbers in the range between 100 and 350, with increments of 50. Since the flow around a circular cylinder becomes three-dimensional at $Re \approx 190$, the results beyond these value of Reynolds number can only be considered as a first approximation to the effect of the splitter plates on the flow.

Figure 2 compares the total forces around the cylinder with the splitter plates to the forces acting on a plain cylinder, for several values of Reynolds number. In Fig. 2a the drag force is presented along with its viscous and pressure components. The influence of the Reynolds number is remarkable: at $Re = 100$ the splitter plates lead to an increase in the drag force, due to the viscous contribution; however, as the Reynolds number is increased, this difference in viscous drag becomes less pronounced, while the configuration with splitter plates starts to present lower values of pressure drag. The compositions of both these factors leads to the splitter plates reducing the drag only for $Re > 200$. Also, the reduction of drag at $Re = 350$ appears to be consistent with the results from [2], which show that at Re around $30,000$ a configuration similar to the one studied here led to a drag reduction from 1.03 to 0.69.

Figure 2b shows that the influence of the splitter plates on the lift force is also strongly dependent on the Reynolds number. In this case, however, the splitter plates always lead to reductions in the lift force, with the effect being more pronounced at higher values of Reynolds number. Also, it was observed that the results for the Strouhal number followed a trend similar to the lift coefficient.

To obtain further information on the flow physics, vorticity and pressure contours (not presented here) were obtained over half a period of vortex shedding. It was observed that most of the pressure fluctuations occur at the splitter plates, opposed to smaller variations on the cylinder surface. Also, the zero lift configuration is
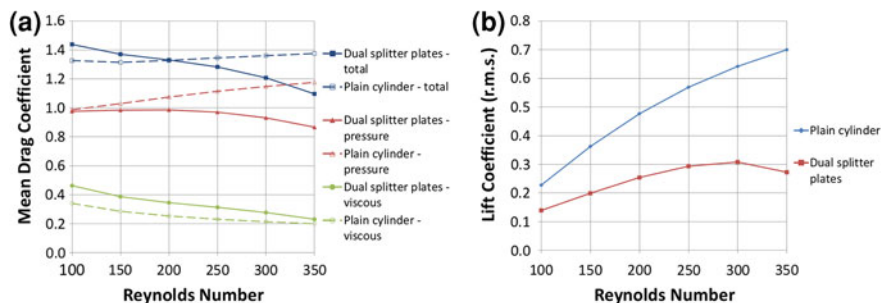
Fig. 2 Comparison between forces for plain cylinder and cylinder with dual splitter plates at different values of Re **a** mean drag coefficient and its pressure and viscous components; **b** fluctuating lift coefficient measured by its root-mean square value

characterized by a balance between outward forces on both plates, with significant pressure differences inside the cavity formed by them. This zero lift configuration occurs when a vortex is starting to form near one of the splitter plates. As this vortex grows, the pressure inside the cavity becomes more homogeneous, such that there is a reduction in the lift force at the splitter plate on the opposite side of the vortex, breaking the aforementioned balance and generating a lift force on the overall system. At the maximum lift configuration, the pressure inside the cavity is almost the same at both splitter plates.

4 Conclusions

The ability of a pair of parallel splitter plates to reduce the forces around a circular cylinder was examined using two-dimensional direct numerical simulations based on the Spectral Element Method. Both the lift and the drag forces presented strong dependence on the Reynolds number in the range $100 \leq Re \leq 350$, with the use of the splitter plates being more beneficial at higher Reynolds numbers.

References

1. Apelt CJ, West GS, Szewczyk AA (1973) The effects of wake splitter plates on the flow past a circular cylinder in the range $10^4 < R < 5 \times 10^4$. J Fluid Mech 61(1):187–198
2. Assi GRS, Bearman PW, Kitney N (2009) Low drag solutions for suppressing vortex-induced vibration of circular cylinders. J Fluids Struct 25:666–675

3. Bao Y, Tao J (2013) The passive control of wake flow behind a circular cylinder by parallel dual plates. J Fluids Struct 37:201–219
4. Barkley D, Henderson RD (1996) Three-dimensional floquet stability analysis of the wake of a circular cylinder. J Fluid Mech 332:215–241
5. Bearman PW (1965) Investigation of the flow behind a two-dimensional model with a blunt trailing edge and fitted with splitter plates. J Fluid Mech 21(2):241–255
6. Chieregatti BG, Carmo BS, Volpe EV (2012) An investigation of the influence of splitter plates on the vortical wake behind a circular cylinder in cross-flow. In: 10th World Congress on computational mechanics, pp 1–14.
7. Gerrard JH (1966) The mechanics of the formation region of vortices behind bluff bodies. J Fluid Mech 25(2):401–413
8. Grimminger G (1945) The effect of rigid guide vanes on the vibration and drag of a towed circular cylinder. David Taylor Model Basin, Report 504
9. Igarashi T (1982) Investigation on the flow behind a circular cylinder with a wake splitter plate. Bulletin JSME 25(202):528–535
10. Karniadakis GE, Sherwin SJ (2005) Spectral/hp element methods for computational fluid dynamics, 2nd edn. Oxford University Press, Oxford
11. Karniadakis GE, Israeli M, Orszag SA (1991) High-order splitting methods for the incompressible navier-stokes equations. J Comput Phys 97(2):414–443
12. Kawai H (1990) Discrete vortex simulation for flow around a circular cylinder with a splitter plate. J Wind Eng Ind Aerodyn 33(1–2):153–160
13. Kwon K, Choi H (1996) Control of laminar vortex shedding behind a circular cylinder using splitter plates. Physics Fluids 8(2):479–486
14. Roshko A (1954) On the drag and sheddind frequency of two-dimensional bluff bodies. Tech. Rep. 3169, NACA Technical Note.

Part VIII
Separation in Diverging Channel and Duct Flows

Laminar Separation Bubbles in Two-Dimensional Straight-Diverging-Straight Channel Flows

Mamta Jotkar, José Miguel Pérez, Vassilis Theofilis and Rama Govindarajan

Abstract Geometries with sudden expansion have been a subject of study for decades now, owing to its engineering applications. While attention has been lavished on flow through symmetric channels with sudden expansion (SE) and backward-facing step (BFS), channels with other divergent angles are studied far less. Straight-diverging-straight (SDS) channels with finite angle of divergences have been studied here. Our focus is on the formation of the laminar separation bubble, typically in the diverging region, and its reattachment downstream. Computations have been carried out to estimate the effect of various parameters such as the angle of divergence (α), the outlet to intet height ratios (D/d) and the Reynolds numbers (Re) on the formation of the recirculation bubble. The extreme case with $\alpha = 90°$ can be compared to the flow through a symmetric sudden-expansion (SE) flow. The base flow obtained from the two open source codes is characterized for the formation of laminar separation bubble for very low Reynolds numbers (Re) in the parametric space including the angle of divergence, α and the expansion ratio, $\kappa = D/d$ and Re.

1 Introduction

The critical Reynolds number in a plane channel or the plane Poiseuille flow (PPF) is 5772.2 according to the linear stability theory. However, the presence of a small divergence in the channel destabilizes the flow drastically. The effect of change in geometry on the flow properties of system can be exploited for various

M. Jotkar (✉) and R. Govindarajan
Tata Institute of Fundamental Research, Centre for Interdisciplinary Sciences,
Hyderabad, India
e-mail: mamtaj@tifrh.res.in

J. M. Pérez and V. Theofilis
School of Aeronautics, Universidad Politécnica de Madrid, Plaza del Cardenal Cisneros 3,
28040 Madrid, Spain

engineering applications such as heat combustion and microfluidic devices. The problem of sudden-expansion channels (SE) and that of the backward-facing step flow (BFS) has been studied in great detail over decades. The link between the PPF and SE is missing and it will be interesting to understand the transition mechanism in such shear flows. As a primary step towards aiming this; it would be useful to analyse the characteristics of the base flow and the formation of recirculation zones as a function of the Reynolds number in the parameteric space.

Shapira et al. [7] studied the first bifurcation by linear global stability analysis and characterized the laminar separation bubble formation for such SDS flows and the extreme case included that of the SE flow. It was also found that at very low Reynolds numbers (Re) the flow is symmetric and steady with no recirculation zones. With an increase in Re two symmetric recirculation zones of equal lengths are formed at the walls; the length of which increase almostly linearly with Re. With a further increase in Re the two-dimensional flow undergoes a pitchforke bifurcation, loosing its symmetry and thus leading to a new steady asymmetric base state. Further increase in Re leads to breakdown of the steady asymmetric states and further destabilization of the flow. This has been shown experimentally by Sobey [8] for different angle of divergence, α.

The SE case has been extensively studied over a decade [1–3, 6]. However, the SDS flows have been studied far lesser. The SDS flow has been investigated for its stability criterion by Sobey [8], Shapira et al. [7], Swaminathan et al. [9].

This work concentrates on the two-dimensional base flow analyses through the SDS and SE channels in terms of the formation of the recirculation zones for the various parameters involved including the angle of divergence of the channel, α and the expansion ratio, $\kappa = D/d$. The separation and reattachment points of the flows at very low Re have been compared to that obtained by Shapira [7] qualitatively. Thus, confirming the trend in the recirculation zone formation.

2 Problem Formulation

Consider the motion of a viscous fluid in a channel with straight section followed by a diverging section and a straight section in the end (SDS channels) as shown in the Fig. 1 with variable aspect ratio (κ) i.e. outlet height ($2D$) to inlet height ($2d$) i.e. $\kappa = D/d$ and variable angle of divergence, α. A two-dimensional flow is considered here with homogeneity in the z-direction. The origin of the co-ordiante system coincides with the centreline at the inlet. The beginning of the diverging section, x_d is kept constant i.e. 10 in this work. The end of the diverging section, x_e depends on the aspect ratio, κ and the angle of divergence, α. The total domain length, L considered is 100. The Reynolds number, Re is defined on the channel half-width (d) at the inlet and the maximum velocity at the inlet. The extreme case of $\alpha = 0°$ can be compared to that of a PPF while that of $\alpha = 90°$ can be compared to that of the SE. In this paper, the channels with angle of divergence, $\alpha = 0°, 5°, 15°, 30°, 45°, 60°$ and $90°$ and aspect ratios, $\kappa = 2$ and 3 have been studied in detail.
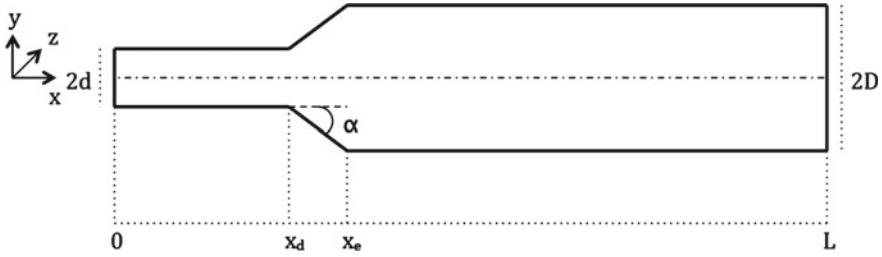
Fig. 1 The flow geometry for the straight-diverging-straight channels. The origin of the co-ordinate system is the centreline of the *inlet* as shown above. D and d are the channel half-widths at the outlet and the inlet respectively; where $D = \kappa d$. α is the angle of divergence varying from 0° to 90° systematically. x_d is the beginning of the diverging section while x_e is the end of the diverging section respectively. L is the total domain length of the channel

The fluid motion is governed by the incompressible Navier-Stokes equations, written in non-dimensional form as,

$$\frac{\partial \mathbf{u}}{\partial t} + \mathbf{u} \cdot \nabla \mathbf{u} = -\nabla p + \frac{1}{Re}\nabla^2 \mathbf{u} \ \ in \ \ \Omega, \tag{1}$$
$$\nabla \cdot \mathbf{u} = 0 \ \ in \ \ \Omega,$$

where $\mathbf{u}(\mathbf{x}, t)$ is the velocity field, $p(\mathbf{x}, t)$ is the static pressure, Ω is the computational domain.

The domain length, L is large enough so that the results are independent of it. The boundary conditions used are parabolic inflow and no-slip boundary condition at the walls for both the codes, Nektar++ and FreeFem++. For the outlet, the traction free condition i.e. $p - Re^{-1}\partial_x u = 0, \ \partial_x v = 0$ is used in FreeFem++. For Nektar++, the outlet boundary condition is as used is homogenous neumann for the velocity components and homogenous dirichlet for the pressure.

3 Numerical Considerations

The open-source code implemented here for obtaining the base flow is FreeFem++ which is based on finite element method (See http://www.freefem.org/ff++ for more details). The Navier-Stokes equations in two-dimensions have been solved at low Reynolds numbers to obtain the steady, converged solution by an iterative Newton method which requires a good initial guess. The base state at the different Re is obtained successively from that of a creeping flow approximation. The Newton method requires the inversion of a non-symmetric sparse matrix of size $N_b = 2N_{2b} + N_{1b}$ where N_{1b} and N_{2b} are the number of nodes associated with the elements $P1$ and $P2$ respectively. The inversion is carried out by the use of the UMFPACK library which performs a sparse LU factorization. Steady 'converged'

Table 1 Recirculation bubble at $\alpha = 90°$ for the case, 1:3 or expansion ratio $\kappa = 3$

Freefem++				Nektar++			
Re x_{lb}	x_{lt}	$R(\%)$	$R(x - x_d, y)$	x_{lb}	x_{lt}	$R(\%)$	$R(x - x_d, y)$
70 4.734667	4.751346	9.066027	(1.48, 1.19625)	4.710855	4.658638	9.05335	(1.428, −1.185)
77 5.187589	5.237220	9.338586	(1.6, 1.1925)	5.218305	5.081855	9.33548	(1.5395, 1.192)
80 5.326284	5.499954	9.439642	(1.63, −1.1925)	5.561157	5.129609	9.44249	(1.62392, 1.18617)
85 5.781986	5.718781	9.596362	(1.72, 1.1925)	6.655223	4.472236	9.65108	(1.61083, 1.20983)

x_s and x_r are the separation and reattachment points while x_{lb} and x_{lt} is the length of the recirculation bubble at the *bottom* and *top* walls respectively. R is the percentage of maximum reverse flow given as $R = -|u_{\min}/u_{\max}|\%$ while $R(x - x_d, y)$ is the location of its occurence. The x-location is rescaled as the distance from the expansion corner; x_d being the edge of the expansion corner. For this case of $\alpha = 90°$ the points x_s and x_d coincide. (Re is defined based on the definition used in [7] i.e. on channel width as opposed to channel half-width as defined in the result of our results)

base flow can be obtained by this methods at supercritical Reynolds numbers too. The results are compared to that obtained by Nektar++ which is based on finite element/hp formulation [5]. The results obtained from the two different codes are consistent as seen in Table 1. The convergence in terms of the grid and cross-validation between the two codes is as studied in [4].

4 Results

The base flow is investigated in order to characterize the laminar separation bubble formation for the various parameters involved. The pressure gradient caused due to the variable aspect ratios of the channel causes the laminar flow to separate from the walls which can be analysed by the change of sign in the skin friction co-efficient,

$$C_f(x) = \frac{-2}{Re}\mathbf{t} \cdot (\nabla \mathbf{u} + \nabla \mathbf{u}^t) \cdot \mathbf{n}, \tag{2}$$

where t and n are the tangential (oriented downwards) and normal (oriented outwards from the solid wall) directions of the fluid flow.

The flow typically reattaches itself to the walls further downstream of the channels. The distance between the reattachment point (x_r) and the point of separation (x_s) is the length of the laminar separation bubble (x_l). The amount of recirculation (R) is given as the percentage of the magnitude of the fractional maximum reverse flow. The flow separates forming bubbles at both the two walls. At the Re considered here the recirculation zone is symmetric and steady. As shown in Fig. 3, the bubbles appear first beyond a certain Re thereafter increasing almost linearly with Re which is consistent with the available literature [6–8]. With a further increase in Re the
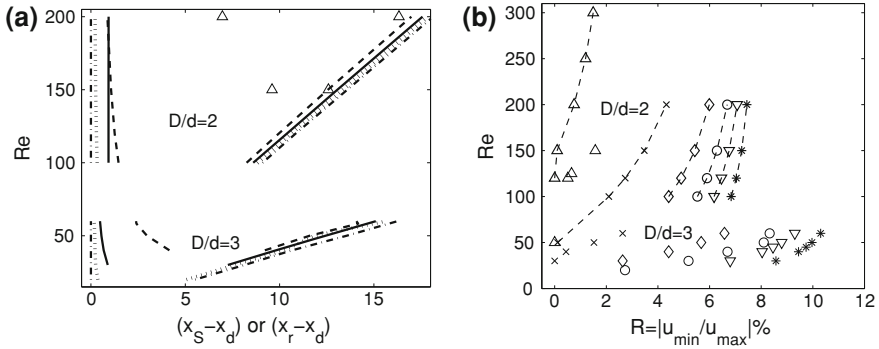
Fig. 2 a The separation point, $x_s - x_d$ (*left*) and the reattachment point, $x_r - x_d$ (*right*) (x_d being the edge of the expansion corner) as a function of *Re* for the different expansion ratio, $D/d = 2$ (*top*) and $D/d = 3$ (*bottom*). The *triangle* ($\triangle$), *dash lines* (- -), the *thick lines* (–), the *dotted lines* (..) and the *dash-dot lines* (-.-) correspond to $\alpha = 5°, 15°, 30°, 45°$ and $90°$ respectively. **b** The percentage recirculation for different *Re* and expansion ratio, $D/d = 2$ [*top, dash lines* (- -)] and 3 (*bottom, no lines*). The *triangle, times, diamond, opencircle, bigtriangledown* and *asterisk* correspond to $\alpha = 5°, 15°, 30°, 45°, 60°, 90°$ respectively
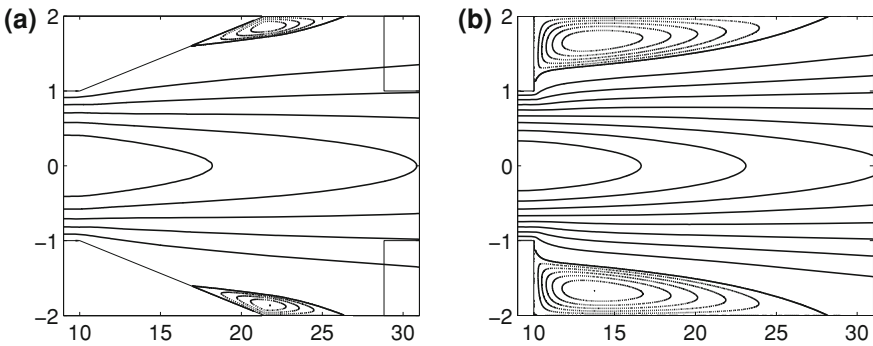
Fig. 3 The base flow for the aspect ratio $\kappa = 2$ and $Re = 200$ at the different α. The *dotted line* represent reverse flow while the *solid line* represents forward flow. (A part of the domain close to the recirculation bubble has been shown in this case with total domain length, $L = 100$)

separation point, x_s starts moving towards x_d, the corner of expansion; while the reattachment point, x_r starts moving further downstream. It is worth mentioning that the laminar flow separates just at the corner i.e. at $x_s = x_d$ for the case $\alpha = 90°$. The separation point for the flow in the rest of the cases with different α is further downstream. The length of the bubble (x_l) in terms of the separation (x_s) and reattachment points (x_r) and the percentage recirculation ($R = u_{min}/u_{max}$ %) as a function of α, *Re* and $\kappa = D/d$ is shown in the figure. The observed trends are qualitatively similar to that obtained by Shapira et al. [7]. However, no quantitative data is provided for comparsion for the same. The length of the bubble increases drastically upto a certain value of $\alpha \approx 15°$ and thereafter the change is rather gradual.

Figure 2 shows the recirulation bubble for $\alpha = 5°$ and $90°$ and the $\kappa = 2, \ Re = 200$. Thus, the base flow has been evaluated to study the effect of channel geometry and Reynolds number on the formation of the recirculation bubble in the SDS channels.

References

1. Alleborn N, Nandakumar K, Raszillier H, Durst F (1997) Further contributions on the two-dimensional flow in a sudden-expansion flow. J Fluid Mech 330:169–188
2. Battaglia F, Tavener SJ, Kulkarni AK, Merkle CL (1997) Bifurcation of low reynolds number flows in symmetric channels. J Am Inst Aeronaut Astronaut 35:99–105
3. Drikakis D (1997) Bifurcation phenomena in incompressible sudden expansion flows. Phys Fluids 9:76
4. Jotkar MR, Pérez JM, Theofilis V, Govindarajan R (2013) A unified framework for global instability mechanims in the plane channel, diverging channel and backward-facing step flow. In: 43rd American institute of aeronautics and astronautics, San Diego, CA, p 2463.
5. Karniadakis GE, Israeli M, Orszag SA (1991) High-order splitting methods for the incompressible navierstokes equations. J Comput Phys 97(2):414–443
6. Lanzerstorfer D, Kuhlmann HC (2012) Global stability of multiple solutions in plane sudden-expansion flow. J Fluid Mech 702:378–402
7. Shapira M, Degani D, Weihs D (1990) Stability and existence of multiple solutions for viscous flow in suddenly enlarged channels. Comput Fluids 18:239–258
8. Sobey IJ (1985) Observation of waves during oscillatory channel flow. J Fluid Mech 151:395
9. Swaminathan G, Sahu KC, Sameen A, Govindarajan R (2011) Global instabilities in diverging channel flows. Theoret Computat Fluid Dyn 25:53–64

Characterisation of the Transient Dynamics of a Controlled Separated Flow Using Phase Averaged PIV

C. Raibaudo, F. Kerhervé and M. Stanislas

Abstract The transient dynamics of a high Reynolds number two-dimensional boundary layer flow undergoing a massive separation is investigated. A spanwise array of pulsed round jets, located upstream of the separated region, is used as actuators. Spatial and temporal organisation of the separation and reattachment processes are investigated using phase-averaged PIV measurements in combination with the survey of wall friction along the separation region with the overall objective to develop closed-loop controllers. While different sets of parameters including freestream flow to jet velocities ratio, duty cycle and jets frequency have been considered in the overall work, preliminary results for two cases are presented within.

1 Introduction

Extensive research has been done in the area of separated flows in order to understand the dominant flow structures in the separated shear layer and the general characteristics of the flow field. Since this flow phenomena is generally accompanied by negative effects on the performance, controlling the separation has gained in interest. Active control based on fluidic actuators is believed to offer the best potential in terms of performance and flexibility compared to passive control based on mechanical devices. Among active control devices, extensive studies have been conducted on pulsed vortex fluidic generators [3–6] for which the flow rate needed to reattach the flow is smaller than for continuous actuation. These devices introduce vortices into the flow which interact with the natural instabilities of the boundary layer and re-energize the latter. Before attempting to develop any robust closed-loop controllers, the flow physics under consideration must be characterized. In particular, the transient dynamics leading to reattachement or separation must be fully understood. This is the

C. Raibaudo · F. Kerhervé (✉) · M. Stanislas
Laboratoire de Mécanique de Lille, UMR CNRS 8107, Lille, France
e-mail: franck.kerherve@ec-lille.fr

objective of the present work. The flow considered here is a high Reynolds number turbulent boundary layer with massive separation. Open-loop control is performed using an array of round jets located upstream of the separation. The influence on the transient dynamics of the flow of different control parameters is examined in details using phase-averaged PIV measurements and wall-friction surveys.

2 Flow Configuration and Experimental Set-up

The experiments are conducted in the closed-loop boundary layer wind-tunnel at Laboratoire de Mécanique de Lille. The boundary layer developing section is 20 m × 2 m × 1 m. The maximum free stream velocity is 10 m/s. Full details on the wind tunnel can be found in [1].

At 14.4 m from the beginning of the test section, the boundary layer encounters a two-dimensional ramp. The ramp model is shown in Fig. 1a. It is made of four parts: (1) a smooth converge part with contraction ratio of 0.75, (2) an articulated 2.14 m long flat plate with an angle of $\alpha = -2°$ relative to the floor of the wind-tunnel, (3) a short flap with angle of $\beta = -22°$, and finally, (4) a flexible plate ensuring smooth connection between the end of the flap and the floor of the wind tunnel. For the free stream velocities used in the present work and details below, and with the given ramp configuration given, the flow separates at the sharp edge between the inclined flat plate and the flap. The height H_{step} of the ramp at the separation line is 17.5 cm. A large separation bubble is observed along the flap, while the flow reattaches downstream on the floor of the wind-tunnel. At $U_\infty = 10$ m/s the boundary layer thickness just before separation is $\delta = 19$ cm.

A spanwise array of 22 round jets located upstream of the flap performs the actuation. Festo valves are used to generate continuous and pulsed jets. To fix the flow rate, a sonic throat with a 1.3 mm^2 cross section is implemented downstream of the valve. These actuators have been fully characterised by [7]. The jets are blowing upstream with an angle of 125° relative to the main flow, and that is 35° relatively to the wall-normal. This configuration generates co-rotating vortices which are transported downstream, re-energizing the boundary layer and forcing it to almost reattach—reduction about 90 % of the length of separation—along the wall [2]. The spacing between two consecutives jets is about 0.43δ and the exit jet diameter is 0.03δ. The excitation signal consists of pulsed or continuous square signals with a given duty cycle and frequency leading to periodic sequences during which the flow is successively partly/fully reattached and separated. The separation and reattachement phases are examined for different values of the control parameters. These are here considered in open-loop control tests with the objective of investigating the receptivity of the flow. The overall test matrix is given in Table 1.

Two-component two-dimensional PIV measurements are performed. The region covered includes the region upstream of the separation where actuators are located, the region of separation and the region where the flow reattaches. Full details on the optical set-tup can be found in [2].
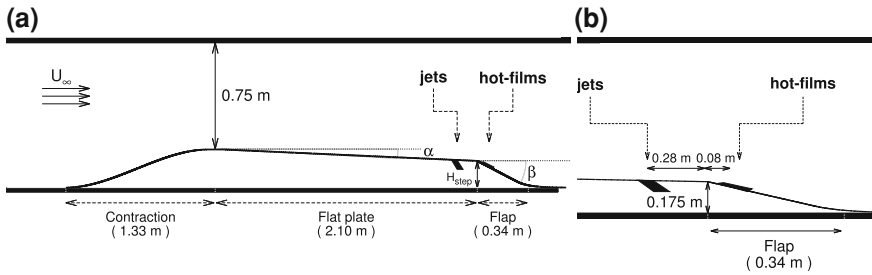
Fig. 1 a Scheme of the ramp model (AVERT). **b** Location of the hot-film sensor relative to the actuators

Table 1 Test matrix of the control parameters

U_∞ (m/s)	5	10											
VR	5	3				5							
f(Hz)	4	8		80	∞	4	8		10	80			∞
DC	50	50	80	50		50	80	50	80	50	50	80	
nº	I	II	III	IV	V	VI	VII	VIII	IX	X	XI	XII	XIII

The velocity ratio VR is defined by U_{jets}/U_{local}. Only case nº VI and XIII are presented here

In addition, hot-film sensors located on the inclined flat plate inside the separation bubble are used as illustrated in Fig. 1b. The time response of the hot-film is negligeable compared to the dynamics we are interested here.

Both measurements are synchronised with the actuators thanks to a master clock. Sequences of 10 s are repeated. These sequences are divided into two phases corresponding to 5 s of forcing for flow reattachement (jets actuation turns on) and 5 s during which the flow is unforced and recovers a separated state (jets actuation turns off). For each set of parameters of the test matrix, 600 of these sequences are acquired to ensure statistical convergence. The duration of the two phases of a single sequence has been chosen based on the results of [7] and allows the flow to reach stationary attached/separated states before a new transition.

To perform temporal analysis of the transient dynamics during the separation and reattachement regimes of the flow, PIV measurements are operated under a phase-averaging procedure. Time instants (hereafter denoted "phases") of the transition are selected and PIV fields corresponding to these phases are collected and averaged. It is noteworthy that by shifting in time the intial PIV phase, an increase of the time resolution of the final phase-averaged description can be obtained.

3 Experimental Results

Two controlled configurations are here considered: continuous and pulsed blowing cases XIII and VI respectively (see Table 1).

The hot-film response for the continuous blowing jets case is shown in Fig. 2a. These were obtained by averaging over 600 successive sequences of controlled and
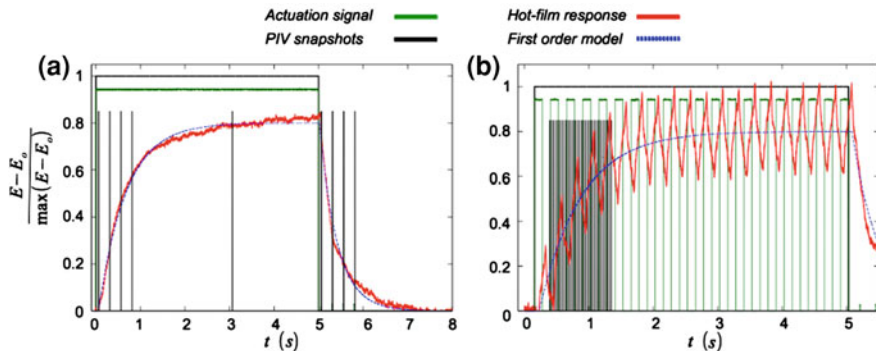
Fig. 2 Averaged hot-film response to **a** continuous jets blowing and **b** pulsed jet blowing

uncontrolled phases as described above. The red line shows the hot-film response to jets actuation driven by the signal shown as the green line. The hot-film response is found to be characterised by two regimes corresponding to the control and uncontrolled phases. In the first regime, between $t = 0$ s en $t = 5$ s, the hot-film signal increases rapidly towards a plateau suggesting the flow has reached a steady state. During this regime the actuation attempts to force the flow to reattach to the wall. When the actuation is turned off, at $t = 5$ s, the hot-film response shows a rapid decrease towards a new plateau associated with the natural separated state of the flow. It is noteworthy that this happens with some time delay between the actuation and the flow response.

As described by [7], the transition between the separation and reattachment can be modelled as a first-order system. The transition towards separation can also be described by a similar system. While not described here, the different model parameters have been estimated for each test case of Table 1. These global quantities are of particular interest for further work in developing a closed-loop control of the flow.

The hot-film averaged response for the pulsed actuation is shown in Fig. 2b. The signal driving the actuator consists now of periodic pulses. Again, the two regimes associated with reattachment and separation are manifest. During the controlled regime (first 5 s), fairly periodic oscillations are observed with large amplitude and superimpose on a first-order response similar to that observed in the continous case. For each pulse, a vortical structure is generated by each jet. The oscillations observed in the hot-film response correspond to the signature of the interaction of these convected structures with the boundary layer. The phase shift between the pulses and the oscillations is directly related to the distance between the hot-wire probe and the actuators giving the convection velocity of the generated structures.

The characteristics of the first-order model for a set of control parameters can be obtained. But the fluctuations around this overall behavior are not modelled. For this consideration, refined models based on adaptive autoregressive algorithms (AARMA, ARMAX) have been implemented. Although not detailed here—more details can be found in future publications—the algorithm takes into account the
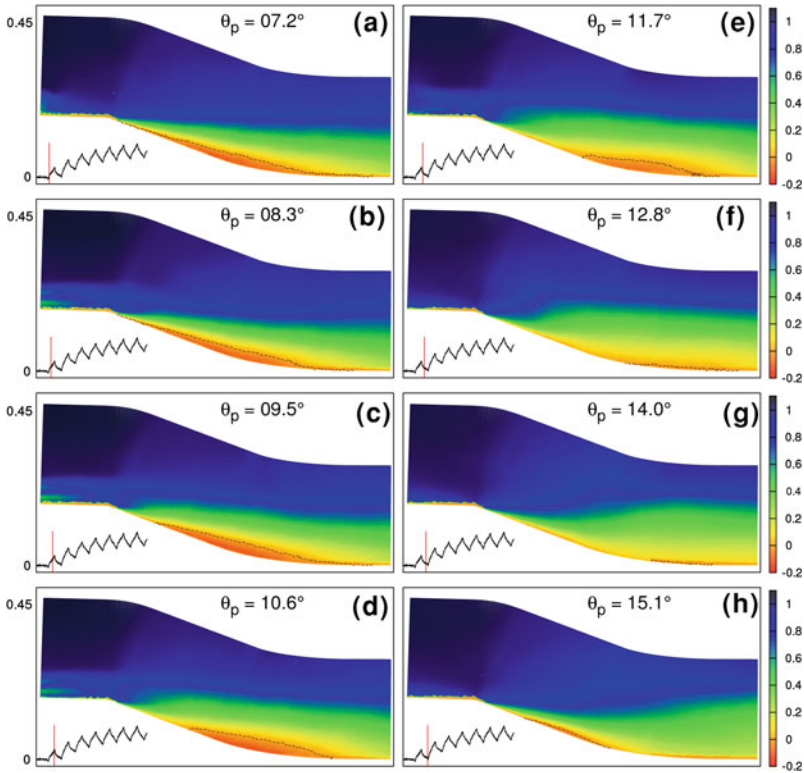
Fig. 3 Phase-averaged flow response (streamwise velocity component) to the pulsed case *V I* during the first eight phases associated with hot-film response shown and position in time in Fig. 2b. The sequence shown here covers the first pulses shown by the *green line* in Fig. 2b

effect of the pulsed actuation on the hot-wire signal. The error between the original response and the predicted one is negligible (<0.5 %). This offers the opportunity to predict the sensor's response which is a particular interest in a control perspective.

Phase-averaged snaphots of the streamwise velocity components obtained from PIV are shown in Fig. 3. These cover the first 250 ms of reattachment regime highlighted in Fig. 2 by the hot-film response (first pulse of the actuation). Each instant of the phase-averaged measurement is identified with its phase $\theta = t * 360 / T_{cycle}$. The first snapshot ($\theta = 7.2°$) corresponds to the separated flow state. The following phases highlight the passage of a large convecting structure through the region of separation. A decrease of the recirculation bubble is first observed while the flow is "pushed" towards the wall ($\theta = 8.3°$ to $\theta = 11.7°$). When the large structure passes half of the flap ($\theta = 12.8°$), the flow becomes almost fully reattached. The flow remains in this state until the structure reaches the end of the flap ($\theta = 14°$) after which a recirculation bubble reappears along the flap ($\theta = 15.1°$) but with dimensions significantly smaller than for the fully separated state. As already mentioned, these 8 snapshots cover only one pulse of actuation. While not shown here,

when looking at the response of the flow to the following pulses, the flow behaves like between $\theta = 10.6°$ and $\theta = 15.1°$. A bubble of separation is observed but with dimensions drastically reduced and located further downstream along the flap.

In order to understand the low-dimensional organization of the flow dynamics during the transient regimes, further POD analysis will be conducted. The behavior of indivual modes during the transient regimes will be examined in the perspective of closed-loop control based on low-order models.

4 Conclusion

A detailed survey of a separated turbulent boundary layer flow is presented using phase-locked PIV measurements and hot-film sensors. Elements required for robust closed-loop control are discussed such as predictive model of the sensor's response low-order organization of the flow and receptivity of the flow and sensor to control parameters. The spatial and temporal organisation of the flow during transient regimes of separation/reattachement is examined. Spatial and temporal integral quantities can be extracted in order to better understand the role of the actuation on the boundary layer, and particularly the influence of the actuation parameters. The overall behaviour of the flow evidences a complex unsteadiness, so that advanced analysis is necessary to extract local information on the flow transient from separated to attached and vice versa. Eventually, this information will be used to develop robust closed-loop controllers.

References

1. Carlier J, Stanislas M (2005) Experimental study of eddy structures in a turbulent boundary layer using particle image velocimetry. J Fluid Mech 535(36):143–188
2. Cuvier C (2012) Active control of a separated turbulent boundary layer in adverse pressure gradient. phD Thesis, Ecole Centrale de Lille, France.
3. Jim Kostas, Jean-Marc Foucaut, Michel Stanislas (2007) The flow structure produced by pulsed-jet vortex generators in a turbulent boundary layer in an adverse pressure gradient. Flow Turbulence Combustion 78(3–4):331–363
4. Mathis R, Lebedev A, Collin E, Delville J, Bonnet J-P (2009) Experimental study of transient forced turbulent separation and reattachment on a bevelled trailing edge. Exp Fluids 46(1):131–146
5. McManus KR, Legner HH, Davis SJ (1994) Pulsed vortex generator jets for active control of flow separation. AIAA paper 94–2218:5
6. Scholz P, Ortmanns J, Kähler CJ, Radespiel R (2006) Leading edge separation control by means of pulsed jet actuators. In: AIAA Flow Control Conference, San Francisco, California.
7. Shaqarin T (2011) Active control to reattach a thick turbulent boundary layer. phD Thesis, Université de Lille 1, France.

Active Control by Surface Dielectric Barrier Discharge Actuator of a Reattached Shear Layer

P. Sujar-Garrido, N. Benard, E. Moreau and J. P. Bonnet

Abstract The objective of this paper is to investigate the effects produced by a dielectric barrier discharge plasma actuator on the separated shear layer flow downstream a backward-facing step. It was highlighted that the electric wind created by the actuator results in an important modification in the flow dynamics when the Strouhal number of the perturbation is equal to 0.25. Then, a lock-on of the vortical flow structures is observed.

1 Introduction

The backward-facing step (BFS) is a fundamental case to study all the complexity of massively separated flows. The main features are very similar to those of a plane mixing layer in the initial region, where the separated shear layer behaves as a free shear layer. Further downstream, the flow is affected by the presence of the bottom wall where it reattaches. The shear layer impingement provokes a backflow and a recirculating region that is continuously feeding the shear layer.

This paper is devoted to the characterization of the shear layer and the reattachment region. Therefore, by using a suitable flow control device, different parameters such as Reynolds stress tensor or reattachment point, even the large-scale structures, can be manipulated. Different flow control devices have been used over past years either passive, such as fences, or active, such as speaker [1] and flapping foil [2]. All results confirmed a reduction of the reattachment length when the frequency of the perturbation is within a certain range (St $\approx 0.2 - 0.3$) [2, 3].

Surface non-thermal plasma actuators are now recognized for being effective in different aerodynamic configurations [4]. Here, a single dielectric barrier discharge

P. Sujar-Garrido (✉) · N. Benard · E. Moreau · J. P. Bonnet
Institut PPRIME (CNRS UPR3346, Université de Poitiers, ISAE-ENSMA),
Bd Marie and Pierre Curie, BP 30279, 86962 Futuroscope, Poitiers, France
e-mail: patricia.sujar.garrido@univ-poitiers.fr

Fig. 1 Sketch of the model
equipped with a single DBD
actuator, units in mm
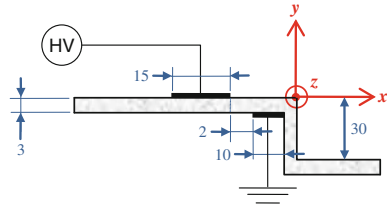
(DBD) actuator is mounted upstream the separation point to explore the possibility
of influencing the main features of the BFS flow. The main objective is to clarify
the ability of this device for manipulating the shear layer with the final objective of
being able to control/reduce the parasitic effects present in this type of flows such as
unsteadiness, noise, etc.

2 Experimental Configuration

The step model configuration is installed in a closed-loop wind tunnel (turbulence
intensity level of 1 %) with a $300 \times 300 \, mm^2$ test section. The boundary layer is
forced by a zig-zag tripping device installed 10 h upstream the separation point, with
h being the height of the step equal to 30 mm. The model covers the full span so the
aspect ratio (span/step height) is equal to 10 and the expansion ratio, corresponding
to the relation between test section and step height, is equal to 1.1.

2D LDV measurement technique is used in order to access to time-resolved data.
The system is composed of a laser argon-ion used at 1.2 W. The seeding particles are
obtained by atomization of dielectric oil (Shell Ondina 917). Their mean diameter is
equal to $0.4 \, \mu m$. The minimum number of samples needed to obtain a meaningful
average and the convergence of the second central moments is about 100,000 sam-
ples. The method used for the spectra analysis was sample-and-hold, considering a
maximum of 500,000 samples and Fast Fourier Transform (FFT) size of 2,048 points.

The model includes a recess at the step corner where the dielectric barrier dis-
charge is installed. The DBD device and the electrode arrangement can be seen in
Fig. 1. It is composed of one high voltage air-exposed electrode and an encapsu-
lated grounded electrode. This arrangement produces an electric field that generates
a surface discharge between both electrodes due to air ionization. The produced
ElectroHydroDynamic (EHD) volumic force results in a wall jet, tangentially to the
dielectric wall and blowing in the positive x direction [4].

3 Uncontrolled Flow

The step flow can be divided into several regions. The zone upstream the step includes
the inlet conditions which are essential for the behaviour of the separated shear layer.
The first stage of this shear layer ('free') is not affected by the presence of the bottom

Table 1 Reference boundary layer parameters for x/h = −1 position

h (mm)	δ (mm)	δ*(mm)	θ (mm)	H	U_{ref}	Re_h	Re_δ	Re_θ
30	13	2	1.4	1.43	15	3×10^4	1.3×10^4	1400

wall up to almost 3 h distance downstream. Then, the separated shear layer curves down and impinges into the wall (reattachment zone) [1–3].

The measurements presented here are performed for a freestream velocity of 15 m/s ($Re_h = 30 \times 10^4$). The boundary layer parameters are computed from the LDV data measured at one step height h upstream the separation (see Table 1). The air-exposed electrode is only superposed to the plate so the thickness of the electrode (70 μm) can be considered as a protuberance in the boundary layer region. However, preliminary measurements showed that the electrode thickness has no substantial influence on the shear layer development.

In the first 2 h distance, the separated shear layer behaves as a single stream mixing layer growing with the streamwise position. The estimation of the local vorticity thickness shows a longitudinal gradient of 0.164, which is a very good approximation compared with the typical experimental values of a mixing layer in the case of two identical fluids: $d\delta_\omega/dx = 0.16\lambda$ with λ = 1 [5].

In this region, turbulence spectra have been estimated at different locations in streamwise and normal directions. For a fixed point, x/h = 2, several measurements in normal direction were recorded (Fig. 2a). From these results, it is found a zone where the spectra show a turbulent activity increase related to the free shear layer flow with a noticeable signature of quasi-periodic events at 130 Hz and a bandwidth of 50–200 Hz. At y = 5 mm, Fig. 2b shows the PSD for three positions in streamwise direction. The hump frequency decreases as the shear layer grows.

Measurements of the streamwise velocity component in the wall vicinity locate the time-averaged point of reattachment at x ≈ 177 mm (5.9 h). Figure 2c shows the spectra at this location for several points in normal direction. Within the reattachment area, spectra are typical of a fully turbulent flow but above the reattached region (y = 0 − 15 mm), a signature of a periodic perturbation is observed at roughly 60 Hz. As illustrated in Fig. 2d, the quasi-periodic frequency decreases along the shear layer. This matches with results for the same configuration such as [1] where the frequency was identified as St/2.

3.1 Actuator Characterization

The most common used signal for this kind of actuators is a sinusoidal wave of some kV of amplitude (24 kV here) driven at a frequency f_{AC} of some kHz (1 kHz here). This sinusoid wave can be modulated using a gate or a trigger to switch on/off the discharge and to produce a deep modulation of the applied signal (unsteady mode).

The time-averaged evolution of the electric wind is shown in Fig. 3a at a middle distance of the grounded electrode (x = −7 mm) where the produced electric wind is
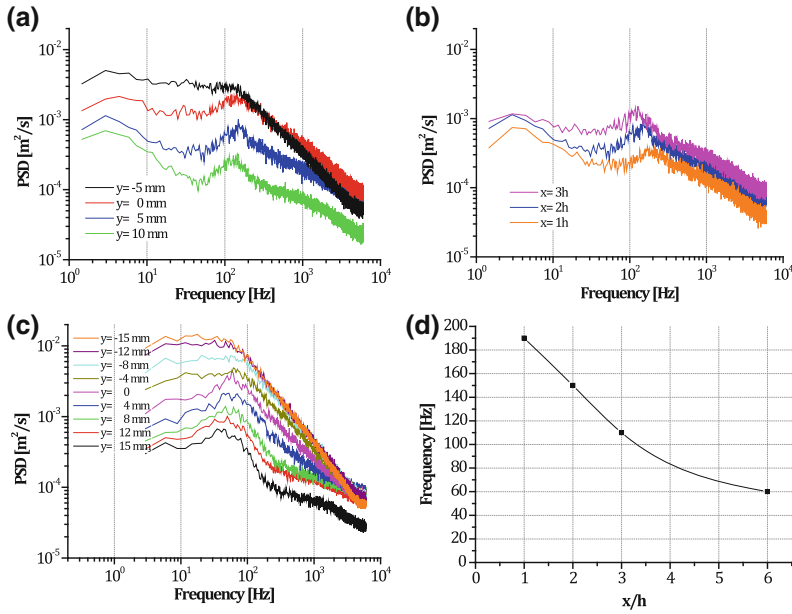
Fig. 2 **a** Spectra at x/h = 2 for several normal positions. **b** Spectra at y = 5 mm for three streamwise positions. **c** Spectra at x/h = 5.9 at several normal positions. **d** Frequency signature of the free shear layer along the x axis
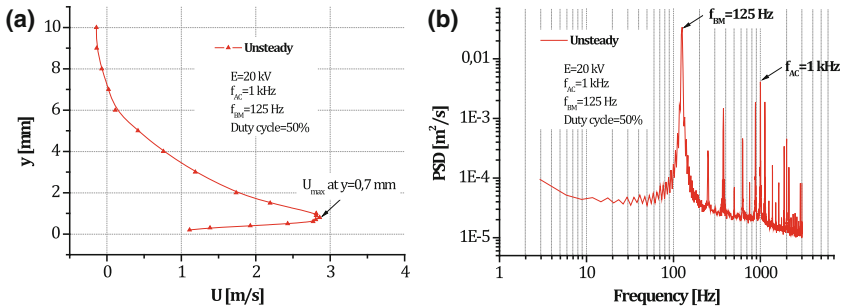
Fig. 3 **a** Velocity profiles induced by unsteady actuation by burst modulation with duty-cycle of 50 %. **b** Spectra of the induced flow at x = −7 mm and y = 0.7 mm

maximized [4]. The velocity profile corresponds to a wall jet behaviour in which the maximum mean velocity reached here is almost 3 m/s. The produced flow is highly unsteady as it is illustrated by the spectrum of the time-resolved flow measurements (Fig. 3b). The modulating frequency f_{BM} and carrier frequency f_{AC} are clearly visible in the produced flow and they have almost the same amplitude for several streamwise positions. However, the modulation frequency and its harmonics dominate and are transmitted to the flow dynamics. Thus, the frequency f_{BM} interacts with the boundary
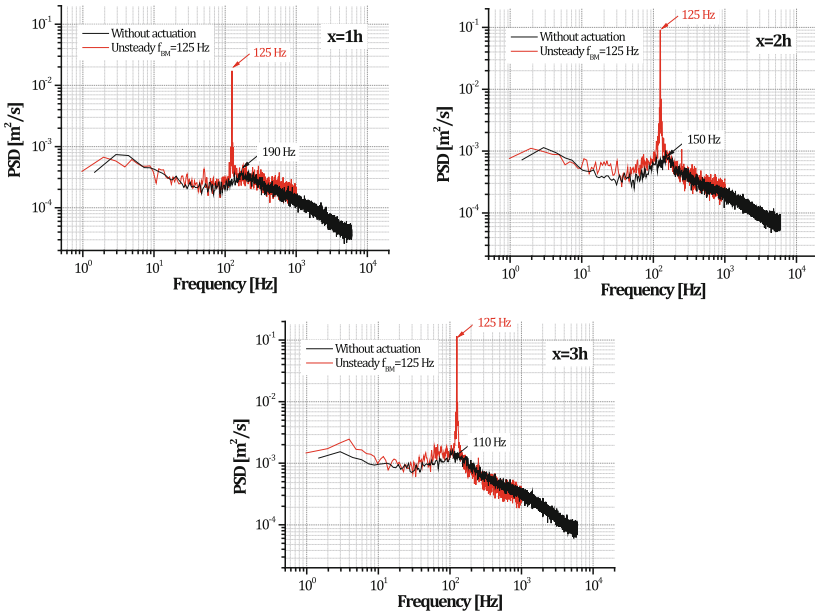
Fig. 4 Spectra without plasma and with plasma at x/h = 1, 2 and 3

layer flow before the separation in the initial stage of the shear layer formation caused by the Kelvin Helmholtz instability [6].

4 Results for Controlled Flow

In the present case, all the results are for a perturbation frequency of 125 Hz (duty-cycle of 50 %), which correspond to a Strouhal number of perturbation equal to 0.25, in agreement with literature [2, 3]. This actuation only produces a small modification in the turbulent boundary layer because the electric wind produced by the actuator is low in comparison with the free stream velocity. However, this actuation produces significant changes in the development of the mean flow downstream separation. Measurements of the streamwise velocity component near the wall indicate that the time-averaged reattachment point moved downstream to 4.6 h (from the reference 5.9 h, i.e. a gain of 22 %). This reduction in the recirculation is the result of an increase in the Reynolds stress that is highlighted by several other publications [7]. This is currently been investigated by time-resolved PIV.

In particular, the present results focus on the most significant changes occurring in the region related to the large-scale vortex shedding. It has been shown in Fig. 2d that the characteristic frequency exhibited by the coherent quasi-deterministic structures decreases with the streamwise position from 190 to 110 Hz at a distance of 1–3 h downstream separation. Then, the Strouhal number computed with the local vorticity thickness is maintained around 0.25. This is the mode related with the Kelvin

Helmholtz instabilities present in the shear layer and responsible for the formation of large-scale flow structures. For the case of actuation at $St_{fBM} = 0.25$ by surface plasma discharge, the flow positively reacts to the forcing, not only with a large reduction in mean reattachment length but also with a new organization of the vortex street embedded in the background turbulence (see Fig. 4). When the actuator is turned on, the original bump at low frequency reported previously is modified in its central frequency value, frequency range and amplitude. At all of the downstream positions, plasma actuation results in a quasi-discrete frequency peak (similar to those found when loudspeaker are used as active flow control system [1]) with only a weak first harmonic. The amplitude of this peak is two orders of magnitude larger than without plasma discharge and its frequency is perfectly locked on the applied excitation frequency f_{BM}.

All the natural frequencies contained in the flow are modified with the actuation. The use of the plasma actuator operated at optimal regime conduces to a "lock-in" effect. Thus, the local frequencies representing the periodic structures are modified and imposed at a discrete frequency, the frequency of the plasma actuation.

5 Conclusion

This paper focused on the modification produced by an active plasma device on a backward-facing step flow. The results showed the authority of unsteady plasma discharge to manipulate this particular case of separated flow. A perturbation imposed at a frequency of 125 Hz reduces the mean reattachment distance by 22 % but it also influences the large-scale eddy dynamics. The excitation produces a regularisation activity indicated by a discrete frequency over the entire separated flow caused by a "lock-in" effect.

References

1. Chun KB, Sung HJ (1996) Control of turbulent separated flow over a backward-facing step by local forcing. Exp Fluids 21:417–426
2. Lai SJC, Yue J, Platzer MF (2002) Control of a backward-facing step flow using a flapping foil. Exp Fluids 32:44–54
3. Yoshioka S, Obi S, Masuda S (2001) Organized vortex motion in periodically perturbed turbulent separated flow over a backward-facing step. Int J Heat Fluid Flow 22:301–307
4. Benard N, Moreau E (2012) EHD force and electric wind produced by surface dielectric barrier discharge plasma actuators used for airflow control. In: 6th AIAA flow control conference, Louisiana, USA, New Orleans.
5. Fiedler HE (1987) Coherent structures. In: Comte-Bellot G, Mathieu J (eds) Advances in turbulence. Springer, Berlin
6. Ho CM, Huerre P (1984) Perturbed free shear layers. Ann Rev Fluid Mech 16:365–424
7. Roos FW, Kegelman T (1986) Control of coherent structures in reattaching laminar and turbulent shear layers. AIAA J 24(12):1956–1963

Part IX
Separation in Duct and Cavity Flows

Numerical Simulation of a Synthetic Jet with OpenFOAM

**Qiong Liu, Asimina Kazakidi, Marcello A. F. Medeiros
and Vassilis Theofilis**

Abstract Numerical simulations of flow surrounding a synthetic jet actuating device
are presented. By modifying a dynamic mesh technique available in OpenFOAM,
a well-documented open-source solver for fluid dynamics, detailed computations
of the sinusoidal motion of the synthetic jet diaphragm were possible. Numerical
solutions were obtained by solving the two dimensional incompressible viscous N–
S equations, with the use of a second order implicit time marching scheme and
a central finite volume method for spatial discretization in both streamwise and
crossflow directions. A systematic parameter study is reported here, in which the
external Reynolds number, the diaphragm amplitude and frequency, and the slot
dimensions are varied.

1 Introduction

Synthetic jets are commonly generated by the time-periodic ejection and suction of
fluid across an orifice, resulting in zero-net mass flux [4]. Since the experimental
work of Ingård and Labate [6] in the '50s, the study of synthetic jets has become one
of the most attractive subjects of research in fluid mechanics. The primary reason
behind is that the synthetic jet can be utilized as a flow control method, with several

Q. Liu (✉) · V. Theofilis
School of Aeronautics, Universidad politècnica de Madrid, Pza. Cardenal Cisneros 3,
E-28040 Madrid, Spain
e-mail: liuqiong.upm@gmail.com

A. Kazakidi
Institute of Computer Science Foundation for Research and Technology—Hellas (FORTH),
GR70013 Heraklion, Greece

M. A. F. Medeiros
University of São Paulo, Escola de Engenharia de São Carlos EESC,
São Carlos-SP 13566-590, Brazil
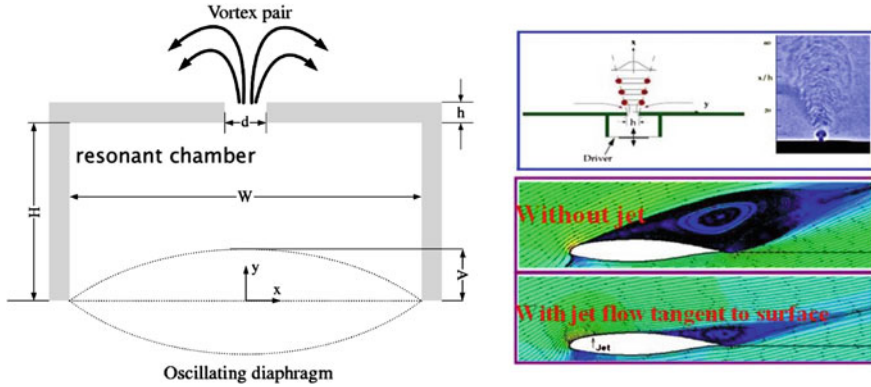
Fig. 1 (*Left*) Schematic diagram of a synthetic jet actuator [3]. (*Right*) Application of a jet actuator on an airfoil, with evident decrease of the downstream separated region [5]

engineering applications [2, 4]. Originally demonstrated in the laboratory by Wiltse and Glezer [11], synthetic jets can further work as micro-fluidic devices with a potential implementation to thrust vectoring of jet engines.

A series of studies have been devoted to the control of synthetic jets in the past years. Mittal et al. [9] studied the performance of a synthetic jet actuator, based on a number of geometrical, structural and flow parameters. Amitay et al. [1] demonstrated the usage of synthetic jets in delaying separation. Further works on synthetic jets included two-dimensional simultions in quiescent flow conditions by Kral et al. [7] and Lee and Goldstein [8].

The basic features of a synthetic jet actuator are illustrated schematically in Fig. 1. Trains of vortices induced by the harmonic motion of a diaphragm located opposite to the slot, interact to produce the jet. The diaphragm amplitude and frequency, and the slot dimensions may change the characteristics of the jet's evolution.

In the current study, we modified a dynamic mesh technique available in Open-FOAM. The paper is organized as follows: Sect. 2 presents the numerical framework, Sect. 3 discusses the computational results, and Sect. 4 summarizes the results of this study.

2 Methods

2.1 Actuator Geometry and Computational Mesh

The two-dimensional synthetic jet actuator considered in this study was comprised of a rectangular cavity, the upper wall of which included a thin slot of width d and width-to-height ratio (d/h) of 1; the lower wall opposite to the slot formed an oscillating diaphragm (cf. Fig. 2). The cavity was $20d$ in width and $4d$ in height, connected via
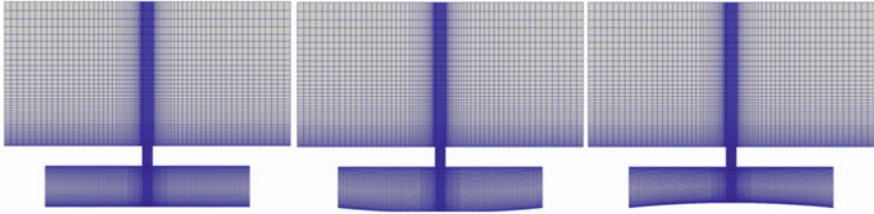
Fig. 2 Dynamic mesh displacement during the harmonic motion of the diaphragm in the synthetic jet actuator

the slot to a rectangular space that was d in width and $2d$ in height, above the cavity. This geometry was used as a reference geometry upon which several geometrical and flow parameters were tested (see Sect. 2.3).

A mesh of 107×54 quadrilateral elements was used for the overall computational domain, of which 30×25 elements were used inside the slot and 118×58 elements inside the rectangular cavity. A very fine boundary layer mesh was constructed near the walls to adequately capture the viscous flow effects.

2.2 Governing Equations and Numerical Tools

The 2-D incompressible viscous Navier–Stokes equations are written in conservation form as follows, assuming unit fluid density:

$$\nabla \cdot \mathbf{u} = 0 \tag{1}$$

$$\frac{\partial \mathbf{u}}{\partial t} + (\mathbf{u} \cdot \nabla)\mathbf{u} = -\nabla P + \nu \nabla^2 \mathbf{u} \tag{2}$$

where $\mathbf{u}$ is the velocity vector, P is the pressure and ν is the kinematic viscosity of the Newtonian fluid.

Numerical simulations were carried out with OpenFOAM. Solution of the governing equations was achieved with a second order implicit time marching scheme and a central finite volume method for spatial discretization. The mesh motion was controlled by changing the frequency and the amplitude of the diaphragm's forced oscillation. Figure 2 shows an example of the dynamic mesh displacement during the periodic movement of the diaphragm.

Table 1 The values of frequency, amplitude and slot width-to-height ratio chosen for the presented parametric study

	a	b	c	d	e	f
Re_d	0	0	0	0	71.426	250
d/h	1	1	0.5	1	1	1
f	0.05	0.05	0.05	0.1	0.05	0.05
A	0.1	0.2	0.2	0.2	0.2	0.1
Stokes number	3.32	3.32	3.32	4.7	3.32	3.32

Fig. 3 Profile of velocity necessary for jet formation at $t/T = 0.25$ for $d = 0.0051$ m
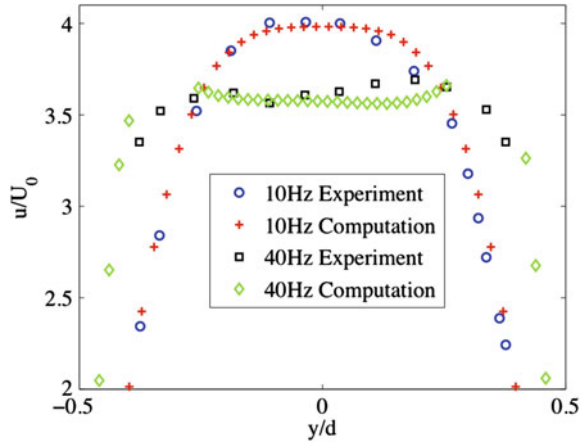
2.3 Boundary Conditions and Fluid Parameters

The diaphragm is modeled as a plate oscillating in its fundamental mode, according to the following motion profile:

$$0.5 * (\cos(2\pi t f) - 1). \tag{3}$$

The diaphragm has its maximum deflection at the center of the cavity and zero deflection at the two ends. Focusing on the parameters that are expected to have a strong influence on the characteristics of the synthetic jet, in the current study, we chose to systematically study the diaphragm amplitude A/H, the frequency f, the width-to-height ratio of the slot (d/h), and the external flow Reynolds number Re_d, based on the slot width. The selected parameters are shown in Table 1.

Assuming no external flow, the pressure gradient is zero. The Neumann and Dirichelet boundary conditions were used. For the cases where external flow is considered, the direction of flow is from left to right, according to Fig. 2.
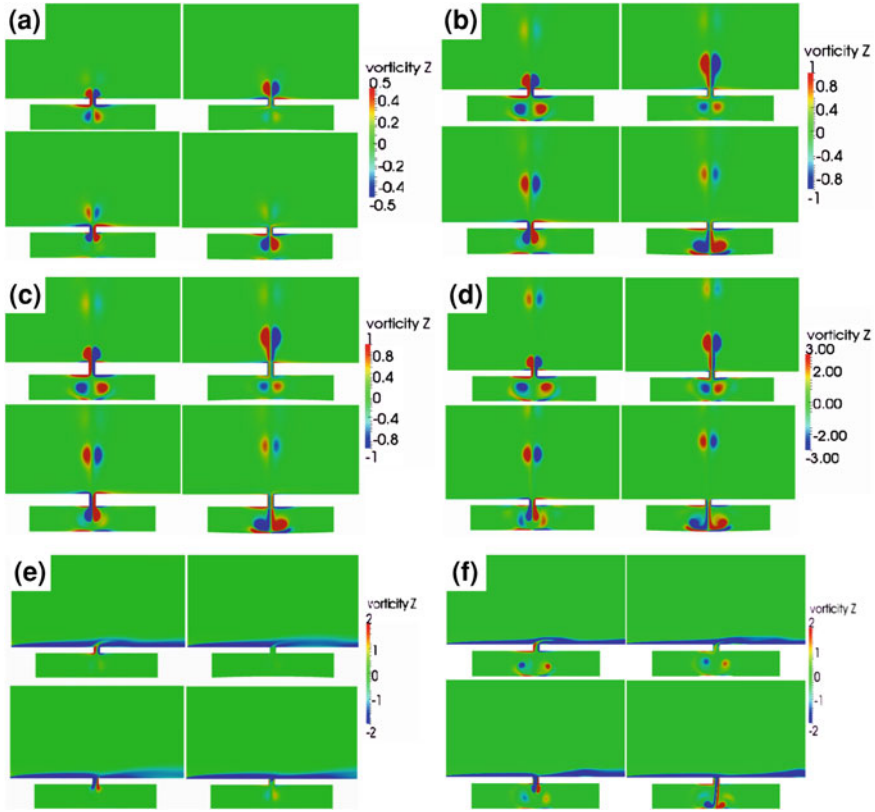
Fig. 4 Instantaneous contours of vorticity at four different stages of the diaphragm oscillation, in the absence (cases **a** to **d**) and in the presence (cases **e** and **f**) of external flow. The parameters used for the simulations are presented in Table 1

3 Results

Velocity profiles at the peak of the blowing stroke ($t/T = 0.25$) are shown in Fig. 3, which are good agreement with the experiment data [10]. Figure 4 shows sequences of instantaneous contour plots of spanwise vorticity, at maximum expulsion, minimum volume, maximum ingestion and maximum volume. The first four cases (a to d) are simulated with no external flow, i.e. $Re_d = 0$, whereas the last two cases (e to f) assume the presence of external flow. The parameters used for all numerical simulations are those shown in Table 1.

In case a, the diaphragm amplitude is small, and therefore vortices generated near the slot during each stage of the cycle, remain in the region without escaping the cavity. Doubling the amplitude of the diaphragm oscillation (case b) resulted in vortices that escape the cavity, during the maximum expulsion stage, and travel inside the external space. These vortices do not interact further with the synthetic jet.

Increasing the height of the slot at twice the previous value, while maintaining the same oscillation amplitude (case c), had no significant influence on the evolution of the synthetic jet. Increase of the diaphragm frequency to the double value of that in case b, while maintaining the same amplitude and slot width-to-height ratio (case d), had only a small influence on the evolution of the vortices, as compared to case b, with slightly greater separation. In the final two cases e and f, the presence of external flow drastically alters the evolution of the synthetic jet, which through interaction with the external flow, reshapes and becomes highly asymmetric within the cavity.

4 Conclusion

A synthetic jet actuator has been parametrically studied here, by utilizing a modified dynamic mesh technique. The diaphragm is modeled to undergo harmonic oscillations. The evolution of the synthetic jet in the absence of external flow, showed that the amplitude and frequency have a stronger influence on the characteristics of the jet, than the slot height. In the presence of external flow, the synthetic jet is greatly varied. By using appropriate parameters, the jet can control the flow development downstream of the slot.

References

1. Amitay M, Honohan A, Trautman M, Glezer A (1997) Modification of the aerodynamic characteristic of bluff bodies using fluidic actuators. AIAA 97–2004.
2. Cattafesta LN III, Sheplak M (2011) Actuators for active flow control. Ann Rev Fluid Mech 43:247–272
3. Celik B, Edis FO (2009) Micro-scale synthetic-jet actuator flow simulation with characteristic-based-split method. Aircr Eng Aerosp Technol 81:239–246
4. Glezer A, Amitay M (2002) Synthetic jets. Ann Rev Fluid Mech 34:503–529
5. http://hangkong.nwpu.edu.cn/home/Department/dptshow/DepartmentxofxHydromechanics.htm
6. Ingård U, Labate S (1950) Acoustic circulation effects and the nonlinear impedance of orifices. J Acoust Soc Am 22(2):211–218
7. Kral LD, Donovan JF, Cain AB, Cary AW (1997) Numerical simulation of synthetic jet actuators. AIAA 97–1824.
8. Lee CY, Goldstein DB (2002) Two dimensional synthetic jet simulation. AIAA 40:510–516
9. Mittal R, Rampunggoon P, Udaykumar HS (2001) Interaction of a synthetic jet with a flat plate boundary layer. AIAA 2001–2773.
10. Smith BL, Swift GW (2001) Synthetic jet at large Reynolds number and comparison to contimuous jets. AIAA 3030.
11. Wiltse J, Glezer A (1993) Manipulation of free shear flows using piezoelectric actuators. J Fluid Mech 249:261–285

Three-Dimensional Analysis of Incompressible Flow Over an Open Cavity Using Direct Numerical Simulation: From Linear to Saturated Regime

F. Meseguer-Garrido, J. de Vicente and E. Valero

Abstract The features of the incompressible flow over a rectangular open cavity are studied both numerically, using linear stability analysis, and experimentally in previous works by the authors [5, 7]. Those approaches refer to different states of the flow. The numerical analysis refers to a linear small perturbation superimposed over a two dimensional steady state, while the experimental work studies the complete saturated flow regime, with spanwise walls. Even with such different conditions, both approaches have revealed common features, with the main structures of the experimental flow being recognizable from the corresponding modes of the linear analysis, albeit with certain differences, mainly in the oscillating frequencies [7]. The aim of this work is to fill the breach that separates those two states studying the saturation of the flow using a three dimensional non-steady Direct Numerical Simulation (DNS). In this first stage periodic boundary conditions in the spanwise direction will be considered.

1 Problem Description

There are numerous works focusing on the instability of the flow over an open cavity. To mention the most influential in this work, [6] is an excellent review of the state of the art in the stability analysis of flows. From a numerical point of view, [1] full three-dimensional global instability analysis of compressible flow over a two-dimensional rectangular open cavity has been chosen to select the flow parameters in the cases of study. Faure [2] presents a comparison of DNS results with experimental data for an open cavity of different aspect ratios. In the present contribution a rectangular open cavity with aspect ratio, length over depth, $L/D = 2$, is analyzed.

F. Meseguer-Garrido (✉) · J. de Vicente · E. Valero
School of Aerospace Engineering, Universidad Politécnica de Madrid, Pza. Cardenal
Cisneros 3, E-28040 Madrid, Spain
e-mail: fernando.meseguer@upm.es

The main parameters affecting flow stability are incoming boundary layer displacement thickness θ_0/D and the Reynolds number based on cavity depth Re_D.

The characteristics of the modes present in the linear analysis are the spanwise wavenumber β, the amplification-damping rate of the eigenmode σ and its dimensionless frequency, the Strouhal number St. The BiGlobal stability analysis and velocity experimental measurements do not highlight the same state of the system. Linear stability analysis concerns the onset, nature and three dimensional structure of the flow instabilities, with an ideal noiseless basic flow with periodic spanwise conditions. On the other hand, experiments involve the study of the permanent regime, with non-linearly saturated dynamics, complex boundary conditions and partial imperfect measurements. To explain the evolution of the initial disturbances predicted by linear analysis into the final saturated flow, a set of DNS computations were performed.

2 Numerical Methodology

Linear stability theory is concerned with the evolution of small-amplitude disturbances superimposed upon a basic state $(\bar{\mathbf{q}})$. BiGlobal instability analysis, where three-dimensional space comprises an inhomogeneous two-dimensional domain which is extended periodically in z, was used to analyze the flow over an open cavity of aspect ratio length-to-depth $L/D = 2$. The spanwise periodicity length L_z is related to a real spanwise wavenumber $\beta = 2\pi/L_z$. Linearizing the incompressible fluid flow equation results in:

$$\mathbf{q}(x, y, z, t) = \bar{\mathbf{q}}(x, y) + \varepsilon\hat{\mathbf{q}}(x, y)\exp\{\mathrm{i}(\beta z - \omega t)\} \tag{1}$$

And then the associated eigenvalue problem is solved. For this configuration, and in the range of parameters close to the limit of stability, the linear analysis performed shows the presence of two main branches of unstable eigenmodes. The mode that becomes unstable at lower Reynolds number, Mode I, is a traveling disturbance which is more unstable in the proximity of $\beta \simeq 6$ and $\beta \simeq 12$. The second unstable mode, Mode II, is stationary at higher β, while undergoing a bifurcation at $\beta \simeq 9$, resulting in a pair of complex conjugate eigenvalues for values of β lower than that. A more detailed description of the BiGlobal analysis performed, and the nature and behavior of the aforementioned modes can be found in [5].

The DNS solver used employs a Chebyshev Discontinuous Galerkin method decomposing the computational geometry into a series of domains where the compressible laminar Navier-Stokes equations are discretized. Additional details of the methodology employed and the implementation technique can be found in [4] or the numerical validation in [3].

The spanwise length of the computational domain (L_z) was selected in order to reduce the amount of interaction between different modes. If L_z is big enough a wide variety of β on the unstable regime of the branches of eigenmodes can appear in the DNS solution. By selecting a L_z of $2\pi/6$ only modes of $\beta = 6$, $\beta = 12$ or

$\beta = 18$ can coexist, thus reducing the interaction between different branches of modes. To avoid the effect of spanwise walls the DNS computations have been performed using a periodic spanwise boundary condition.

The computations for the chosen conditions were performed as follows. First, the two dimensional solution was extended in the spanwise direction in the whole domain. Then random noise of 10^{-8} was introduced everywhere in the domain to kick-start the growth of the linearly unstable modes. The flow variables were recorded in a point in the middle of the cavity, and snapshots of the flowfield were saved periodically. For the DNS results shown here, L_∞-norm of the spanwise velocity component of the perturbed flow is monitored as a function of non-dimensional time on the control point. Since the value of said variable is zero in the two dimensional base flow, the whole effect corresponds to perturbation, thus giving the greater detail about the modes.

3 Results

A wide variety of points on the parameter space could be chosen for this exercise, but conditions similar to the experimental cases of the aforementioned [7] were used. To that effect, two different Direct Numerical Simulations were performed. The first one, Case A, for Re $= 1,500$ and $\theta_0/D = 0.038$, and the second one, Case B, Re $= 2,400$, $\theta_0/D = 0.036$. According to linear instability analysis in Case A only a single branch of eigenmodes is unstable. This case was used as a first test case of the validity of the linear regime. As it was previously said, this perturbation (Mode I) is a traveling disturbance, characterized by a dimensionless frequency of St $= 0.0258$ for the β of maximum amplification. The evolution of the absolute value of the spanwise velocity component in the control point can be seen in Fig. 1 (left). The first instability to appear in the DNS flow, is, as expected, a pulsating traveling mode, enveloped by an exponential growth curve (note the log scale). The values of St and σ for the DNS and the leading BiGlobal disturbance can be seen in Table 1. The morphology of the modes is also similar.

Case B, shows a different behavior. In this region of the parameter space there are two main branches of unstable modes. The first corresponding to Mode I, and the second corresponding to the bifurcated Mode II. As it can be seen in Fig. 1 (right), four main types of instability could be recovered in the DNS simulation, corresponding to the high and low β branches of Modes I and II. The most unstable of those points corresponds to the stationary part of mode II, with $\beta = 12$.

In Fig. 2 the evolution of the spanwise velocity component in the control point can be seen. The purely exponential growth shows that the most unstable mode in this case is the one predicted by linear analysis. Table 1 shows the growth rates of the DNS and the predicted linear σ.

The morphology of this mode can be seen in Fig. 3 for the BiGlobal linear analysis—left—and the isosurfaces of the spanwise velocity component in the DNS—right. The structures presented here are morphologically similar to the ones
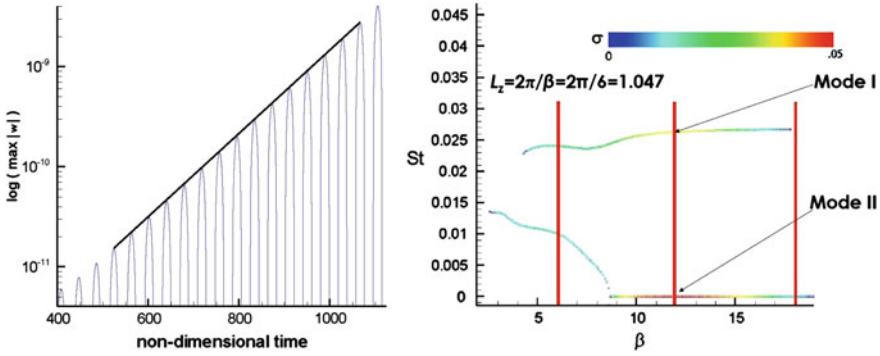
Fig. 1 Temporal evolution of the absolute value of the spanwise velocity component in the control point for Case A (*left*), and Strouhal versus β map of unstable eigenmodes for Case B, and selected DNS β (*right*)

Table 1 Amplification rate (σ) and frequency (St) of the leading BiGlobal mode and the linear part of the DNS, for both cases

Case	Method	St	σ
Case A	BiGlobal	0.0258	0.00981
Case A	DNS	0.0260	0.00978
Case B	BiGlobal	0	0.0439
Case B	DNS	0	0.0440
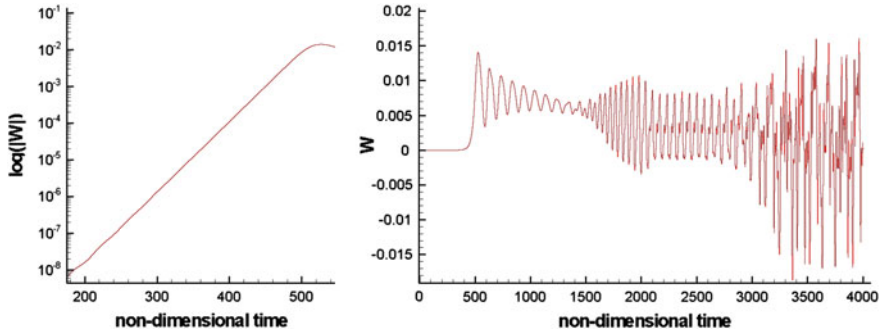
Fig. 2 Temporal evolution of the absolute value of the spanwise velocity component in the control point for Case B. Detail of the linear zone in log scale (*left*). Complete temporal run (*right*)

seen in [2]. In that work, the L/D ratio was 1, but the most unstable structure was the same bifurcated mode of $\beta = 12$.

In both cases A and B the characteristics of the flow on the first stages of linear growth are perfectly captured by the BiGlobal predictions.

After the linear growth phase there is a saturation ($t = 500$), and then the stationary mode starts to pulsate with St= 0.0098. The physical morphology of the mode does not change, and the oscillations gets dampened with time. The Strouhal number of said oscillations is the same as the St of the low β branch of Mode II (St= 0.0099),
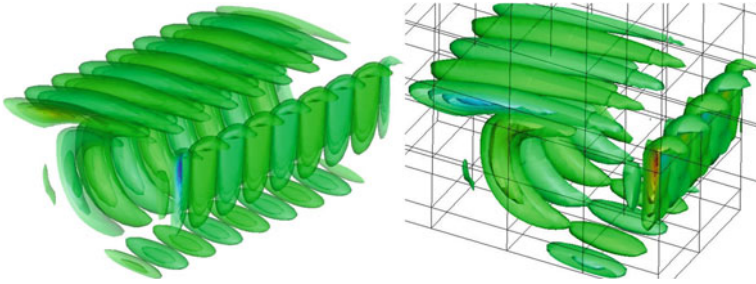
Fig. 3 3D Visualization of spanwise velocity disturbance obtained at $\mathrm{Re}_D = 2,400$ using BiGlobal analysis (*left*) and DNS at $t = 400$ (*right*)
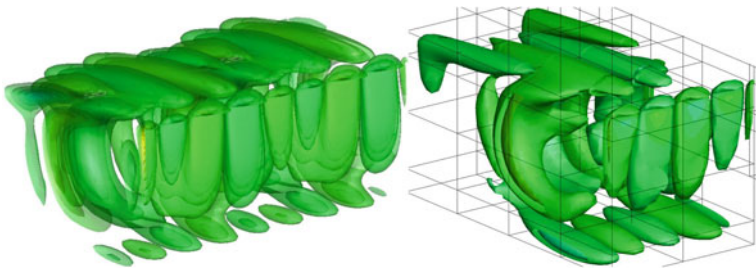
Fig. 4 3D Visualization of spanwise velocity at $\mathrm{Re}_D = 2,400$. Composition of leading disturbance (stationary $\beta = 12$ part of Mode II) and $\beta = 6$ part of Mode I according to BiGlobal analysis on the *left*, DNS solution at $t = 1,900$ on the *right*

according to linear analysis. So the behavior seems to be that after saturation the stationary mode starts vibrating, that vibration is progressively dampened, and in this case, with strong selection of L_z the perturbations resonates at the characteristic frequency of the same branch of mode, in the low β regime, even though the structures do not change their characteristic $\beta = 12$.

After these oscillations have almost completely dampened a new mode starts to grow, and during a period ($t = 1,500$ to $t = 2,100$) a sustained oscillation is superimposed with the stationary perturbation. The oscillating mode has $\beta = 6$, and $\mathrm{St} = 0.0194$. That frequency is smaller than the linear analysis predicted St of 0.025, but the mode present is the same Mode I, as it can be seen in Fig. 4. The linear composition of the low β branch of mode I and the high β branch of mode II leads to structures which are significantly similar to those present in the DNS computation in this stage. The reduction of the characteristic frequency of this dominant mode of $\beta = 6$ was already observed in the previous experimental work of [7].

The next step in the DNS is the apparition of a secondary oscillation in counterphase with the main one, producing a shifting of the frequency to $\mathrm{St} = 0.015$. In this stage the structures of the isocontours of spanwise velocity component no longer resemble easily constructable combinations of linear modes. This frequency is once more in the range of frequencies of high energy in the experiments of [7]. Finally, in

the last stage of the performed DNS computations there is a breaking in the symmetry of the solutions with the mid-plane, and the structures start to entwine and coil in the spanwise direction. The clear periodicity of the spanwise velocity component on the control point is lost at this stage, as the movement of the different structures affect it, but the frequency of the oscillations is between $St = 0.015$ and $St = 0.020$.

4 Conclusions

This work shows the good agreement between the flow obtained by DNS calculations in the linear regime and the predictions of the BiGlobal analysis. First stages of saturation have been explored, detecting remarkable interactions between both branches of Mode II. As time goes on, linearly unstable structures start to appear. The reduction of characteristic frequencies observed in the experiments [7] has been also identified in DNS results with periodic boundary conditions, which seem to indicate that it is not an effect of the walls. Future work will focus in those effects and interactions.

References

1. Brès GA, Colonius T (2008) Three-dimensional instabilities in compressible flow over open cavities. J Fluid Mech 599:309–339
2. Faure TM, Pastur LR, Lusseyran F, Fraigneau Y, Bisch D (2009) Three-dimensional centrifugal instabilities development inside a parallelepipedic open cavity of various shape. Exp Fluids 47:395–410
3. Jacobs GB, Kopriva DA, Mashayek F (1998) Validation study of a multidomain element code for simulatin of turbulent flows. AIAA 2004–0659
4. Kopriva DA (1998) A staggered-grid multidomain spectral method for the compressible Navier–Stokes equations. J Comput Phys 244:142–158
5. Meseguer-Garrido F, de Vicente J, Valero E, Theofilis V (2014) On linear instability mechanisms in the incompressible open cavity flow. Submitted to JFM
6. Theofilis V (2011) Global linear instability. Ann Rev Fluid Mech 43:319–352
7. de Vicente J, Basley J, Meseguer-Garrido F, Soria J, Theofilis V (2014) Three-dimensional instabilities over a rectangular open cavity: from linear stability analysis to experimentation. Submitted to JFM

Three-Dimensional Waves Inside an Open Cavity and Interactions with the Impinging Shear Layer

Jérémy Basley, Julio Soria, Luc R. Pastur and François Lusseyran

1 Motivations

A separated flow over an open cavity (Fig. 1) is primarily characterised by the enhancement of self-sustained oscillations [12]. *Kelvin-Helmholtz* travelling waves arise in the shear layer and *lock on* to the cavity length L due to an acoustic feedback loop [11, 13]. This leads to locked-on modes of oscillations often referred to as *Rossiter* frequencies in the compressible regime. When the external velocity is small with regards to sound speed ($U_0 \ll c$), the corresponding frequencies f_n typically verify

$$f_n L / U_0 \approx n/2, \qquad (1)$$

where $n = \{1, 2, 3\}$ is the number of periods (or wavelengths) over L. Self-sustained oscillations represent highly energetic fluctuations, generating noise and drag and fluid-structure interactions. However, the envelope of those self-sustained oscillations is often disregarded, although drastic amplitude modulation is generally observed

J. Basley (✉) · L. R. Pastur · F. Lusseyran
Laboratoire d'Informatique pour la Mécanique et les Sciences de l'Ingénieur
(LIMSI/CNRS), BP 133, 91403 Orsay Cedex, France
e-mail: jeremy.basley@limsi.fr

F. Lusseyran
e-mail: francois.lusseyran@limsi.fr

J. Basley · L. R. Pastur
Université Paris-Sud, F-91405 Orsay Cedex, France
e-mail: luc.pastur@limsi.fr

J. Soria
Laboratory for Turbulence Research in Aerospace and Combustion (LTRAC),
Department of Mechanical and Aerospace Engineering, Monash University,
Melbourne, VIC 3800, Australia
e-mail: julio.soria@monash.edu.au

Fig. 1 Sketch of the geometry
under study. Flow features are
illustrated in the xy-plane
(normal to the *bottom* of the
cavity)
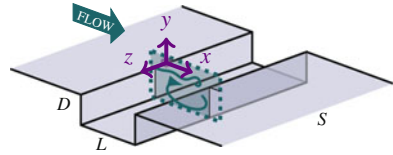
[6, 10]. An example of *very low* frequency modulations is shown in Fig. 2. The
shear layer locked-on mode constitutes the carrier while the envelope evolves over
20 times larger time-scales (about 40 D/U_0 time-steps).

This contribution aims at identifying the flow dynamics responsible for such low
frequencies. The three-dimensional (3D) organisation of the flow is believed to be
the source of the amplitude modulation [10]. In particular, the extensive literature
on the recirculating flow inside the cavity has shown how *centrifugal instabilities*
lead to slow 3D waves. In both lid-driven [1, 16] and shear-driven cavity flows
[7–9], vortical structures are observed along the span of the cavity. They are typically
associated with low frequencies f_{ci} such that

$$f_{ci} D/U_0 \leqslant 0.05, \tag{2}$$

consistent with the time scales of the envelope observed in Fig. 2. Furthermore, Brès
and Colonius [5] have already pointed out such low frequencies co-existing with
Rossiter oscillations of the shear layer, in direct numerical simulations (DNS) of
compressible open cavity flows.

2 Experiments

The present study deals with an experimental cavity flow in the incompressible
regime. Consider a laminar incoming flow, for which θ_0 is the momentum thick-
ness of the Blasius boundary layer at separation. The dimensionless cavity length
L/θ_0 and the Reynolds number $\text{Re}_D = U_0 D/\nu$ are primary control parameters. Two
campaigns have been conducted to encompass a wide range of the parameter space:
$1,500 \leqslant \text{Re}_D \leqslant 9,000$ and $23 \leqslant L/\theta_0 \leqslant 104$. The space-time evolution of the
3D flow dynamics is investigated through Time-Resolved Particle Image Velocime-
try (TRPIV) measurements performed in two planes. On one hand, wind-tunnel
experiments at LIMSI focus on the shear layer waves and the primary dynamics.
High-speed PIV measurements (500 Hz) are performed in a xy-plane, streamwise
normal to the bottom of the cavity [2–4]. On the other hand, the water-tunnel cam-
paign at LTRAC is concerned with the spanwise extension of the flow [2]. It consists
of high-resolution PIV data out of a zx-plane, parallel to the bottom of the cavity at
$y/D = -0.1$. Velocity fields are obtained from particle images recorded by three
synchronised cameras and processed using a cross-correlation algorithm [15]. Cav-
ity span is larger at LTRAC ($S = 10 D$) than at LIMSI ($S = 6 D$) so as to better
identify spanwise wavelengths. Note that the spanwise extension is large enough in
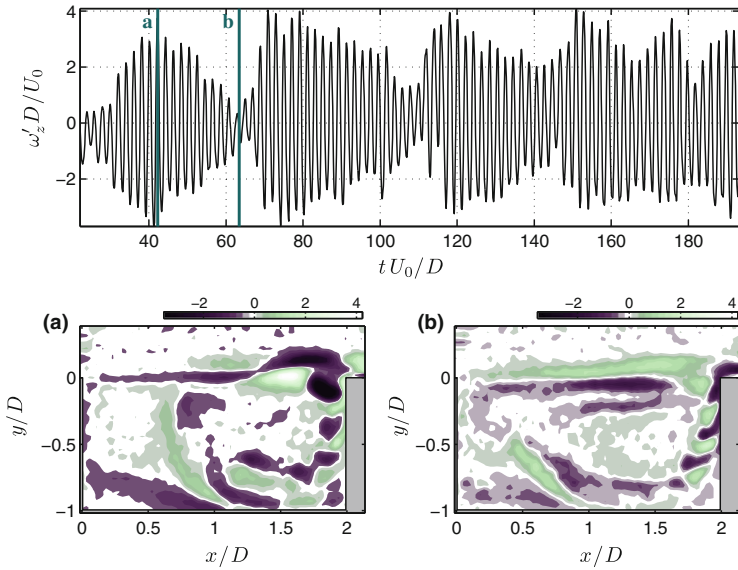
Fig. 2 Vorticity fluctuations $\omega_z' D/U_0$ out of time-resolved particle image velocimetry data in a xy-plane, for $L/D = 2.0$ and $L/\theta_0 = 82$ ($U_0 = 1.38$ m/s). *Top* Time-series extracted near the impingement $(x, y) = (1.5\,D, 0)$ and *bottom* picked-up snapshots
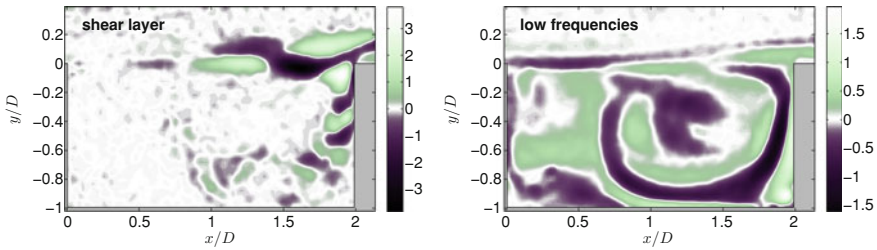
Fig. 3 Filtered vorticity fluctuations in a xy-plane (LIMSI), for $L/D = 2.0$ and $L/\theta_0 = 82$. Examples of filtered snapshots, *left*, around shear layer frequencies, *right*, for low frequencies only

both cases to ensure that influence of the end-walls remains secondary to intrinsic stability properties of the recirculating inner-flow.

3 Slow Dynamics Inside the Cavity

Since PIV data are time-resolved, spectral filtering can be performed to separate the low frequency range from the dominant locked-on frequency and its harmonics. Such a decomposition is illustrated in Fig. 3. The locked-on frequency of the shear layer f_a is such that $\mathrm{St}_a = f_a D/U_0 = 0.49$, while the local maximum of the low frequency range is observed at $\mathrm{St}_\Delta = f_\Delta D/U_0 = 0.024$.
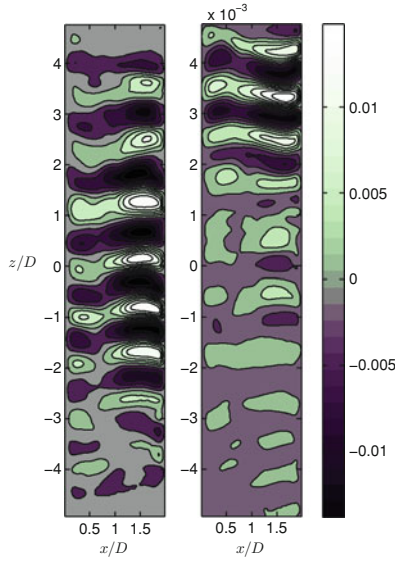
Fig. 4 Example of global Fourier modes in the zx-plane (LTRAC) for $L/D = 2.0$, $L/\theta_0 = 59.2$, $\mathrm{Re}_D = 2400$. Using streamwise velocity fluctuations $u'_x D/U_0$, real parts of the Fourier modes associated with *left*, St $= 0.019$, *right*, St $= 0.013$, corresponding to two counter-travelling waves

As expected, the dynamics corresponding to f_a is restricted to the shear layer and to inflows along the downstream wall of the cavity. On the contrary, low frequency dynamics encompasses the entire inner-flow. More particularly, slow dynamics organises as large-scale fluctuations winding up around the main recirculation and implying outflows near the impingement. Such a spatial structure associated with frequencies matching (Eq. 2) suggests 3D waves resulting from centrifugal instabilities, as observed in numerical studies by [5, 9]. The identification of those waves requires an investigation of the spanwise extension of the flow.

4 Spanwise Travelling Waves

The spanwise extension of the inner-flow is investigated through PIV measurements in a zx-plane at $y/D = -0.1$. Since recordings are time-resolved, Fourier transform can be applied to the time-series at each point of the velocity fields [4, 14]. Spatial structures associated with a single frequency are hence identified. They are referred to as *global Fourier modes* in the following.

The most energetic global Fourier modes are always associated with Strouhal numbers matching $\mathrm{St}_\Delta = f_\Delta D/U_0 \approx 0.02$, as shown in Fig. 4. The salient dynamics of the inner-flow organise as planar spanwise-travelling waves. Highly coherent spanwise oscillations appear for large areas of the zx-plane, yielding a unique spanwise wavelength $\lambda \approx D$. In other words, the dominant 3D dynamics of the inner-flow can be represented by *monochromatic spanwise travelling waves*. Such space-time
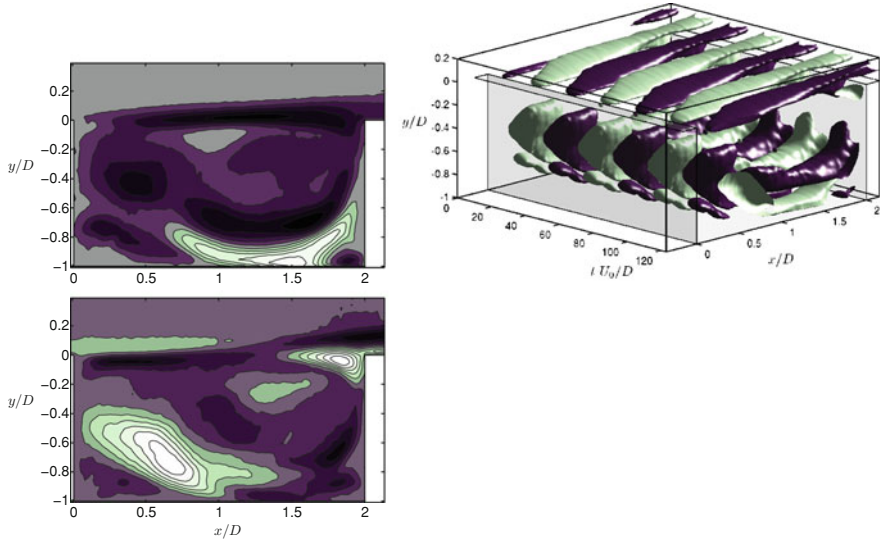
Fig. 5 Example of coherent structures associated with the dominant low frequency $f_\Delta D/U_0 = 0.024$, in the case $L/\theta_0 = 82$, $L/D = 2.0$, $\mathrm{Re}_D = 4{,}500$. Global Fourier mode $\zeta_\Delta(x, y)$ in a xy-plane is displayed using velocity fluctuations u'_x. *Top-left*, real part, *bottom-left*, imaginary part and *right*, reconstruction in the space-time volume (x, y, t) with iso-surfaces $u'_x D/U_0 = \pm 0.006$

feature typically come by pair of counter-propagating waves, which may exclude each other or partially overlap. In the latter case, interference leads locally to a (quasi) *standing wave* [2].

With increasing control parameters, shear layer disturbances get stronger and make the inner-flow more unsteady. However, the most salient modes connected to slow dynamics persist as monochromatic spanwise travelling waves. This is shown in [3], for $L/\theta_0 = 76$, $\mathrm{Re}_D = 6{,}800$. Hence, it is reasonable to assume that 3D dynamics corresponding to frequency St_Δ can write in the (dimensionless) form

$$\psi_\Delta(x, y, z, t) = \zeta_\Delta(x, y) \times \exp\left[i\left(\beta z - 2\pi \mathrm{St}_\Delta t\right)\right], \tag{3}$$

where β is the spanwise wavenumber and $\zeta_\Delta(x, y)$ stands for the global Fourier mode associated with St_Δ in a xy-plane. With that assumption, the spanwise dynamics of ψ_Δ is equivalent to the temporal dynamics in a single xy-plane. Through a simple dispersion relationship, it comes

$$\frac{\partial \psi_\Delta}{\partial z} \propto \frac{\partial \psi_\Delta}{\partial t} \qquad \left(\frac{\partial \psi_\Delta}{\partial z} = \beta \psi_\Delta = \frac{2\pi \mathrm{St}_\Delta}{c_\Delta} \psi_\Delta = -\frac{1}{c_\Delta} \frac{\partial \psi_\Delta}{\partial t}\right), \tag{4}$$

with c_Δ the (constant) spanwise phase velocity of the wave. Three-dimensional dynamics associated with frequency St_Δ can therefore be estimated through a reconstruction in the space-time volume (x, y, t) using the xy-plane Fourier mode $\zeta_\Delta(x, y)$ (Fig. 5). Time-wise axis here stands for the spanwise extension of the flow.

5 Conclusion and Outlook

We have shown that the lowest amplitude modulations of the shear layer waves are related to centrifugal instabilities inside the cavity. In fact, inner-flow fluctuations can be primarily modelled as monochromatic spanwise travelling waves of frequency $f_\Delta D/U_0 \approx 0.02$. Such a model implies spanwise derivatives become proportional to temporal derivatives. As a result, 3D structures associated with f_Δ can be estimated out of the two-dimensional space-time dynamics at a given position z. Future works will aim to characterise more precisely the non-linear interactions between shear layer waves and 3D slow dynamics inside the cavity.

References

1. Albensoeder S, Kuhlmann HC, Rath HJ (2001) Three-dimensional centrifugal-flow instabilities in the lid-driven-cavity problem. Phys Fluids 13:121–135
2. Basley J (2012) An experimental investigation on waves and coherent structures in a three-dimensional open cavity flow. Ph.D. thesis, Université Paris-Sud, Orsay; Monash University, Melbourne
3. Basley J, Pastur LR, Delprat N, Lusseyran F (2013) Space-time aspects of a three-dimensional multi-modulated open cavity flow. Phys Fluids 25(6):064105. doi:10.1063/1.4811692
4. Basley J, Pastur LR, Lusseyran F, Faure TM, Delprat N (2011) Experimental investigation of global structures in an incompressible cavity flow using time-resolved piv. Exp Fluids 50:905–918. doi:10.1007/s00348-010-0942-9
5. Brès GA, Colonius T (2008) Three-dimensional instabilities in compressible flow over open cavities. J Fluid Mech 599:309–339. doi:10.1017/S0022112007009925
6. Delprat N (2010) Low-frequency components and modulation processes in compressible cavity flows. J Sound Vibr 329(22):4797–4809
7. Faure TM, Pastur LR, Lusseyran F, Fraigneau Y, Bisch D (2009) Three-dimensional centrifugal instabilities development inside a parallelepipedic open cavity of various shape. Exp Fluids 47(3):395–410
8. Koseff JR, Street RL (1984) Visualization studies of a shear driven three-dimensional recirculating flow. Trans ASME J Fluids Eng 106:21–29
9. Meseguer-Garrido F, de Vicente J, Valero E, Theofilis V (2011) Effect of aspect ratio on the three-dimensional global instability analysis of incompressible open cavity flows. AIAA Paper, vol 3605. doi:10.2514/6.2011-3605
10. Neary MD, Stephanoff KD (1987) Shear-layer-driven transition in a rectangular cavity. Phys Fluids 30(10):2936–2946
11. Powell A (1953) On edge tones and associated phenomena. Acustica 3:233–243
12. Rockwell D, Naudascher E (1978) Review—self-sustaining oscillations of flow past cavities. J Fluids Eng 100:152–165
13. Rossiter J (1964) Wind-tunnel experiments on the flow over rectangular cavities at subsonic and transonic speeds. Aeronautical Research Council Report No. 3438
14. Rowley CW, Colonius T, Basu AJ (2002) On self-sustained oscillations in two-dimensional compressible flow over rectangular cavities. J Fluid Mech 455:315–346
15. Soria J (1998) Multigrid approach to cross-correlation digital piv and hpiv analysis. In: 13th Australasian fluid mechanics conference, Sydney
16. Theofilis V (2003) Advances in global linear instability of nonparallel and three-dimensional flows. Prog Aerosp Sci 39(4):249–315

Part X
Classic and Alternative Numerical Methods

Minimal Gain Time Marching Schemes for the Construction of Accurate Steady-States

Renan de S. Teixeira and Leonardo S. de B. Alves

Abstract Accurate reference solutions are very important in stability analysis, where they must act as a reliable base-state. They are also quite useful for unsteady numerical simulations, where they play key roles as initial conditions and in the implementation of boundary conditions, such as buffer zones. Quite often they are approximate solutions for a simplified version of the particular problem at hand, such as boundary-layer solutions. However, these approximate solutions are usually not available, their development is problem dependent and they may not be accurate enough. Hence, there is a need for methodologies that are capable of generating steady-states for arbitrary unsteady differential models. One attempt in this direction is the selective frequency damping technique, despite being developed for problems with a well defined self-excitation frequency. Another attempt to do so is the physical-time damping technique, but temporal dissipation is proportional to the time step. Since numerical instability can keep this time step too small in many nonlinear problems, this technique may not be able to introduce enough dissipation for the damping of all perturbations in very unstable flows. The present work overcomes this problem by noting that optimal damping is not introduced through maximum temporal dissipation, but minimal gain. The implicit Euler scheme employed in the physical-time damping technique achieves both in the limit of infinite CFL numbers, which usually cannot be imposed due to nonlinear effects. This time marching scheme was modified in order for its minimal gain to occur at smaller CFL numbers. Several test cases confirm the efficacy of this new approach.

R. de S. Teixeira
Pós-Graduação em Engenharia de Defesa, Instituto Militar de Engenharia,
Praça General Tibúrcio 80, Praia Vermelha, Rio de Janeiro, RJ 22290-270, Brazil
e-mail: renannovoser@gmail.com

L. S. de B. Alves (✉)
Departamento de Engenharia Mecânica, Universidade Federal Fluminense,
Rua Passo da Pátria 156, Bloco D, Sala 302, Niterói, RJ 24210-240, Brazil
e-mail: leonardo.alves@mec.uff.br

1 Introduction

Reference solutions are not only useful but often required for numerical simulation studies in many different areas. Stability analysis is one such example, where the reference solution should be a representative profile of the flow under consideration. It is usually called base flow in this context. In order to verify the stability of a given flow field, one must perturb its base flow and measure the growth or decay of the perturbations introduced. In a rigorous sense, this base flow should be a solution of the unperturbed governing equations, although early studies employed approximate profiles that fit well available experimental data [1]. However, such a procedure might lead to incorrect predictions, since numerical residues in the base flow become forcing terms in the perturbation governing equations. This difficulty is transformed into an asset by the Method of Manufactured Solutions for code verification [2, 3], where the force term created is reintroduced into the governing equations. Hence, an approximate solution of the original governing equations becomes an exact solution of the modified governing equations. Both approaches have been blended recently, where a linear stability analysis of a time-averaged solution is performed through direct numerical simulations of the modified governing equations [4]. On the other hand, this approach makes the numerical residue an integral part of the model, which undermines its ability to reproduce the correct flow physics. A preferred alternative in this field is the development of similarity solutions of a simplified model to be used as base flows [5]. However, this may not be enough to improve accuracy in the analysis of complex flow fields. Linear stability analyzes of transverse jets using approximate [6] and similar [7] profiles as base flows show opposite trends for the range of unstable frequencies with respect to the jet to cross flow velocity ratio. This is compelling evidence that an inaccurate base flow can and will lead to qualitatively incorrect predictions [8]. As the numerical tools available for eigenvalue calculations improved over the years, the computer time required by a linear stability analysis of complex base flows became smaller to the point such studies are commonplace nowadays [9]. Hence, the need for new methods capable of generating accurate base flows is greater than ever.

Initial and boundary conditions are yet another example where accurate reference solutions are important. Both approximate and similar solutions introduce unwanted oscillations when used as initial conditions in the unsteady numerical simulation of absolutely unstable mixing-layers [10]. Although the amplitude of these oscillations is much smaller in the latter case, their frequency content is much richer as well. This problem manifests itself in the calculation of the temporal growth rates, which can have relative errors as high as 18 % due to the use of approximate initial conditions even though high order schemes are employed [11]. It is important to emphasize another problem caused by inaccurate initial conditions. Their use in the simulation of flows around two-dimensional bodies lead to the presence of large perturbations at early times [12, 13]. Hence, large simulation times are required for these numerical waves to be convected out of the simulated domain before accurate flow statistics can be extracted. Accurate reference solutions are also very useful for a type of boundary condition known as absorbing layers [14] or sponge zones [15], since

they can improve its effectiveness. This is specially relevant in aeroacoustics [16] and receptivity [17] studies, where both problems become quite worse since the perturbations of interest are much smaller in magnitude than the vorticity waves that feed them. In the simulation of acoustic fields over airfoils [18, 19], these problems were minimized with the use of steady-states as reference solutions for both initial condition and sponge zones. A similar procedure was adopted to minimize numerical errors in receptivity studies of compressible mixing-layers [20]. Hence, a new method that is able to generate steady-states from the governing equations of interest would yield the most accurate reference solutions available.

A few methods exist today for the construction of accurate steady-states. The most traditional one is the class of Newton iteration methods, usually adapted to use continuation techniques as well [21]. However, they are very sensitive to initial conditions, require heavy computational resources for large systems and have severe convergence difficulties for globally unstable problems. Selective frequency damping (SFD) was developed to overcome these difficulties [22]. It works by introducing a source term in the governing equations that forces the time marching scheme to converge towards a reference solution, which is a filtered version of the unsteady solution being marched in time. Since this source term disappears at steady-state, the reference solution becomes the steady-state in this limit. Furthermore, it is quite simple to implement and requires the adjustment of only two additional parameters. However, this method has been applied to flows that only have a single dominant self-excited frequency that needs to be filtered. Applications where a broad range of frequencies must be damped, such as convectively unstable flows with intrinsic sources of noise, have yet to be investigated with this method. Recently, Physical-Time Damping (PTD) was developed to generate steady-states for both convectively and absolutely unstable flows [23]. This method uses a dual-time-stepping technique to switch the time-marching scheme of the unsteady code being used to an implicit Euler scheme. Since time marching schemes used by most codes are explicit, doing so avoids the need to implement the more complex algorithms associated with implicit time marching schemes. If the dissipative properties of the implicit Euler scheme are able to damp perturbations, a steady-state is reached without jeopardizing spatial resolution accuracy. Furthermore, it is quite easy to implement, requiring only a simple source term to switch time marching schemes and an outer loop for the dual-time-stepping. It works well for convectively unstable flows, but its temporal dissipation might not be strong enough for absolutely unstable flows with large temporal growth rates. This is caused by nonlinear effects, which limit the maximum time steps and, hence, the dissipative properties of the implicit Euler scheme. The present paper describes an attempt to improve this method.

2 Minimal Gain Schemes

In order to improve the damping capabilities of a time marching scheme, one must first quantify this property. This is traditionally done in numerical analysis through an evaluation of its gain. If one considers the differential system of equations
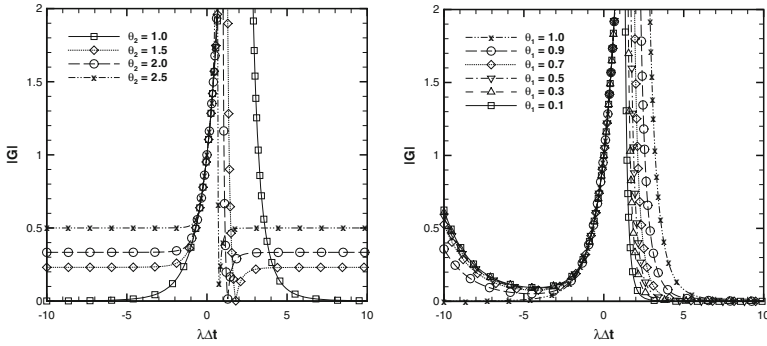
Fig. 1 Absolute value of the nonlinear gain function in Eq. (3) for $\theta_1 = 1$ (*left*) and $\theta_2 = 1$ (*right*)

$$\frac{\partial \mathbf{q}}{\partial t} = \mathbf{f}(\mathbf{q}) \,, \tag{1}$$

where t is time, $\mathbf{q}$ is the unknown variable vector and $\mathbf{f}$ is the steady-state residue. A possible generalization of the implicit Euler scheme (IES) is

$$\theta_1 \frac{\mathbf{q}^{n+1} - \mathbf{q}^n}{\Delta t} + (1 - \theta_1) \frac{\mathbf{q}^{n+1} - \mathbf{q}^{n-1}}{2\Delta t} = \theta_2 \mathbf{f}(\mathbf{q}^{n+1}) + (1 - \theta_2) \mathbf{f}(\mathbf{q}^n) \,, \tag{2}$$

where the IES is recovered when $\theta_1 = \theta_2 = 1$. The truncation error of Eq. (2) requires $\theta_1 \neq 2\theta_2$ to maintain its dissipative properties. Assuming $\mathbf{f}(\mathbf{q}) = \lambda \mathbf{q}$, a traditional linear stability analysis of this new numerical scheme yields the gain G as a funtion of $\beta = \lambda \Delta t$, where Δt is the time step and λ is the overall growth or decay rate of the solution. Linearization can be avoided if the modified equation is employed to estimate $\mathbf{f}(\mathbf{q})$ [24], leading to the nonlinear stability result

$$\begin{aligned}
G = e^{-\beta} &\left(e^{\beta} \left(\beta(\theta_2 - 1) \left(\beta \left(6\beta\theta_2^2 - 3(\beta + 2)\theta_2 + \beta \right) + 6 \right) - 3\theta_1 \right. \right. \tag{3} \\
&\times \left. \left(\beta^2 (\theta_2 - 1)(\beta\theta_2 - 1) + 2 \right) \right) + 3\theta_1 - 3 \right) / \left(\beta^3 \theta_2 (1 - 3 \right. \\
&\times (\theta_1 - 2\theta_2 + 1)\theta_2) + 3\beta^2 (\theta_1 - 2\theta_2) \theta_2 + 6\beta\theta_2 - 3 (\theta_1 + 1) \bigg) ,
\end{aligned}$$

whose behavior is shown in Fig. 1 for $\theta_1 = 1$ and $\theta_2 = 1$. Equation (3) yields a similar behavior and will not be discussed here. It is important to note that $\lambda < 0$ implies the governing equation is stable and a steady-state can always be achieved without modifications to the marching scheme. Hence, we focus on the behavior of the new scheme when $\lambda > 0$. This figure indicates that it is possible to achieve improved damping properties at small time steps by decreasing θ_1 or increasing θ_2. Hence, the new scheme is less sensitive to the maximum time step restriction caused by the loss of numerical stability due to nonlinear effects.
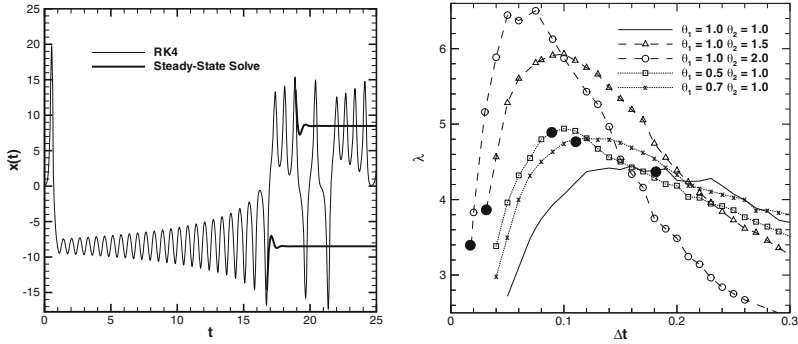
Fig. 2 Lorenz solution unsteady behavior with physical-time damping turned on and off (*left*) as well as the overall temporal decay rate of Eq. (2) when applied to the Lorenz equations (*right*). *Solid circles* are the smallest time steps that are able to generate a solution at the specified tolerance

3 Results

3.1 Lorenz Equations

Two test cases are utilized to evaluate the performance of Physical-Time Damping when the implicit Euler scheme is replaced by Eq. (2). The first one is given by the Lorenz equations. Figure 2 (left) shows the unsteady behavior of a solution of this problem for a set of control parameters that do not allow the fourth-order explicit Runge-Kutta scheme to reach steady-state. However, it does so with Physical-Time Damping, even if it is turned on after the exponential temporal growth leads the solution to nonlinear saturation. Figure 2 (right) shows the measured overall damping rate λ as a function of Δt. It confirms the theoretical finding that improved damping rates are achieved by decreasing θ_1 or increasing θ_2 at small Δt. This result is important because it confirms that a linear stability analysis can be utilized to construct minimal gain time marching schemes.

3.2 Spatially Periodic Planar Mixing-Layer

In order to provide a more difficult challenge to the new method, the absolutely unstable planar mixing-layer is simulated with the new minimal gain scheme given in Eq. (2). Details of this code are provided elsewhere [23]. Figure 3 shows a performance comparison between the implicit Euler scheme ($\theta_1 = \theta_2 = 1$) and a modified scheme with $\theta_1 = 1$ and $\theta_2 = 1.5$. The left plot in this figure shows that the number of pseudo-time iterations versus physical-time step only asymptotes to one for the modified scheme. The reason why is clear in the right plot of this figure, which shows that only the modified scheme is able to reduce the residue of the streamwise velocity component until it reaches steady-state.
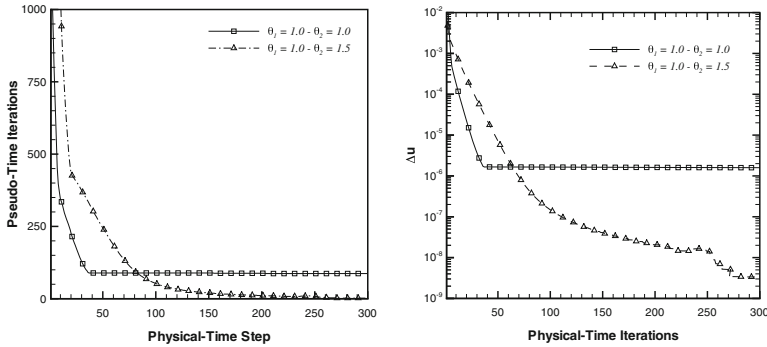
Fig. 3 Number of pseudo-time iterations (*left*) and streamwise velocity component increment (*right*) per physical-time step for $\theta_1 = \theta_2 = 1.0$ as well as $\theta_1 = 1.0$ and $\theta_2 = 1.5$

4 Conclusions

A new method was developed to improve the performance of PTD. It is based on constructing time marching schemes that achieve minimal gain at the smallest time step possible. Future work will compare it with SFD using different test cases.

References

1. Michalke A (1984) Prog Aerosp Sci 21:159
2. Steinberg S, Roache PJ (1985) J Comput Phys 57:251
3. Roache PJ (2002) J Fluids Eng 124:4
4. Jones LE, Sandberg RD, Sandham ND (2010) J Fluid Mech 648:257
5. Theofilis V (2003) Prog Aerosp Sci 39:249
6. Alves LSdeB, Kelly RE, Karagozian AR (2008) J Fluid Mech 602:383.
7. Kelly RE, Alves LSdeB (2008) Philos Trans R Soc Lond Ser A: Math Phys Sci 366:2729.
8. Bagheri S, Schlatter P, Schmid PJ, Henningson DS (2009) J Fluid Mech 624:33
9. Theofilis V (2011) Annu Rev Fluid Mech 43:319
10. Lardjane N, Fedioun I, Gokalp I (2004) Comput Fluids 33:549
11. Germanos RAC, de Souza LF, de Medeiros MAF (2009) J Braz Soc Mech Sci Eng 31(2):125
12. Bijl H, Carpenter MH, Vatsa VN, Kennedy CA (2002) J Comput Phy 179:313
13. Wang L, Mavriplis DJ (2007) J Comput Phys 225(2):1994
14. Blaschak JG, Kriegsmann GA (1988) J Comput Phys 77:109
15. Bodony DJ (2006) J Comput Phys 212(2):681
16. Colonius T, Lele SK (2004) Prog Aerosp Sci 40:345
17. Saric WS, Reed HL, White EB (2003) Annu Rev Fluid Dyn 35:413
18. Collis SS, Lele SK (1999) J Fluid Mech 380:141
19. Barone MF, Lele SK (2002) In: AIAA conference paper 0226, pp 1–12.
20. Barone MF, Lele SK (2005) J Fluid Mech 540:301
21. Tuckerman LS, Barkley D (2000) Bifurcation analysis for time steppers. In: Numerical methods for bifurcation problems and large-scale dynamical systems (The IMA volumes in mathematics and its applications, 2000), vol 119, pp 453–466.
22. Åkervik E, Brandt L, Henningson DS, Hoepffner J, Marxen O, Schlatter P (2006) Phys Fluids 18(6):068102
23. RdeS Teixeira, Alves LSdeB, (2012) Int J Comput. Fluid Dyn 26:67
24. Tannehill JC, Anderson DA, Pletcher RH (1997) Computational fluid mechanics and heat transfer. Taylor & Francis, Philadelphia

Molecular Dynamics Simulations
of Couette Flow

Juan A. Martín, Julio R. Meneghini and Vassilis Theofilis

Abstract In this work, the first steps towards developing a continuum-molecular coupled simulation technique are presented, for the purpose of computing macroscopic systems of confined fluids. The idea is to compute the interface wall-fluid by Molecular Dynamics (MD) simulations, where Lennard-Jones potential (and others) have been employed for the molecular interactions, so the usual no slip boundary condition is not specified. Instead, a shear rate can be imposed at the wall, which allows the calculation of wall material properties by means of an iterative method. The remaining fluid region will be computed by a spectral hp method. We present MD simulations of a Couette flow, and the results of the developed boundary conditions from the wall fluid interaction.

1 Introduction

In the continuum hypothesis, the analysis of macroscopic flows over a specific solid geometry needs to impose boundary conditions for the velocity of the fluid at the solid wall [1]. It is generally used the no slip condition at the boundaries, which specifies that the velocity of the fluid relative to the wall is zero at the solid-fluid interface. At the molecular scale, the description of nano and micro-fluids has been achieved by MD simulations. They are capable of accurately describing the dynamics of the wall-fluid interaction, and also can take into account the effect of wall material properties and the morphology of the surface. MD simulations consist of solving the

J. A. Martín (✉) · V. Theofilis
ETSI Aeronáuticos, Universidad Politécnica de Madrid, Pza. Cardenal Cisneros 3,
28040 Madrid, Spain
e-mail: jamartin@fmetsia.upm.es

J. R. Meneghini
Núcleo de Dinâmica e Fluidos, Departmento de Engenharia Mecânica, Escola Politécnica da
Universidade de São Paulo, Av. Professor Mello Moraes 2231, São Paulo 05508-030, Brazil

Newton's equations of motion for a system of interacting discrete molecules, in order to follow its evolution at the molecular scale [2–4]. The obtained microscopic results by this method are usually averaged by statistical mechanics, in order to provide macroscopic properties. In this case, there is no need to make any assumptions about the boundary conditions (apart from using particles with prescribed velocity) at the interface wall-fluid, instead, they will be given as an output of the numerical model, and then, will be translated to the macroscopic scale.

2 Molecular Dynamics Simulation Model

The model system consists of a monoatomic fluid confined between two atomistic walls. The top wall was set to be moving in parallel to the bottom wall, that remains stationary. With this configuration the steady-state of Couette flow is developed. All simulations included in this work were performed using the parallelized MD code LAMMPS [5].

The fluid molecules interact through the Lennard-Jones (LJ) potential

$$V_{ij}(r) = 4\varepsilon_{ij} \left[\left(\frac{\sigma_{ij}}{r} \right)^{12} - \left(\frac{\sigma_{ij}}{r} \right)^{6} \right], \tag{1}$$

in which ε is the energy scale, σ is the length scale, the value of r where the potential is zero, and the indexes represent the interaction between the atom i and the atom j. The results obtained are expressed in terms of these values, and will be given in reduced dimensionless units. A cutoff distance r_c is applied ($r_c = 1.12\sigma$), beyond which the value of the potential is set to zero. The equation of motion for atom i with mass m_i is

$$m_i \frac{d^2 \mathbf{r}_i}{dt^2} = \mathbf{F}_i = - \sum_{i \neq j} \frac{\partial V_{ij}}{\partial \mathbf{r}_i} \tag{2}$$

The temperature of the fluid was controlled by applying a thermostat to the fluid atoms, a very simple re-scaling of the velocities, in order to maintain the target temperature of the system, set to $T_0 = 1.0$ in LJ units.

The equations of motions were solved using a velocity-Verlet algorithm with a time step of 0.001 LJ time units, ($\tau = \sqrt{m\sigma^2}$) and the top wall was given a sliding velocity of $U_0 = 3.0$ at the start of the simulation, time $t = 0$. Periodic boundary conditions in the horizontal coordinate are imposed. The solid wall thickness was considered reviewing the values found in the literature, from 5 to 10 rows of atoms in [6–8], finding no differences when our simulations were carried out. Finally, 8 rows of atoms were selected to represent the wall.

Fig. 1 Streamwise velocity profile at times $\tau = 2^n$, for $n = 3, 4, 5, ...12$ from *right* to *left*. The *black line* represents the analytical solution and the average of streamwise velocity profile obtained by MD simulations is in *blue dots*, for different vertical locations. Simulation with 250,000 atoms
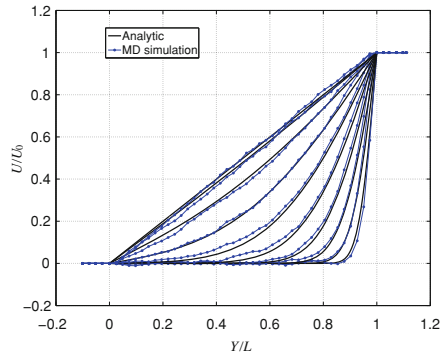
3 MD Simulations Results

Different simulations were performed, for two-dimensional domains. The biggest one with a size of 600×200 length units in the horizontal and vertical directions, containing a total number of atoms simulated of 250,000. With our computing capabilities, this simulation takes 2 weeks to completely develop the Couette flow. Regarding the CPU cost, smaller simulations (6,000 atoms) were used to analyze the LJ parameters effect. The density of the lattice was $\rho = 0.8$.

The planar Couette flow with no body forces can be described by the incompressible Navier-Stokes equations [9], which provide the one dimensional solution to the geometry presented. The x-component of the momentum equation is given by

$$\rho \frac{\partial u}{\partial t} = \mu \frac{\partial^2 u}{\partial y^2}, \tag{3}$$

with boundary and initial conditions

$$u(0, t) = 0, \quad u(L, t) = U_0, \quad u(y, 0) = 0,$$

where the boundaries between wall and the liquid are $y = 0$ at the bottom, and $y = L$ at the top. The solution of Eq. (3) can be expressed by Fourier series [10] and it is used to compare MD results with the analytic solution.

In a first case, the MD simulations were performed using the same interaction between fluid atoms and wall atoms, $\varepsilon_{f,w}$, (f stands for fluid and w stands for wall) than the interaction between fluid atoms themselves, $\varepsilon_{f,f}$. In other words, the system is $\varepsilon_{w,f} = \varepsilon_{f,f}$. The velocity profile obtained by MD simulations is compared with the analytic solution in Fig. 1. The streamwise velocity is spatial and time averaged in N horizontal slices along the vertical coordinate. The continuum analytic profile is calculated by Eq. (3) with $\mu = 1.6$, value taken from [11] when $\rho = 0.8$ and $T = 1.0$.
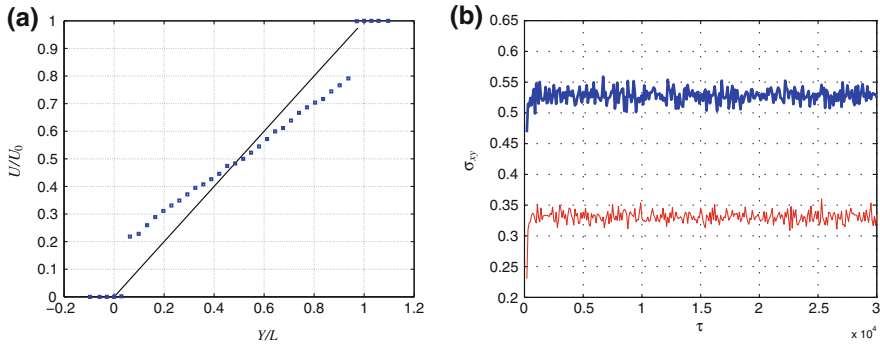
Fig. 2 a In *blue squares*, the steady state flow profile for a system with $\varepsilon_{w,f} = 0.6\varepsilon_{f,f}$, and $\rho_w = 2.8\rho_f$. The *black line* indicates the steady Couette flow. **b** Shear stress evolution. *Thick blue line* represents $\varepsilon_{w,f} = \varepsilon_{f,f}$ and $\rho_w = \rho_f$, while *thin red line* stands for $\varepsilon_{w,f} = 0.6\varepsilon_{f,f}$ and $\rho_w = 2.8\rho_f$. Both simulations with 6,000 atoms

As observed in Fig. 1, the start-up and steady Couette flow is well captured with the molecular model used, and it is capable of reproducing the different stages of the flow development, recovering the expected behavior from continuum hydrodynamics. The differences observed during the transient process might be due to the impossibility of imposing a constant pressure in the MD simulations.

A second round of simulations were launched, modifying the interaction between fluid and walls. In that case, the wall has an interaction with the fluid characterized by $\varepsilon_{w,f} = 0.6\varepsilon_{f,f}$, and also the atomistic walls have a reduce density of $\rho_w = 2.8\rho_f$. These values were chosen looking into [6]. The steady-state velocity profile obtained can be appreciated in Fig. 2a, where a slip at the solid-fluid interface is evident. This result is coherent with that reported in [6, 12], and the simulations were performed with a geometry of 120×40 length units in the horizontal and vertical directions, accounting 6,000 atoms.

It is also interesting to analyze the results concerning the shear stress at the wall, measuring the output shear force on the walls divided by the walls surface. Its time evolution is represented in Fig. 2b. As can be appreciated, the values of the shear stress (unlike the velocity values) exhibit a wide fluctuation, so very long simulation times must be considered to statistically obtain a representative value. From Fig. 2b, a reduction of the shear stress is observed for the simulation where interfacial slip is developed.

The main application of these simulations consists of the possibility of representing the different interfacial scenarios provided by textured or coated surfaces, which can consider the properties of the wall material, and can take into account the dynamics of the interfacial region. So, a tool to design low friction drag can be developed from this simulation, looking for the interaction between wall and fluid which can provide the drag force level required for a particular application (such as oil pumping in petrol enterprises).

4 Conclusions

MD simulations have the drawback of the heavy computational load required, which limits the simulations to a length scale of tens of nano-meters. So, in order to develop a useful simulation tool, these results can be used towards developing boundary conditions that will be applied in a continuum model. These integral boundary conditions will substitute the usual no slip condition by the velocity profile or shear stress obtained in this stage of the simulation, to elaborate a hybrid method which can combine both, molecular and continuum simulations in order to accurately describe the wall-fluid interaction and also represent the rest of the bulk fluid with a remarkable reduction of the computational cost.

In this work, the first steps to develop a code that includes Molecular Dynamics simulations and continuum hypothesis is developed. The canonical problem of Couette flow has been used to validate the numerical technique, obtaining very good agreement with the results given by MD simulations. The dynamics at the molecular scale plays a crucial role when determining the interaction between fluid and solid, which can define the level of shear stress at the wall. Therefore, the design of the wall surface can be achieved by MD simulations, and used as a passive way to reduce skin-friction drag, and to delay transition to turbulence.

The high computational cost of MD simulations forces us to combine this method with a continuum hypothesis which can provide a way to simulate a bulk fluid around a solid. This technique will take accurately into account the influence of the material properties, the texture of the surface or the coatings applied to the surface.

5 Future and On-Going Work

Currently, the main efforts are focused on the development of an iterative method to calculate potential parameters from the shear stress required at wall, in order to obtain the surface properties that best suit particular applications. Also, although the flow viscosity is tabulated in several works (see e.g. [11]), it will be calculated as a part of the simulation, to have an independent numerical technique. Likewise, LJ parameters are being matched with the Knudsen number, solving Eq. (3) with slip boundary conditions, to provide more physical meaning. Finally, some complex flows are being considered, such as an open cavity Fig. 3a, or the flow over textured surfaces Fig. 3b.
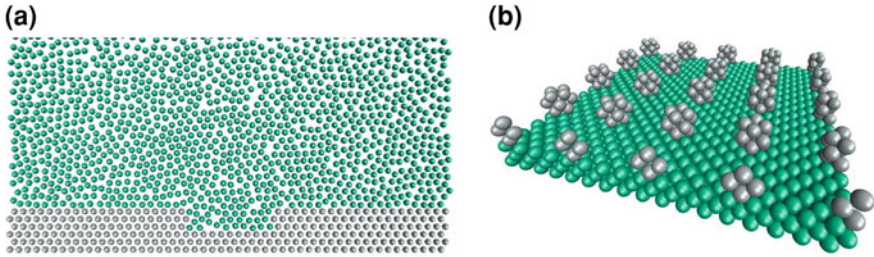
Fig. 3 Sketches of the ongoing work, **a** open cavity and **b** textured surface

References

1. Batchelor GK (2000) Introduction to fluid dynamics. Cambridge University Press, Cambridge, p 60
2. Haile JM (1992) Molecular dynamics simulations, elementary methods. Wiley, New York
3. Allen MP, Tildesley DJ (1987) Computer simulation of liquids. Oxford University Press, Oxford
4. Rapaport DC (1995) The art of molecular dynamics simulations. Cambridge University Press, Cambridge
5. Plimpton S (1995) Fast parallel algorithms for short-range molecular dynamics. J Comp Phys 117:1–19
6. Thompson PA, Troian SM (1997) A general boundary condition for liquid flow at solid surfaces. Nature 389(6649):360–362
7. Smith ER et al (2012) Control volume representation of molecular dynamics. Phys Rev E 85:056705
8. Heyes DM et al (2012) Pressure dependence of confined liquid behavior subjected to boundary-driven shear. J Chem Phys 136:134705
9. Schlichting H (2000) Boundary layer theory. Springer, New York, p 130
10. Strauss WA (1992) Partial differential equations. Wiley, New Jersey
11. da Costa Silva F et al (2003) Shear viscosity calculated by perturbation theory and molecular dynamics for dense fluids. J Quantum Chem 95:79–87
12. Cieplak M et al (2001) Boundary conditions at a fluid-solid interface. Phys Rev Lett 86(5):803–806

Vortex Filament and Global Instability Analysis of the Crow Mode

Juan Ángel Tendero, Pedro Paredes, Miquel Roura, Rama Govindarajan and Vassilios Theofilis

Abstract Aircraft trailing vortices and their wakes are important to understand in order to shorten the minimum aircraft distances for safe operation in commercial flights. The mechanisms of wake destruction are studied by predictions by both inviscid vortex filament and viscous BiGlobal instability analyses. The two methods have already been applied to the wake problem, but a more detailed comparison is carried out here. The results show excellent agreement between the two methodologies predicting the long wave symmetric instability of a counter-rotating pair of vortices, namely the Crow instability, even at low Reynolds numbers.

1 Introduction

This work, as well as many others, is dedicated to the understanding of the vortical aircraft wakes. This is an important problem for the aeronautical industry, as Spalart [13] highlighted, because the commercial planes have to fly maintaining long distances among them due to the high risk that vortical wakes impose. Despite

J. Á. Tendero (✉) · P. Paredes · V. Theofilis
School of Aeronautics, Universidad Politécnica de Madrid, Pza. Cardenal Cisneros 3,
28040 Madrid, Spain
e-mail: juanangel.tendero.ventanas@upm.es

P. Paredes
e-mail: pedro.paredes@upm.es

V. Theofilis
e-mail: vassilios.theofilis@upm.es

M. Roura
Gamesa Innovation and Technology S.L., Calle Ramírez de Arellano, 37, 28043 Madrid, Spain
e-mail: mroura@gamesacorp.com

R. Govindarajan
TIFR Centre for Interdisciplinary Sciences, 21, Brundavan Colony, Narsingi,
Hyderabad 500075, India
e-mail: rama@tifrh.res.in

the numerous research efforts, the underlying physical mechanisms responsible for the vortex destruction are only partly understood and distances still rely on empirical prediction criteria, being too conservative. Therefore, a deeper understanding of this phenomena is crucial.

The present study follows two different approaches to cover this problem and finds quite good agreement between them. These two are: the vortex filament instability method, as the one used by Crow [3], where the vortices are assumed to be inviscid and infinitely thin; and the viscous BiGlobal modal instability analysis, which is a modal analysis of the linearized Navier-Stokes equations for a two-dimensional basic flow, firstly applied to vortical wakes by Hein and Theofilis [7].

The two methods offer good results and have their own advantages and disadvantages. First of all, the filament methods are inviscid,[1] grid-less and unbounded. In contrast to the BiGlobal method that is viscous, uses a grid and needs boundaries. However, the grid methods are more realistic since they are based on the full Navier-Stokes equations and account for vortical shape and size, as well as axial flow. It will be seen that the filament methods have a parameter called the cutoff parameter that is related to the real vortex core and where axial flow could be included, but this is only an approach to the whole field.

The inviscid vortex methods for stability have been used from a long time ago, as the studies of Kármán [9] show. However, in those analysis, there are not perturbations in the third direction and they are, therefore, point vortex instability analyses. These points, which are infinite parallel lines, can be perturbed sinusoidally, and that is what has been analyzed in several works as Crow [3] for two counter-rotating vortices, Jiménez [8] for two co-rotating vortices and Crouch [2] and Fabre and Jaquin [4] for configurations of four vortices.

The BiGlobal viscous method, on the contrary, is more modern, and is found to be very computational demanding when using Chebyshev-Gauss-Lobatto points and sparse allocation is not implemented, see Rodríguez and Theofilis [11]. Other approaches could be followed to make the problem more feasible, as the low order finite elements used by González et al. [6] or the method used by Gómez et al. [5], that only obtains a few eigenvalues, but offers the possibility to study even thee-dimensional basic flows (TriGlobal). However, a different methodology is used here, that consist of the combination of a special set of high order finite differences with sparse allocation, following the method of Paredes et al. [10].

The present analysis is a continuation of Tendero et al. [14], presented recently. Other works as Brion et al. [1] have also compared results from the two methods, but less details are given. In this case, the comparison is studied more extensively in the range and amount of parameters. The structure of the work is to present first the vortex wake configuration, which is composed by two counter-rotating vortices. After that, the vortex filament stability method and later the BiGlobal method are exposed. Afterwards it is shown a comparison of results from the two methodologies and finally a section of conclusions is given where the most relevant results are discussed, as well as future lines of work.

---

[1] There exist several cases where viscosity is added to filament methods applied to evolution problems, but its introduction to eigenvalue problems is still an open issue.

2 Configuration of Study, the Counter-Rotating Vortex Pair

The configuration chosen is the counter-rotating vortex pair. Despite of its simplicity, it is capable of reproducing many of the most relevant aircraft wake instabilities, e.g., the Crow [3] instability. As done in other works, the vorticity of the right vortex will be positive, and consequently, negative for the left one. The frame of reference used is a right handed system $[x, y, z]$ moving with the vortices, where the $[x, y]$ plane is perpendicular to the direction of the vorticity, x is the horizontal, y the vertical and z the perpendicular direction, pointing opposite to the flight direction.

The main parameters of the problem are the distance between the centroids of the vortices, b, and the circulation of the vortices, Γ for the right vortex and $-\Gamma$ for the left one. These two magnitudes define a characteristic time, $t_c = 2\pi b^2 / \Gamma$, which is the time needed for the vortices to descend a distance b. The down wash speed of the vortices will then be $\bar{U} = -(\Gamma/2\pi b)\mathbf{e_y}$. Other important parameter is the vortex radius, a, which is a single parameter to measure the vortex size. However, the shapes of the vortices and the existence of axial flow are also of importance. b and t_c will be used for non-dimensionalization. When doing so, the new non-dimensional variables will be written with tilde.

3 Vortex Filaments Stability Method

In this section, the vortex filament stability equations particularized for the case of study are exposed. These equations are obtained after perturbation and linearization of the kinematic relation between velocities and positions known as the Biot-Savart law for vortex filaments. For more details of the deduction of the equations and the assumptions made, review Tendero et al. [14] and of course the work of Crow [3].

Along this study, the right vortex will be addressed as vortex 1 and the left one as vortex 2. The basic state is therefore, $X_1 = b/2$, $X_2 = -b/2$, $Y_1 = Y_2 = 0$. ω is the complex frequency, unknown of the problem and obtained as complex eigenvalues. k is the wavenumber, which appear when substituting the perturbations by exponential expansions, and d is the cutoff parameter, the distance that needs to be removed from the integrals to avoid divergence when the influence of one filament over itself is calculated. $K_0(\alpha)$ and $K_1(\alpha)$ are the modified Bessel functions of the second kind, and $Ci(\alpha)$ is the integral cosine. The equations are non-dimensionalized using the variables defined in Sect. 2 and finally, the eigenvalue problem can be written as Eq. 1. It is the same as in Eq. 8 of Crow [3], but the notation has changed, the coordinates $[x, y, z]$, used here, are interchanged by $[y, z, x]$ there and also vortex numbers 1 and 2 are interchanged. In a similar fashion as in that paper, a function $\tau(\theta) = \cos\theta - 1 + \theta\sin\theta - \theta^2 Ci(\theta)$ is defined to shorten the equations shown.

$$-\mathrm{i}\tilde{\omega}\begin{pmatrix}\tilde{x}_1 \\ \tilde{y}_1 \\ \tilde{x}_2 \\ \tilde{y}_2\end{pmatrix} = \begin{pmatrix} 0 & 1 + \frac{\tau(\tilde{k}\tilde{d})}{2\tilde{d}^2} & 0 & -\tilde{k}^2 K_0(\tilde{k}) - \tilde{k} K_1(\tilde{k}) \\ 1 - \frac{\tau(\tilde{k}\tilde{d})}{2\tilde{d}^2} & 0 & -\tilde{k} K_1(\tilde{k}) & 0 \\ 0 & \tilde{k}^2 K_0(\tilde{k}) + \tilde{k} K_1(\tilde{k}) & 0 & -1 - \frac{\tau(\tilde{k}\tilde{d})}{2\tilde{d}^2} \\ \tilde{k} K_1(\tilde{k}) & 0 & -1 + \frac{\tau(\tilde{k}\tilde{d})}{2\tilde{d}^2} & 0 \end{pmatrix}\begin{pmatrix}\tilde{x}_1 \\ \tilde{y}_1 \\ \tilde{x}_2 \\ \tilde{y}_2\end{pmatrix} \quad (1)$$

Table 1 BiGlobal convergence results for $\tilde{\omega}_i$ given $\tilde{a} = 0.0721$, $\tilde{k} = 0.73$ and two sets of Re

Re	N × 75Ny150	N × 100Ny200	N × 125Ny250	N × 150Ny300
100	0.64...	0.7955...	0.79510...	0.7950411...
10,000	0.84...	0.88...	0.8257...	0.8229593...

Fig. 1 Comparison between the vortex filament (*solid line*) and BiGlobal results for $Re = 100$ (*squares*) and $Re = 10,000$ (*circles*). Cutoff, $\tilde{d} = 0.0630$, in the filament code and radius, $\tilde{a} = 0.0721$, in the BiGlobal simulations
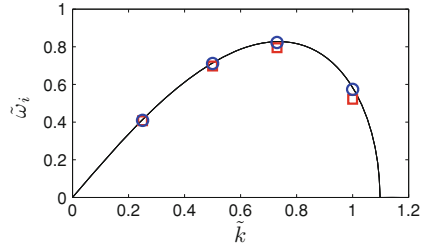
4 BiGlobal Stability Method

The BiGlobal equations are deduced after perturbation an linearization of the Navier-Stokes equations, again, Tendero et al. [14] is the main reference, but others as Theofilis [15, 16] offer more details. The BiGlobal approach assumes a basic flow only dependent on two coordinates, $\mathbf{Q} = [U, V, W, P]^T(x, y)$, as well as the perturbations dependence on the third coordinate is homogeneous: $\mathbf{q}(x, y, z, t) = \hat{\mathbf{q}}(x, y)e^{i(\beta z - \omega t)}$. The BiGlobal equations are written as an eigenvalue problem with $[\hat{u}, \hat{v}, \hat{w}, \hat{p}]^T$ as eigenvectors and ω as eigenvalues:

$$\begin{pmatrix} \mathscr{L}_{2D} + U_x & U_y & 0 & \mathscr{D}_x \\ V_x & \mathscr{L}_{2D} + V_y & 0 & \mathscr{D}_y \\ W_x & W_y & \mathscr{L}_{2D} & ik \\ \mathscr{D}_x & \mathscr{D}_y & ik & 0 \end{pmatrix} \begin{pmatrix} \hat{u} \\ \hat{v} \\ \hat{w} \\ \hat{p} \end{pmatrix} = \begin{pmatrix} i\omega & 0 & 0 & 0 \\ 0 & i\omega & 0 & 0 \\ 0 & 0 & i\omega & 0 \\ 0 & 0 & 0 & 0 \end{pmatrix} \begin{pmatrix} \hat{u} \\ \hat{v} \\ \hat{w} \\ \hat{p} \end{pmatrix} \qquad (2)$$

where $\mathscr{L}_{2D} = U\mathscr{D}_x + V\mathscr{D}_y + Wik - \frac{1}{Re}(\mathscr{D}_{xx} + \mathscr{D}_{yy} - k^2)$. For details of the derivation matrices used and the numerical solution of the problem, see Paredes et al. [10]. Symmetry boundary conditions are imposed in the mid-plane, so half of the domain has to be computed and the Lamb-Oseen vortex is used as a basic flow. For more details of the boundary conditions and other mesh properties, as well as for the basic flow, the reader is referred again to Tendero et al. [14].

5 Results Discussion

Results from both methodologies are compared. First of all, a correct analogy of d from the filament method and a from the basic flow in the BiGlobal analysis needs to be made. Crow [3] showed that for a Rankine vortex, the effective core size relation
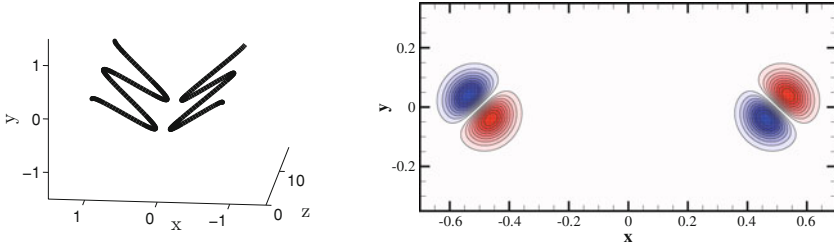
Fig. 2 Most amplified mode for $\tilde{k} = 0.7300$. Vortex and perturbation for $\tilde{d} = 0.0630$ using the vortex filament method (*left*) and contours of the imaginary part of vorticity eigenfunction (*red* for positive and *blue* for negative), normalized with the maximum attained over x and y, plotted at nine equally spaced contour levels from 0.1 to 0.9 by the BiGlobal simulations using the finest mesh, $Re = 10,000$ and $\tilde{a} = 0.0721$ (*right*)

with the cutoff parameter was $d/a_e = 0.6420$. Later, more approximations were made to be able to fit any vorticity shape or even axial flow [17]. Summarizing, the radius a corresponding to any vortical shape was related to an effective radius a_e which could be compared to the cutoff by the previously given formula. The formula that relates the two radius is $\ln(a_e/a) = 1/4 - A + C$ where A and C are given by:

$$A = \lim_{\tilde{r} \to \infty} \left[\int_0^{\tilde{r}} r' \tilde{v}_\theta(r')^2 dr' - \ln(\tilde{r}/\tilde{a}) \right] \qquad C = 2 \int_0^\infty \tilde{r} \tilde{w}(\tilde{r})^2 d\tilde{r} \qquad (3)$$

where $\tilde{v}_\theta(\tilde{r})$ is the swirl velocity and $\tilde{w}(\tilde{r})$ the axial velocity, both non-dimensionalized in the way defined in Sect. 2. In the Lamb-Oseen case, $A = (1/2)[\gamma - \ln(2)]$ and $C = 0$, where $\gamma \approx 0.5772$. It is chosen $\tilde{d} = 0.0630$ to have realistic parameters, as done by Crow [3]. Therefore, $\tilde{a} = 0.0721$ is the value to introduce in the basic flow for the BiGlobal analysis.

Two values for the Reynolds number (defined as $Re = \Gamma/2\pi\nu$ following the same non-dimensionalization as before) are studied, 100 and 10,000. Table 1 shows the convergence analysis, and Fig. 1 summarizes the results, showing pretty good agreement between the vortex filament and BiGlobal methods, being the two curves coincident for $Re = 10,000$, and just a little damp is seen for a quite low $Re = 100$. Consequently, the results for the Crow mode are perfectly matched using the BiGlobal and the vortex filament instability methods, that are based in quite different sets of equations. One explanation for the small influence of the Reynolds number may be that the viscosity effect is small when the vortices are well apart, and only the convective mechanisms are important. Sipp et al. [12] could be reviewed to find more about vortex dipoles where the vortices are nearer and, therefore, deformed. The shape of the most amplified mode is shown in Fig. 2.

6 Conclusions

The main outcome of this work is to show how the Crow instability can be found both by vortex filament instability methods, as well as by the BiGlobal approach. Agreement is excellent, and the damping for $Re = 100$ is still very little, so the mode can be found using viscous analysis. Further work will be focused on extending the range of wavenumbers studied and vortex sizes, as well as axial flow also need to be checked for agreement between the two methodologies. In addition, other vortical configurations are of interest and intended to be studied.

References

1. Brion V, Sipp D, Jacquin L (2007) Optimal amplification of the crow instability. Phys Fluids 19(11):111703
2. Crouch JD (1997) Instability and transient growth for two trailing-vortex pairs. J Fluid Mech 350:311–330
3. Crow SC (1970) Stability theory for a pair of trailing vortices. AIAA J 8:2172–2179
4. Fabre D, Jacquin L (2000) Stability of a four-vortex aircraft wake model. Phys Fluids 12(10):2438–2443
5. Gómez F, Gómez R, Theofilis V (2014) On three-dimensional global linear instability analysis of flows with standard aerodynamics codes. Aerosp Sci Technol 32(1):223–234
6. Gonzalez LM, Gomez-Blanco R, Theofilis V (2008) Eigenmodes of a counter-rotating vortex dipole. AIAA J 46(11):2796–2805
7. Hein S, Theofilis V (2004) On instability characteristics of isolated vortices and models of trailing-vortex systems. Comp Fluids 33(5–6):741–753
8. Jiménez J (1970) Stability of a pair of co-rotating vortices. Phys Fluids 18(11):1580–1581
9. Kármán TV (1912) Über den mechanismus des widerstandes, den ein bewegter Körper in einer Flüssigkeit erfährt. Nachr Ges Wissenschaft Göttingen, pp 547–556
10. Paredes P, Hermanns M, Le Clainche S, Theofilis V (2013) Order 10^4 speedup in global linear instability analysis using matrix formation. Comput Method Appl M 253:287–304
11. Rodríguez D, Theofilis V (2009) Massively parallel solution of the BiGlobal eigenvalue problem using dense linear algebra. AIAA J 47(10):2449–2459
12. Sipp D, Jacquin L, Cossu C (2000) Self-adaptation and viscous selection in concentrated two-dimensional vortex dipoles. Phys Fluids 12(2):245–248
13. Spalart P (1998) Airplane trailing vortices. Annu Rev Fluid Mech 30:107–138
14. Tendero JA, Paredes P, Roura M, Govindarajan R, Theofilis V (2013) Biglobal and point vortex methods for the instability analysis of wakes. AIAA Paper 2013–2820
15. Theofilis V (2003) Advances in global linear instability analysis of nonparallel and three-dimensional flows. Prog Aerosp Sci 39(4):249–315
16. Theofilis V (2011) Global linear instability. Annu Rev Fluid Mech 43:319–352
17. Widnall SE (1975) Structure and dynamics of vortex filaments. Annu Rev Fluid Mech 7:141–165

Part XI
Sound Generation and Control in Separated Flows

Proper Orthogonal Decomposition Analysis of Noise Generation Mechanisms in the Slat Cove

Daniel S. Souza, Daniel Rodríguez and Marcello A. F. de Medeiros

Abstract Airframe became a relevant source of noise in commercial aircrafts because of the introduction of high by-pass ratio turbofans. The slat is one of the most important airframe noise source, since it represents a source distributed along the wing span. The flow mechanism responsible for noise generation is not completely understood yet. Time-accurate Lattice-Boltzmann simulations were carried out in order to deliver flow data for the calculations of coherent structures in the slat cove by means of the Proper Orthogonal Decomposition (POD) technique. The first two POD-modes are dominated by mixing-layer like structures. Power Spectral Density of the amplitude of these leading POD-functions present the highest level at frequencies that are dominant in the spectrum of far-field acoustic fluctuations.

1 Introduction

With the reductions in engine noise attained in the last decades, in combination with the low-thrust conditions, airframe noise has become one of the most important noise sources during landing phase [5]. Among other significant sources such as the landing gear and flap-side edges, the slat is particularly important as it is a distributed source along the whole wing span.

D. S. Souza (✉) · M. A. F. de Medeiros
Universidade de São Paulo, Rua Jõao Dagnone 1100, São Carlos 13563-120, Brazil
e-mail: dss_em@yahoo.com.br

M. A. F. de Medeiros
e-mail: marcello@sc.usp.br

D. Rodríguez
School of Aeronautics, Universidad Politécnica de Madrid, Plaza del Cardenal Cisneros 3, 28040 Madrid, Spain
e-mail: dani@torroja.dmt.upm.es

Experiments addressing the slat noise identified three different components in the radiated sound pressure spectrum: a high-frequency tone, a broadband noise at low and medium frequencies and a series of tonal peaks overlapping the low-medium frequency broadband noise [4, 5]. Several experiments [9, 13] and three-dimensional numerical simulations [14, 15] have shown the series of tonal peaks in the slat noise spectrum. Its origin is however controversial. Some experiments indicate that at high Reynolds numbers, these tones do not arise [6, 17], while numerical simulations at similar Reynolds numbers still show the peaks [16].

The present work further investigates the flow structures existing in the slat cove and their relation with the noise radiated. Following previous experiences, time-accurate 3D simulations are carried out using a Lattice-Boltzmann formulation. Aflalo et al. [1] compared instantaneous vorticity fields and near-field pressure spectra computed using the present approach with results from Navier-Stokes simulations, showing good agreement. Noting that at low angles of attack the boundary layers on the slat did not significantly affect the computed low-medium frequency slat noise, Simões et al. [18] proposed a model considering free-slip boundary conditions on the slat surface, allowing more efficient computations. Analogous time-accurate simulations are presented herein for a high-lift airfoil configuration. A time-domain proper orthogonal decomposition (POD) [8] is then performed using the velocity field in the slat cove region, to educe the most coherent structures existing within the cove, and to study their relation to the dominant frequencies in the acoustic near-field.

2 Lattice-Boltzmann Simulation of a High-Lift Airfoil

The McDonnell Douglas 30P30N high-lift airfoil geometry is studied in this work. The slat and flap chords are, respectively, 15 and 30 % of the airfoil stowed chord ($c_{stowed} = 0.457$ m, in the present simulations). This model has been extensively studied by NASA and further details of the geometry can be found in [3, 4, 10–12]. The trailing edges of the airfoil end in a sharp cusp, except for the slat trailing edge that has a finite thickness of 0.092 % of c_{stowed}. The simulation model is scaled to match the experiments from Jenkins et al. [10], resulting in a Reynolds number of 1.7 million based on the stowed chord of the airfoil and free stream velocity, $U_\infty = 56$ m/s, with a Mach number of $M = 0.17$.

The simulations are computed using the commercial code PowerFLOW 4.3a, based on the Lattice-Boltzmann method. Subgrid turbulence scales are acounted for by a modified version of the $k - \epsilon$ turbulence model [7]. The calculation of the sound propagated to the far-field is made by means of the Farassat's formulation of the Ffowcs Williams-Hawkings analogy [2]; the integration surface is located at the slat surface and at the aft half part of the main element surface [14]. A Free-slip wall condition was used at the slat surface except for the cove wall, where a no-slip wall condition was imposed [18]. The mesh employed in the solution of the Boltzmann equation has its smallest element, of size 0.2 mm within the slat cove and a total of

1.04×10^8 voxels. It was shown to produce grid independent results in the near- and far-field [18].

Periodicity is imposed at the spanwise direction. The simulated span is equal to 11 % of the stowed chord. As prior tests revealed [14], this spanwise dimension is larger than the coherence length. The angle of attack, defined with respect to the main element, is $4°$. Simulations comprise a physical time period of 0.25 s. Analysis of first and second order statistics indicated that this simulation time, after discarding the initial transient of 0.1 s, is enough to achieve statistical convergence of the frequencies of interest.

3 Proper Orthogonal Decomposition

The Proper Orthogonal Decomposition (POD) is a correlation technique that delivers a basis of orthogonal functions $\{\phi_k\}$, referred to as POD functions or modes, that optimally decompose a set of empirical (either from experiments of numerical simulations) data $\{\mathbf{q}^{(l)}\}$ [8]. Each element $\mathbf{q}^{(l)}$ in the empirical data is a *realization* of the flow, and usually corresponds to the flow at a given time-instant (or snapshot). Another possibility is the use of finite-time Fourier transforms of different time segments, as was done in Souza et al. [21]. The present work employs a vector-valued variation of the snapshots-based method by Sirovich [19]. Noting that the POD modes can be expanded as a linear combination of the flow realizations conforming the empirical data

$$\phi_k = \sum_l \beta_l^k \mathbf{q}^{(l)}, \tag{1}$$

a cross-correlation matrix can be calculated in which the correlations are defined between different empirical realizations through a general inner product:

$$\tilde{\mathbf{R}}_{ij} = \langle \mathbf{q}^{(j)}, \mathbf{q}^{(i)} \rangle. \tag{2}$$

The principal directions of the cross-correlation matrix are obtained from the solution of the eigenvalue problem

$$\tilde{\mathbf{R}} \beta^k = \lambda_k \beta^k, \tag{3}$$

where λ_k is the kth POD eigenvalue and β^k is the kth eigenvector of $\tilde{\mathbf{R}}$. The POD functions are retrieved from (1).

POD modes are orthogonal under the inner product used. This property can be used to expand the empirical data as a linear combination of the POD modes, following

$$\tilde{\mathbf{q}}^{(j)} = \sum_k a_k(t^{(j)})\phi_k, \quad a_k(t^{(j)}) = \langle \mathbf{q}^{(j)}, \phi_k \rangle / \langle \phi_k, \phi_k \rangle. \tag{4}$$
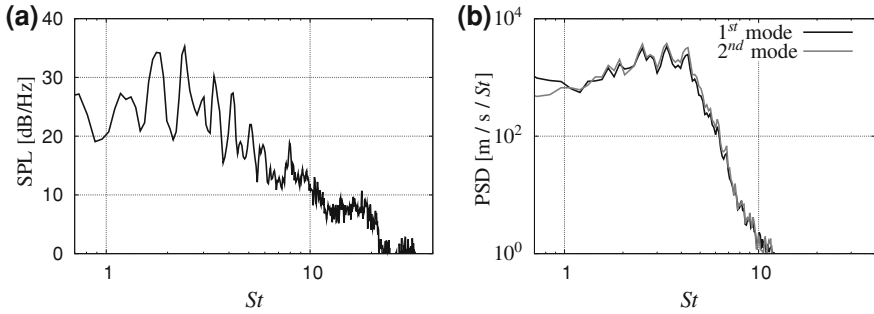
Fig. 1 a Sound pressure level at the acoustic far-field. Fluctuations calculated with Ffowcs Williams-Hawkings analogy for a point under the airfoil at a distance from the cove equal to ten times the airfoil stowed chord. **b** Power spectral density of the time-dependent amplitude of the first two POD-modes

In this last equation, $t^{(j)}$ stands for the jth time instant or realization and the amplitude coefficient a_k is computed by the projection of the empirical data on the kth POD mode. By construction, the ensemble average of a_k verifies $\bar{a}_k = \sqrt{\lambda_k}$; the POD modes are consequently ranked according to their importance in the flow by λ_k.

4 Results

The Sound Pressure Level (SPL) spectra at a point in the far-field, computed by the Lattice-Boltzmann simulation and the FW-H method, is presented in Fig. 1a. A number of tonal peaks are visible for $St = f U_\infty / c_{stowed} < 7$.

Based on the data from the time-accurate simulation, POD modes are calculated with the zero-mean velocity field in the region of the slat. The spectrum of the first 100 POD eigenvalues is presented in Fig. 2a. The spectrum shows that many modes are significant in the dynamics of the flow inside the cove. The first mode correspond to less than 4 % of the sum of all N=9,000 eigenvalues and 100 eigenmodes are needed to represent only 66 % of the coherence of streamwise velocity component.

The first two POD-functions illustrate important aspects of the unsteady flow in the cove. The x-velocity components of these functions are presented in Fig. 2b and c. The first couple of modes correspond to traveling large-scale structures typical of mixing-layer instability waves [22].

The Power Spectral Density (PSD) of the projections $a(t^{(j)})$ (see Eq. 4) were calculated for the first and second POD-modes, and are shown in Fig. 1b. They present a hump with its maximum at $St = 2.5$. Using the same flow configuration as the present work, Souza et al. [20] presented frequency-domain POD-modes, considering flow realizations comprised of finite-time Fourier transform of the flow-field for the peak frequency observed at the far-field, $St = 2.42$ (Fig. 1a). The leading
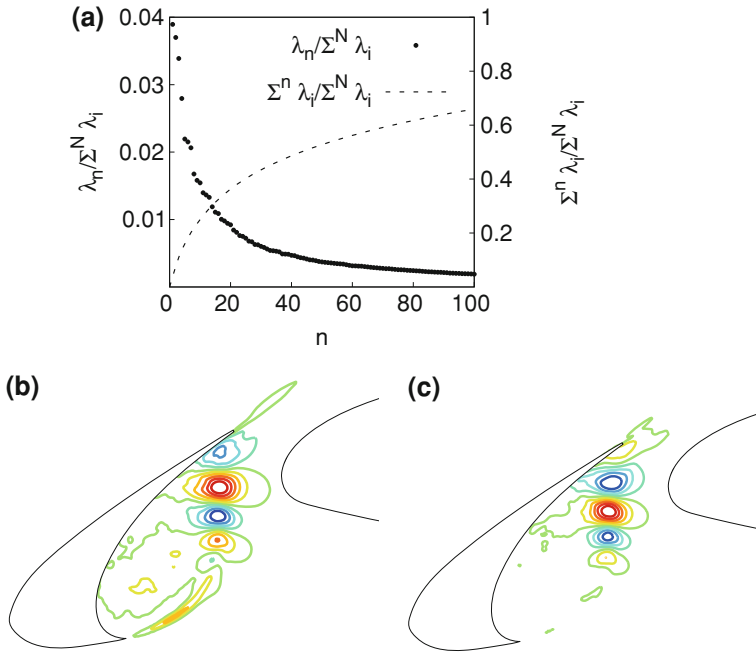
Fig. 2 a Spectrum of POD-eigenvalues and X-velocity component of the **b** first and **c** second POD-functions

frequential POD-functions exhibited distinct large-scale structures associated with the mixing-layer instability, very similar to those presented here.

5 Final Remarks

A time-accurate Lattice-Boltzmann simulation was carried out for the geometry of a high-lift airfoil to enable the study of the unsteady flow inside the cavity of the slat, which is responsible for noise generation. Coherent structures inside the slat cove were educed by means of Proper Orthogonal Decomposition. The first two POD-modes indicate the dominance of vortices generated by mixing-layer instability. Power Spectral Density of the time-dependent amplitude of these two POD-modes showed that their dominant frequency agrees with the strongest tone in the spectrum of noise radiated from the slat to the far-field.

References

1. B. S. Aflalo, L. G. C. Simões, R. G. Silva, and M. A. F. Medeiros. Comparative analysis of turbulence models for slat noise source calculations employing unstructured meshes. AIAA Paper 2010–3838, 2010.
2. G. A. Brès, F. Pérot, and F. Freed. A Ffowcs Williams-Hawkings solver for Lattice-Boltzmann based computational aeroacoustics. AIAA Paper 2010–3711, 2010.
3. M. M. Choudhari, M. R. Khorrami, D. P. Lockard, H. L. Atkins, and G. M. Lilley. Slat cove noise modeling: A posteriori analysis of unsteady RANS simulations. AIAA Paper 2002–2468, 2002.
4. M. M. Choudhari, D. P. Lockard, M. G. Macaraeg, B. A. Singer, C. L. Streett, G. R. Neubert, R. W. Stoker, J. R. Underbrink, M. E. Berkman, M. R. Khorrami, and S. S. Sadowski. Aeroacoustic experiments in the Langley low-turbulence pressure tunnel. Technical Report NASA TM 2002–211432, 2002.
5. W. Dobrzynski. Almost 40 years of airframe noise research: What did we achieve? Journal of Aircraft, 47(2), 2010.
6. W. Dobrzynski and M. Pott-Pollenske. Slat noise source studies for farfield noise prediction. AIAA Paper 2001–2158, 2001.
7. Fares E (2006) Unsteady flow simulation of the Ahmed reference body using a Lattice Boltzmann approach. Computers and Fluids 35:940–950
8. Holmes P, Lumley J, Berkooz G (1996) Turbulence, Coherent Structures. Cambridge University Press, Dynamical Systems and Symmetry
9. T. Imamura, H. Ura, Y. Yokokawa, and K. Yamamoto. A far-field noise and near-field unsteadiness of a simplified high-lift-configuration model (Slat). AIAA Paper 2009–1239, 2009.
10. L. N. Jenkins, M. R. Khorrami, and M. M. Choudhari. Characterization of unsteady flow structures near leading-edge slat: Part I. PIV measurements. AIAA Paper 2004–2801, 2004.
11. M. R. Khorrami, M. M. Choudhari, and L. N. Jenkins. Characterization of unsteady flow structures near leading-edge slat: Part II. 2D computations. AIAA Paper 2004–2802, 2004.
12. Khorrami MR, Singer BA, Berkman ME (2002) Time-accurate simulations and acoustic analysis of slat free-shear-layer. AIAA Journal 40(7):1284–1291
13. A. Kolb, P. Faulhaber, R. Drobietz, and M. Grünewald. Aeroacoustic wind tunnel measurements on a 2D high-lift configuration. AIAA Paper 2007–3447, 2007.
14. D. P. Lockard and M. M. Choudhari. Noise radiation from a leading-edge slat. AIAA Paper 2009–3101, 2009.
15. D. P. Lockard and M. M. Choudhari. The effect of cross flow on slat noise. AIAA Paper 2010–3835, 2010.
16. D. P. Lockard and M. M. Choudhari. The influence of realistic Reynolds numbers on slat noise simulations. AIAA Paper 2012–2101, 2012.
17. M. Pott-Pollenske, J. Delfs, and J. Reichenberger. A testbed for large scale and high Reynolds number airframe noise research. AIAA Paper 2013–2260, 2013.
18. L. G. C. Simões, D. S. Souza, and M. A. F. Medeiros. On the small effect of boundary layer thicknesses on slat noise. AIAA Paper 2011–2906, 2011.
19. L. Sirovich. Chaotic dynamics of coherent structures. Parts I-III. Quarterly Applied Math., XLV(3), 1987.
20. D. S. Souza, D. Rodríguez, and M. A. F. Medeiros. Effect of an excrescence in the slat cove: Flow-field, acoustic radiation and coherent structures. Aerospace Science and Technology, 2013.
21. D. S. Souza, D. Rodríguez, and M. A. F. Medeiros. A study of the sources of slat noise using proper orthogonal decomposition. AIAA Paper 2013–2163, 2013.
22. M. Wei and J. B. Freund. A noise-controlled free shear flow. Journal Fluid Mechanics, 546, 2006.

Noise Predictions of the Advanced Noise Control Fan Using a Lattice Boltzmann Method and Ffowcs Williams–Hawkings Analogy

R. M. Orselli, B. S. Carmo, J. R. Meneghini, R. L. Queiroz and A. S. Bonatto

Abstract The purpose is to simulate numerically the flow and noise on the Advanced Noise Control Fan (ANCF). The ANCF model was developed by the NASA Glenn Research Center to provide measurement data of a turbofan flow and its corresponding generated noise. The aim of the numerical simulations is to predict accurately the tonal noise as well as the broadband content of the ducted rotor/stator model using as a reference the provided far-field noise measurements.

1 Introduction

Noise generated by turbofan engine is one of the major noise sources in an airplane. Turbo compressors and turbines are not only used in the engines but also in the compact air conditioning packs and in the auxiliary power units. In contrast to open rotors like propellers, helicopter rotors and wind turbines, most of those turbomachines are attached to ducts, which influence the sound generation and propagation.

We focus on the fan noise which is one of the main noise sources of turbofan engines. The far-field sound propagation of the rotor-stator system within a nacelle has two significant main features: (a) an overall broadband noise radiation due to the motion and stretching of turbulent flow eddies; (b) an intense tonal noise generation at specific frequencies as a result of rotor-stator interaction coupled with duct mode propagation in the nacelle. In the present study, compressible transient direct aeroacoustics computations are performed on the Advanced Noise Control Fan (ANCF)

R. M. Orselli · B. S. Carmo (✉) · J. R. Meneghini
Fluid Dynamics Research Group, Department of Mechanical Engineering,
Escola Politecnica, University of Sao Paulo, Sao Paulo-SP 05508-030, Brazil
e-mail: bruno.carmo@usp.br

R. L. Queiroz · A. S. Bonatto
Embraer, Sao Jose dos Campos-SP 12227-901, Brazil
e-mail: rudner.queiroz@embraer.com.br

geometry. The simulations aim to compute the tonal noise as well as the broadband content. The focus of this study is the comparison of the simulated results to the detailed far-field noise measurements linking that to the origin of the tonal and broadband content. The present ANCF geometry noise measurements were obtained through the experimental tests conducted at the NASA Glenn Research Center in 2008; a summary of the data was published in [1]. The sound propagation is computed directly by the simulation as well as by applying the Ffowcs Williams and Hawkings acoustic analogy. This study is an extension of a previous numerical simulation of the ANCF geometry published in [2] as the sound is also computed by the Ffowcs Williams and Hawkings acoustic analogy, which gives further insight into the noise sources and propagation.

2 Governing Equation and Numerical Methods

The software PowerFlow is used to compute the transient compressible flow on the ANCF configuration as well as the corresponding aerodynamic noise generation and propagation. The code is based on the Lattice Boltzmann Method (LBM). The LBM is based on the Boltzmann equation which allows to obtain the macroscopic fluid variables [3]. A modified $k - \varepsilon$ model is used to describe the subgrid turbulence contributions. More details about the LBM within the PowerFlow code are given in [4].

As sound waves propagate over very large distances with little dissipation, the use of the LBM to compute the sound propagation may be computationally challenging including strategies to avoid numerical dissipation. To overcome this problem, some analytical methods such as the acoustic analogy may be used to compute sound propagation. In the acoustic analogy, the fluid dynamic equations are manipulated in order to obtain a wave equation on the left hand side, and nonlinear terms, usually related to sound sources, on the right hand side. This strategy was applied to derive a formulation known as Ffwocs Williams and Hawkings analogy (FW–H). The original formulation can be rearranged in a more general way so as to consider a fictitious integration surface enclosing all sound sources, approach known as porous FW–H formulation. More details about the FW–H formulation as well as its implementation within the LBM PowerFlow code may be found in [5].

3 ANCF Fan Noise Simulation Setup

The ANCF geometry used for the experiments comprises a fan surrounded by a 4 foot duct installed in the anechoic test facility of the Aeroacoustics Propulsion Laboratory at the NASA Glenn Research Center. The rotor/stator system with 16 rotor-blades and 13 stator-vanes operates at 1,800 rpm. The induced mass flow due to the fan has a Mach number of M $\sim$ 0.15. The fundamental Blade Passing Frequency (BPF) is
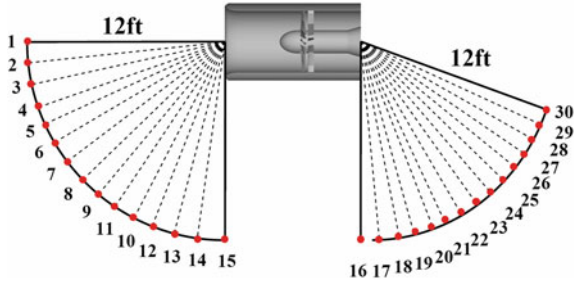
Fig. 1 Position of the microphones used for the measurements. The microphone angles are referred to their upstream positions 0°–90° and to their downstream positions 90°–160°. Extracted from [2]

$f_0 = 480\,\text{Hz}$ (rotor frequency times the number of blades). The acoustic pressure around the fan was measured at thirty far-field microphones located at a 12-feet distance regarding the duct inlet and outlet center [6] as depicted in Fig. 1.

The tip clearance of the fan is not considered in the simulation. The coarse mesh applied in the outermost regions combined with the use of buffer zones reproduce the anechoic behavior so that all perturbations towards the external boundaries are damped. The local atmospheric static pressure and zero flow velocity are prescribed at all computational external boundaries. The computational domain was discretized with a total number of 16.74×10^7 voxels (LBM basic elemental cubic cell) divided by zones from the most refined to the least refined resolution. In the LBM, the time step advancement is explicit linked to the voxel size of each zone. In the finest zone, the time step is $dt = 2.44 \times 10^{-6}$ s. The flow is simulated to an equivalent physical time of 21 full turns of the rotor. The simulation of the rotor rotation is done by using a Local Reference Frame (LRF) approach: a cylindrical region around the rotor is considered to rotate in the same relative motion with respect to the rotor. More details of the LRF approach can be found in [7].

4 Numerical Results and Discussions

Besides the direct sound computation (LBM), the sound at each of the 30 microphone positions (see Fig. 1) is also computed by FW–H acoustic analogy. According to the porous FW–H formulation, two spherical surfaces, respectively, around the duct inlet and exhaust are used as FW–H integration surface from which the sound is computed at the 30 microphones. Both sphere surfaces are placed so as to capture all sound sources (provided by the direct simulation) that comes out from the nacelle.

In order to evaluate the computed acoustic results, their sound spectra are compared to the corresponding experimental values provided by NASA Glenn Research Center as well as from [1]. The sound pressure levels obtained at microphones 4 and 20 are presented in Fig. 2. Comparing the tonal levels with the corresponding
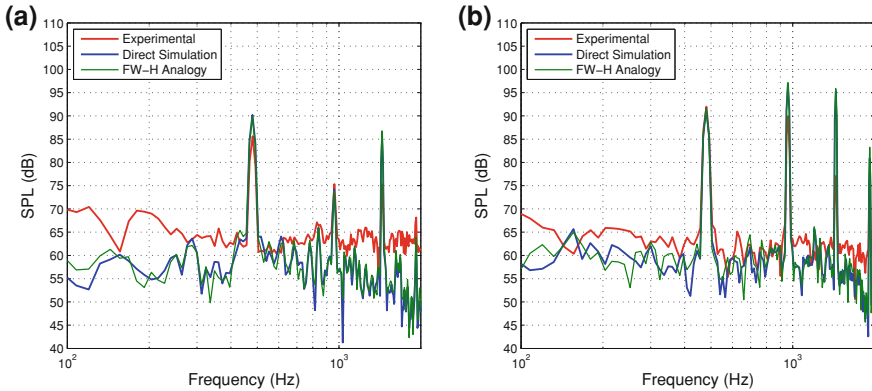
Fig. 2 Sound spectrum (SPL) at microphones 4 and 20, respectively, (**a**) and (**b**). *Red* indicates the experimental data, *blue* and *green* are, respectively, the levels of the simulation and FW–H

experimental data, at the BPF frequency ($f_0 = 480$ Hz) the levels agree well for microphone 20 and do not match for microphone 4. At first harmonic frequency ($f_1 = 960$ Hz), despite the fact that the tonal levels do not agree very well with the corresponding experimental levels, a better agreement was obtained for microphone 4. At the second harmony frequency ($f_2 = 1,440$ Hz), the tonal levels do not agree at all with the corresponding experimental ones, in fact, the levels are much higher in relation to the experimental levels. Regarding the average levels of the broadband noise, a slight decrease of the broadband sound levels for frequencies higher than approximately 1,200 Hz is observed. In addition, at lower frequencies the levels are mostly 5–10 dB below the experimental values. A possible explanation may be due to details or parts of the geometry that were not considered in the simulations as well as the grid resolution at the boundary layers inside the duct which contribute as sound sources to the broadband content. With regard to the noise levels obtained by the FW–H method, they agree very well with the corresponding levels predicted by the direct simulation. In fact, as the spherical integration surfaces were positioned to capture most of the sound sources from the fan including the nacelle bellmouth and the fact that the assumption of quiescent flow between observer and source of the FW–H formulation was not too restrictive in this particular case resulted in the good agreement obtained between the results. At least for these microphones for which good agreement was obtained, the results indicate that the FW–H method can be used in place of the direct simulation as the later has an additional computational cost. By the direct method, the noise is computed by the numerical simulation based on the LBM, whereas, in the FW–H approach, the sound is obtained straightforwardly by resolving surface integrals [5]. The similar results obtained by the direct computation and the FW–H analogy show that the grid resolution between the microphone and the FW–H integration surface is fine enough to compute the wave propagation at the frequencies range 100 Hz–2 kHz. Therefore, the broadband sound levels as well as the tones discrepancies (regarding the experimental values) are probably related to the
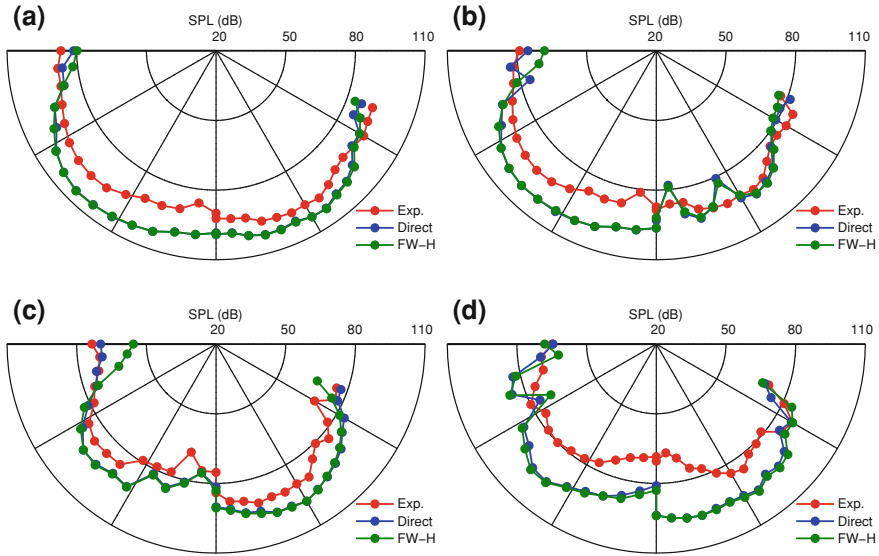
Fig. 3 Sound directivity at microphones 1–30. **a** OASPL, **b** $f_0 = 480$ Hz, **c** $f_1 = 960$ Hz, and **d** $f_2 = 1,440$ Hz. *Red* indicates the experimental data, *blue* and *green* are, respectively, the levels of the simulation and FW–H

flow inside the duct, that is, it is due to sound sources rather than sound propagation. As the microphones are positioned not too far from the nacelle, the computational cost involved in the direct sound propagation computation is not too challenging which makes the direct computation still an option.

The noise directivity levels around the ANCF geometry considering the BPF, its first and second harmonics frequencies are shown in Fig. 3. The corresponding OverAll Sound Pressure Level (OASPL) compiled at the frequencies range 100 Hz– 2 kHz is also presented in Fig. 3. In the polar graphs, the radial coordinate corresponds to the sound levels and the angle coordinate represents the angular position of each microphone with regard to the streamwise direction (according to Fig. 1). Analysing the obtained noise levels at the BPF frequency, it can be noticed an overall better agreement with the experimental levels at the downstream microphones (angles 90°– 160°) in comparison with the upstream ones (angles 0°–90°) where the noise levels are approximately 10–15 dB higher, except for the first three microphones where the sound levels present an irregular behaviour. At the first harmonic frequency, the predicted noise levels generally follows the corresponding experimental levels but with average values approximately 10 dB higher. On the other hand, at microphones 1, 2, 3 and 30, the FW–H noise levels are significantly lower than the experimental ones. Therefore, the FW–H acoustic analogy combined with its integration surface location cannot predict the noise propagation behaviour at these particular microphones where the sound levels are lower (silent zone). The sound diffraction interaction with the upcoming flow upstream the duct inlet, not taken into account by the FW–H analogy,

might be a reason for the discrepancy between the FW–H and the direct computation sound levels. Finally, at the second harmonic frequency, observing the noise level pattern in Fig. 3d, the predicted levels are approximately 10–15 dB higher than the corresponding experimental levels.

The absence of tip clearance and outlet shaft are also good candidates to explain the discrepancies. In fact, according to the experimental results presented in [8] of another NASA fan model, the tip clearance may contribute on the order of 1–5 dB in the broadband and tonal levels at least towards the aft-radiating side. The discrepancies of the results also relies on the fact that inflow non-uniformness may affect tonal and broadband levels significantly, i.e., the noise levels may be very sensitive to the inlet flow conditions including missing geometrical details which may not be fully represented by the numerical simulation.

An accurate prediction of the fan noise is still very challenging at the present day in terms of computational cost as well as representation of the geometrical details, however the present one showed that it is possible to well capture noise level tendencies such as directivity and spectral shapes as well as the tonal frequencies (BPF and harmonics), which gives great insight into the noise generation mechanism. Finally, it should be pointed out that broadband noise and tonal noise are generated due to quite different mechanisms [9], which may be a possible explanation, on the one hand, for the over-prediction behavior of tonal levels and, on the other hand, for the under-prediction of the broadband levels.

References

1. McAllister J, Loew RA, Lauer JT, Sutliff DL (2009) 47th Aerospace sciences meeting and exhibit. Paper number AIAA 2009-0624
2. Mann A, Perot F, Kim M, Casalino D, Fares E (2012) 18th AIAA/CEAS Aeroacoustics conference and exhibit). Paper number AIAA 2012-2287
3. Chen S, Doolen GD (1998) Lattice Boltzmann method for fluid flows. Ann Rev Fluid Mech 30:329
4. Li Y (2012) An improved volumetric LBM boundary approach and its extension for sliding mesh simulation. Ph.D. thesis, Iowa State University
5. Brés G, Perot F, Freed D (2010) 16th AIAA/CEAS aeroacoustics conference. Paper AIAA 2010-3711. Stockholm, Sweden
6. Loew RA, Lauer JT, McAllister J, Sutliff DL (2006) 36th AIAA fluid dynamic conference and exhibit, San Francisco. Paper number AIAA 2006-3150
7. Pérot F, Kim M, Moreau S, Henner M, Neal D (2010) 16th AIAA/CEAS aeroacoustics conference and exhibit. Paper number AIAA 2010-3887
8. Hughes C, Woodward R, Podboy G (2005) 11th AIAA/CEAS aeroacoustics conference. Paper AIAA 2005-2875. Monterey, California
9. Smith MJT (1989) Aircraft noise. Cambridge University Press, Cambridge

Acoustic Resonances in Open and Closed 3D Cavities

L. M. González, S. Ortiz and P. Cobo

Abstract Airframe noise is a significant component of the total noise radiated by an aircraft on approach. Although these tones are generated as the result of a complex interaction between the turbulent air flow and the cavity, it is expected that the acoustic resonances of the cavity approach the noise tones at low Mach numbers. Moreover, an accurate design of noise control systems of these cavity tones can be facilitated through an advanced knowledge of the acoustic resonances of the open cavity. The present work presents a computational method to predict the acoustic resonances of a 3D open cavity. A multi-dimensional Helmholtz equation closed with appropriate Perfectly Matched Layer absorbing boundary conditions is solved. Results of the method in the presented three dimensional cavity configuration are shown, the results of which have been compared with experimental measurements in a three-dimensional (cubic) open cavity. Moreover, the noise generated by an electric machine inside of a wind turbine is also studied as direct application of the numerical methodology dealing with very complex geometries.

1 Introduction

Aerodynamical noise is omnipresent in the context of air and ground transportation, penalizing the acoustic comfort inside airplanes and vehicles, and increasing the environmental noise in the vicinity of airports. Wheel well compartments are sources

L. M. González (✉)
School of Aerospace Engineering, Avda. Arco del Triunfo 4, 28004 Madrid, Spain
e-mail: leo.gonzalez@upm.es

S. Ortiz · P. Cobo
Centro de Acústica Aplicada y Evaluación No Destructiva (CAEND), CSIC, Serrano 144, 28006 Madrid, Spain
e-mail: santiago.ortiz@caend.upm-csic.es

P. Cobo
e-mail: pcobo@caend.upm-csic.es

of high level cavity tones during landing and takeoff airplane operations. The fundamental mechanisms underlying the coupling between the flow instability and the underneath open cavity have been elucidated by many investigators [3, 4, 6, 10]. Several researches have reported numerical methods to provide the eigenvalues (resonant frequencies) and eigenfunctions (normal modes) of open cavities without flow. More recently, Koch [8] and Hein et al. [7] proposed to find the acoustic resonances of two dimensional (2D) and three dimensional (3D) rectangular open cavities by solving the Helmholtz wave equation through high order finite element methods. A seminal experiment performed by Verdugo et al. [12] shows that most of the resonant frequencies computed by the Helmholtz model are in excellent agreement with those obtained when using the response of a microphone located inside the cavity for a tunnel flow velocity of approximately 21 m/s. The method presented herein provides the resonant frequencies and the normal modes of an open cavity and needs to implement absorbing conditions (PML) at the boundaries of the numerical domain to avoid unphysical reflections at such computational boundaries. A direct comparison with measurements can straightforwardly be carried out. The layout of the paper is as follows. Section 2 re-examines the computational model based on the Helmholtz equation and the PML implementation. In Sect. 3, the numerical results of the model are presented for a variety of problems, starting with a 2D open cavity and finishing with a complex 3D cavity placed in a wind turbine, some of these results have been validated with experiments. Concluding remarks are given in Sect. 4.

2 Physical Model and Computational Implementation

The acoustic wave equation can be developed from the linearized Euler equations assuming an adiabatic process of an ideal gas where the velocity field **v** has no base flow contribution and is just created by the acoustic perturbation. The equation of state can be formulated as a function of the acoustic pressure p, the density perturbation ρ, the reference density ρ_0 and the bulk modulus B as $p = B\rho/\rho_0$.

Substituting the linearized equation of state, the final result is the acoustic wave equation, which models the propagation of small pressure perturbations in a homogeneous physical medium:

$$\frac{1}{c^2}\frac{\partial^2 p}{\partial t^2} = \nabla^2 p \tag{1}$$

where $c^2 = B/\rho_0$ is the square of the propagation speed. In the following equations, those variables with an asterisk superscript imply dimensional quantities, whilst those that have no asterisk, are non-dimensional. In order to obtain a non-dimensional formulation, velocities will be non-dimensionalized with the ambient speed of sound, denoted by $c = c_0^*$, while the scales for length, density and pressure were taken as D^*, $\rho_0 = \rho_0^*$ and $\rho_0^*(c_0^*)^2$.

The last step to obtain the Helmholtz equation is using separation of variables and assuming a harmonic time dependence of the form $p(\mathbf{x}, \mathbf{t}) = \phi(\mathbf{x})e^{-\mathbf{i}\omega^*\mathbf{t}^*}$, where $\phi(x, y)$ is the potential velocity field, ω^* represents the circular frequency and t^* is time. After the non-dimensionalization process the Helmholtz equation (2) is finally obtained.

$$\nabla^2\phi + \omega^2\phi = 0 \tag{2}$$

where ω is a non-dimensional frequency given by the expression

$$\omega = \frac{\omega^* D^*}{c_0^*}. \tag{3}$$

In those cases where open boundaries and the radiation of energy to the infinity are present, a non-reflecting or absorbing boundary condition has been implemented. This kind of boundary condition absorbs the outgoing energy without un-physical wave reflections. Here a PML methodology [2, 8] has been chosen to overcome this difficulty, see [5, 9] for implementation details in a simple 2D open cavity.

Solid boundaries have a Neumann type boundary condition, implying a zero derivative in the normal direction $\frac{\partial\phi}{\partial n} = 0$. Using similar arguments as in [8], homogeneous Dirichlet boundary conditions on the external boundary of the PML subdomain have been used.

The variational formulation of Eq. (2), taking into account the boundary conditions, finally leads to the following generalized eigenvalue problem

$$\mathbf{R}^{PML}\hat{\phi} = \omega^2\mathbf{M}^{PML}\hat{\phi} \tag{4}$$

where $\mathbf{R}^{PML}$ and $\mathbf{M}^{PML}$ are the modified stiffness and mass matrices respectively, affected by the local coefficients from the PML implementation, see [5, 9].

As can be observed in this generalized eigenvalue problem, the eigenvalues are represented by ω^2 and the eigenvectors are $\hat{\phi}$. This problem has been solved through an iterative method such as the shift and inverse Arnoldi algorithm [1, 11] as the memory and CPU-time requirements of the direct method do become excessive.

The PML parameters have been chosen according to the experience of previous authors [7, 8]. Most of these parameters, including the shift parameter, have been varied and their influence on the results has been studied, concluding that the selected values herein, are the optimal ones for this problem.

Table 1 Open cavity resonant frequencies results

Mode (i, j, k)	Measurements f (Hz)	Helmholtz f (Hz)	Error (%)
(0, 0, 0)	155	151.7	2.1
(0, 0, 1)	568	567.3	0.1
(2, 0, 0)	673	679.4	0.9
(2, 0, 1)	843	857.5	1.7
(0, 0, 2)	1,088	1,088.4	0.03
(2, 0, 2)	1,270	1,273.1	0.2

Comparison between measured and numerical simulations. These results have been obtained after a convergence process with different computational domains and mesh refinements

Fig. 1 Modes (0,0,1) (*left*) and (2,0,0) (*right*) computed by the Helmholtz-PML technique
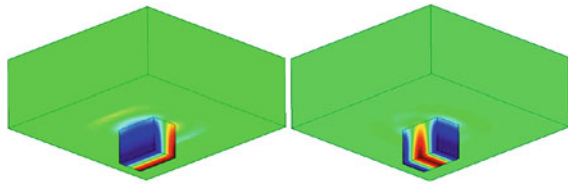

3 Results

3.1 Open Cavity

In order to solve the 3D open cavity a non-structured mesh with $N_{el} = 293,045$ tetrahedral elements and $N = 406,004$ nodes was used. The mesh size inside the cavity was $h = 0.03$. A three-dimensional rectangular open cavity was built to compare the numerical method previously described with measurements. The open cavity has dimensions $(L, D, W) = (53, 38, 32)$ cm, corresponding to the (x, y, z) axis and the open surface is placed parallel to the xz plane. A loudspeaker and eight microphones were used to measure the loudspeaker-microphone time responses in the cavity. The real part of the normalized eigenvalues corresponds to the frequency of the resonant modes while the imaginary part is a measure of the radiation loss. Each resonant mode is denoted by three integer numbers (i, j, k), where $i, j, k = 0, 1, \ldots$ are the length, depth and width mode numbers inside the cavity corresponding to the x, y and z directions respectively. Table 1 shows a comparison between the resonant frequencies obtained by two different methods: Helmholtz eigenvalue problem and experimental measurements. As can be observed, the agreement among them is remarkable. Finally, let us illustrate some of the revealed normal modes. Figure 1 shows the 3D representations of the axial modes (0,0,1) and (2,0,0), respectively.

Fig. 2 Inner part of the geometry of the nacelle (*left*). External view of the computed mode corresponding with frequency $f = 3{,}099.5$ Hz
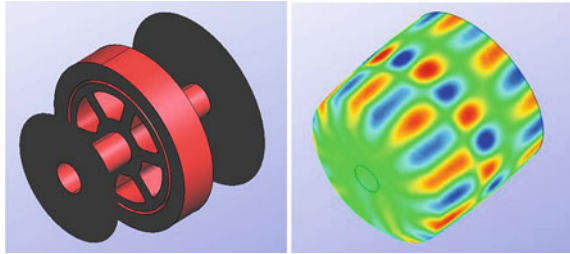
3.2 Closed Cavity Inside the Nacelle of a Wind Turbine

A second example is an industrial application for the detection of a tonal noise generated inside the nacelle of a wind turbine. As can be appreciated in Fig. 2 the 3D geometry inside the nacelle of the turbine contains the gearbox and the electric generator and consequently is extremely complex in its mesh generation. For this complex geometry a non structured tetrahedral mesh with mesh size $h = 0.03$ was used, the number of elements and nodes in this case was $N_{el} = 331{,}678$ and $N = 500{,}788$. Figure 2 shows the 3D representations of the mode corresponding to a frequency of $f = 3{,}099.5$ Hz.

   Due to the fact that the noise could be generated by the resonance effect created by the nacelle cavity when the generator works at its characteristic frequency, a detailed study of this characteristic frequency range was performed. This can be done using a shift parameter in the Arnoldi algorithm equal to the frequency displacement. The characteristic frequency of the electric generator depends on the rotation velocity as:

$$f_g(\text{Hz}) = 90 \cdot n(\text{Hz}) \tag{5}$$

where f_g is the characteristic frequency of the generator and n is the rotation velocity of the rotor, both expressed in Hz. Due to wind variations, the rotation velocity range goes from 80 up to 240 rpm, where the characteristic rotation velocity is 230 rpm. This velocity corresponds to a characteristic frequency of $f_g = 345$ Hz. As the first computed mode has a frequency equal to 351.43 Hz, which is very close to f_g, this explains the upcoming noise generated by the resonant effect.

   To solve this problem a new design of the nacelle was implemented where the first resonant frequency has moved to another value far from the characteristic value f_g.

4 Conclusions

The acoustic resonances of two different geometries have been studied from a computational point of view and the results have been validated experimentally. The numerical study was based on a finite element discretization of the Helmholtz

equation where the presence of an open domain was included through the use of a PML methodology. These conditions absorb the energy radiated by the cavity and avoid spurious reflections of the acoustic waves. The quadratic non-structured mesh used was locally refined near the inner corners when Neumann boundary condition were implemented. In the case of the 3D open cavity an experimental characterization of the cavity based on the measurement of the time responses between a tweeter and microphones was performed. Experimental and numerical results have been obtained and compared within a certain frequency range. An excellent agreement has been obtained between the frequency of the calculated eigenvalues, representing the modal frequencies, and the maxima of the tweeter-microphone transfer functions. The geometric flexibility of the numerical approach allows for industrial uses of the proposed methodology to study resonances. Three-dimensional objects of arbitrary geometric complexity such as the interior of the nacelle of a wind turbine have also been studied herein and the cause of the noise has been linked to the characteristic frequency of the machine.

References

1. Arnoldi WE (1951) The principle of minimized iterations in the solution of the matrix eigenvalue problem. Q Appl Math 9:1729
2. Berenger J (1994) A perfectly matched layer for the absorption of electromagnetic waves. J Comp Phys 114:185–200
3. Bres GA, Colonius T (2008) Three-dimensional instabilities in compressible flow over open cavities. J Fluid Mech 599:309–339
4. Gloerfelt X (2009) Cavity noise. VKI lectures: aerodynamic noise from wall-bounded flows, Chap. 0. Von Karman Institute
5. Gonzalez L, Cobo P, Valero E, Theofilis V (2013) Acoustic resonances in 2d open cavities. Acta Acustica United Acustica 99:572–581
6. Plumbee HE, Gibson JS, Lassiter L (1962) A theoretical and experimental investigation of the acoustic response of cavities in an aerodynamic flow. Wright-Patterson AFB, Dayton, OH WADD-TR-61-75
7. Hein S, Koch W, Schoberl J (2005) Acoustic resonances in a 2d high lift configuration and 3d open cavity. In: AIAA proceedings, no. 2867 in 11th AIAA aeroacustics conference, Monterey CA, pp 1–15
8. Koch W (2005) Acoustic resonances in rectangular open cavities. AIAA J 43(11):2342–2349
9. Ortiz S, Cobo P, Gonzalez L, Rodriguez D, Theofilis V (2012) Acoustic resonances in a 3d open cavity: comparison of experimental and numerical results. In: Internoise 2012 proceedings, internoise 2012, New York, pp 1–12
10. Rossiter J (1964) Wind-tunnel experiments on the flow over rectangular cavities at subsonic and transonic speeds. Aeronautical Research Council Reports and Memoranda, London, N 3438
11. Saad Y (1992) Numerical methods for large eigenvalue problems. Manchester University Press
12. Verdugo FR, Stephens DB, Bennett GJ (2012) Partially covered cylindrical cavity flow: resonance identification. In: fiv 2012 Proceedings, flow induced vibration 2012, Dublin, pp 267–274